NANYANG TECHNOLOGICAL UNIVERSITY

FAB. OF VHAR μ-MOLD BY SU-8 LITHO & E-FORMING

FABRICATION OF VERY HIGH ASPECT RATIO MICROMOLD BY SU-8 PHOTOLITHOGRAPHY AND ELECTROFORMING

ZHANG JUN

ZHANG JUN

SCHOOL OF MECHANICAL & AEROSPACE ENGINEERING

2007

2007

Fabrication of Very High Aspect ratio Micromold by SU-8 Photolithography and Electroforming

Zhang Jun

School of Mechanical and Aerospace Engineering

A thesis submitted to the Nanyang Technological University
in fulfilment of the requirement for the degree of
Doctor of Philosophy

2007

Acknowledgement

I would like to take this chance to express my deep thanks and appreciation to my advisor Professor Mary Chan Bee Eng, for her great support and enormous enthusiasm in guiding me through the study of my dissertation and carefully reviewing the draft, and for her great suggestions in the progress. She supported me in every possible way to advance my academic skills. Without her continuing encouragement, this work would definitely not be as it appears today.

I would also like to thank professor Miao Jianmin for his ingenious suggestions and insight, Mr. Sam Conner for the useful discussion. The author also would like to acknowledge Asst. professor Xu Rong, Dr. Jeyagowry Thirugnana, Dr Tietun Sun, Dr Jianxia Gao, Dr Ciprian Iliescu, Miss Shen Jinye and Mr Zhou Wenxiu for their help and the willingness to share their knowledge.

Thanks also go to Nanyang Technological University for funding the research. Assistance provided by technical staff in the *Micromachine Centre*, *Materials Lab* and *BCPE 1 Lab* is gratefully acknowledged. Special thanks go to Miss Tan Ruo Shan, the lab manager of BCPE 1 Lab for her help on supporting all the experimental affairs.

Lastly, I thank my dearest parents and my lovely family for love, support, encouragement and everything.

CONTENT

List of Figures

List of Tables

List of abbreviation

SEM	scanning electron microscopy
AR	aspect ratio
CPMAS	cross-polarization and magic angle spinning
DCE	downstream chemical etching
DGEBA	diglycidyl ether of bisphenol A
DI	deionized
DMA	dynamic mechanical analysis
DRIE	reactive ion etching
DRR	diffraction-refraction-reflection
DSC	differential scanning calorimeter
FTIR	Fourier transform infrared
GBL	gamma-butyrolactone
GC/MS	gas chromatography-mass spectrometry
HAR	high aspect ratio
HB	hard-baked
IPA	isopropyl alcohol
LIGA	Lithografie Galvanik Abformung
MAE	mechanical and aerospace engineering
MEMS	micro electro mechanical systems
MIBK	methyl iso-butyl ketone
MMC	micro-machine center
NMR	nuclear magnetic resonance spectroscopy
NTU	Nanyang Technological University
OP	optical profilometry
PDMS	polydimethylsiloxane
PEB	post exposure bake
PGMEA	propylene glycol methyl ether acetate
PMMA	polymethylmethacrylate
RIE	reactive ion etching
SOE	spiroorthoester
TECs	thermal expansion coefficients
TGA	thermal gravimetric analysis
VHAR	very high aspect ratio
VHARMs	very high aspect ratio microstructures
VH	Vickers hardness
TMS	tetramethylsilane
VSI	vertical scan imaging

List of photo mask

Mask label	Description	Figure index
Mask A1	23μm-wide by 2cm-long dark fields separated by 40μm-wide light fields, covering a rectangular area of 4.5 cm by 4.5 cm at the mask center	Figure 3.2(a)
Mask A2	10μm-wide by 2cm-long dark fields separated by 80μm-wide light fields, covering a rectangular area of 4.5 cm by 4.5 cm at the mask center	Figure 3.2(b)
Mask B	80μm-wide by 1000μm-long dark fields separated by 10μm-wide light fields, covering a 4-inch diameter circular area.	Figure 4.1(a)
Mask C	10μm-wide by 1000μm-long dark fields separated by 80μm-wide light fields, covering a 4-inch diameter circular area.	Figure 4.1(b)
Mask D	10μm-wide by 1000μm-long dark fields separated by 10μm-wide light fields, covering a 4-inch diameter circular area.	Figure 4.1(c)

Summary

Microstructures with very high aspect ratio (VHAR) have diverse applications because the increased surface area leads to increased volume handling and sensitivity desired for many MicroElectroMechanical Systems (MEMS). Polymer replication, rather than direct patterning, is desired for economically viable MEMS. One key factor to successful VHAR polymer replication is the fabrication of a suitable mold. In this project, micromold with VHAR (>10) and dense microchannels was fabricated by SU-8 photolithography followed by electroforming. The fabricated SU-8 mold was then used for electroforming and Ultra-Violet (UV) embossing.

A new theoretical model incorporating effects of diffraction, refraction and reflection on the profile characteristics of VHAR microchannels in thick resist has been developed to predict the profiles of micro channels in thick SU-8. Previous model for the profile of microstructures only included effects of diffraction. When applied to our VHAR dense microchannels, the model cannot predict the unsuccessful processing of such channels since the effects of light reflection at the wafer and diffraction at the mask dark field and high sensitivity of SU-8 lead to crosslinking under the shadowed area. Detailed studies were carried out to investigate the effect of UV exposure on the profile of VHAR microchannels. Our predicted values (i.e. channel widths and taper angle) compared well with experimental values. A process combining soft cushion technology and dose reduction was developed to fabricate whole-wafer-covered dense SU-8 gratings with both VHAR microchannels and VHAR SU-8 walls.

Kinetics during the curing of SU-8 resist in the presence of gamma-butyrolactone (GBL) was investigated. GBL was a reactive solvent during the photolithography process.

Network properties and degradation kinetics of cured SU-8 were also studied. In generals, a high epoxy conversion leads to dense cross-linked network. The presence of GBL also leads to long chains between cross-links and low cross-link density. Kinetic studies showed that the network properties of cured SU-8 strongly affected the degradability. The thermal degradation activation energy of SU-8 decreased exponentially with the increase of molecular weight between cross-links. Also, the presence of GBL gave better degradability of cured SU-8 because GBL resulted in long chains between cross-links and low cross-link density as well as GBL offered additional ester structural units with C-O bond. Chemical degradation of cured SU-8 was studied, using concentrated sulfuric acid. The network was broken into water soluble fragments by sulfuric acid dissolution and the fragments contained carbonyl, aromatic, alkyl and other groups.

SU-8 is intrinsically hydrophobic. However, dense micropatterns further made the SU-8 surface super-hydrophobic. When attempting to electroform on SU-8 surfaces patterned with dense VHAR microchannels, the electrolyte cannot contact the seed layer and the circuit was mostly open even with agitation - the process cannot proceed. Argon plasma was therefore used to overcome the hydrophobicity. Detailed studies to monitor changes in SU-8 roughness, surface energy and chemical composition were conducted to determine the optimum process window. A large area VHAR and dense copper grating with alternate microwalls and microchannels of aspect ratios of 15.3 and 9.2 respectively over the entire 100mm-diameter area were fabricated by copper electroforming from a plasma treated SU-8 master. This copper mold was used as a mold for UV embossing, demonstrating the feasibility of this technique for the creation of durable molds for mass replication.

Chapter 1 Introduction

1.1 Background and motivation

Microstructures with very high aspect ratio (VHAR, defined as height/width>10, Figure 1.1) offer a high active area per unit substrate surface area, the possibility of high packing density and high throughput in continuous flow systems due to high cross-sectional area per unit substrate area. High surface area microstructures are particularly important for chemical or biochemical applications like microreactors, micromixers, chromatographic columns or DNA concentrators as they allow high volumetric throughput for high-sensitivity performance and multitasking within a small area. Higher packing densities and planar multifunctionality are needed in many multi-functional Micro Electromechanical Systems (MEMS) for diverse applications such as DNA separations, protein microarrays, biosensors or nano well-plates.

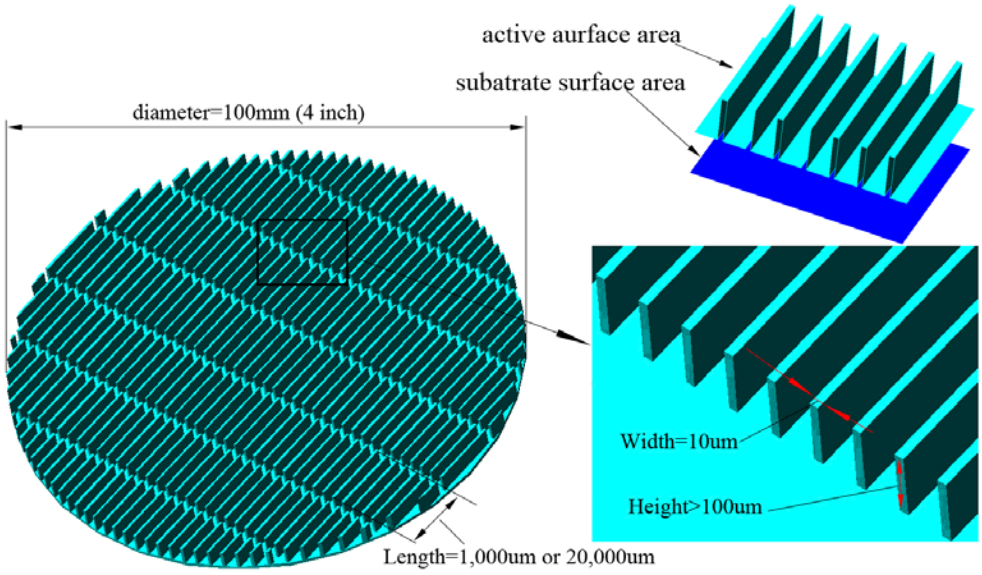

Figure 1.1 Sketch of the microstructures with VHAR over large area

Polymeric replication is a pattern transfer technique using a microstructured metallic or rigid plastic mold to imprint into liquid polymer which is subsequently hardened. It

offers a convenient method of micropatterning. Polymeric replication is a low-cost alternative to silicon-based MEMS technologies for a range of present and future commercially viable products. Ultra-violet (UV) embossing, also known as UV-based imprint technique, involves using a microstructured mold to imprint into liquid polymer which is subsequently UV polymerized. UV embossing is a low temperature and low-pressure process. It enables high accuracy replication across large areas. Molds can be polymeric or metallic. Typically, the mold used for UV embossing is a child mold replicated from a master mold which is in turn replicated from a microstructured master (Figure 1.2). The process of making the VHAR master mold is typically tedious and expensive. One key factor to successful high aspect ratio UV embossing is the fabrication of a suitable master, which is the focus of this project. One or more methods such as thick resist photolithography, deep reactive ion etching (DRIE), diamond fly cutting or LIGA (LIthografie Galvanik Abformung) can be used. In this research, thick resist photolithography using epoxy-based SU-8 is used for the master mold.

In this study, we are interested in making UV embossing molds with long (length>1000 μm), straight, dense (spacing<100 μm) and VHAR microchannels covering the entire 100mm-diameter wafer. An UV embossed micro-array from the mold will have a large opening volume to lateral surface area ratio. Such micro-arrays are being investigated for cell guidance in tissue engineering and Lab-On-Chip protein separation studies in our laboratory. For cell culture and tissue engineering, a large area scaffold (generally in cent meters) is needed and covered with cells. A large area dense pattern with significant depth is required for *in vivo*-like three-dimensional (3-D) cell culture. Whole-wafer-covered SU-8 microstructures will be used as master for poly(dimethylsiloxane) (PDMS) molding and copper electroforming. The PDMS structure and metal mold will then be used as molds in UV embossing to fabricate scaffolds for tissue engineering.

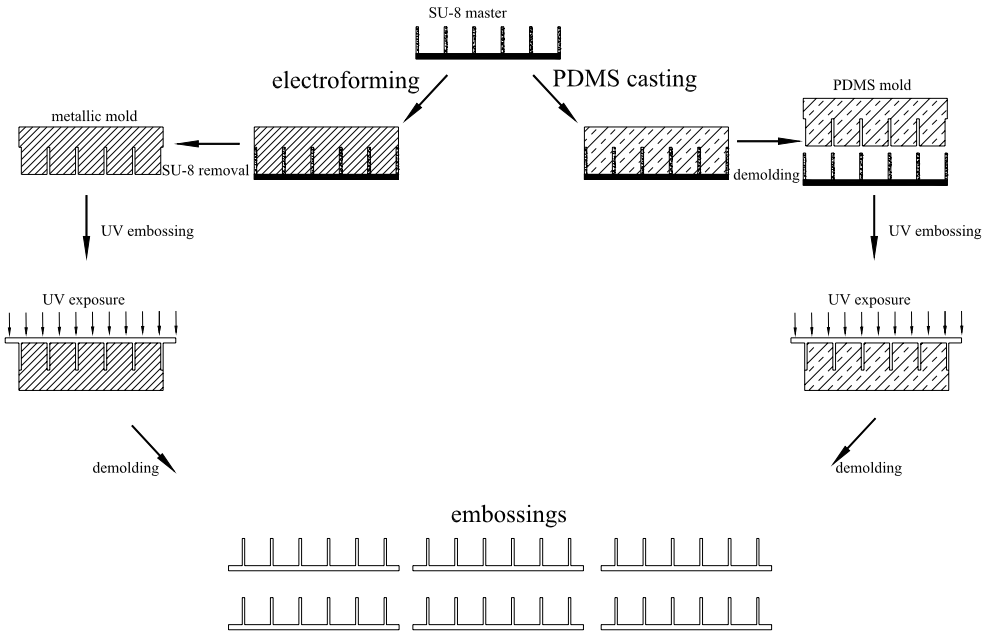

Figure 1.2 Sketch of the replication process by UV embossing

1.2 Problem statement

For use as mold, the profile SU-8 characteristics such as the taper angle of the side wall and surface roughness of the microstructures are very important. A slight taper angle (<5˚) facilitates demolding. Fabrication of VHAR SU-8 microstructures has been studied in the past, but much less effort has focused on the profile characteristics, especially the side wall taper angle and side wall roughness. The profile characteristics of dense gratings separated by microchannels with VHAR are affected by the widths of the light field lines and dark field lines on the mask, UV exposure and edge bead. Other challenges in processing long straight dense microstructures are insufficient strength of the pattern, adhesion of adjacent SU-8 bars to each other after solvent development and insufficient adhesion strength of the pattern to the substrate.

Typical high aspect ratio microstructures fabricated by others have a relatively large distance between them, i.e. the microchannels are wide compared to the resist bars. With sparse gratings, the effect of diffraction behind the mask and reflection at the

silicon wafer can be ignored. With dense gratings as in the present research, diffraction and reflection have significant effects on the profile characteristics and processability of the pattern. Fresnel diffraction behind the mask limits the attainable uniformity of the UV dose across the photoresist thickness. In fact, research has shown that diffraction strongly affects the size of patterns and sidewall profiles in UV lithography printing. Further, although the optical reflection from a highly reflective substrate such as silicon has a strong influence on the attainable resolution and profile of gratings, very little research has been conducted to understand the effect of reflection on the profiles of deep channels in thick resist. With dense grating, the reflection of light from the silicon wafer can cause stray light to the unexposed area under the dark field, resulting in unresolved grating.

Further, the removal of cured and microstructured epoxy-based SU-8 resist after electroforming is a great challenge. In this regard, we used concentrated sulfuric acid for SU-8 removal. It is also important to understand crosslinking reactions, network properties and degradation kinetics in order to ensure the successful removal of thick resist after electroforming. Although crosslinking reaction of SU-8 has been reported, curing reactions and network vary significantly, depending on the processing conditions. Simple and basic reactions described in the literature are not able to explain the actual complex SU-8 resist curing process. Network properties and degradation kinetics of cured SU-8 have not been reported.

1.3 Objectives

Following from the above, the objectives of this research are to

1) Theoretically simulate and verify the UV intensity distribution across SU-8 resist

during photolithography and to predict the profile characteristics of VHAR microchannel. The effects of reflection, refraction as well as diffraction on the profiles of microchannels in thick resist are also studied.

2) Develop processes to fabricate SU-8 gratings with both VHAR (AR>10) bars and VHAR (AR>10) microchannels over a large area (100 mm- diameter wafer).

3) Study the chemical reactions in SU-8 curing and acid degradation and investigate the effects of processing parameters on the network properties and degradability of SU-8.

4) Fabricate metallic mold from SU-8 gratings by electroforming and effective removal of SU-8 after electroforming.

5) Demonstrate the suitability of electroformed micro mold for UV embossing.

1.4 Outline

Chapter 2 of this dissertation surveys the literature on high aspect ratio fabrication, especially the properties and processing of SU-8 resist. Chapter 3 discussed the diffraction, refraction and reflection effects during UV lithography, using thick SU-8 resist. A new diffraction-refraction-reflection model has been developed to predict the SU-8 pattern size and profiles of microchannels in SU-8 resist. The theoretically predicted results are compared with experimentally observed results to confirm the applicability of the new model. Chapter 4 develops process techniques to fabricate whole-wafer-covered high aspect ratio dense SU-8 gratings. Soft cushion technique and exposure dose reduction are employed in the process. Chapter 5 presents detailed studies on the curing and degradation of SU-8 resist. Chemical reactions during the curing of SU-8 and network of cured SU-8 are proposed. Kinetics of thermal

degradation of SU-8 are also investigated. Chapter 6 discusses the electroforming of copper mold from SU-8 master. Surface modification procedures for improved hydrophilicity are developed. The UV embossing of VHAR polymeric micro pattern is demonstrated in this chapter. Finally, the conclusions of this dissertation are drawn and future areas of research are suggested in chapter 7.

Chapter 2 Literature review

2.1 MEMS and Lithography

Micro **E**lectro **M**echanical **S**ystems (**MEMS**) devices and microstructures have been fabricated mostly with technologies derived from the microelectronics industry, in which photolithography is widely used. Conceptually, photolithography is simple. A pre-cleaned substrate is first spin-coated with a uniform layer of resist pre-dissolved in organic liquid solvent. A soft-bake of the resist is usually necessary to remove the resist solvent and promote adhesion. Selected areas of the resist are then exposed to a radiation source, often through a mask[2], thereby transferring the pattern from the mask to the wafer. Upon sufficient exposure dose, differential solubility of the exposed and unexposed areas of resist in solvent is created. For positive resists, exposure results in the breakdown of molecules, leading to improved resist solubility in subsequent solvent development. For negative resists, exposure causes the molecules to react with each other, resulting in reduced solvent solubility. As the lithography process transforms a 2-dimensional pattern on the mask into a 3-dimensional structure in the resist and eventually the patterned film, the depth profiles are important. By choosing the right developer, temperature and developing time, one can obtain straight, round-off or undercut depth profiles in the resist[3]. Lithography resolution limit is determined by the radiation wavelength [4]. State-of-the-art lithography typically employs optical projection printing operating at the conventional Raleigh diffraction limit. With contact printing, the smallest dimension that can be reliably printed is equal to the wavelength of the light being used [5].

2.2 Very high aspect ratio microstructures (VHARMs) in patterned polymer films

VHARMs offer a number of advantages. For example, in sensor applications, VHARMs offer higher sensitivity by virtue of a large mass and surface area.

For many applications, particularly in the biochemistry and biomedical fields, polymeric materials are a better choice of fabrication material because of biocompatibility[6-8]. Patterned polymer films are important for diverse applications such as organic electronic devices, biomedical engineering, sensors and microfluidics[9-18]. Molding polymeric microstructure is relatively less expensive, but such a process requires a master mold. Patterned polymer films are used as matrix or scaffolding to guide tissue development [19] by controlling the shape, size, and the spatial position of cells anchored to a surface. VHARMs in patterned polymer films combine the merits of VHARMs and polymer materials which include economical costs, mechanical flexibility, transparency biodegradability, and ease of surface modification.

2.3 Replication for patterning polymer films

Plastic molding or replication techniques offer significant cost saving over metal-forming technologies. Replication, rather than direct patterning, is rapidly becoming the industry standard for microstructure fabrication because of low cost, ease of fabrication and desirable properties of polymers[7, 8, 14, 20-26]. Replication processes can fabricate large numbers of highly precise and complex microstructures from a single similarly precise master[6] and are well suited to transfer patterns from several micrometers down to the nanometer scale.

Polymer replication techniques include micro injection molding [27, 28], imprint lithography [29-31] and soft lithography[31-34]. Imprinting is a key process for diverse

and cost-efficient replication of micro- and nano- structures. In the process, a prepatterned mold is brought into soft contact with a thin polymer film located on top of a substrate. By applying pressure and increasing the temperature or exposing to radiation, the mold pattern is transferred into the polymer. Imprint lithography is capable of high throughput due to parallel processing and can be envisaged to be a commercially viable alternative to expensive or capital-intensive photolithography or silicon etching or deposition techniques[35-38]. The varieties of imprint lithography include thermal[39-41] and UV[42-45] embossing. With a single master or stamp, identical structures can be produced over large surfaces. The technique can be used for multi-layer structures and also diverse materials which include polymers and organically modified ceramics (ORMOCERs) [44].This technique is well established for low aspect ratio microstructure fabrication, for example, in compact disc molding and in the manufacture of holographic security features [41]. In comparison with optical lithography, it is not limited by light diffraction when a transparent mold is used and thin resist films can be patterned down to 10 nm[46, 47].

2.4 Master for replication

The difficult and expensive step for VHAR replication is the fabrication of the master or mold tool with proper taper angle, surface roughness and surface chemistry. Once this is made, it can be replicated into the desired polymer substrate by a number of techniques within a short turnaround time[8]. For use as a master for subsequent child mold generation, the profile characteristics of the microstructures, such as taper angle of the sidewall, are very important[48]. If the side-walls of the mold are perfectly vertical, i.e. with a taper angle of 90°, then the removal of the replicated microstructure from the master will involve the initial detachment and frictional sliding of the wall of the replicated microstructures from the trench of the master. If the taper angle is less than

90° (Figure 2.1), the inclination of the sidewalls reduces post-detachment contact and frictional resistance between the replicated microstructure and master. However, taper angles substantially smaller than 90° are geometrically incompatible with VHARMs. Consequently, precise control of the sidewall taper angle of master to a small but finite deviation from verticality is imperative for the use of microstructure as a mold for VHAR replication.

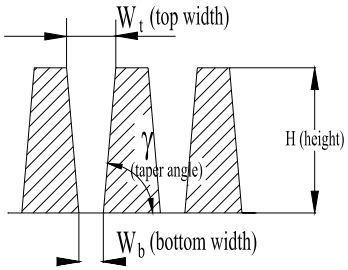

Figure 2.1 Sketch of profiles of VHAR master

2.5 Thick resist for VHARMs microfabrication

Interest in thick-photoresist applications is steadily growing [49-59]. Thick resist can be used for fabrication of the master mold[53, 60-62]. Many challenges exist in the processing of very tall and narrow microstructures (i.e. VHARMs) in these ultra-thick photoresist films. These include uniform photoresist coating, a gentle and uniform baking process, developing efficiency of deep photoresist trenches and tremendous residual stress formed after the curing[63]. Photoresist used for high-resolution integrated circuit (IC) manufacturing are typically coated thinly on the substrate. Issues and challenges related to VHAR photoresist processing do not pose a problem in IC manufacturing. Furthermore, lithographic modeling and characterization tools are not available for photoresist films in the tens and hundreds of microns thickness range of interest to VHAR fabrication [59].

Thick and ultra-thick positive (e.g. Novolak based AZ 9260, AZ4562 and ma-P 100 [53, 60, 61, 64-70]) and negative (e.g. JSR THB-430N and SU-8[54, 69, 71, 72]) resist have

been used for applications in MEMS. Novolak-type positive photoresists (e.g. AZ 4620 and AZ 9260 (Clariant)) have been presented for use in the UV-LIGA process[53, 60-62]; an aspect ratio of up to 15 for a 100 μm deep mold has been obtained, using ZA9260 and a standard UV mask aligner [60]. However, line shapes using Novolak and ma-P 100 positive photoresists are not completely perpendicular but have a "mushroom" or “T” shape[53, 60, 61] which is unsuitable for replicating mold. Light diffraction results in unexpected exposure under the dark field of mask pattern, leading to "mushroom" or "T" shaped structures in positive resists and sloped side wall or "V" shaped channel in negative resists. The thicknesses of Novolak based AZ-series photoresists are typically limited to about 100 μm [60, 73] because the transmitted energy decreases towards zero at about 90 μ m thickness[60]. The ma-P 100 is less sensitive to UV light between 350 nm to 450 nm and the sensitivity needs to be improved for better resolution [53]..

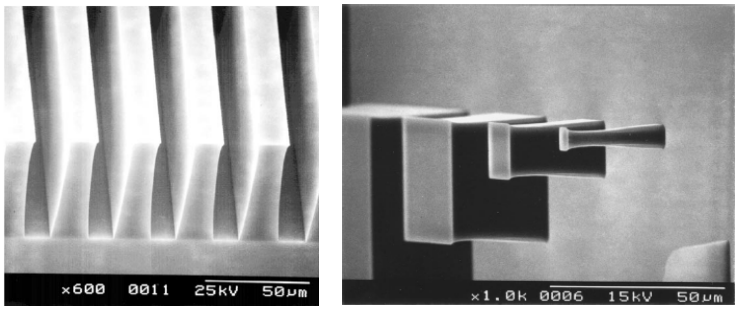

Figure 2.2 Typical line shape of UV patterned positive photoresist (a) AZ 4562 [53] and (b) mp-100 [74].

Negative resist JSR THB-430 N was reported[54] to be suitable for ultrathick photoresist fabrication. The thickness of JSR THB-430N can be as high as 110 μm formed by single-spin coating, using a conventional spin coater. Thick photoresist layer with thickness of up to 1.4 mm has been realized by multi-spin coating[54]. An open microstructure with an aspect ratio of 8 has been fabricated, using ultrasonic agitation

during development. However, this photoresist has the shortcomings of poor line-width resolution, easy undercut[73, 75] and high surface roughness [76, 77] .

One particularly good negative epoxy-based resist is SU-8, which is able to provide features with VHAR (>10) using UV-lithography.

2.6 SU-8 for dense gratings with VHARMs

2.6.1 SU-8 and its properties

Nano^{TM} SU-8 was first developed by IBM [78]. The reported absorption coefficient of this resist at 365nm wavelength is less than 30/cm[79] and has very high optical transparency (more than 80% for 100 um thick SU-8 film[80]) above 360nm, making it ideally suited for imaging near vertical side walls in very thick films and has been widely used in MEMS on different substrates [52, 58, 72, 77, 80-108]. SU-8 is now a standard resist for HAR micromachining [109] and its ability to produce VHARMs in photolithography has been demonstrated [110-113]. SU-8 also has been shown to have attractive mechanical properties [114-118]. The reported Young's module (E) of SU-8 was 4.3-5.3 GPa[115] and the thermal expansion coefficient was $52\pm5.1\times10^{-6}$ /°C[114]. Microfabricated SU-8 was widely used as the mold for electroplating and electroforming[88, 94, 95, 119].

SU-8 has 8 epoxy groups per SU-8 molecule (Figure 2.3). The SU-8 photoresist is prepared by dissolving the resin SU-8 in gamma-butyrolactone (GBL). The quantity of GBL solvent determines the viscosity and hence the range of possible resist thickness[120-122]. The resist contains 10 weight percent of triaryl sulfonium hexafluoroantimonate salt acting as a cationic photoinitiator. SU-8 can be dissolved in a

variety of organic solvents such as propylene glycol methyl ether acetate (PGMEA), GBL, or methyl iso-butyl ketone (MIBK) to provide solutions containing up to 85% solids by weight. The low molecular weight of the resin provides excellent solubility and planarizing capability, and the high epoxy functionality provides sensitivity. [123]

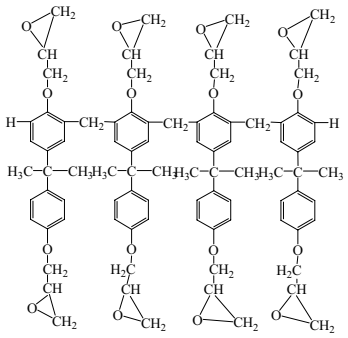

SU-8

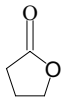

GBL

Figure 2.3 Molecule of SU-8 and GBL

SU-8 is most commonly processed with the near UV (350-400nm) radiation or i-line (365nm), although it may be imaged with e-beam, ion beam or x-ray[58, 98, 99, 104, 112, 124-130]. The general processing steps of SU-8 include coating, soft bake, exposure, post exposure bake (PEB) and development (Figure 2.4). The coating process is normally done by spin coating. The desired SU-8 films thickness can be achieved by selecting appropriate SU-8 resist formulation and spinning conditions. After SU-8 has been applied to the substrate, it must be soft baked to evaporate the solvent and densify the film. Upon exposure to near UV radiation, a photochemical transformation takes place; upon absorption of a photon (i.e. light), a strong acid ($HSbF_6$) is generated[131] from the photoinitiator. The acid is only formed where the SU-8 has been exposed to

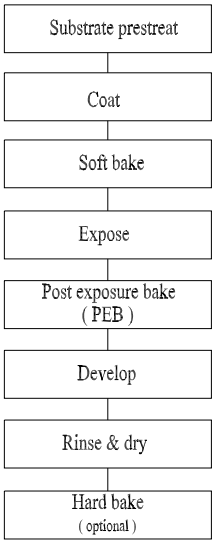

Figure 2.4 Processing procedures

light. After exposure, SU-8 is heated in PEB above the glass transition temperature (T_g) of SU-8 (50°C) [110] above which molecular motion is less constrained. The PEB selectively cross-links the exposed portions of the film.

(a) Lewis acid generated from the decomposition of triarylsulfonium hexafluoroantimonate salt upon UV exposure

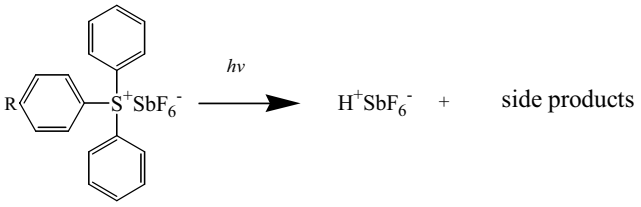

(b) Initiation of the polymerization by ring opening of the epoxy during PEB

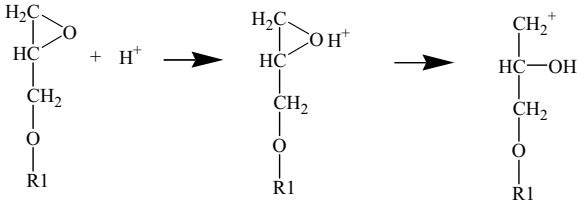

(c) Chain propagation of the cross-linking reaction during PEB

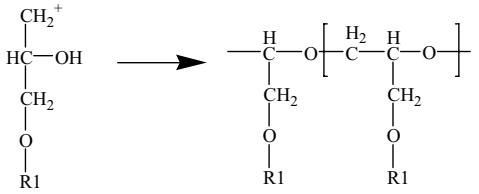

Figure 2.5 Chemical reaction of SU-8 cross-linking

The photo-initiated cationic polymerization of epoxy has been thoroughly investigated [132-134]. Reported chemical reaction of SU-8 cross-linking is shown in Figure 2.5 [123, 135, 136]. Lewis acid is generated from the decomposition of triarylsulfonium hexafluoroantimonate salt upon UV exposure (Figure 2.5 a). The cross-linking reaction occurs when SU-8 is heated over its T_g (50°C[137, 138]). The acid acts as the catalyst to initiate the polymerization by opening the epoxy ring in the SU-8 molecule (Figure 2.5 b). Then the chain propagation cross-links the SU-8 resist to tight network (Figure 2.5 c). It is noteworthy that light is required in the above processes only in amounts sufficient to generate trace quantities of a catalytic substance. The polymerization itself proceeds by a dark or nonphotochemical process [139]. In the cross-linking reaction,

each epoxy group can react with others in the same and other molecules. The number of epoxy groups on the SU-8 leads to extensive cross-linking and dense network, which is insoluble in the developer. The unexposed material is then removed with the developers.

As previously stated, the octa-functionality of SU-8 provides sensitivity. The optimal exposure dose also depends on film thickness (thicker films require higher dosage) and process parameters. The sensitivity of SU-8 depends on the thickness, which is 30 mJ/cm^2 for layer thickness of 20 μm and 90 mJ/cm^2 for layer thickness of 200 μm [140]. Optimum cross-link density is obtained through careful adjustments of exposure and PEB process conditions.

2.6.2 Challenges in fabrication dense VHARMs in ultra thick SU-8 films

Although SU-8 has been widely employed in MEMS, recommended operational parameters differ in previous works[141-145]. The process data depend not only on the fabrication facilities, but also on the mask pattern and structure geometry. For a successful fabrication of dense SU-8 gratings (Figure 1.1, Chapter 1) with VHARMs which are used as the master for replication and electroforming, there are challenges need to be overcome.

2.6.2.1 Diffraction, refraction and reflection in ultra thick SU-8 photolithography

Previous work on processing parameters on profile characteristics of VHAR microchannels in SU-8 has been limited. Hagouel et al. [146] showed experimentally, using a 400 nm pitch periodic grating mask, that when the exposure energy dose increased, the exposed line width of the negative resist increased whilst the microchannel width between exposed lines decreased and the microchannel profile

slopes became more concave. Since the lithographic process relies on shadow printing, Fresnel diffraction behind the mask limits the attainable uniformity of the energy dose across the photoresist. Experimental research has also shown that diffraction strongly affects the size of patterns and sidewall profile in the UV lithography printing [147]. Typically, when the exposure energy dose increases the line width increases; the distance between lines decreases; and profile slopes become more concave[49]. Furthermore, light is reflected from the surface of silicon wafer substrate, affecting the resist profile.

Further, Cheng et al[74] predicted the profile characteristics of microchannels in SU-8, using a simplified model accounting for only Fresnel diffraction behind the mask. However, the model accounting for diffraction only is inadequate to accurately predict the profile characteristics of VHAR microchannels in SU-8. Light is reflected from the surface of silicon wafer substrate, affecting the resist profile. Although the reflection effect is very significant in UV lithography, there is no reported research that has quantified the effect of reflection under the shadow area in thick-resist UV lithography. Detailed studies of the effect of UV exposure dose on the taper angle and mask replication fidelity of VHAR microchannels in thick SU-8 have not been previously reported. It is, therefore, necessary to find a simple way of estimating the effect of diffraction and reflection on profiles, especially for dense gratings with VHARMs.

2.6.2.2 Edge bead of ultra-thick SU-8 layer

"Edge bead effect" occurs for thick films. It is resist buildup on the outer edge of the mounted substrate[61] introduced by the surface tension. The edge bead can only be removed by dissolving with some certain solvent [143]. During the baking process, the gravity force can affect the flatness of the SU-8 film and decrease the height of edge

bead, the re-flow of the photoresist also changes the thickness of the coated films during the soft-baking process. The presence of the edge bead will decrease the flatness of the coated surface; thus, photomask will not be completely in contact with the photoresist during exposure. Consequently, this will cause a poor lithography image due to the air gap between the photomask and the photoresist. For VHARMs application, close contact during exposure is critical to obtaining successful structures. A common method to remove the edge bead is chemical edge bead removal. A known drawback to this approach is the swelling of the resist along the wafer perimeter. Alternatively, one can fill the air gap with organic solvents [148]. However, the organic solvent will form a slippery layer, which may diffuse into SU-8 layer, forming a fragile structure[59].

2.6.2.3 Dense gratings with VHAR in thick SU-8 films

Although the process required to produce SU-8 structures remains challenging, it is the only resist used to expose 20 to 1500 um deep with aspect-ratios greater than 10:1 using either optical [149] or deep X-ray [127, 128] lithography. Recent publications reported 1 mm tall isolated SU-8 structures using optical lithography with aspect ratios exceeding 10:1 [53, 150] and 1.5 mm structures with 15:1 aspect ratios in the pattern[63]. Typical SU-8 microstructures fabricated by others were sparse structures [84, 151], i.e. the microchannels are wide compared to the SU-8 structures. No work has been found on dense VHARMs, such as dense gratings, in thick SU-8 films. The following factors limit the aspect ratio available for dense gratings in thick SU-8 films:

Firstly, with sparse structures, the effect of diffraction behind the mask and reflection at the wafer can be ignored. With dense VHARMs, diffraction and reflection have significant effects on profile characteristics and processability of the SU-8 pattern. The stray light under the dark field lines arising from diffraction and reflection will cause

problems in making highly dense VHARMs on a reflective surface. For the dense gratings with VHARMs, it is important that the microstructures accurately replicate the mask dimensions for such narrow and deep microchannels.

Secondly, the edge bead leads to thickness variation and non-uniform air gap between resist and the mask, which then results in very poor pattern uniformity for dense VHARMs over a large area.

Thirdly, SU-8 structure rigidity also plays a critical role in dense VHARMs fabrication. The target aspect ratio of this project is AR>10 over a large area. The target value is smaller than reported values of 66[151] and 26[152], which were obtained using isolated and zig-zag-shaped microstructure, but the structure rigidity is more critical for the long straight dense gratings than for those short or isolated structures.

Finally the difficulty of refreshing the developer in narrow and deep trenches is also a limitation to get a higher aspect ratio for VHAR dense narrow channels of dense gratings; and the adhesion caused by the surface tension force of solvents is also likely to collapse the structures during the drying.

2.6.2.4 Residual stress in SU-8 photoresist

Residual stress due to thick photoresist coatings is a key challenge for many applications. The residual stress can cause debonding at the resist–substrate interface[153] because if there is a larger stress between two bonded layers, it will be much easier to separate them[154]. For an ultra-thick SU-8 photoresist layer, the main stress comes from two sources. The first one arises from the difference between the thermal expansion coefficients (TECs) of the substrate and SU-8 photoresist. The TEC

of silicon is 2.6×10^{-6}/°C while the TEC of SU-8 is as high as 52×10^{-6}/°C [114]. The TEC difference between substrate and photoresist will introduce stress during heat treatment such as soft baking and PEB. In ultra-thick photoresist coating, this stress can be high; consequently, the wafer can be bowed after thermal processing [149]. The main stress is generated as the cross-linked photoresist cooling down[149]. Less stress is introduced during soft baking since polymer chain rearrangements can take place in the un-cross-linked photoresist and the residual solvent in the resist acts as a plasticiser to release stress. The second main source of stress in thick SU-8 layer is the crosslinking shrinkage during exposure and post exposure bake. The shrinkage of SU-8 is 7.5% [155] and constrained shrinkage induce high stress [53]. If they are excessively cross-linked, the patterns are likely to be deformed [152], causing adhesion failure between the SU-8 and substrate; the adhesion problem is more serious with some metals such as gold, copper, titanium and chromium than with silicon wafer.

There are three feasible ways to control stress. One method is to control the amount of exposure. The second is to adjust the heat treatment such as soft baking and post exposure baking. Gradual ramp heating up and cooling down, especially in the cooling down steps will decrease the residual stress. The third method is to relax the resist after processing.

2.6.3 Curing and degradation of SU-8 in presence of GBL

As the removal of this resist remains a great challenge, understanding the crosslinking reaction and network structure of cured SU-8 is very important for both the process optimization for VHARMs fabrication and removal of this resist after electroforming. The curing and chemical reactions are vital for process optimization and removal of this resist. Reported curing and chemical reaction of SU-8 was the cross-linking of epoxy

resin[123, 135, 136] (section 2.6.1), without consideration of the presence of GBL. GBL is the solvent added into SU-8 to achieve varied viscosity and hence the range of possible resist thickness for photolithography processing. It is typically assumed to only act as the solvent and would be removed in soft bake process before it was exposed to UV light. In a practical process, SU-8 is mainly used for thick resist application, with SU-8 thickness of hundreds micrometers to millimeters[156]. With the high coating thickness value, it is not easy to totally remove GBL. Thus, there is always GBL in SU-8 resist. No work on the role of GBL in the cross-linking reaction of SU-8 resist has been reported.

Known as un-homopolymerizable, GBL has a ring structure and double bond. There may be ring opening of the GBL as well as the ring opening polymerization of epoxy groups in SU-8 with the catalyst of Lewis acid generated by UV exposure. Reports on copolymerization of GBL are found in the literature[157-162]. GBL were copolymerized with epoxy resin[163-167] and kinetic study of the curing of a mixture of DGEBA and GBL was also reported[161, 164, 168]. GBL reacts with activated epoxide to form spiroorthoesters and copolymers[163, 168-170]. Four parallel reactions are expected in cationic copolymerization of epoxy and GBL solvent: (1) homopolymerization of epoxy groups (Figure 2.5), (2)formation of spiroorthoester (SOE) by reaction of epoxy with GBL (Figure 2.6I), (3) homopolymerization of SOE (Figure 2.6II) and (4) copolymerization of SOE and epoxy groups (Figure 2.6III)[161, 164-166, 168, 171]. SU-8 is chemically a multifunctional epoxy derivative of a bis-phenol-A novolac[123]. The cross-linking reaction of SU-8 photoresist in the presence of GBL and Lewis acid as the catalyst may not be as simple as polymerization of epoxy groups. The presence of GBL solvent in the resist during curing results in additional reactions and makes the curing of SU-8 complex. Reactions involved in SU-8 resist crosslinking include reactions

between GBL and SU-8 as well as the reaction of epoxy groups of SU-8. Further, bulk properties of cured SU-8 are highly dependent on the network structure which in turn determines its thermal degradability. By far, little research has been done to investigate the network and degradation of the crosslinked SU-8.

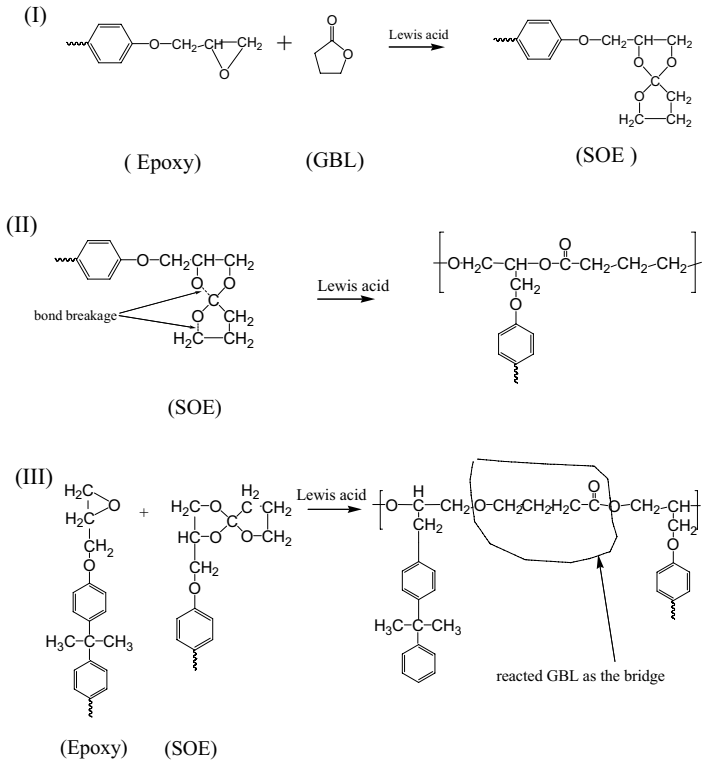

Figure 2.6 Chemical reactions of epoxy and GBL. (I) formation of SOE, (II) homopolymerization of SOE and (III) copolymerization of epoxy and SOE

SU-8 is epoxy-based resist. Various techniques have been used to follow the kinetics of curing of epoxy resins[172]. Fourier transform infrared spectroscopy (FTIR) is one of the techniques used, because it is possible to detect the variation of functional groups during curing. The peak at 910-916 cm^{-1} due to the epoxide ring absorbance[173-176], and the absorption band at 1600cm^{-1} due to the aromatic rings[177-181] chosen as internal standard [178, 181] are commonly used to monitor the curing of epoxy resin. The network of crosslinked polymer can be described by its crosslink density and molecular weight between crosslinks (Mc). DMA was widely used to study the network properties of crosslinked polymers[182].

Nuclear magnetic resonance spectroscopy (NMR) has been widely used to characterize polymers as a source of information on the molecular of the polymer blends[183-188]. Gas Chromatography-Mass Spectrometry (GC/MS) is a method that combines the features of gas-liquid chromatography and mass spectrometry to identify different substances within a test sample. NMR has relatively low sensitivity[189, 190], and the minimum detectable concentration is in the order of mMol/l[191]. GC/MS has been widely used in study of thermal degradation of polymers[177, 192] and polymer structural identification[193]. It offers high sensitivity with detection limits of 0.01-0.1 *u*g/L[194].

2.6.4 Removal of cross-linked SU-8

SU-8 can cross-link to a tight network[195]. The highly crosslinked network can be difficult to remove after utilization as an electroplating mold. In particular, reliable removal without damage to the plated metal has been a particularly difficult challenge [196] due to the very high cross-linking density [197]. Various methods of SU-8 removal have been investigated by others[78, 196-201]. For instance, Paul M. Dentinger et al [196] tried a number of solvents, such as *N*-methyl pyrollidinone (NMP) and MS-111 (a mixture of methylene chloride, phenol, and organic acids from Miller-Stephenson, Danbury, CT) and conditions and found that simple dissolution of the cross-linked polymer is not feasible. The solvent removal of SU-8 with electroplated metal is considerably more difficult than the removal of SU-8 from Si wafers, because the removal of SU-8 from Si is by stripping, cracking, delaminating, rather than dissolution. Isotropic etcher such as plasma and reactive ion etching (RIE) was also used for removal of cross-linked SU-8 [195, 196, 202]. RIE is an excellent alternative for thin films, but has not proved useful to scaling towards several hundred micron thick

films. Downstream chemical etching (DCE) was also tried to remove the SU-8[196, 199]. A necessity of CF concentration in DCE indicated the importance of fluoride chemistry on SU-8 removal. One possibility for the removal of SU-8 is to chemically disrupt the network by cleaving the aryl ether bonds. Lithium iodide (LiI), collidine and sodium sulfide (NaS) were used [198] to craze the SU-8 into small pieces. However, when the treatment was attempted with Ni interplated, the NaS dissolved the Ni leaving the SU-8 chunks still available. M. K. Ghantasala et al [78] showed that the laser micromachining technique has the potential to thoroughly remove SU-8 after electroplating a microstructure with copper.

It may be possible to include a sacrificial layer as reported by McGall [200]. On the other extreme, exceedingly oxidative methods have been used to remove and clean a variety of organic materials. Peroxydisulfate radical can be generated electrochemically in good yield and oxidizes effectively all organic matter [201]. Additionally, other highly oxidizing materials have been studied. Unfortunately, these highly oxidizing materials tend to be rather non-specific and oxidize most metals as well [196].

There is no reported fundamental investigation on the mechanism of chemical removal of SU-8 resist.

2.6.5 Dense SU-8 gratings for electroforming

Electroforming is a process for creating 3-dimensional metal parts by using a carefully controlled long-duration electroplating process. To fabricate microstructures by electroforming, a conductive plating base or seed layer and a means to induce the electrodeposit are needed. Portions of the seed layer are covered with an insulating masking, which is illustrated in Figure 2.7. Because of the ionic action of the process,

an exact replica of the mandrel surface is produced. This replica may itself then be used as a mandrel to replicate the original form. Therefore, a large number of identical forms can be produced from a single master [203].

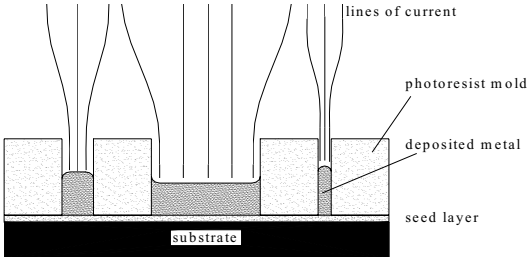

Figure 2.7 Sketch of electroforming setup

Electroforming has been widely used in MEMS[88, 94, 95, 119]. It is suitable for depositing microstructured conductors and electrically conductive magnetic structures[69]. Much has been reported on improving the electroforming quality by adjusting the bath composition[204-208], waveform[209-213] and operation conditions[72, 214-217]. Many researchers have used SU-8 structures as templating molds for Cu[87, 88, 145, 218] and Ni[219] electroforming but most of these reports have focused on HAR (AR~5) and spatially sparse microstructures, and no published work has been found on dense VHARMs electroforming using SU-8 as the mold. In the electroforming of VHAR narrow metallic structures over a large area, a difficulty arises in delivering the electrolyte to the seed layer and in refreshing the electrolyte in the deep narrow cavities of the master mold. The problem becomes more serious when SU-8 is used as the master mold because of the hydrophobic nature and consequent low wettability of plastic surfaces.

SU-8 has intrinsic hydrophobic properties; the water contact angle on a flat SU-8 surface is 80°[220-223]. Further, dense micropatterns make a surface super-hydrophobic [219], the water contact angle can be as high as 145º. When electroforming on SU-8

surfaces patterned with VHAR and dense microchannels, the electrolyte cannot contact the seed layer and the electroforming circuit is mostly open, even with agitation - the process cannot proceed. Further, there is poor refreshing of the electrolyte and hydrogen bubbles produced at the cathode fill up the microchannels; the resulting incomplete metal microstructure is filled with pores[224].

In order to overcome the hydrophobicity and consequent low wettability of polymeric surfaces, surface treatment is essential. Nordström et al[225-227] activated SU-8 surface by wet chemical treatment using ethanolamine dissolved in sodium phosphate buffer at pH 7.6. But the wet methods are unsuitable for dense SU-8 gratings with VHAR. Uniform coating is not easy for the hydrophobic SU-8, especially for the deep narrow channels. Further, liquids trapped in the VHAR and dense channels may deform the structures, the surface tension of the solvent may spoil the VHAR dense gratings during the treatment and drying process.

Plasma treatment has been widely used for surface cleaning and modification of polymers to improve the surface energy, adhesion and wettability[228] because wetting properties can be remarkably enhanced without affecting bulk properties[229]. Plasma treatment utilizes excited gas-plasma to chemically crack and dislodge contaminants from the surface and to activate the surface. The plasma is created by application of a radio frequency or microwave frequency radiation to a gas in a hermetically sealed, low-pressure reaction chamber. Plasmas contain several activated species such as electrons, ions, free radicals and some neutral species[230]. It is now well established that the glow discharge treatment creates physical and chemical changes such as cross-linking, degradation, and formation of free radicals[231] which modify the surface characteristics. The plasma under low pressure gives uniform contact of the reactive

atoms to SU-8 surface. Tseng et al [74, 141, 143, 232] used O_2 plasma to activate SU-8 surface in the fabrication of a surface tension driven fluidic system. However, O_2 plasma will result in undesirable extensive oxidation of our metallic seed layer leading to poor electrical contact with the electrolyte. We used argon plasma for increasing the hydrophilicity of SU-8.

2.7 Summary

SU-8 is suitable for the fabrication of VHARMs using UV lithography, but it is challenging to fabricate dense grating of VHARMs using this photoresist. As the dense grating will be used as a micro-mold for electroforming and polymer replication, the profile characteristics are very important and need to be studied in detail. Fabrication of VHAR SU-8 micro-structures using UV lithography has been widely investigated[71, 109, 143, 233], but little study has focused on the profiles of the HAR structures such as the side wall angle, which is very important for use as a mold. The profiles of the channels can be manipulated by varying the processing parameters. Both theoretical and experimental studies are needed to investigate the effect of processing conditions on the profiles made using SU-8 photoresist. Further, edge bead and SU-8 removal after electroforming from the SU-8 master are also potential difficulties for making flat and smooth metallic mold with uniform structures. Processing parameters affect the mechanical properties of the fabricated microstructures as well as the pattern dimensions of the VHARMs in SU-8. Research has been done on the optimized processing of SU-8[152]. With sparse L-shaped structures, SU-8 structure with aspect ratio as high as 26 has been reported [149]. But for the deep and narrow channel (i.e. HAR microchannels) in SU-8 layer, the reported highest aspect ratio was 17. Dense SU-8 gratings with HAR microchannels in SU-8 cannot be processed by conventional or

manufacturer's recommended processing parameters. Optimization should be done to obtain well controlled dimensions and good mechanical properties.

For dense SU-8 gratings to be used as a master for electroforming, surface modification is essential to increase the electrolyte wettability. Detailed studies to monitor changes in SU-8 roughness, surface energy and chemical composition are essential to determine the optimum process window for desired hydrophilicity.

The removal of the crosslinked SU-8 after electroforming remains a problem for the electroformed structures to be used as mold for polymer replication. Commercial SU-8 removers are available. But the removing mechanism and principle are not clear. Understanding the crosslinking reaction and network properties of cured SU-8 is very important for both the process optimization for VHAR structure fabrication and the removal of this resist after electroforming. So far, there is no research work has been done to investigate the curing reactions and degradation of SU-8. Studies should be done to investigate the curing, network properties and degradation of cured SU-8.

Chapter 3 Diffraction, refraction and reflection during exposure in lithography

3.1 Introduction

We are interested in using the dense SU-8 gratings with VHAR channels as a master for polymer replication. For use as a master mold for subsequent child mold generation, the profile characteristics of the microstructures (sketched in Figure 2.1), such as the taper angle of the sidewall, are very important[48]. Precise control of the sidewall taper angle of the master to a small but finite deviation from verticality is imperative for the use of the microstructure as a mold for VHAR replication.

The objective of this chapter is to theoretically simulate and predict the profile characteristics of VHAR microchannels in ultra thick SU-8 films (>50 μm). In order to develop a new model for simulation of the profiles, detailed experimental studies were also carried out to investigate the profile characteristics. We developed a new improved model incorporating effects of diffraction, refraction and reflection from the substrate surface on the profile characteristics of VHAR microchannels in SU-8 films. Huygens′ principle and superposition of spherical waves were employed in the theoretical deduction. Two grating masks (Figure3.1, denoted as Mask A1 and Mask A2) were used for sample calculation and experimental confirmation. For Mask A1, the length of the mask light field is 20 mm, the width of the mask light field is 40 μm and the width of mask dark field is 23 μm, and the pattern covered a rectangular area of 45 mm by 45 mm at the mask center. Dimensions of Mask A2 are the same as those of Mask A1 except that the width of the light field is 80 μm and the width of dark field is 10 μm.

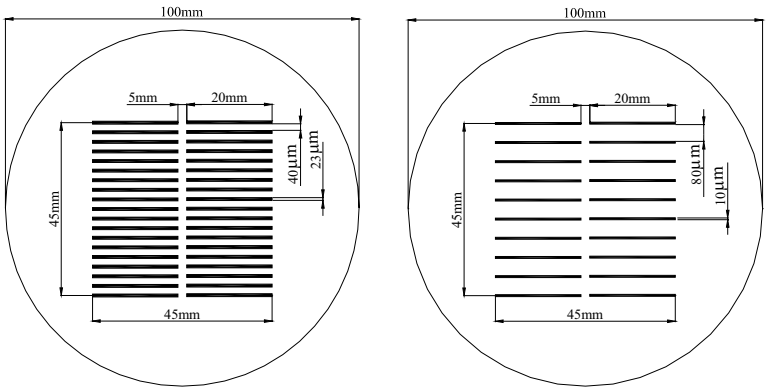

(a) (b)

Figure 3.1 Sketch of (a) mask pattern A1 and (b) mask pattern A2

The calculated mask replication fidelity and taper angle using the new diffraction-refraction-reflection (DRR) model was compared with the experimental results. The effects of light reflection, UV exposure time and air gap between SU-8 and mask were studied. Optimized processing parameters were then used to process the VHAR microchannels in SU-8.

3.2 Experimental details

All sample processing and characterization described in this section, unless otherwise stated, were carried out at the Micromachines Centre, School of Mechanical and Aerospace Engineering, Nanyang Techanological University, Singapore.

100-mm <1 0 0> p-type silicon wafers were used as substrates. The photoresist and developer used were NANO™ Epon® SU-8 100 and SU-8 developer supplied by Microchem Corporation (Newton, Massachusetts). Wafers were cleaned by immersion in Piranha solution (15:1 (v/v) 96%wt H_2SO_4: H_2O_2) at 120°C for 20 min followed by six de-ionized water rinses each lasting 3 min. To dehydrate the wafer, the acid cleaned wafer was then baked at 200°C for 30 min in a convection oven. SU-8-100 was spin coated onto silicon wafer at spin speed of 3000 rpm (SU-8 thickness of 100μm) or

5500rpm (SU-8 thickness of 66μm) for 30 s. The coated photoresist was then soft baked at 65°C and 95°C for 10 min and 30 min, respectively. It was then exposed to UV through Mask A1 or A2 (Figure 3.1) with a wavelength of 365 nm. (An I-line filter with a center wavelength of 365 nm and bandwidth of 10nm was used.)

The exposure was done using a J500-IR/VIS mask aligner (Optical Associate Inc., Milpitas, California, USA). The measured UV intensity was 10 mW/cm^2. The photoresist was exposed for different times (t_{exp}) of 35 s to 90 s to study the effect of exposure dose on the profile of the microchannels. Then the SU-8 was post-exposure baked (PEB) at 65°C and 95°C for 3 min and 10 min, respectively. For both the soft baking and PEB, the hotplate was pre-set at 65 °C before samples were placed on it; after the 65°C-bake, the temperature was ramped up to 95 °C in 1 min. Both the soft baking and PEB were completed by ramp cooling the sample from 95°C to room temperature in 60 min. After each step, i.e. spin coating, soft baking and UV exposure, SU-8 was "relaxed" by placing the wafer on a horizontal surface for 15 min at room temperature. The exposed resist was developed with Microchem SU-8 Developer at room temperature.

The cross-sectional profile of the dense gratings was examined using scanning electron microscopy (SEM) and optical profilometry (OP). SEM was done using a JEOL JSM-5600LV scanning electron microscope (JEOL USA, Inc. Peabody, MA, USA) or a HITACH S3500N (Kanda-Surugadai 4-chome, Chiyoda-ku, Tokyo 101-8010, Japan). OP was done using a WYKO optical profilometer (WYKO Corporation, Tucson, Arizona, USA), using the Vertical Scan Imaging (VSI) mode. The thickness of processed SU-8 films was measured using OP after the SU-8 films were patterned. The

experimental average aspect ratio (*AR*) of microchannels was defined as the ratio of thickness to the average width as in Equation (3-1). The side wall taper angle γ (Figure 2.1) is the average angle defined as in Equation (3-2).

$$AR = \frac{H}{\frac{1}{2}(W_t + W_b)} \tag{3-1}$$

$$\gamma = 90^{\circ} - \tan^{-1}\left(\frac{H}{0.5(W_t - W_b)}\right) \tag{3-2}$$

where *AR* is aspect ratio,

H is the thickness of photoresist,

W_t and W_b are top width and bottom width of the microchannels.

The gelation energy of 100-μm thick SU-8 was determined by varying the exposure time in small increments and evaluating the solubility of the exposed resist in the developer. During UV exposure, small octa-functional SU-8 molecules react to become a large cross-linked network molecule. At the gelation point, the network is one large molecule and becomes insoluble in the developer. We determined the minimum UV energy required by 100μm-thick SU-8 for gelation, i.e. the threshold gelation energy, by varying the exposure time in small increments. 100-μm thick SU-8 photoresist was spin coated onto a silicon wafer and then soft baked at 65°C for 10 min and 95°C for 30 min. The SU-8 was then UV exposed through a mask with a 5 mm by 5 mm square light field opening; the mask was moved from place to place on the coated wafer to produce an array of exposures. The exposure time varied from 0.5 s to 40 s in increments of 0.5 s, i.e. the exposure dose was varied from 5 to 400 mJ/cm^2 in increments of 5 mJ/cm^2. The PEB was done at 65°C for 3 min and 95°C for 10 min. The exposed samples were developed with the SU-8 developer for 20 minutes. The minimum UV dose required for non-solvation of the SU-8 in the developer, which was evident from visual inspection of the developed exposure array, was adopted as the “threshold gelation energy”.

The absorption coefficient of exposed and unexposed SU-8 was obtained by measuring the transparency of SU-8 films. Films with thickness of 50 μm, 100 μm and 150 μm were prepared by spin coating SU-8 onto 1mm-thick glass slices at 6200 rpm, 3000 rpm and 1800 rpm respectively and soft baking at 65°C for 6 min, 10 min, 20 min and 95°C for 20 min, 30 min and 50 min respectively. The exposure times were 40 s, 50 s and 60 s respectively. The transparency was measured using a Shimadzu UV-3101PC UV-VIS-NIR Scanning Spectrophotometer.

Dynamic mechanical analysis (DMA) was used to determine the elastic storage modulus of SU-8. The storage modulus is defined as the ratio [234]of the amplitude of the stress in phase with the strain to the amplitude of the strain in the forced oscillation of a material. SU-8 samples were prepared as in the above paragraph. The samples were scanned from 25°C to 250°C in nitrogen, using the 3-point bending mode. The frequency used was 1 Hz and the heating rate was 3 °C/min. The epoxy conversion in SU-8 was determined by measuring the residual epoxy group content in the SU-8 using a Nicolet Magna-IR 560 Fourier Transform Infrared (FTIR) spectrometer. The residual epoxy content was calculated using the peak area at 910 cm^{-1} which was normalized using the reference peak at 1600 cm^{-1}.

3.3 The Kirchhoff-Fresnel integral

According to Huygens' principle[235], every point on a wave can be considered as the source of a circular or spherical wavelet which expands outward from that point. The net displacement of the wave at any time in the future is the superposed sum of the wavelets from all points on the wave. The incident light from the point light source arrives at the aperture and then comes to the measured point (Figure 3.2). A spherical wave emitted from the point source can be represented by[235]

$$u(R') = A_0 \frac{e^{i(\mathrm{k}R' - \omega t)}}{R'} \tag{3-3}$$

where u is the amplitud

A_0 is the amplitude at R=0

R' is the distance measured from the source located at R=0.

ω is the angular frequency, $\omega = 2\pi f$, f is the frequency of the wave

t is traveling time of the wave

k is the wave number which is defined as $2\pi/\lambda$, λ is the wavelength

i is imaginary number defined by the property that i squared equals -1.

A wave arriving at an aperture generates secondary spherical waves. These newly generated waves, which have a fixed phase relation with the incident wave, propagate only in the forward direction. The origins of these secondary spherical waves are created in the plane of the aperture according to Huygens' principle. The amplitude of secondary generated waves arriving at the measured point is (Figure 3.2)

$$u = A_0 \frac{e^{i\mathrm{k}R'}}{R'} e^{i\alpha} \frac{e^{i\mathrm{k}R}}{R} \tag{3-4}$$

where R is the distance from the secondary point sources to the measured point.

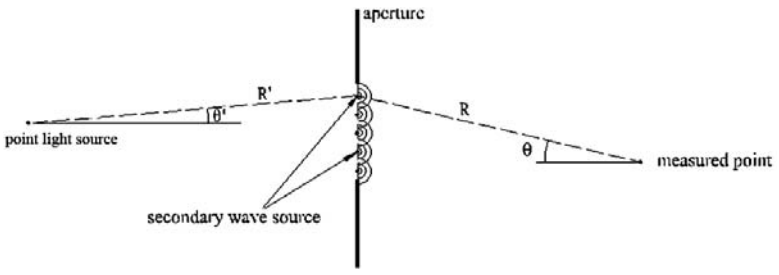

Figure 3.2 Geometry for Kirchhoff-Fresnel integral

Considering the phase difference of α between the primary wave and the secondary waves, the amplitude of the wave diffracted by the aperture can be represented in the form of Kirchhoff-Fresnel integral[235]: (Figure 3.2)

$$u = \int_{aperture} \frac{iA_0}{\lambda} \cdot \frac{e^{ikR'}}{R'} e^{i\alpha} \frac{e^{ikR}}{R} \frac{(\cos\theta + \cos\theta')}{2} d\sigma \tag{3-5}$$

where θ and θ' are defined in Figure 3.2, σ is the differential aperture area.

In photolithography processing, the primary light course is far away from the aperture plane, which is typically the mask plane and the incident light can be treated as plane wave. We can assume the factor $A_0 \frac{e^{ikR'}}{R'} e^{i\alpha}$ in equation 3-5 to be a constant and can be taken outside the integral, and the angle θ is a constant equal to 0. Then Equation 3-5 can be rewritten as

$$u = \frac{iA}{\lambda} \int_{aperture} \frac{1}{R} e^{ikR} (1 + \cos\theta) d\sigma \tag{3-6}$$

If the aperture is described using a function *f(x,y)* defined on the aperture plan of aperture and the incident wave is a plane wave whose value at R=0 is $u(R)$=A, the Kirchhoff-Fresnel integral can be written as:

$$u = \frac{iA}{\lambda} \iint f(x,y) \frac{1}{R} e^{ikR} (1 + \cos\theta) dx dy \tag{3-7}$$

where A contains all constants, its value equals to the wave amplitude at the aperture (R=0).

According to Huygens' principle, newly generated waves are continuous over the aperture. Because the incident light wave is assumed to be a plane wave, the intensity reaching the aperture is uniformly distributed across the slit. As the energy of the wave is proportional to the square of the amplitude, so

$$|u| = \mathrm{A} \tag{3-8}$$

where A^2 is the incident intensity at the aperture.

We shall consider light passing through the aperture into the resist and point ***M*** as a point in the photoresist under the mask (Figure 3.3). The light wave arriving at point ***M*** comes from two sources, one part coming directly from the newly generated point sources and another part comeing from the reflection of silicon wafer. The wave at point ***M*** can be expressed by superposing these two fractions.

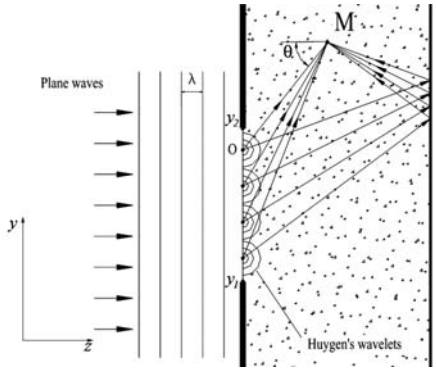

Figure 3.3 General optical diagram for the light arriving at a point under the mask

The mask dimensions (Figure 3.1) make it valid to treat the mask as a long narrow slit. Thus we can limit our study of light intensity to one dimension and equation (3-7) is rewritten as:

$$u = \frac{iA}{\lambda}\int_{y_1}^{y_2}\frac{1}{R}e^{ikR}\frac{(1+\cos\theta)}{2}dy \tag{3-9}$$

where y is the horizontal coordinate along the width of the slit aperture in Figure 3.3.

It should be noted that the Fresnel integral is a one-dimensional integral across the width of the aperture. This is an approximate formula in which the full two-dimensional integral of the Kirchoff diffraction integral is simplified in such a way that it is possible to perform the integral along the length of the slit in closed form, so that all that remains is the integral in the second dimension. There are two potential problems in applying this approximation to our absorption and reflection problem. First, the absorption along each ray depends on the path length for each spherical wave in the full 2-D Kirchhoff calculation. In making the Fresnel approximation, the increased absorption that occurs

for rays not in the plane of the diagram is ignored. Second, the reflection coefficient depends on the full three-dimensional angle at which each "wavelet" strikes the substrate. This angle is clearly different for those wavelets that are integrated over in arriving at the Fresnel approximation.

However, the 1-D Fresnel approximation is close enough for the present case because:

1) The rays that are integrated over in the first integral along the length of the slit are not a major consideration because the largest contribution to the net wave amplitude arises from "wavelets" that are close to the plane of the diagram, and for these, the absorption differs slightly from that in the plane. Another way of thinking about this is to consider the effective length of the slit implied by the finite absorption of the resist. In a conventional Fresnel calculation, the slit length is taken to be infinite. In this study, the length cannot be strictly considered to be infinite due to the finite absorption of the resist. The measured absorption coefficient of SU-8 is 52/cm or 0.0052/μm, so that the intensity falls by e^{-1} over a resist path length of about 200 μm. The effective slit length is consequently of order twice this distance, which is several times larger than the characteristic dimensions of our problem (slit width, resist depth) and much larger than the wavelength of the radiation, 0.365 μm. In view of this, it seems highly reasonable to neglect the second dimension of the full 2-D Kirchhoff integral and to adapt the conventional 1-D Kirchhoff-Fresnel integral to our problem.

2) Since the largest contribution to the total integral (along the length of the slit) arises from those "wavelets" that are close to the plane of the diagram and for those the angles are very similar to the angles in the diagram, the deviation of the true 3-D reflection geometry from the simplified "in the plane" geometry should not be a large consideration.

3.4 Diffraction and reflection in the photoresist

3.4.1 Air gap introduces UV refraction

The edge bead introduces an air gap between the mask and photoresist. Hence, at the air/SU-8 interface, there is refraction since the refractive indexes of the two media are different. Refraction leads to increased path length and changes the propagation direction. This direction change bends the UV light laterally away from the dark field (Fig. 3.4). The total direct path length from the secondary point source to the measured point M is R_d and can be defined by Equation (3-10). Similarly, the total path length from the secondary point source to the measured point I on the silicon substrate surface is R_i (Equation (3-11)).

$$R_{\mathrm{d}} = R_d^{'} + R_d^{''} \tag{3-10}$$

$$R_i = R_i^{'} + R_i^{''} \tag{3-11}$$

where R'_d, R'_i are the path lengths in air and R''_d , R''_i the path lengths in SU-8 and these values can be determined as follows:

$$R_d^{'} = \sqrt{g^2 + (y - y_d)^2} \tag{3-12}$$

$$R_d^{''} = \sqrt{(z - g)^2 + (y_d - x)^2} \tag{3-13}$$

$$R_i^{'} = \sqrt{g^2 + (y - y_i)^2} \tag{3-14}$$

$$R_i^{''} = \sqrt{(2T - z - g)^2 + (y_i - x)^2} \cdot \frac{T - g}{2T - z - g} \tag{3-15}$$

$$R_r = \sqrt{(2T - z - g)^2 + (y_i - x)^2} \cdot \frac{T - z}{2T - z - g} \tag{3-16}$$

where g is the air gap;

x, y are the horizontal distances from dark field edge to the measured point M and the secondary point source O';

y_i and y_d are the horizontal distances from dark field edge to the intersection points of the light and the air/SU-8 interface;

z and T are the vertical distances from dark field edge on the mask to the

measured point *M* and silicon wafer surface respectively.

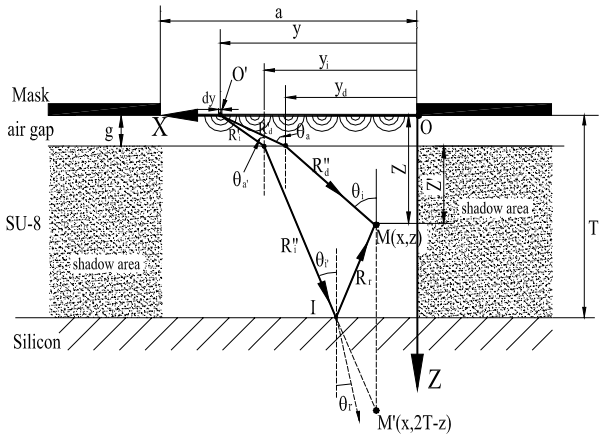

Figure 3.4 Sketch of the geometry of resist exposed through a single slit

The path lengths are determined by Snell's Law

$$n_0 \sin\theta_a = n_1 \sin\theta_i \tag{3-17}$$

$$n_0 \sin\theta_{a'} = n_1 \sin\theta_{i'} \tag{3-18}$$

where n_0 and n_1 are the refractive indices of air and SU-8;

θ_a and $\theta_{a'}$ are the incident angles at the air/SU-8 interface,

θ_i is the incident angle at point *M,*

$\theta_{i'}$ is the incident angle at point I (Figure 3.5).

$$\sin\theta_a = \frac{y - y_d}{R_d^{'}} \tag{3-19}$$

$$\sin\theta_i = \frac{y_d - x}{R_d^{''}} \tag{3-20}$$

$$\sin\theta_{a'} = \frac{y - y_i}{R_i^{'}} \tag{3-21}$$

$$\sin\theta_{i'} = \frac{y_i - x}{R_i^{''} + R_r} \tag{3-22}$$

3.4.2 Diffraction

Light due to diffraction comes directly from the secondary point sources along the aperture. So the diffraction wave arriving at point *M* can be represented in the form of Kirchhoff-Fresnel integral:

$$u_d = \frac{iA}{\lambda}\int_0^a \frac{1}{R_d} e^{ikR_d} \frac{(1+\cos\theta_i)}{2} dy \tag{3-23}$$

where R_d (defined in equation 3-10)is the path length from secondary point source to the measured point ***M***, a is the width of aperture opening .

3.4.3 Reflection from the wafer

The light coming from source O' reaches point ***I*** on the silicon wafer and is reflected by the silicon wafer. It is then reflected towards point *M*. The wave u_i arriving at point ***I*** is

$$u_i = \frac{iA}{\lambda}\int_0^a \frac{1}{R_i} e^{ikR_i} \frac{1+\cos\theta_{i'}}{2} dy \tag{3-24}$$

Reflected wave at point ***I*** can be expressed as

$$u_{i,r} = c_{ref}\, u_i \tag{3-25}$$

where c_{ref} is the coefficient of amplitude reflection and can be calculated using Fresnel's formula as[235, 236]:

$$c_{ref} = \frac{1-b}{1+b} \tag{3-26}$$

where
$$b = \left(\frac{n_1}{n_2}\right)^2 \frac{\sqrt{n_2^2 - (n_1\sin\theta_{i'})^2}}{n_1\cos\theta_{i'}} \tag{3-27}$$

In equation (3-27), $\theta_{i'}$ refers to the angle of incident at point ***I*** (Figure 3.5) and n_1 and n_2 refer to the refractive index of photoresist and silicon respectively. $n_1$is 1 and n_2 is 6.55[237, 238]

After traveling a distance of R_r(Figure 3.5), the reflected wave arriving at point ***M*** is

$$u_r = c_{ref}\frac{iA}{\lambda}\int_0^a \frac{1}{R_i} e^{ikR_i} \cdot \frac{1+\cos\theta_{i'}}{2} \cdot \frac{1}{R_r} e^{ikR_r} dy \tag{3-28}$$

Considering the attenuation due to the absorption of light, the intensity at a distance r from the light source can be represented as[239, 240]

$$I = I_0 e^{-\beta r} \tag{3-29}$$

where β is the absorption coefficient of the photoresist and *r* is the travel distance. Note that the intensity of light is assumed to be proportional to the square of the amplitude of the wave so that the equations (3-23, 3-14 and 3-28) can be rewritten as

$$u_{\mathrm{d}} = \frac{iA}{\lambda}\int_0^a \frac{1}{R_d} e^{i\mathrm{k}R_d}\frac{1+\cos\theta_i}{2} e^{-\frac{1}{2}\beta R_d''} dy \tag{3-30}$$

$$u_{\mathrm{i}} = \frac{iA}{\lambda}\int_0^a \frac{1}{R_i} e^{i\mathrm{k}R_i}\frac{1+\cos\theta_{i'}}{2} e^{-\frac{1}{2}\beta R_i''} dy \tag{3-31}$$

$$u_{\mathrm{r}} = c_{ref}\frac{iA}{\lambda}\int_0^a \frac{1}{R_i} e^{i\mathrm{k}R_i}\cdot\frac{1+\cos\theta_{i'}}{2}\cdot\frac{1}{R_r} e^{i\mathrm{k}R_r}\cdot e^{-\frac{1}{2}\beta(R_i''+R_r)} dy \tag{3-32}$$

3.4.4 Superposition of spherical waves

The sum of a number of harmonic waves of the same frequency leads to a resultant wave that is also a sinusoidal wave with the same frequency[235]. With n waves given by the forms of

$$u_1 = A_1 e^{ir_1},\ \ldots,\ u_i = A_i e^{ir_i},\ \ldots,\ u_n = A_n e^{ir_n} \tag{3-33}$$

the sum of these n waves is written as:

$$u = \sum_{i=1}^{n} A_i e^{ir_i} \tag{3-34}$$

The light arriving at point ***M*** includes diffraction and reflected parts. Each of these two fractions is the sum of harmonic waves. The sums are also harmonic waves. UV light at point ***M*** can be obtained by superposition of the two fractions. Substituting Equations (3-30) and (3-32) into Equation (3-34), the light arriving at point ***M*** can be written as:

$$u_{\mathrm{d}} = \frac{iA}{\lambda}\int_0^a \frac{1}{R_d} e^{i\mathrm{k}R_d}\frac{1+\cos\theta_i}{2} e^{-\frac{1}{2}\beta R_d''} dy +$$

$$c_{ref}\frac{iA}{\lambda}\int_0^a \frac{1}{R_i} e^{i\mathrm{k}R_i}\cdot\frac{1+\cos\theta_{i'}}{2}\cdot\frac{1}{R_r} e^{i\mathrm{k}R_r}\cdot e^{-\frac{1}{2}\beta(R_i''+R_r)} dy \tag{3-35}$$

The expression e^{ix} can be expressed by $\cos x + i \sin x$. The intensity of light is proportional to the square of the amplitude of the obtained wave.

3.5 The modeling details

The UV light wave amplitude across the thickness of SU-8 was calculated using equation (3-35). The UV intensity is the square of the calculated amplitude. Fresnel approximation [235] was used to do the integration. FORTRAN language was used to compile the calculation program. The calculated results were then processed using software of Matlab to obtain the intensity distribution images and contour lines. In the calculation, the absorption coefficient of the photoresist was 52/cm (measured using a UV-3101PC scanning spectrophotometer from SHIMADZU Company, Japan), the wavelength of UV light in air was 365 nm.

For the model, an air gap of 40 μm and a SU-8 thickness of 110 μm which are close to experimental values and dark field and light field widths of 23 μm and 40 μm respectively (same as those of mask A1) were used. In order to study the effect of diffraction, refraction (air gap) and reflection, 3 modeling were carried out: one modeling is the calculation of only the diffraction for 110 μm thick SU-8 without air gap (counting diffraction only, denoted as D modeling); the second one is the calculation of the diffraction and refraction for 110 μm thick SU-8 with 40 μm air gap (counting diffraction and refraction, denoted as D-Rr modeling); the third one is the calculation of the diffraction, refraction and reflection for 110 μm thick SU-8 with 40 μm air gap (counting diffraction, refraction and reflectin, denoted as D-Rr-Rl modeling). Another sample with SU-8 thickness of 66 μm, 40 μm air gap and dimensions of Mask A2 was used for conformation. Only D-Rr-Rl modeling was done for this sample.

3.6 Results and discussion

3.6.1 Calculated results

The calculated contour lines of constant relative intensity (I/I_o, I_o is the incident intensity) under dark field using Mask A1 are shown in Figure 3.5. The SU-8 gels wherever the exposure energy equals or exceeds the gelation energy. The exposure energy across SU-8 was determined by multiplying UV intensity by exposure time.

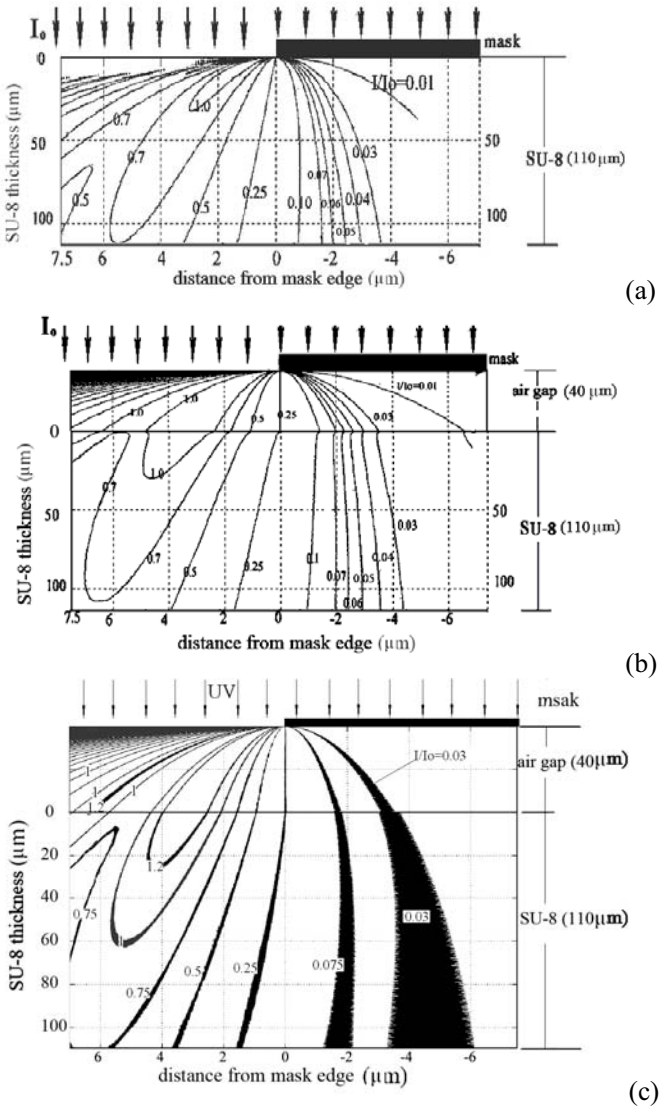

Figure 3.5 Contour lines of constant UV light intensity under the dark field of the mask (a) D modeling, (b) D-Rr modeling and (c) D-Rr-Rl modeling

Since the measured gelation energy of SU-8 is 30mJ/cm^2, specially studied, the contour lines of exposure energy=30mJ/cm^2 were hereafter denoted as iso-gelation-energy

contour lines. The predicted SU-8 post-exposure/post-development profile thus can be defined as the iso-gelation-energy line. Due to interference between the incident light from above and the reflected light from below, the iso-energy surfaces oscillate back and forth with a wavelength of one-half the UV wavelength, essentially "standing waves" in the UV light field. The profile surface was taken to be the outer envelope of the theoretical iso-gelation energy surface, as illustrated in Figure 3.6. The presence of a dense "comb" of gelled resist within the gelation-energy "band" will probably stabilize the dense "comb" of less than fully gelled resist that is interleaved with it since the "comb" spacing is very small (only about 180 nm) while the achievable resolution of UV negative resist is typically 1 μm. Surface tension effects can be expected to make it difficult to wash out less than fully gelled resist from within the "comb" of gelled resist during development and rinse. The less than fully gelled resist interleaved in the "comb" of gelled resist will then harden during PEB. Diffusion in SU-8 will also smooth the "comb teeth" structure during PEB.

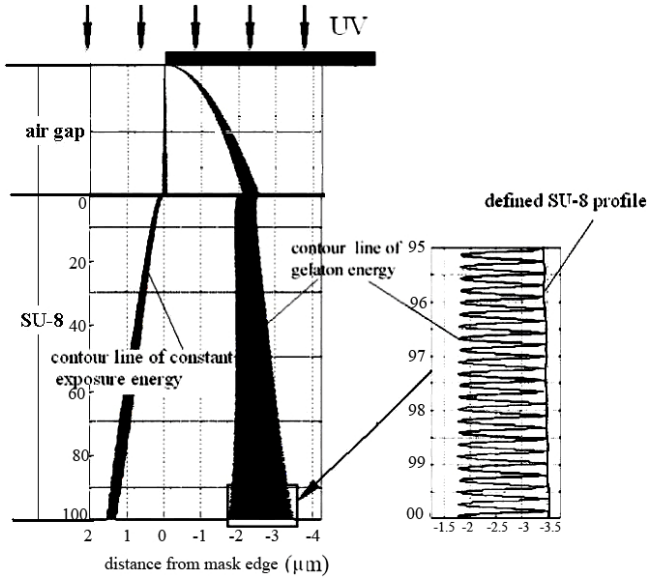

Figure 3.6 Schematic drawing of iso-gelation energy line and definition of SU-8 profile

Figure 3.7 shows the predicted channel profiles in SU-8 resist exposed for different times. In the case of 70 s exposure (i.e. UV exposure dose of 700 mJ/cm^2), the gelation

energy line predicted using D-Dr-Dl modeling (Figure 3.7(a)) goes 2.9 μm and 4.5 μm into the shadowed region at the top and bottom of the SU-8 respectively. This means that the microchannel width will be 9.0 μm narrower at its base than the width of the dark field on the mask. For a 10μm-wide dark field, the channel width would decrease to 4.2 μm at the top and form a V-shaped profile rather than well developed channels. The channel profile exposed for 35 s is nearly vertical while the profile of the channel exposed for 70 s is sloped and the profile of channel exposed for 90 s is even more sloped. The 70 s exposure leads to a channel that is 1.3 μm and 3.7 μm narrower at the top and bottom respectively than the 50 s exposure, with a correspondingly less steep sidewall. These results indicate that increased exposure dose will reduce sidewall verticality and decrease channel bottom width and also that a certain minimum exposure dose is required to avoid an "undercut" sidewall (i.e. the "mushroom" profile).

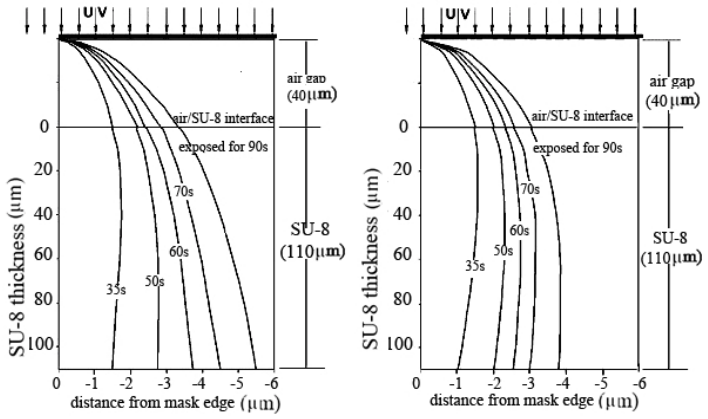

Figure 3.7 Calculated SU-8 profile of microchannel in 110 μm SU-8 exposed for varied time. (a) D-Rr-Rl modeling and (b)D modeling

The incorporation of reflection at the substrate into the model manifestly makes a significant difference to the channel profiles. At longer exposures, the iso-gelation-energy contour penetrates deeper into the shadowed area and the width of the gelation energy "band" produced by interference between refracted-diffracted and refracted-reflected rays is greater.

3.6.2 Experimental results

The spin-coated SU-8 layer is quite uniform except the edge area. For the SU-8 coated using spin speed of 3000 rpm, the measured SU-8 thickness is 107.2±1.9 μm at wafer center. The thickness increases to 110.4±1.8 μm, 114.8±2.1 μm, 117.5±2.6 μm and 128.7±2.8 μm when the radius increases to 1.0 cm, 2.0 cm, 3.0 cm and 4.0 cm respectively. It then increases rapidly and reaches a maximum value of 151.8±2.6 μm at a radius of 4.3 cm because of the edge bead effect, and decreases to 112.7±3.5 μm at the radius of 4.8 cm. For the SU-8 coated using spin speed of 5500 rpm, the measured SU-8 thickness is 51.2±1.1 μm at wafer center. The measured maximum value of 97.3±2.7 μm is at a radius of 4.3 cm because of the edge bead effect. All dimensions reported in this chapter were measured in the area with a radius of 30 mm at wafer center and each data averaged from 10 readings.

Experimental microchannel profiles were significantly affected by the exposure dose. Figures 3.8 compare the SEM micrographs of microchannels fabricated using different exposure times (35 s, 50 s, 70 s and 90 s). They clearly show the effect of exposure on the channel width and channel profile. In particular, longer exposure time gives narrower microchannels and more sloped sidewall. For the channels fabricated by 35 s exposure, the top and bottom width of the channel is 21.7±0.4 μm and 21.7±0.4 μm respectively (Figure 8(a)). Since OP measures the profiles by light reflection, it is not able to give profile data of the undercut structure. The SEM micrograph shows the nearly vertical sidewall and slight undercut for the deep channels (Figure 3.8(a2)). As the exposure time increases, the channels become narrower and the side wall becomes sloped (cross sections in Figure 3.8).

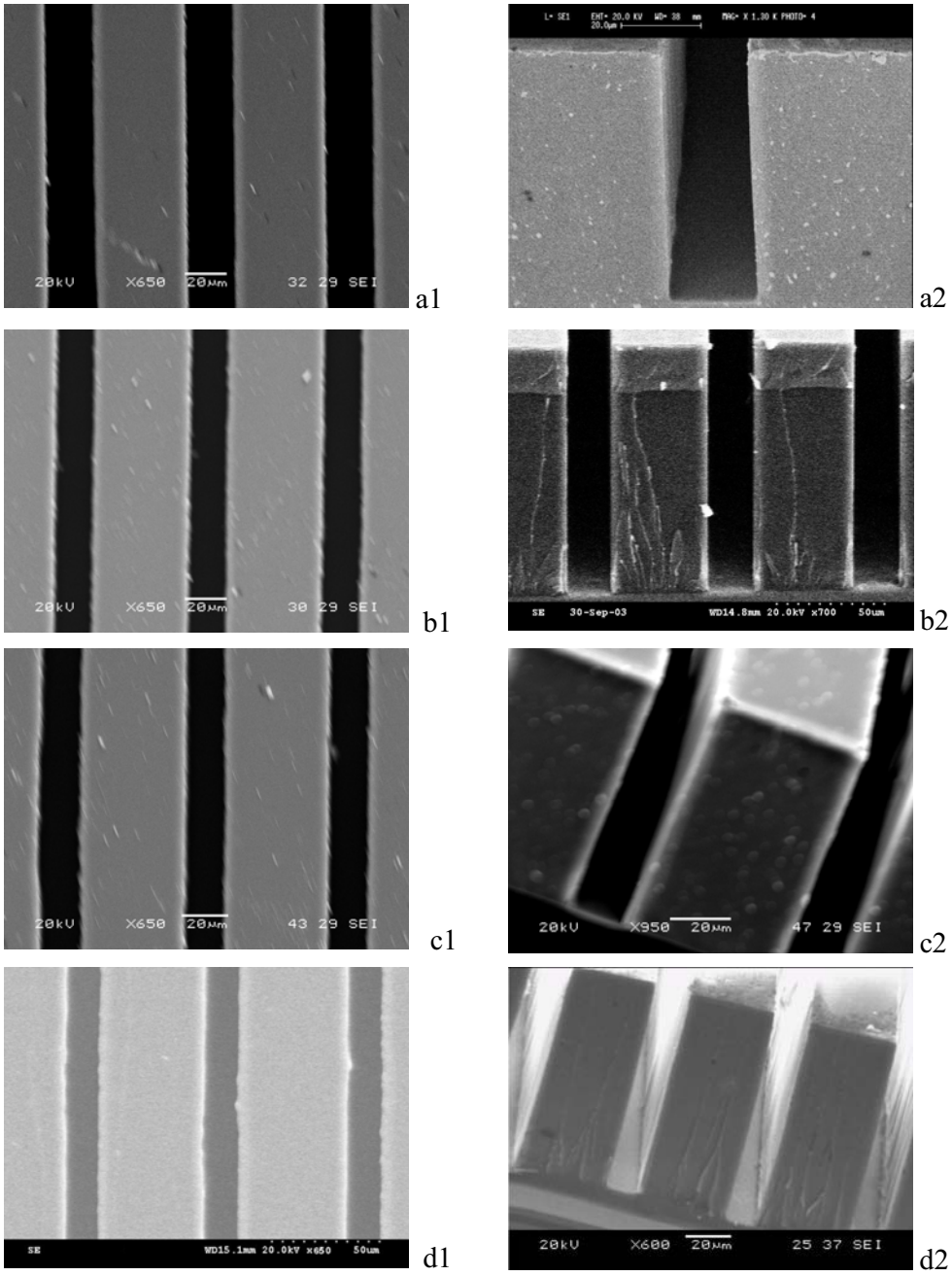

Figure 3.8 (1) Top view and (2) cross section of microchannels in SU-8 exposed (a) 35 s, (b) 50s, (c) 70 s and (d) 90 (thickness of 110µm, exposed through Mask A1)

The measured gelation energy for 100 um thick SU-8 coating was 30 mJ/cm^2. This value was used to theoretically predict the SU-8 profiles with our DRR model.

3.6.3 Comparison of model and experimental results

The comparison of predicted and experimentally observed trends for channel top- and

bottom-width and channel side wall taper angle in 110 μm thick SU-8 is shown in Figures 3.9, 3.10 and 3.11. Higher exposure dose causes narrower and less vertical microchannels. When the expose time (t_{exp}) was increased from 50 s to 90 s, the experimental microchannel top width (W_t) shows a decrease from 19.2±0.4 μm to 15.5±0.5 μm. The calculations using the DRR model predict that W_t processed by 50 s and 90 s exposure will be about 18.6μm and 16.1μm respectively. The experimental bottom width (W_b) shows a decrease from 16.8±0.3 μm to 11.0±0.4 μm for exposure times of 50 s and 90 s respectively. Similarly, the calculations using the DRR model predict W_b to decrease from 17.5μm to 12.0 μm (Figure 3.10). With increase of UV time, the width of SU-8 bar became larger. Figure 3.11 shows the corresponding trend in sidewall angle with UV time; the experimental sidewall angle (γ) shows a decrease from 89.7±0.1° to 88.7±0.1° when the exposure time increased from 35 s to 90 s. The predicted angle using the DRR model closely follows the measured trend.

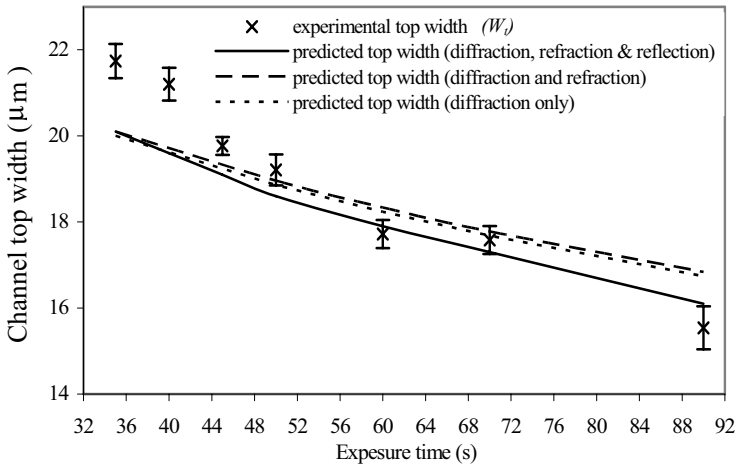

Figure 3.9 Effect of exposure time on the top channel width (W_t) (110μm thick SU-8, Mask A1, 40μm air gap was employed in predicting calculation)

The air gap between the mask and SU-8 top surface leads to UV light refraction which leads to increased path length and changes the propagation direction. The calculated results indicate that the predicted channel calculated with refraction is wider than the

channel calculated without refraction. For 110 μm thick SU-8, 50 s exposure and 40 μm air gap, the top channel width and bottom channel width calculated with refraction is 0.1μm and 0.3 μm wider than the corresponding values calculated with diffraction-only model respectively. This is because 1) additional path length leads to more UV attenuation and 2) the change of propagation direction bends the UV light away from the dark field. The effect of the refraction is to approximately shift the UV light laterally away from the dark field. The difference between lines 1 and 2 in Figure 3.9 is less than that in Figure 3.10, which means the effect of refraction is more significant at the bottom than at the top. But the effect of refraction is generally not significant.

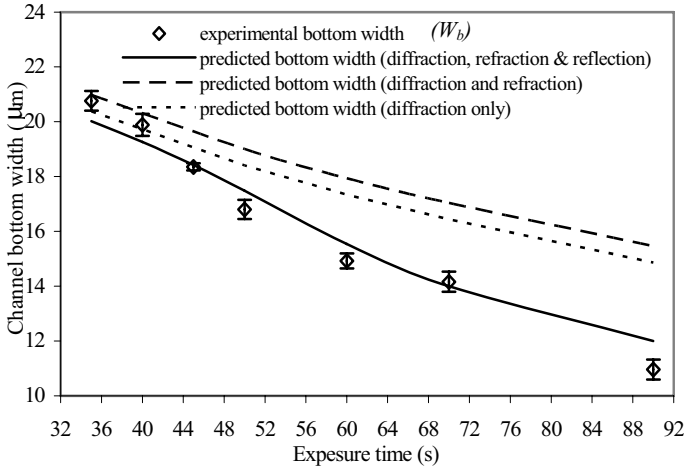

Figure 3.10 Effect of exposure time on the bottom channel width (W_b) (110μm thick SU-8, Mask A1, 40μm air gap was employed in predicting calculation)

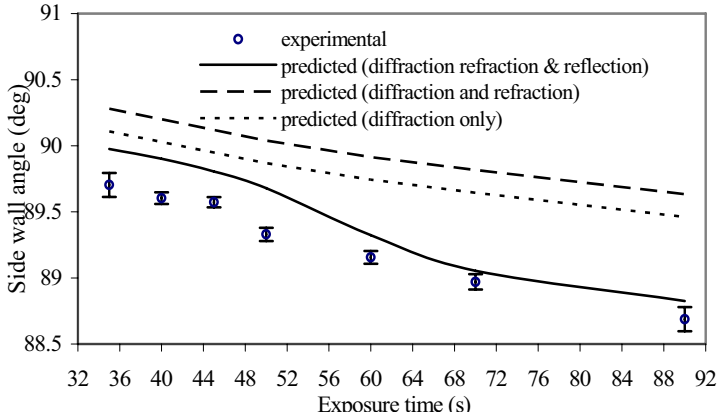

Figure 3.11 Effect of exposure time on the side wall angle of the channel (110μm thick SU-8, Mask A1, 40μm air gap was employed in predicting calculation)

Although theoretical studies of the profiles in lithography have been done[74, 241], only diffraction was considered in such studies; additionally, such work which includes reflection from the substrate and refraction at the air/resist interface has not previously been done. The diffraction plus refraction plus reflection calculation better predicts the observed widths than the diffraction-only calculation at longer exposures and better predicts the observed sidewall taper at all exposures. Neither calculation does a good job of predicting the channel widths at short exposures (< 50s). As expected from simple interference considerations, the inclusion of reflection leads to narrower and less steeply sloped developed channel widths.

Our results show that diffraction-only calculations are not adequate to accurately predict photolithographic profiles of HAR microchannels in thick SU-8 resist; reflection must also be taken into account. The difference between the diffraction-only and the DRR calculation is significant and can mean the difference between a profile which is impossible to demold and one for which demolding is possible. For example, the diffraction-only profile is undercut at exposure times up to 60 s (Figure 3.7b), whereas the DRR profile ceases to be undercut at slightly more than 35 s exposure (Figure 3.7a). The DRR calculations are in good qualitative and quantitative agreement with measured profiles, especially at the longer exposure times.

The observed dependence of microchannel profile on exposure is due to the diffraction of incident UV light at the edge of the dark field lines of the mask, refraction of light at the air/SU-8 interface and the reflection from the silicon wafer surface. This diffraction, refraction and reflection effectively decollimates or angularly broadens the incident radiation pattern with respect to a perfect geometrical shadow of the mask. Since stray UV light goes further laterally into the shadowed area when the traversed distance (i.e.

SU-8 resist thickness) is increased, the stray light effect is more significant in the patterning of thick photoresist coatings and high aspect ratio structures.

There is a systematic deviation between experimental results and the DRR model predictions for the absolute channel widths and the wall slopes in the lower exposure range (Figures 3.9, 3.10 and 3.11). The predicted channel widths are less than the experimentally observed data. The larger experimental channel width, i.e. smaller SU-8 bar width, compared to the theoretical values, are due to low cross-link density leading to "washing away" of SU-8 during the development. The cross-link density is inversely proportional to the molecular weight between cross-links (*Mc*). *Mc* can be calculated using equation (3-36) [242].

$$M_c = \frac{3\rho RT}{E} \tag{3-36}$$

where E is the storage elastic modulus of polymer in the rubbery state;

ρ is the density of SU-8, R is the universal gas constant (8.314J/mole·K);

T is the temperature (K).

Figure 3.12 shows the effect of exposure time on the molecular weight between cross-links. There are two inflexion points for the *Mc* versus UV exposure time curve at 50 s exposure and 90 s exposure. The cross-link density remains at a low level when the exposure time is less than 50 s and increases rapidly after the exposure time exceeds this first critical point. Matějka and coworkers [164] studied the cationic polymerization of diglycidyl ether of Bisphenol A in the presence of γ-butyrolactone and found that the cross-link density also remains at a low level until a fairly high conversion (about 75%) whereafter the rise is rapid. The calculated *Mc* is 2860 g/mol when the exposure time is 20 s. This value is higher than the molecular weight of uncross-linked SU-8 which is 1396 g/mol. The residual solvent (i.e. GBL) in SU-8 may cause high value of measured

Mc. Also, when the exposure time is short, although SU-8 is gelled, chain extension rather than crosslinking can predominate. Long chains and loosely cross-linked domains largely account for the low deformation modulus [243]. In the lower exposure range, although the SU-8 has gelled, the epoxy conversion is low (<40%) (Figure 3.13), leading to low cross-link density. The first critical point occurs at a lower conversion than that predicted by Matějka et al.; this is reasonable since SU-8 is octa-functional compared to the bi-functional epoxy used by them. When the exposure time is increased to 50 s or more, rapid decrease in *Mc* occurs until 90 s where vitrification takes place.

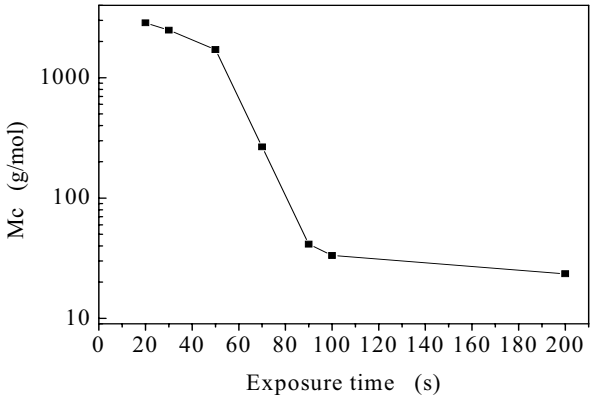

Figure 3.12 Effect of exposure on *Mc*

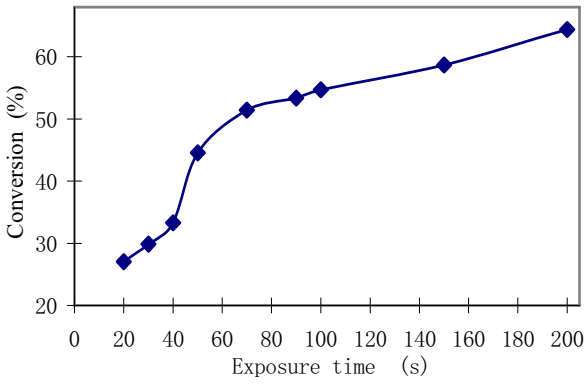

Figure 3.13 Effect of exposure time on epoxy conversion during SU-8 cross-linking

The glass transition temperature (T_g) (Figure 3.14) of SU-8 confirms the vitrification. T_g increases from 60°C to 95°C, which is also the PEB temperature, when the exposure time increases from 20 s to 90 s. With 90 s exposure, T_g is more or less the processing

(PEB) temperature (95°C). T_g only slightly increases from 95°C to 100°C when the exposure time increases from 90 s to 200 s. After vitrification, T_g does not change significantly.

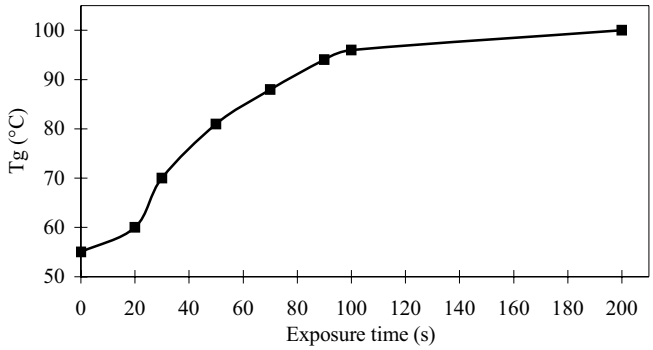

Figure 3.14 T_g of SU-8 cross-linked SU-8 exposed for varied time

The DMA result explains the deviation between the experimental and the predicted profile for low UV exposure time. High value of *Mc* in the low exposure range (<50s) indicates that SU-8 has very low cross-link density. The very low cross-link density at these short exposures can lead to extraction of SU-8 during development and rinse, leading to smaller SU-8 width and wider channel than predicted (Figures 3.9 and 3.10). The wash-away-of-SU-8 at low exposure dose agrees with reported investigation. Kurdryashov et al. [104] investigated the contrast of SU-8 using 700 nm thick SU-8 films and UV radiation. They found that the developed SU-8 film thickness processed by low exposure dose was different from the original thickness. The dependence of the remaining resist thickness after development upon UV exposure showed that 50% thickness was washed away in the development process when the UV exposure dose was 70 mJ/cm^2 for their given experimental conditions.

Diffraction and reflection have significant effects on profile characteristics and processability of high aspect ratio channels. Narrow microchannels in thick SU-8 cannot be formed successfully using high exposure dose. With high UV exposure dose,

diffracted and reflected UV light in the shadowed region cause SU-8 exposure and produce underresolved or unresolved resist structure. SU-8 resist is sufficiently predictable and reproducible in its response to photoinitiation that it is possible to finely adjust the exposure dose, as we have done in this report, to avoid overexposure under the mask dark fields while simultaneously avoiding underexposure and consequent deformation, during development and rinse, of the desired solid structures. By so doing, we have been able to successfully fabricate SU-8 gratings separated by dense and high aspect ratio microchannels. Lowering the exposure dose decreases the stray UV light diffracted and reflected into the shadowed photoresist. The lower cross-link density, and hence mechanical strength and hardness, of the exposed resist can be compensated by longer or higher-temperature post exposure baking.

In order to confirm the validity of the new D-Rr-Rl model, another sample was experimentally and theoretically investigated. The sample was patterned using Mask A2 and the measured SU-8 thickness was 66.4±3.4 μm at wafer center (within 30mm diameter). The measured difference between maximum and minimum thickness within the whole wafer was 41 μm. Figure 3.15 shows the effect of exposure time on channel profiles. Slight under cut was seen in the 25sec-exposed channel. The width decreased with the increase of exposure time and the 90sec-exposed sample was unresolvable.

The comparison of experimental results to the predicted results was shown in Figure 3.16. The theoretical prediction was done using thickness of 66 μm, 40 μm air gap and the dimensions of Mask A2 (Figure 3.1 b). For those successfully fabricated channel, the experimentally observed results agree with the predicted results except that the experimental bottom width of 70sec-exposed channel is smaller than the predicted value.

Further, although the predicted bottom width is 1.4μm for the 90sec-exposed channel, but the actual channel was unresolved. These can be attributed to the difficulty of dissolving the SU-8 at the bottom of the deep channel.

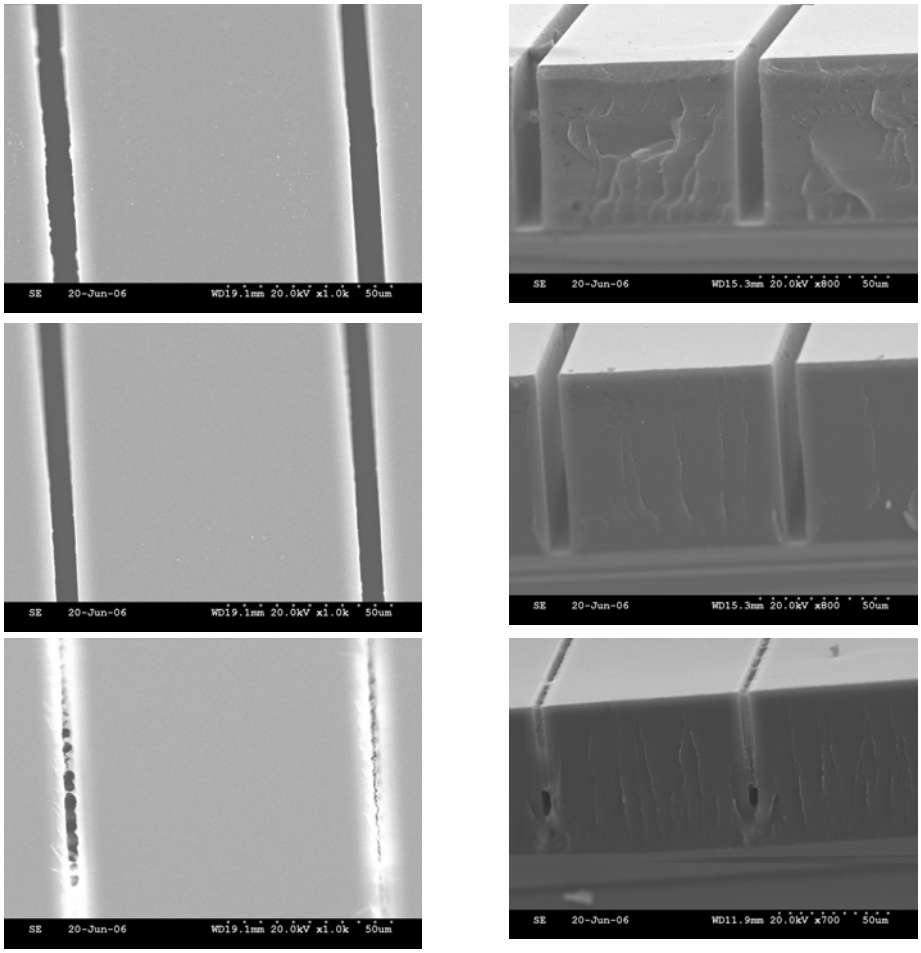

Figure 3.15 Top view and cross section of micro-channle in 66 μm SU-8 exposed for (a) 25s, (b) 50s and (c) 90s

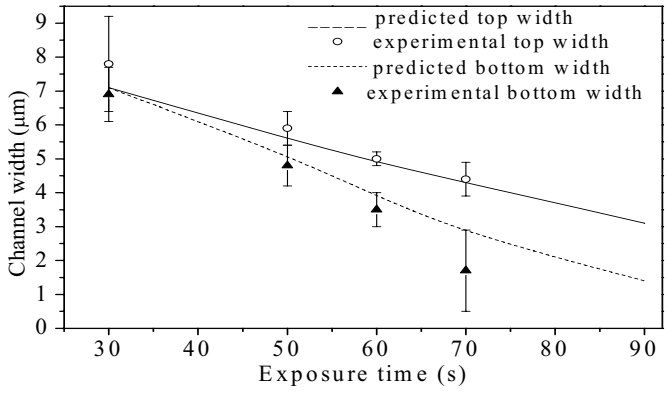

Figure 3.16 comparision of predicted and experimental profiles of micro-channel in 66 μm thick SU-8

3.7 Summary

The effects of light reflection at the wafer surface, UV exposure time and air gap between the resist and mask on pattern size and microchannel profiles were theoretically and experimentally studied. The model accounting for diffraction only was inadequate to accurately predict the profile characteristics of VHAR microchannels in thick resist. A new model incorporating the effects of diffraction at the edge of the dark field mask lines, refraction at the air/resist interface and reflection from the silicon wafer surface was developed to predict the profiles of micro channels in thick SU-8 resist. Reflection and diffraction lead to UV exposure of the photoresist underneath the dark field areas of the mask causing gelation and crosslinking, which then increases the wall width and slopes the SU8 sidewall and even produces underresolved or unresolved resist structure. The calculated mask replication fidelity and taper angle using the new diffraction-refraction-reflection (DRR) model was compared with experimental results. The new DRR model produced much superior predictions of the observed trends and actual microchannel width and sidewall angle as a function of exposure dose compared with the classic diffraction-only model. The calculated microchannel width and sidewall angle at high exposure dose agreed well with the experimentally observed values, indicating that reflection at the silicon substrate was significant. The predicted channel widths are less than the experimentally observed data in the lower exposure range. The DMA result explains the deviation between the experimental and the predicted profile for low UV exposure time. The larger than calculated actual microchannel width for low exposure dose was shown to be due to leaching of unreacted resist in the developer.

Chapter 4 Whole-wafer-covered dense SU-8 gratings with very high aspect ratio microchannels

4.1 Introduction

We are interested in the fabrication of dense SU-8 gratings having VHAR channels (Figure 4.1) over the entire 100-mm diameter wafer for use as a mold for UV embossing. The fabrication of dense SU-8 gratings with VHAR microchannels over a large area is non-trivial due to the contrary imperatives of mold hardness and faithful replication of the photomask pattern. Narrow microchannels can be "close-up" when the SU-8 is over-exposed, especially when the edge bead effect is significant. To date, most of the VHAR SU-8 structures processed by others are sparse[84, 151], i.e. not densely packed on the substrate. There is no reported work on the processing of dense SU-8 gratings with VHAR microchannels (i.e. dense SU-8 gratings separated by narrow and deep channels) over a large area.

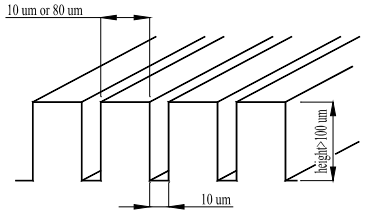

Figure 4.1 Sketch of the dense grating with VHAR microchannels

Edge bead is a difficulty commonly encountered in contact UV lithography using ultra-thick photoresist [63, 143]. The air gap between the mask and SU-8 coating produced by this variation in resist thickness exacerbates diffraction and refraction effect leading to poor dimensional replication, or even unresolved SU-8 processed patterns for very small (a few μm) dark field dimensions. Prior research [74, 147] has found that diffraction at the edge of the dark field of the mask strongly affects the pattern size and

sidewall profile in SU-8 contact UV lithography. Because of the high sensitivity of SU-8[123], even a little "stray" diffracted UV energy dose beneath the dark fields can cause gelation and cross-linking leading to enlarged SU-8 dimensions compared to the mask. Further, the thickness variation over the wafer makes it challenging to fabricate uniform whole-wafer-covered SU-8 patterns since the optimum UV dose depends on the resist thickness [244]. Our previous investigation also shows that the air gap introduces UV light refraction at the air/SU-8 interface, which also leads to poor mask replication fidelity. One possible solution for this problem is to remove the edge bead by standard edge bead removal techniques using GBL[63]. However, this technique requires specialized equipment. It is not very practical for the fabrication of whole-wafer-covered SU-8 microstructures since the SU-8 edge bead can cover a significant area of the wafer. Alternatively, one can fill the air gap with an organic solvent which has a similar refractive index as SU-8 [83]. However, the organic solvent contaminates the SU-8 surface and will diffuse into the SU-8 layer[63] resulting in accelerated diffusion of the photoacid catalyst and, consequently, poorer resolution.

In VHAR dense grating fabrication, SU-8 structure rigidity plays a critical role. Reported HAR SU-8 structures were sparse or had zigzag structures[151, 152]. For sparse or separated structures, the surface tension caused by the solvent can be neglected. Structures with zig-zag-like shape had relatively high structural rigidity. For dense VHAR gratings with narrow channels, the adhesion caused by the surface tension force of solvents is also likely to collapse the structures during the drying. For the long straight dense channels, structural rigidity is more critical than those short or isolated structures. Increased UV exposure time for dense VHAR microchannels, which improves resist hardness and rigidity, is found to result in overexposure of the shadowed resist causing unresolved pattern structures. The supplier's recommended UV

dose, typically suitable for fabricating sparse HAR SU-8 microstructures, results in unresolved dense VHAR channels due to "stray" light from diffraction.

We developed soft cushion and dose reduction technology to successfully fabricate SU-8 microstructures with VHAR microchannels over the entire 100 mm diameter wafer. Details are presented in this chapter. In soft cushion technology, a stack of clean room tissue paper was placed beneath the substrate to produce convex bending of the wafer. Thus the air gap was decreased so that the contact between the mask and SU-8 surface was improved, resulting in reduced UV diffraction at the air/SU-8 interface (Figure 4.2). This procedure improves the pattern replication and uniformity resolution over virtually the entire surface of the 4-inch wafer. Dose reduction technology to reduced the energy deposited at all points in the resist, and in particular the energy deposited under the dark field caused by diffraction at the mask and reflection at the silicon wafer so as to decrease the negative effect of stray UV light on the fabrication of VHAR microchannels.

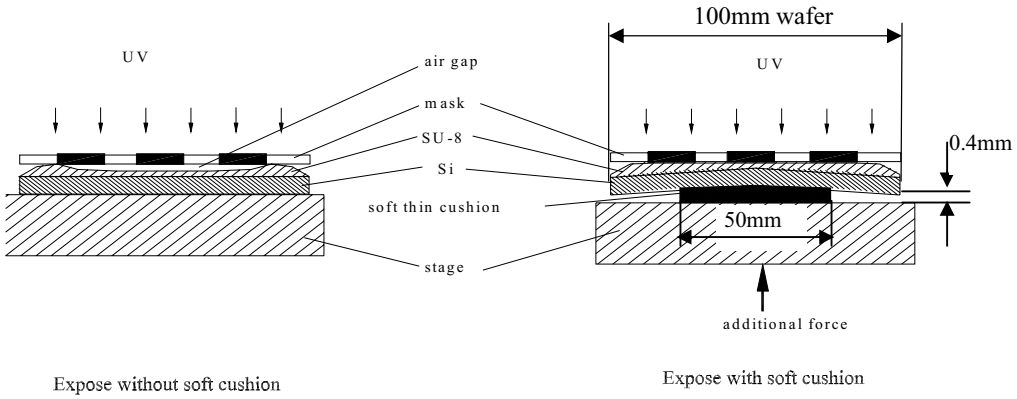

Figure 4.2 Effect of the soft cushion during exposure

4.2 Materials and equipment

The photoresist and developer used were NANO^{TM} SU-8-100 and SU-8 developer provided by Microchem Corp (Newton, Massachusetts). Isopropyl alcohol (IPA) with purity of 99% from Ashland Chemical Company (3849 Fisher RD, Columbus, OH,

USA) was used for rinsing the developed SU-8 patterns. A release coating, specifically Loctite Frekote® 700-NC supplied by Henkel Loctite Corp (Rocky Hill, Connecticut), was wiped on the wafer-side of the mask using tissue paper prior to closing the mask on the resist. 4-inch diameter <1 0 0> P type silicon wafers were used as substrates. Silicon wafers were cleaned, rinsed and dried using the procedure described in section 3.2. Pressurex® pressure-indicating film provided by Sensor Products Inc. (East Hanover NJ, USA) was used to measure the pressure applied to bend the Si wafer substrate.

The experiments were carried out in the Class 10K clean room of Micro-Machine Center (MMC) at the School of MAE, NTU. The SU-8 processing was done in Class 100 clean room. The temperature and humidity in this clean room were kept at 21±1°C and 40~60% respectively. A large area Spin Coater (Karl Suss CT62) was used to apply SU-8 to Silicon wafers. STURT SCIENTIFIC SH10 hotplate was used for the baking processing. The temperature of this hotplate was controllable and the controlling accuracy was ±1°C. J500-IR/VIS Mask Aligner from Optical Associates Inc. (Milpitas, California) was used for the UV exposure. The measured UV intensity was 10 mW/cm^2 at 365 nm. SEM was done using either a JEOL JSM-5600LV or a HITACH S3500N SEM. The SU-8 was platinum coated prior to SEM examination. Optical profilometry (OP) was done using the WYKO optical profilometer in VSI mode at Precision Engineering and Nanotechnolgy Centre (School of MAE, NTU). Hardness test was carried out at Materials Lab A (School of MAE, NTU) using a DMHp-2 Micro hardness tester (Matsuzawa Seiki Co. LTD. Tokyo, Japan).

4.3 Fabrication details

4.3.1 Soft cushion technology

Two masks were used. Mask B has wide dark field line width and narrow light field line

width (Figure 4.3a). It contains 80 μm-wide by 1000 μm-wide dark fields separated by 10μm-wide light field lines over a 4-inch diameter circular area. It produces VHAR SU-8 microstructures and was used to demonstrate the improvement in mask replication and uniformity of the SU-8 pattern over the whole wafer when a soft cushion was used. Two wafers were processed using Mask B with almost similar processing conditions (Table 4.1); one sample was processed without soft cushion (Sample A1) and the other with soft cushion (Sample A2). We are interested in fabricating dense SU-8 gratings with VHAR (>10) microchannels. Mask C (Figure 4.3b) contains 10μm-wide by 1000μm-long dark field lines separated by 80 μm-wide light field lines in the long direction and 10 μm-wide light field lines in the perpendicular direction over a 4-inch diameter circular area. It was used to fabricate grating with VHAR microchannels (Sample B in Table 4.1).

A typical SU-8 process is described here. SU-8 100 was spin coated onto the cleaned wafers for 30s using the speeds shown in Table 4.1. The coated wafers were placed on a leveled surface for 15 min to allow the SU-8 to level out. Soft baking was done at 65°C and 95°C on a well-leveled hotplate for the duration listed in Table 4.1. The wafers were slowly cooled to room temperature after the soft baking.

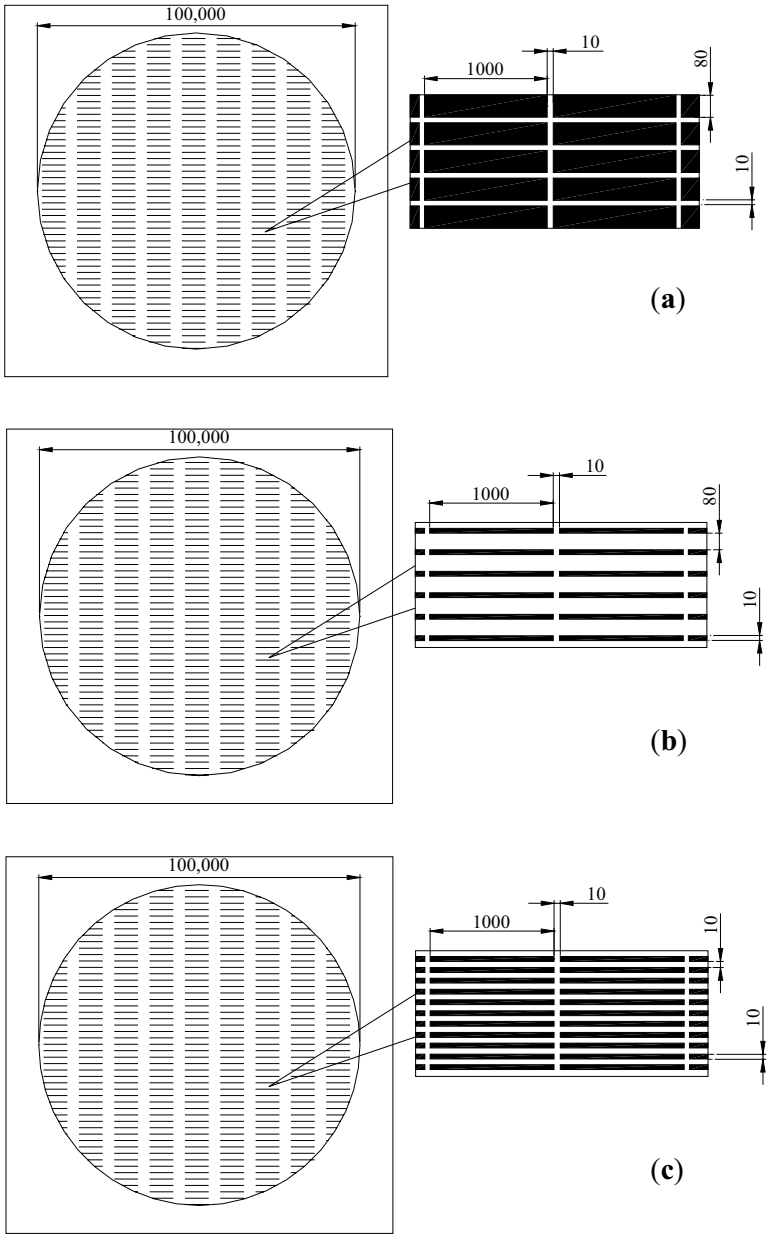

Figure 4.3 Sketch of (a) Mask B, (b) Mask C and (c) Mask D
(all dimensions are in microns)

Table 4.1 Detailed SU-8 processing conditions

Sample	Mask	Soft cushion?	rpm*	Thickness (μm)		Soft bake time (min)		UV time (s)	PEB time(min)		HB time (min)
				Ave	Center	@ 65°C	@95°C		@65°C	@95°C	@95°C
A1	B	No	3100	122.6	99	10	30	70	3	10	-
A2	B	Yes	3200	114.9	91	10	30	70	3	10	-
B1	C	No	2750	145	121	15	50	35	5	25	20
B2	C	Yes	2750	145	121	15	50	35	5	25	20
C1	C	Yes	2750	145	121	15	50	Varied from 20 to 25, 30,35, 40, 45, 50, 55, 60, 70, 80, 100, 120 and 200	5	25	samples exposed Less than 50s were hard baked for 20 min
C2	D	Yes	3200	110	92	10	30		3	10	
D	Nil	No	3200	100	—	10	30	varied from 5 to 150	3	10	varied from 0 to 40 min

For samples A2 and B, a soft cushion, made of a 0.4mm-thick stack of tissue papers 5cm in diameter (half the wafer diameter), was placed under the wafer during exposure. After the wafers were vacuum sucked to the photomask, an additional force was applied onto the back side of the wafer (Figure 4.2) by moving up the wafer. The amount of applied pressure was determined using Pressurex® pressure-indicating film. Circle pressure-indicating film with a diameter of 5 cm was put beneath the soft cushion during exposure. The film image was then compared with the standard image to determine the pressure applied to the film after exposure. The total additional force was then determined by multiplying the pressure by the film area. In order to compare the effect of the cushion, another SU-8 coated wafer (Sample A1) was exposed to UV light without the soft cushion. The exposure times are summarized in Table 4.1. The PEB was done using a hot plate. The PEB baking times and temperatures are also summarized in Table 4.1. After the samples were slowly cooled to room temperature, they were relaxed for 30 min to release the residual stress. The samples were developed in SU-8 developer at room temperature. Following the development, the substrates were rinsed briefly with IPA. Then the substrate with SU-8 pattern was dried with a gentle stream of compressed nitrogen. Sample B was also hard-baked (HB) (Table 4.1).

4.3.2 Exposure dose reduction

The exposure dose reduction was investigated with both wide and narrow microstructures separated by VHAR microchannels using Mask C and D (Figure 4.3b and 4.3c) respectively. Sample groups C1 and C2 using Mask C and D respectively were prepared to investigate the dose reduction for fabrication of dense VHAR microchannels over a large area. SU-8 100 was spin-coated onto the cleaned wafers and soft baked. Then the wafers were exposed to UV light through the previously defined mask C or a new Mask D. Dense gratings with VHAR microchannels are not suitable

for investigating the pattern uniformity and mask replication fidelity in section 4.3.1 because the SU-8 can not be successfully patterned under some investigated processing conditions. The new Mask D pattern was 10 um by 1000 um dark field lines separated by 10 um wide light field lines (Figure 4.3c) The exposure time varied from 20 s to 25s, 30 s, 35 s, 40 s, 45 s, 50 s, 55 s, 60 s, 70 s, 80 s, 100s, 120 s and 150s to study the achievability of the narrow channels. The soft cushion technology was employed during exposure. For the underexposed SU-8 pattern, the SU-8 was also hard-baked at 95°C for 20 minutes after the SU-8 was developed. The detailed processing parameters are summarized in Table 4.1.

4.3.3 Hardness test of cross-linked SU-8

Sample group D (exposure without a mask) was used to study the effect of UV exposure dose and hard baked time on the hardness of SU-8 films. 100 μm thick SU-8 films were spun, soft baked, exposed, PEB and developed. The UV exposure time was varied from 5 s to 100 s (i.e. the exposure varied from 50 mJ/cm^2 to 1000 mJ/cm^2). After development, the structure was hard baked at 95°C with the hard baking time varying from 0 to 45 min. Detailed processing parameters are summarized in Table 4.1. Vickers hardness was determined using the DMHp-2 Micro hardness tester. In the test, the prescribed test force F was 25 g for the samples which were exposed to UV light for less than 30 s, and 50 g for the samples which were exposed to UV light for more than 30 s. The test force was maintained for 15 s. Each reported data was averaged from at least 10 indenting.

4.3.4 Characterization

Profiles of developed SU-8 microstructures were examined using OP and SEM. The thickness of SU-8 films over the wafer is presented by the height of developed SU-8 microstructures. The cross sections of SU-8 gratings were obtained by breaking the

wafer with the SU-8 pattern. The locations of measurements of resist thickness and SU-8 width uniformity across the wafer are shown in Figure 4.4. At least 5 readings were made at each location. The top width of the SU-8 pattern was measured using both optical profilometry and optical microscopy.

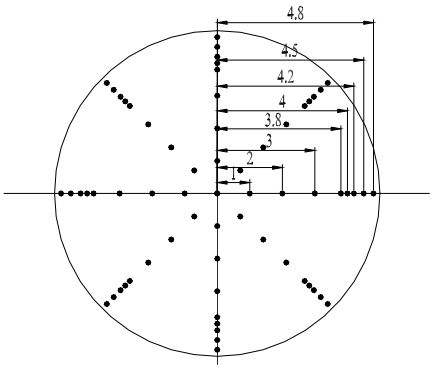

Figure 4.4 Measurement positions over the 100-mm wafer (distances are shown in centimeters)

4.4 Results and discussion

4.4.1 Effect of soft cushion

The additional force applied onto the cushion was determined to be in the range of 10-15 N. The applied force and cushion bent the wafer into a slightly convex shape to eliminate the air gap between the resist and the mask and improved the contact during exposure. The contact vacuum increased from –20 kPa to –70 kPa after using the soft cushion. With the application of Frekote, there was no sticking of SU-8 to photomask and the SU-8 surface remained flat and undamaged.

Samples A1 and A2 were processed similarly (Table 4.1), except the former was done without a soft cushion and the latter with a soft cushion. Figure 4.5 shows the SU-8 thickness variation between the center and the rim of the wafer; the edge bead area is not only at the wafer edge but spreads over an annular strip near the edge. The 1 cm wide annular strip covers more than 36% area of the whole 4-inch wafer. In Figure 4.5(a) the SU-8 was 91.0±0.2μm thick at the center and has an average thickness of

142.4±3.2 μm at the peak of the bead near the wafer edge. This sample was exposed to UV light with the soft cushion beneath the wafer. The thickness variation between the center and the rim of the wafer, even when the coating was relaxed on a well-leveled surface for 15 minutes before it was soft baked, was as large as 51.4 μm. For Sample A1 which was exposed without the soft cushion, the thickness was 99.0±0.2 μm at the center and 152.0±2.4 μm at the bead peak. The thickness variation between the center and rim was 53um (Figure 4.5(b)). The two samples, A1 and A2, have similar thickness variations and dimensions. The thickness variation could be up to 100 μm when the SU-8 coating thickness increased to 200 μm.

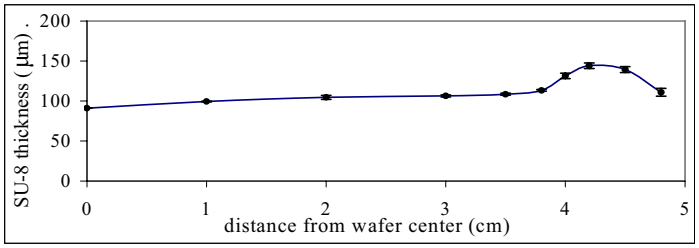

(a)

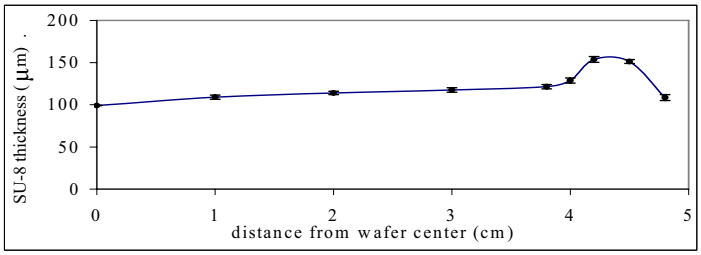

(b)

Figure 4.5 SU-8 thickness variation along the wafer diameter for 2 samples (A2 and A1). (a) A2- with soft cushion (91 μm thick at center) and (b) A1- without soft cushion (99μm thick at center)

The thickness variation leads to a radially variable air gap between the mask and photoresist surface. This variable gap leads to two undesirable consequences. First, the presence of any gap at all results in increased diffracted UV light beneath the dark field of the mask, with undesirable effects on mask width reproduction fidelity. We determined the threshold gelation exposure dose to be only 5% to 6% of the supplier's recommended processing dose (30 mJ/cm^2 for our 100 um thick resist coatings,

compared with the recommended dose of 500 to 600 mJ/cm^2; see chapter 3). Because the gelation dose is such a small fraction of the processing dose, increased penetration of diffracted light into the dark field due to the air gap causes unwanted crosslinking and gelation in the dark field regions of the resist leading to enlarged SU-8 structure. Further, because the thickness increased gradually from the center to the rim of the wafer, the air gap between the SU-8 and the mask was also not radially uniform. The air gap was larger at the center than that at the rim. This non-uniformity leads to variation in the degree of dark-field UV exposure across the wafer and consequent variation in SU-8 pattern width dimension. We defined a parameter "θ" to estimate the uniformity of the pattern dimension:

$$\theta = \frac{W_{\max} - W_{\min}}{W_{mean}} \times 100\% \tag{4.1}$$

where W is the top width of SU-8 wall (Figure 4.6) and subscripts *max, min* and *mean* refer to the maximum, minimum and average values of the dimension, respectively. Smaller θ indicates more uniform SU-8 pattern width dimension over the wafer.

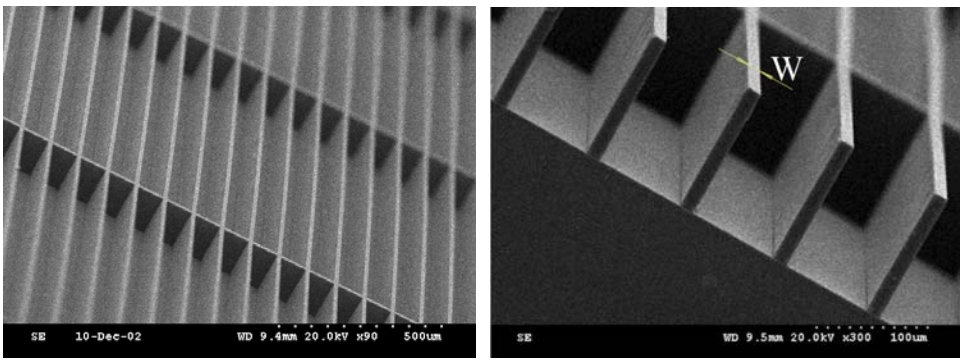

(a) (b)

Figure 4.6 (a) over view and (b) cross section of SU-8 pattern fabricated using Mask B (using soft cushion, exposure time: 70 s)

Table 4.2 shows the theoretically predicted SU-8 pattern top widths using the DRR model developed in chapter 3. The experimentally measured SU-8 thickness (Figure 4.5) was used to define the air gap in the theoretical calculation. The UV exposure intensity across the SU-8 resist was calculated using equation (3-35). The exposure energy was

the product of intensity and exposure time. 70 seconds, the exposure time for Mask B, was used in the calculations. The border of SU-8 structures can be defined where the exposure energy matches the gelation energy of the resist (30 mJ/cm^2, see chapter 3). The designed light field width or SU-8 microwall width (using Mask B, Figure 4.3) is 10μm. The calculated SU-8 pattern is 15.9 μm wide at wafer center where the SU-8 thickness is the minimum value. As the SU-8 thickness increases gradually from the center to the rim of the wafer, the air gap between SU-8 surface and photomask decreases gradually from the center to the rim and the calculated SU-8 pattern width decreases from 15.9 μm to 15.4 μm, 15.1 μm, 14,8 μm and 11.9 μm at a distance of 1 cm, 2 cm, 3 cm and 4 cm respectively from the wafer center. Comparison of the calculated and experimental SU-8 pattern width indicates that the experimental results agree with the theoretical prediction.

Table 4.2 SU-8 wall width over the silicon wafer
(using Mask B, the designed SU-8 wall width was 10μm)

Distance from wafer center (cm)	Sample A1 (Without cushion)			Sample A2 (With cushion)
	Air gap (μm)	Calculated width (μm)	Experimental width (μm)	Experimental width (μm)
0	51.4	15.9	15.4±0.4	12.0±0.4
1	43.1	15.4	14.4±0.3	11.7±0.4
2	37.9	15.1	13.8±0.6	11.5±0.5
3	36	14.8	13.2±0.6	11.4±0.5
3.5	33.9	—	12.8±0.3	11.4±0.5
3.8	29	—	12.5±0.4	11.3±0.4
4	11	11.9	11.6±0.3	11.1±0.4
4.2	0	10.6	11.3±0.3	11.1±0.5
4.5	3	10.2	10.9±0.5	11.0±0.2
4.8	21	—	12.1±0.6	11.7±0.4

Table 4.2 also compares the uniformity of SU-8 patterns fabricated with and without the soft cushion. For the SU-8 patterned without the cushion, the measured pattern width dimension varied from 15.4 μm at the center to 10.9 μm near the wafer rim and the

average value was 12.8 μm, which gave a θ value of 34.8%. It can be seen that the SU-8 pattern width dimension was larger at the wafer center where the SU-8 thickness was smaller and the air gap larger; the SU-8 pattern width dimension was smaller (and closer to the design target of 10 μm) at the rim area where the SU-8 bead was in contact with the mask and the air gap consequently was small. Table 4.2 illustrates the dual problems of the presence of an air gap damaging the lithographic resolution and the variability of the air gap producing non-uniform resolution and feature dimensions across the wafer. For the SU-8 patterned with the cushion beneath the silicon wafer, the measured pattern dimension varied from 12.0 μm at the center to 11.0 μm near the wafer rim and the average value was 11.4 μm, which gave a θ value of 9.1%. It should be noted that the best replicated dimension, near the rim of the wafer where the SU-8 edge bead and mask are contacted, is essentially identical for the two cases (10.9 μm and 11.0 μm), while the worst replicated dimension is dramatically closer to the target dimension for the wafer patterned with the cushion technique. The worst replicated SU-8 width dimension at the wafer center matched more closely the mask width (10 μm) when a soft cushion was used; the SU-8 width at the wafer center was 15.4 μm (54% larger than mask width) without a cushion and reduced to 12.0 μm (20% larger than the mask width) when a soft cushion was used. The soft cushion under the wafer helped to slightly bend the silicon wafer and consequently decreased the air gap and improved the contact during exposure. The contact vacuum increased from –20 kPa to –70 kPa after the soft cushion was used.

For the sparse SU-8 structure made using Mask B, employment of the soft cushion technology improved the pattern dimension replication and uniformity but this was not essential for fabricating the pattern across the entire wafer. Increased diffraction into the dark field due to the air gap increases the width of the sparse SU-8 structures, but

because the dark field is much wider than the light field, some decrease in the cavity width can still result in well-resolved SU-8 structures (Figure 4.6). The situation is much more delicate for dense structures separated by narrow cavities (the Mask C pattern). In this case, the increased penetration of diffracted light from both the long edges of the dark field can lead to the sloping walls of the developed SU-8 structures meeting above the surface of the wafer, resulting in shallow V-shaped channels, rather than the full-depth rectangular or trapezoidal cross-section channels desired (Figure 4.7), which was always observed at wafer center in our experiments if no soft cushion was used during exposure when Mask C was used. Most of the samples fabricated using soft cushion were successfully fabricated, except samples exposed for 90 sec or longer time.

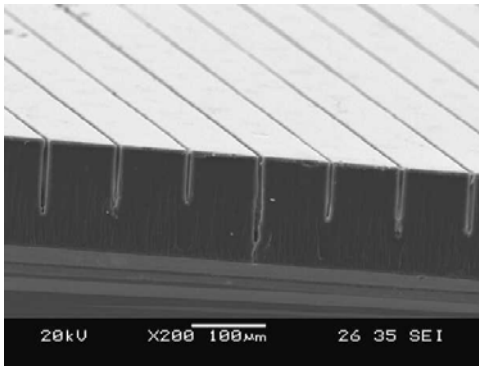

Figure 4.7 VHAR microchannels fabricated without the cushion using Mask C (exposure time: 35 s, 145µm SU-8, sample B1 in Table 4.1)

Using soft cushion technology, whole-wafer-covered 80µm wide SU-8 bars separated by VHAR microchannels was successfully fabricated (Figure 4.8). The average measured top width of these channels is 8µm and the depth is 145.1µm, giving an aspect ratio over 18. As expected, the SU-8 dimension (82µm) is slightly larger than the designed (80µm).

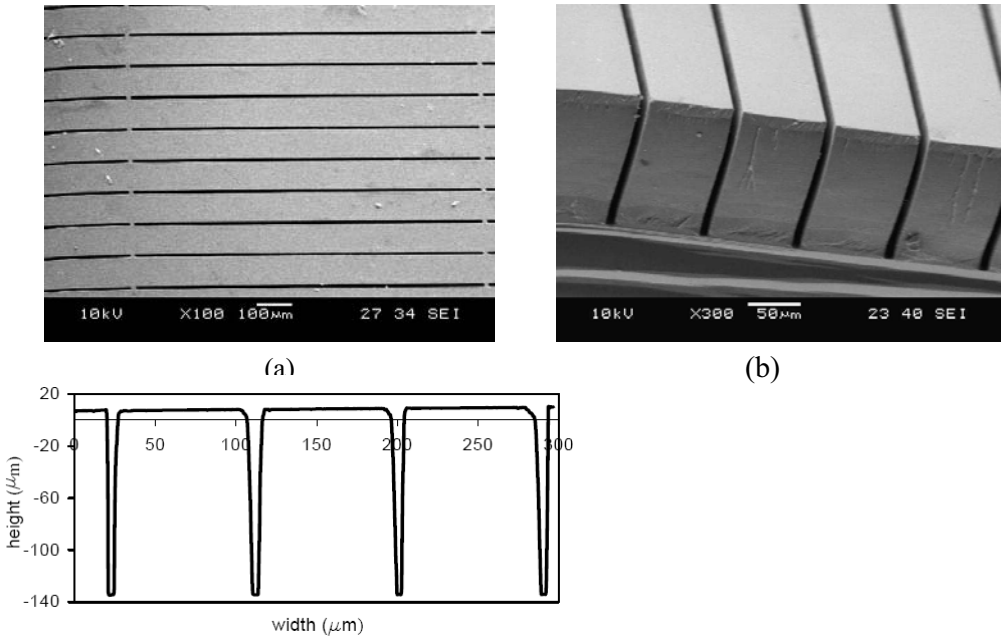

Figure 4.8 VHAR microchannels in SU-8 fabricated with Mask C and soft cushion over 100-mm diameter wafer: (a) SEM top view, (b) SEM cross section and (c) OP image of crossection (exposure time: 35 s, sample B2 in Table 4.1)

4.4.2 Effect of dose reduction

The effect of exposure time on the SU-8 profile has been theoretically and experimentally studied in Chapter 3. Wide channels were studied in Chapter 3 so that even with stray diffraction, refraction and reflection effects, the channels were still clearly developed though they were narrower than designed values. For narrow channels in thick SU-8, stray diffraction, refraction and reflection effects can cause un-resolved structures. An attempt to fabricate whole-wafer-covered gratings with 80µm wide SU-8 bars separated by 10µm wide channels (Mask C) using the supplier recommended dose of 500 to 650 mJ/cm^2 (50 to 60 seconds exposure time) was unsuccessful**.** With UV exposure this high, the channel walls were overexposed and the channels were unresolved and V-shaped. The narrow micro-channel of 10 µm width coupled with the edge bead led to stray exposure above the threshold gelation energy in the shadowed regions. Partial area of the wafer center was unresolved with 70 s UV exposure even with the employment of soft cushion (Figure 4.9).

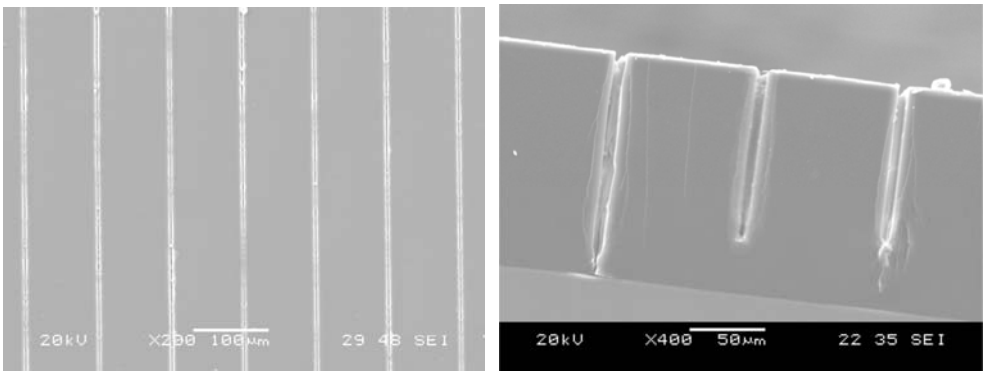

Figure 4.9 Un-resolved VHAR channels with soft cushion technology
(Mask C, SU-8 thickness 145 um, exposure time 70s, sample C1 in Table 4.1)

The observed unresolved VHAR microchannels in Figure 4.9 can be explained by a combination of the stray (diffraction, refracted and/or reflected) light in the "shadowed" region of the SU-8 and the low threshold gelation energy of SU-8 (30 mJ/cm^2 for 100µm-thick SU-8, refer to Chapter 3). UV light was diffracted from the edge of the dark field line of the mask into the "shadowed" area of the photoresist. Increasing the incident exposure dose by increasing the exposure time increased the UV light exposure energy in the "shadowed" areas of the photoresist. With low levels of UV light, some photoacid is generated in the SU-8 but the epoxy reaction is limited and insufficient to cause gelation. As the UV dose increases beyond a threshold value, more photoacid is generated resulting in gelation and crosslinking. With longer exposure, the regions beneath the shadowed regions receive more than the threshold gelation dose, the boundary between over- and under-gelation exposure moves further into the shadowed region and the developed channels become narrower. The stray light-induced narrowing of the channel bottom is a function of the exposure time, resist thickness and dark-field width. For a fixed UV dose and resist thickness, there is a minimum dark field width for successfully resolving the channel between the SU-8 bars. For dark fields narrower than this minimum value, V-shaped rather than rectangular- or trapezoid-shaped channels are formed instead. The problem is exacerbated for whole wafer covered SU-8 processing since spin coating always produces an edge bead. The edge bead leads to an air gap

between the photomask and the surface of the resist, which leads to diffracted light penetrating further into the shadowed area of the SU-8.

To fabricate well-resolved SU-8 gratings with VHAR channels (using Mask C and D) over the entire wafer, it is necessary to reduce the UV exposure dose significantly even with soft cushion technology. When UV exposure times of 25 to 40 seconds were used, well-resolved channels could be successfully developed. Figure 4.10 shows the 80μm wide SU-8 bars fabricated using an exposure time of 25 s, i.e. exposure dose of 250mJ/cm^2, much lower than the 500 to 650 mJ/cm^2 dose recommended by the supplier. Although the SU-8 was soft because of the under exposure, the wide dimension (80 μm) made it rigid enough to stand against the surface tension.

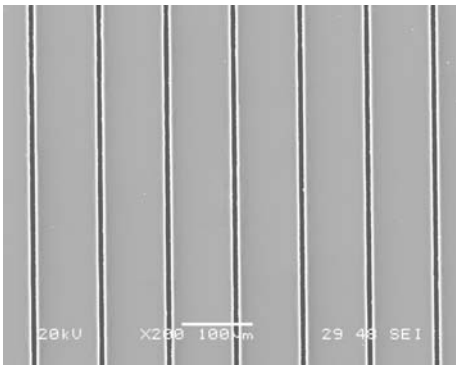

Figure 4.10 Clear microchannels over entire 100-mm diameter wafer
(Mask C, 145 μm SU-8, exposure time 25s, with soft cushion, Sample C1 in Table 4.1)

In fabricating dense micro-channels separated by narrow 10μm-wide SU-8 bars (Mask pattern D), the small distance between narrow SU-8 bars also caused strong adhesion force due to surface tension of the developer. Those SU-8 bars exposed for 30 s or less mostly collapsed or stuck together during or after development (Figure 4.11). This was mainly because the structures were still soft and the structures could not withstand the residual stress in the SU-8 and surface tension of the developing solvent during the development and drying process.

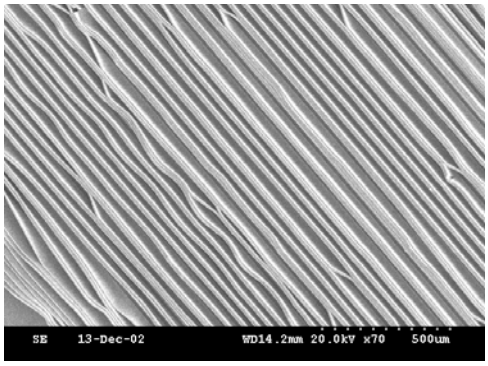

Figure 4.11 Sticking structure fabricated by under exposure (Mask D, exposure time 25 s, with soft cushion)

Increasing the exposure time gives high hardness, but the increased exposure also tends to increase the negative effect of diffraction, refraction and reflection on the profile leading to a decrease in the channel width. If the width of micro-channels (corresponding to dark-field on the mask) was too small or the thickness of the resist was too thick, the micro-channels would not be trapezoidal but V-shaped. Figure 4.12 shows the SEM micrograph of microchannels fabricated by 150 s exposure. The observed experimental top width of SU-8 bars increased to more than 14 μm. The channel width decreased. At the top of the channels, the observed experimental width was less than 6 μm. The excess exposure of UV light led to exposed and cross-linked SU-8 due to diffraction and reflection at the lower part of micro-channels resulting in V-shaped channel. The structure was also deformed because of large internal stress.

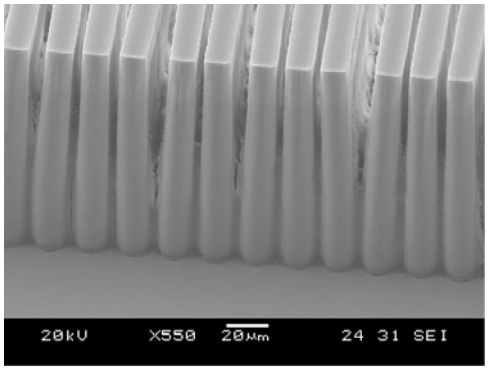

Figure 4.12 V-shaped channels because of over exposure (Mask D, exposure time 150s, with soft cushion)

Higher aspect ratios were easier to achieve for isolated structures (i.e. structures positioned far away). It is much more difficult to achieve VHAR with dense SU-8 gratings than with isolated narrow bars or small cylinders. With thick photoresist coatings, physical properties such as adhesion and structural rigidity play critical roles in obtaining VHAR in dense gratings. With VHAR channels, there is an optimum range of UV exposure dose in well-resolved channels and sufficient SU-8 rigidity prevail

Our results show that 30 s-70 s exposure time was suitable for both narrow and wide SU-8 bars separated by VHAR microchannels (Mask C and D) in 100 um thick SU-8 coating. For this SU-8 thickness, 50 s-70 s exposure sometimes gave whole-wafer-covered good pattern but produced unresolved pattern at the wafer center at other times. Exposure time of more than 70 s usually produced unresolved pattern at the wafer center. Figure 4.13 and 4.14 show whole-wafer-covered dense gratings fabricated with Mask C and D, using the dose-reduction exposure and soft cushion technology.

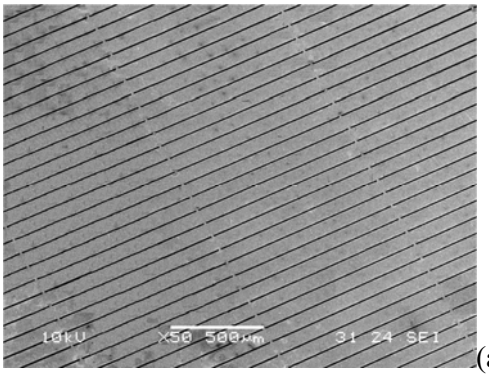

(a)

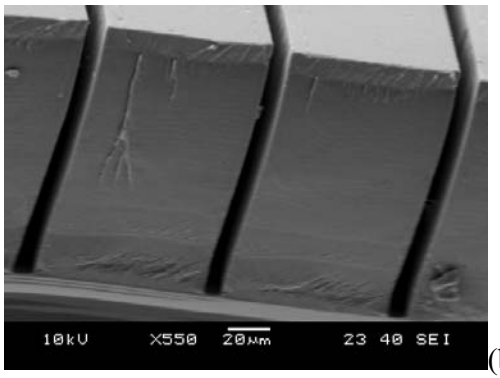

(b)

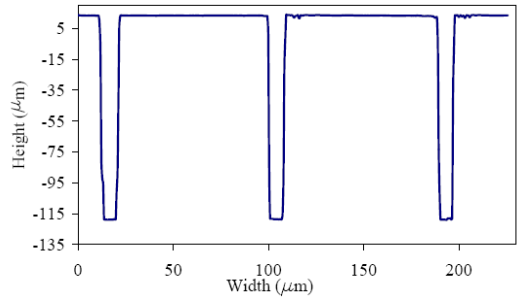

(c)

Figure 4.13 Sparse whole-wafer-covered VHAR channels (aspect ratio of 18) in 145µm-thick SU-8 with reduced exposure (35s), soft cushion and Mask C (before hard bake): (a) SEM over view, (b) SEM cross section and (c) Optical cross section

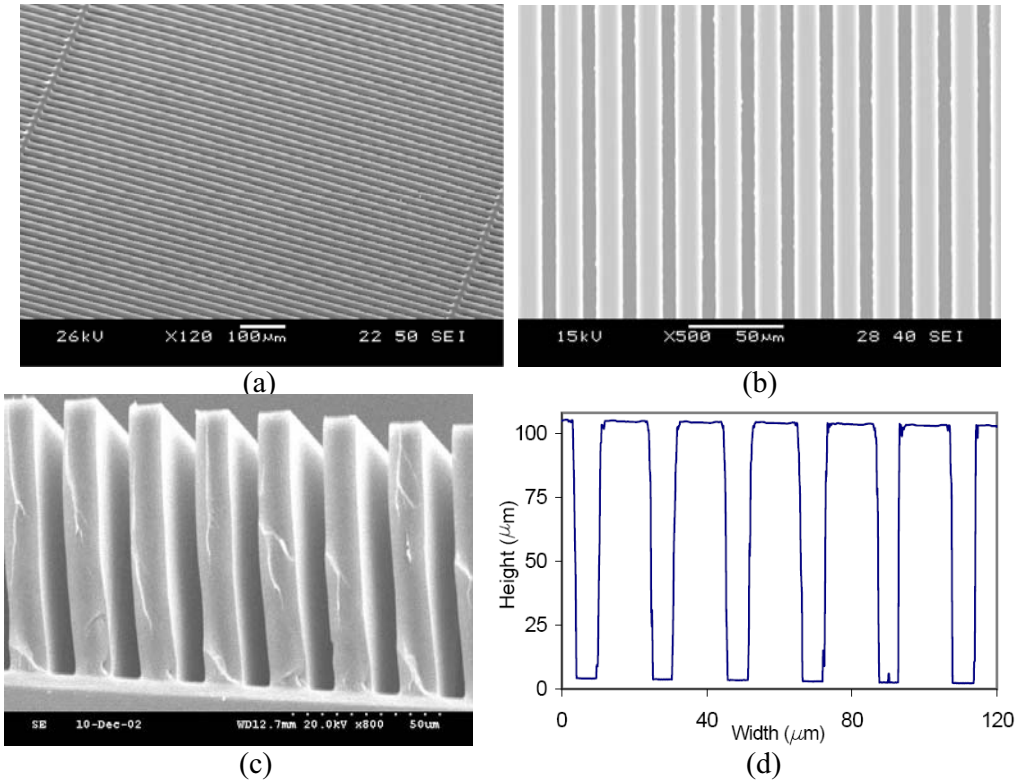

Figure 4.14 Dense whole-wafer-covered VHAR channels (aspect ratio of 12.7) in 100µm-thick SU-8 with reduced exposure (40s), soft cushion and Mask D (before hard bake): (a) SEM over view, (b) SEM top view,(c) SEM cross section, and (d) Optical cross section.

Typically, the SU-8 resist needed to be exposed beyond the gelation point so that it could withstand development and rinse without deformation. Further, an obstacle to the employment of underexposure as a technique for creating dense VHAR channels in microstructured SU-8 mold is that underexposed SU-8 is generally too soft for handling or for use as a mold for replica molding. Further, underexposed SU-8 is likely to adhere to the molding material cast on it. For use as a micro-mold for, SU-8 microstructures should have a certain minimum degree of strength and crosslinking density. Insufficient crosslinking results in diffusion of the molding resin into the SU-8 mold network and consequently, the interlocking of the SU-8 and the cured molding material so that the latter cannot be removed from the SU-8 without cohesive failure within the softer molding material. To compensate for the SU-8 softness and low crosslinking density

resulting from underexposure, additional curing is required in the form of hard-baking to thermally advance the crosslinking after development. The hard bake temperature suggested by the resist supplier to reach full crosslinking is between 150 and 200°C. In our experiments, this range was found to result in cracking of the SU-8 during the hard baking even with gradual heating up and gradual cooling down. A lower hard baking temperature (95°C) was investigated to avoid cracking and this was found to adequately increase crosslinking density and build sufficient strength for the underexposed microstructures.

Figure 4.15 shows that the hardness of a 100-μm thick unstructured cross-linked SU-8 was greatly affected by the UV exposure time (exposure dose is the product of exposure time times UV intensity). We first consider the effect of exposure time on the SU-8 without post-exposure hard baking. The Vickers Hardness (VH) number increased rapidly from 10.0±1.1 to 20.5±0.3 when the exposure time increased from 5 s to 20 s (exposure dose increased from50 to 200 mJ/cm^2). Beyond 20 s, the hardness began to saturate. When the exposure dose increased from 600 to 1000mJ/cm^2, the VH of the SU-8 without hard baking increased only slightly from 26.7±0.2 to 27.4±0.3. The SU-8 processed with the supplier's recommended UV dose (500~600mJ/cm^2) generally resulted in VH number of about 25 (Figure 4.15); and even without hard baking, this hardness was generally found to be sufficient for SU-8 microstructures to be handled and used for soft lithography. Using the reduced UV exposure dose of 350 mJ/cm^2, the hardness was too low (the VH number was about 22) to be used as a mold. When liquid UV molding resin was cast on the underexposed SU-8 microstructures which were not hard baked, the cured resin became interlocked with the soft SU-8.

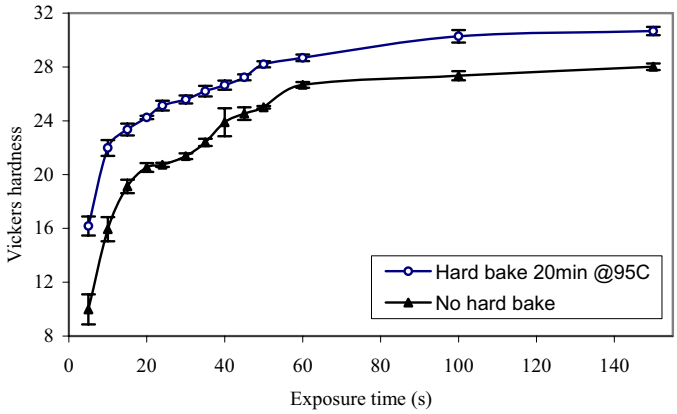

Figure 4.15 Effect of exposure dose on VH of SU-8 (SU-8 thickness:100μm)

Figure 4.16 shows the effect of hard baking time on the hardness of SU-8. Hard baking was found to enhance the crosslinking and hence the hardness, but only to a limited extent in comparison with the effect of exposure on hardness. For an UV exposure dose of 500 mJ/cm^2, the VH number increased from 25±0.1 to 28.2±0.2 when the hard bake time increased from 0 to 20 min. The Vickers Hardness saturated in the range 28.2±0.2 to 28.4±0.2 when the hard bake time increased from 20 minutes to 45 minutes. Saturation of the hardness at bake times beyond 20 minutes was observed for all tested exposures. Figure 4.16 shows that the increase of hardness produced by hard-baking is more pronounced for lower exposures than for higher exposures. Our data permit us to work backwards from the target mold hardness of VH 25 with hardness-saturating hard-baking (20 minutes duration) to the minimum exposure required to yield this target hardness after hard baking. Figure 4.16 shows that for the 100μm-thick SU-8 mold substrates considered here, the minimum exposure is 24 s (exposure dose 240 mJ/cm^2). The VH number after this exposure but prior to hard-bake is 20.7±0.2; this is increased to 25.1±0.4 after 20-minute hard baking at 95°C.

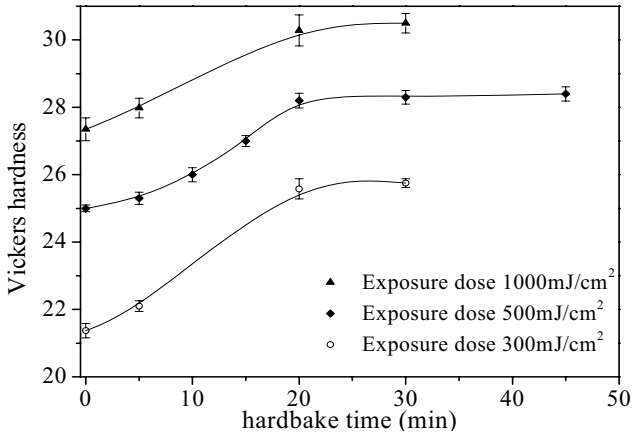

Figure 4.16Effect of exposure hard bake time on VH of SU-8 (SU-8 thickness:100μm)

These tests indicate that well-resolved microstructured SU-8 gratings with VHAR channels can be created using very low exposure doses compensated by hard baking at 95°C. In spite of this structural requirement for exposure beyond the minimum gelation exposure, there was still sufficient latitude to permit underexposure with respect to the manufacturer's recommendation for the purpose of achieving good channel resolution by limiting the stray diffracted, refracted and reflected light under the mask dark fields. The consequent lower cross-link density, and hence mechanical strength and hardness, were compensated by longer or higher-temperature post exposure baking. Our underexposed microstructures withstood the surface tension forces of developing solvent during drying. 20-minute hard baking at 95°C was used to harden the underexposed structures after development. Gradual cooling after PEB and hard baking were found to be essential to avoid structural deformation and distortion.

The experimental results showed that it is easy to fabricate sparse SU-8 gratings with VHAR SU-8 bars. The effect of diffraction, refraction and reflection is negligible because of the large distance between SU-8 bars. For fabrication of gratings using Mask B, a long exposure time produces hard and rigid structure which is good for development and handling.

4.5 Summary

Edge bead due to spin coating has been found to cause an air gap as large as 53μm for a 99μm thick (measured at the wafer center) SU-8 coating over a 100mm diameter wafer. This caused poor mask width replication and non-uniformity of SU-8 pattern width. A process using a soft cushion technology to improve mask dimension replication and large-area pattern uniformity has been developed in this chapter. A soft cushion was placed beneath the substrate to produce convex bending of the wafer in order to improve the contact between the mask and SU-8 top surface; thus, decreasing the stray UV diffraction, refraction and reflection. Dramatic improvements in pattern uniformity, from over 30% variation in SU-8 width across the wafer to less than 10%, and mask width replication, from 54% deviation from mask width to 20%, have been demonstrated.

We have devised a process using soft cushion technology which increases the pattern replication fidelity and uniformity over the whole 4-inch wafer. This technology was also shown to enable the fabrication of dense SU-8 gratings with VHAR microchannels over the 100mm diameter wafer. Increased UV exposure time is found to result in the narrowing of dark-field-pattern structures (or microchannels) due to the stray and low gelation energy of this photoresist. Process combining soft cushion technology with reduction of UV exposure dose to 350 mJ/cm^2 (30 to 40% below the manufacturer's suggested value) enables the successful fabrication of whole-wafer-covered dense SU-gratings with relatively wide (80μm) SU-8 bars separated by narrow (10μm) microchannels with aspect ratio of 18, and dense SU-gratings with narrow (10μm) SU-8 bars separated by narrow (10μm) microchannels with aspect ratio of 12.7.

The whole-wafer-covered SU-8 gratings created using soft cushion technology and the reduced-exposure with compensating hard-bake techniques was ready for further replication application.

Chapter 5 Network properties and degradation of cured of SU-8 resist

5.1 Introduction

Studies have been carried out to determine the thermal, mechanical[114, 118, 137] and viscoelastic[245] properties of cured SU-8. Study has also been carried out to investigate the lithographic properties of SU-8 as the function of photoacid generator concentration[131]. The chemical reaction during SU-8 crosslinking is complex because the chemical components in the resist are varied, depending on the processing conditions. Further, the removal of this resist remains great challenge. Commercial SU-8 removers, such as nano remover PG^{TM} (from MicroChem Corporation) and μChem 130 photoresist stripper (from M-O-T GmbH and Surtec Deutschland GmbH), are available. Only the major components of these removers are specified in the Material Safety Data Sheets (MSDSs). We found that single component concentrated sulfuric acid is also an effective remover. The removal mechanism and principle are not clear. Understanding the crosslinking reaction and network properties of cured SU-8 is very important for both the process optimization for VHAR structure fabrication and removal of this resist after electroforming. By far, no research work has been done to investigate the curing reactions, network formation and degradation of SU-8

The objectives of this chapter involve the fundamental study of curing and degradation of SU-8 resist. Cross-linking reactions and the network properties of cured SU-8 are characterized in this chapter, using various techniques such as Fourier Transform Infrared (FTIR) spectroscopy, Differential Scanning Calorimeter (DSC), Dynamic mechanical analysis (DMA), ^{13}C nuclear magnetic resonance (NMR) spectroscopy and

Gas Chromatography-Mass Spectrometry (GC/MS). The network properties are mainly determined by the molecular weight between crosslinks and the chemical structure of the chains between crosslinks. Kinetic studies were done to investigate the thermal degradation of SU-8 resist.

5.2 Experimental details

NANO™ SU-8 100 and SU-8 developer provided by Microchem Corp (Newton, Massachusetts) and gamma-butyrolactone (GBL) from Sigma-Aldrich Chemie GmbH (Germany) were used. The melting point and boiling point of GBL are -45°C and 204°C respectively, and the vapour pressure at 20°C is 0.2 KPa. 100 μm and 400 μm thick SU-8 films were prepared. The 100-μm-thick SU-8 films were mostly used except DMA characterizations. 400-μm-thick SU-8 films were used for DMA.

Sample preparation, chemical degradation of SU-8 and FTIR characterization were done at the Biological and Chemical Processing Laboratory (BCPE Lab), School of MAE, NTU; Thermal analyses (DSC, DMA, TGA) were carried out at the Materials Laboratory, MAE; NMR characterization was done at the Nuclear Magnetic Resonance Laboratory, Department of Chemistry, National University of Singapore (NMR Lab, NUS); GC/MS characterization was done at the Institute of Chemical & Engineering Sciences (ICES), Singapore. Details of FTIR, DSC, NMR, DMA, GC/MS and other characterizations are described in Sections 5.2.2 to 5.2.7.

5.2.1 Sample preparation

Silicon wafers were used as the substrates in this chapter. The Si wafers were pre-cleaned using the procedures stated in Section 3.2. A SUSS MA6 mask aligner at BCPE Lab was used for the sample exposure. The SUSS MA6 mask aligner has a mercury (Hg)

lamp without any filter. The measured intensity was 10 mW/cm^2 at 365 nm wavelength. Three groups of samples were prepared. The objectives and processing conditions of the sample groups are summarized in Table 5.1 and described in details in the following sub-sections. Group A samples were used to investigate the curing reaction of SU-8 in the presence of GBL. Group B samples were used to investigate the effect of epoxy conversion on the network properties and thermal degradation of SU-8 samples by varying UV exposure time. Group C samples were used to investigate the effect of varying amount of GBL content on the network properties and thermal degradation of cured SU-8. There are two samples in Group A, one is SU-8 cured without GBL, the other one is SU-8 cured with 27% GBL (weight percentage, as supplied). Group B samples have varying epoxy conversion ranging from 0 to 95%. Group C samples have varying GBL content ranging from 1% to 80% (w%).

5.2.1.1 Sample Group A

For samples in Group A, 100 um thick SU-8 100 was coated onto Si wafers by spin coating at 3000 rpm for 30s. Two types of samples were investigated. One (denoted as sample A1) was subjected to long-time softbake. The soft bake was done at 95°C for 4 days (96h) under vacuum condition (<0.01 atm) using a BINDER vacuum oven. Another one (denoted as sample A2) was as-supplied SU-8 100 without any softbake, which contained 27 weight% GBL. GBL content in sample A1 was supposed to be zero which was confirmed by FTIR measurement. Both samples were then exposed to UV light without any mask for 70 s using the SUSS MA6 mask aligner. PEB was done at 65°C for 3 min and 95°C for 10 min respectively, using a hotplate. The processed SU-8 films were then delaminated from substrates by quick cooling from 95°C to -85°C using a SANYO MDF-U50V ultra low refrigerator.

Table 5.1 Processing parameters for sample preparation

	Sample group A		Sample group B		Sample Group C	
	A1	A2	B1	B2	C1	C 2
objective	Investigate the crosslinking reactions of SU-8 with and without the present of GBL		Investigate the effect of UV exposure time (which leads to different epoxy conversion) on the network properties and degradability of SU-8		Investigate the effect of GBL content on the network properties and degradability of SU-8	
Coating	100um-thick SU-8 100 by spin coating		100um-thick, spin coating	400um-thick, spin coating	100um-thick, spin coating for GBL≤30% and spacer coating for GBL>30% (Figure 5.1)	400um-thick, spin coating for GBL≤30% and spacer coating for GBL>30%(Figure 5.1)
Softbake	3h @95°C using hotplate and then 96h @65°C in a vacuumed camber	No softbake	10 min @65°C, 30 min @95°C using hotplate	30 min @65°C, 200 min @95°C using hotplate	Soft baked for varied time @95°C for samples with GBL content lower than 25%; No softbake for samples with GBL content higher than 25%.	
Exposure time	70 s		Varied from 8s to 10s, 15s, 20s, 30s, 40s, 50s, 60s, 70s, 80s, 90s, 100s, 150s, 200s and 500s		70 s	
PEB	10 min @95°C		10 min @95°C	30 min @95°C	10 min @95°C	30 min @95°C
Post-cure-processing	All cured SU-8 samples were baked @65°C using a vacuum oven for 6 days. The chamber was always kept at vacuum condition.					
Characterization	FTIR; solid state ^{13}C NMR, liquid ^{13}C NMR, GC/MS		FTIR; TGA; DMA		FTIR; DMA; TGA. Change of sample weight was also recorded at different processing time.	

5.2.1.2 Sample Group B

In Group B, 100 um (samples B1) and 400 um (samples B2) thick SU-8 100 films were deposited onto silicon wafers by spin coating at 3000rpm for 30 s and 500rpm for 60s respectively. Samples B1 were used for TGA and FTIR examinations while samples B2 were used for DMA measurement. Samples B1 were soft baked at 65°C and 95°C for

10 min and 30min respectively. Samples B2 were soft baked at 65°C and 95°C for 30 min and 200min respectively. All softbaking was done using a hotplate. The samples were then exposed to UV light using the SUSS MA6 mask aligner. Samples B1 were exposed without any mask while samples B2 were exposed through a mask with a 5mm× 10mm rectangle light field opening. The exposure time varied from 0s to 8s, 10s, 15s, 20s, 30s, 40s, 50s, 60s, 70s, 80s, 90s, 100s, 150s, 200s and 500s. The exposed samples were then baked for 10 min at 95°C using a hotplate. SU-8 films for DMA, TGA and FTIR were then delaminated from the substrates by quick cooling from 95°C to -85°C using a SANYO MDF-U50V ultra low refrigerator. Some of the 500s-exposed SU-8 were further hard baked for 6 hours at 150°C to fully cure the SU-8 resist. The processed samples of group B had different epoxy conversion. The epoxy conversion of all samples of group B was determined using FTIR measurement. The GBL content of samples group was also determined using FTIR measurement. The measured GBL content of all samples in group B was 1±0.2% (described as 1% hereafter). The sample with UV exposure time of 0 s was assumed to have 0% epoxy conversion.

5.2.1.3 Sample Group C

Sample Group C was prepared from SU-8 resist mixed with different amounts of GBL. Both 100 um thick (samples C1) and 400 um thick (samples C2) SU-8 films were prepared; C2 was for DMA. For SU-8 with GBL content lower than 30%, the coating was done by spin coating. The coating conditions were the same as those stated in section 5.2.1.2. By soft baking the coated SU-8 100 at 95°C for varied time, varying GBL content of 1%, 3.9%, 4.1%, 6.9%, 15.7% and 27% (measured by FTIR) were achieved. Diluted SU-8, i.e. with GBL content equal to or higher than 30%, and FTIR examination. For SU-8 with GBL content equal to or higher than 30% (denoted as diluted SU-8), were achieved by adding appropriate GBL amount to the original SU-8

100 and stirring for 12 hours using a magnetic stirrer. SU-8 samples with GBL content of 30%, 32%, 35%, 40%, 50%, 70% and 80% were prepared. Diluted SU-8 was coated onto Si wafers using a spacer made of polyester film (specifically Melinex® 454 film from DuPont Company) (see Figure 5.1). The spacer and the substrate form a small reservoir to hold of the liquid diluted SU-8. The low viscosity easily flattens the SU-8 surface and excess SU-8 overflows the spacer. The diluted SU-8 was exposed to UV without any softbake.

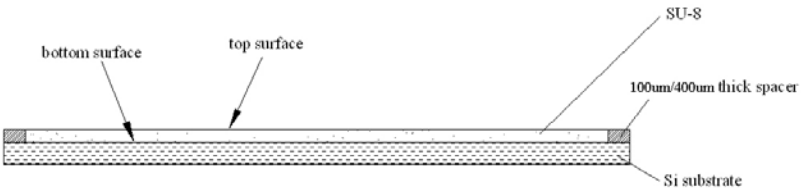

Figure 5.1 Sketch of coating diluted SU-8 using a spacer

After UV exposure and PEB, all samples (sample Groups A, B and C) were kept in a vacuum oven at 65°C under vacuum condition (<0.01 atm) for at least 6 days. This was to extract the excess unreacted GBL in the cured SU-8 resist. For samples of group C, the samples were weighted to record the weight changes during the processing.

5.2.2 FTIR

Fourier Transform Infra-Red-Attenuated Total Reflectance (FTIR-ATR) spectroscopy was used to monitor the epoxy conversion of SU-8[246]. A Nicolet Magna-IR 560 FTIR spectrometer with DTGS KBr detector was used to measure GBL content and epoxy conversion of these cured SU-8 resist. The FTIR characterization was then carefully done to ensure that all SU-8 films were examined at the top surface (Figure 5.1). The top surface was marked before SU-8 films were delaminated from substrates. Thereafter the residual epoxy content was calculated using the epoxy peak area at 910 cm^{-1}. The content of GBL was determined using the peak area at 1770 cm^{-1}.

Unprocessed SU-8 100 and SU-8 10 were also characterized to act as reference for the epoxy group and GBL content. It was assumed that the original SU-8 has an epoxy conversion of 0%. The peak at 1600 cm^{-1} was used as the internal reference peak; it was assigned to aromatic rings in the SU-8 molecule which will not change during cross-linking reaction. All peak areas were normalized using the internal reference.

5.2.3 Differential Scanning Calorimeter (DSC)

A DSC device (TA Instruments, Model 2920) was used to study the thermal curing of SU-8 resist. The material used was unexposed sample B1 (section 5.2.1.2). Samples of approximately 10 mg were sealed in aluminum containers and thermally scanned in helium atmosphere. The helium gas flow rate was 15 ml/min. Two sets of DSC data were collected. One set was scanned from -20°C to 400°C at the heating rate of 5°C/min, using the virgin unexposed sample B1. For the other set of DSC data, the virgin unexposed sample B1 was first scanned from -20°C to 350°C at the heating rate of 5°C/min using the same DSC device, then cooled down to room temperature and then the sample was re-weighted for a second run of DSC scanning. The second run of DCS was done from -20°C to 400°C at the heating rate of 5°C/min.

5.2.4 Solid state ^{13}C NMR

Solid-state cross-polarization and magic angle spinning (CPMAS) nuclear magnetic resonance spectroscopy (NMR) has been widely used to characterize insoluble polymers as a source of information on molecular dynamics of the polymer blends and changes taking place on the macromolecular network [183-188].

Samples which were cured with and without GBL (samples A1 and A2) were cut into very small pieces (smaller than 1mm×1mm), kept under vacuum (<0.01 atm) condition

at 65°C for another 24 hours and then ground to fine powder using a mortar. Room-temperature solid-state ^{13}C CPMAS NMR spectra were recorded at 100.61 MHz on a Bruker Avance 400 spectrometer (Bruker Instruments, Billerica, MA) at 300K. The spin rate was 10 KHz, recycle delay time was 3s, contact time was 2 ms, spectral width was 260.8 ppm. Chemical shifts are quoted in parts per million (ppm) from tetramethylsilane (TMS).

5.2.5 DMA

A Perkin-Elmer DMA7 dynamic mechanical analyzer (DMA) was used to determine the elastic storage modulus and glass transition temperature T_g of cured SU-8 samples. Samples of group B2 and C2 (defined in sections 5.2.1.2 and 5.2.1.3) were examined to study the effect of conversion and GBL on the network properties of cured SU-8 resist. SU-8 samples were scanned from 25°C to 200°C in nitrogen using the 3-point bending mode. The frequency used was 1 Hz and the heating rate was 3 °C/min The cross-link density was inversely proportional to the molecular weight between cross-links (*Mc*); the later was calculated using equation (3-36)[247]

5.2.6 TGA

Thermal degradation of SU-8 cured to varying epoxy conversion (sample Group B) and with varying GBL content (sample Group C) was studied using thermal gravimetric analysis in dynamic mode. Heating rates of 5°C/min, 15°C/min, 25°C/min and 35°C/min using a Perkin-Elmer TGA-7 thermal gravimetric analyzer were investigated. Samples were thermally scanned from 30°C to 700°C under nitrogen atmosphere. The nitrogen flow rate was 20ml/min. Activation energy of thermal degradation was determined using Kissinger's method[248-251]. The data of thermal-gravimetric analysis was introduced to Kissinger equation[252-255]:

$$-\ln\left(\frac{\beta}{T_m^2}\right)=\frac{E_a}{RT_m}-\ln\left(A\ n(1-\alpha)^{n-1}\right) \tag{5-1}$$

where β is heating rate

T_m is the temperature at the peak of DTG curve

E_a is the activation energy

A is a pre-exponential factor

n is the empirical order of reaction

α is the fraction degraded

Thermal degradation activation energies can be obtained from the relationship between heating rate and temperature at the peak value of DTG curve by plotting $\ln(\frac{\beta}{T_m^2})$ versus $\frac{1}{T_m}$ plot (hereafter denoted as Kissinger plot).

5.2.7 Weight change measurement

Weight changes of samples of group C were measured using a Fisher Scientific B220C analytical balance at BCPE Lab. The balance reading had 4 decimal places and the full scale was 220 g. Typical sample weight (before processing) was 1g. Weight fraction of GBL (γ_{GBL}) was defined as below to characterize the GBL trapped in cured SU-8.

$$\gamma_{GBL}=\frac{w-w_{original}\cdot(100\%-GBL\%)}{w} \tag{5-2}$$

where GBL% is the weight fraction of GBL in original mixture,

$w_{original}$ is the weight of original SU-8-GBL mixture before exposure,

w is the weight at the measuring moment after UV exposure,

γ_{GBL} is weight fraction of GBL in the SU-8-GBL system.

5.2.8 Chemical degradation of cured SU-8 using concentrated H_2SO_4

Chemical degradation of cured SU-8 was conducted by dissolving in concentrated H_2SO_4 (98 wt%). Samples A1 and A2 were used to investigate degradation products of

SU-8 cured with and without GBL. Samples of Group B1 were used to investigate the effect of epoxy conversion on the chemical degradability. Samples of Group C1 were used to investigate the effect of GBL content on the chemical degradability. The exposed samples were cut into very small pieces (less than 1mm×1mm). 0.5 ml concentrated sulfuric acid (98%) was then added into 0.15 g SU-8 sample and subjected to ultrasonic agitation for 2 min. The ultrasonic agitation source was 1210E-MT Bransonic® ultrasonic cleaner with a frequency of 47 kHz and power of 80 W. The temperature of H_2SO_4 acid was 25±1°C. The acid was then neutralized using 10% sodium hydroxide solution. The neutralization was carefully done to avoid overheating of the liquid mixture: the acid-SU-8 mixture was first diluted by slowly adding into 5 ml deionized (DI) water and the diluted mixture was then neutralized using sodium hydroxide (NaOH) solution. The pH value of neutralized solution was measured to be 7.0±0.2, measured using an accumet® AB15 pH meter. The residual solid SU-8 was filtered out using filter paper. The neutralized solution was ready for liquid NMR measurement. Room temperature liquid ^{13}C NMR was done using a Bruker AMX-500 NMR Spectrometer at 125.76MHz. The solution for Gas Chromatography-Mass Spectrometry (GC/MS) measurement was prepared by further treatment with diethyl ether. 3 ml diethyl ether was used to extract the organic products from 10 ml of the filtered neutralized solution. The mixture of diethyl ether and neutralized solution was put into a 50-ml-test-tube and manually shaken for 30 min, then settled for 12 hours to let the diethyl ether be separated from the mixture. The organic products in diethyl ether were then ready for GC/MS examination. GC/MS examination was done using an Agilent Technologies 6890/5973 GC/MS system. The sample injection was 2 µl. The GC oven was programmed from 50°C to 150°C at 5°C min^{-1} and then up to 250°C at a rate of 15°C min^{-1}. For the chromatographic separation, Helium was used as the carrier gas. The gas flow rate was 1 ml min^{-1}.

For the measurement of the etching rate, SU-8 coatings on substrates were directly used without delaminating from the substrate. This was to ensure that all dissolution occured from the top surface of SU-8 films. Samples were cut into 2cm×2cm square pieces. The SU-8 coatings of samples Group B and C on substrates were immersed into excess (i.e. 50 ml) concentrated sulfuric acid (98%) and subjected to ultrasonic agitation (1210E-MT Bransonic®) for 5 min. The residual SU-8 after partial dissolution in sulfuric acid was thoroughly rinsed with DI water and blown dry using compressed air. The thickness change was measured using a Mitutoyo ID-C125B micrometer while the residual mass was measured using a Fisher Scientific B220C analytical balance.

5.3 Results and discussion

Both solution NMR and solid state NMR data reported in this section are averaged from 3 measurements. GC/MS data reported are averaged from at least 3 measurements. Reported SU-8 etching rates in H_2SO_4 are averaged from at least 8 measurements. All other data (FTIR, DMA, TGA, DSC, weight change, et. al) are averaged from 5 measurements.

5.3.1 Chemical reactions during curing in presence of GBL

Ring-opening reaction of the epoxy group occurs and further cross-linking takes place in the curing of SU-8 as shown in Figure 2.5. As each SU-8 monomer molecule carries eight epoxy groups, a tightly crosslinked polymer network is formed when crosslinking occurs [256]. It is well known that the cross-linking reaction consumes epoxy in the resist. FTIR was used to monitor the conversion of epoxy group. The area under the 910 cm^{-1} peak duo to epoxy is used to calculate percent conversion, assuming the 100% uncured state is represented before UV curing.

Figure 5.2 shows the FTIR spectra of Sample A1 before and after curing with 70 s exposure followed by 10 min PEB at 95°C. Since sample A1 was subjected to very long time soft baking before it was exposed to UV light, the amount of GBL was below the detection limit of the instrument, the GBL content in the SU-8 resist was assumed to be zero. The FTIR spectra confirmed this assumption. GBL solvent, which has a 1770 cm^{-1} peak due to carbonyl C=O stretching of cyclic ester, was not found in the spectra before curing. In this case, the epoxy group only reacted with another epoxy group, either in the same or different molecule (Figure 2.5). Peak at 910 cm^{-1} decreased, but not disappeared. The curing reaction took place during PEB and SU-8 cross linked to a 3D network[123]. The network structure further decreased the diffusion or segmental movement of SU-8. Thus, full cross-linking was not achieved. The conversion of sample A1 cured for 10 min at 95°C was 63±6%; there remained 37±6% un-reacted epoxy. Previous study found that there was about 40% un-reacted epoxy group in SU-8 even when it was exposed to UV light for 150 s[247].

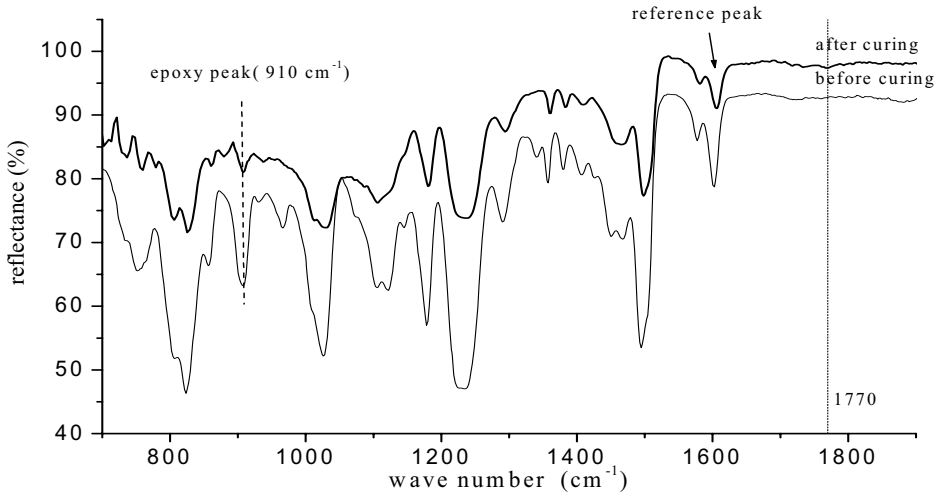

Figure 5.2 FTIR spectra of Sample A1 before and after curing with UV exposure (70s @ 10 mW/cm^2) followed by PEB (10 min @ 95°C on a hotplate)

The cross-linking of SU-8 is much different in the presence of GBL. The original SU-8 100 (sample A2) was studied to investigate the reaction between SU-8 and GBL. Figure

5.3 shows the FTIR spectra of original SU-8 100 before and after curing. The original SU-8 100 is a SU-8-GBL mixture system with 27% (weight %) GBL solvent. The strong peak at 1770 cm^{-1} is the GBL solvent in the non-soft-baked SU-8. The presence of GBL led to high epoxy conversion. The peak at 910 cm^{-1} totally disappeared, indicating that all epoxy groups were consumed during the curing cycle. Figure 5.4 shows the effect of GBL content on epoxy conversion with 70s UV exposure (samples of Group C). For the sample without GBL, the epoxy conversion was 63%. The conversion increased to 66%, 67%, 75%, 80% and 99% when the GBL weight percentage increased to 0.6%, 1%, 4%, 5% and 8.5% respectively. Nearly all epoxy groups in SU-8 reacted and gave a 100% conversion when the GBL content was higher than 15%.

The GBL led to higher epoxy conversion in two ways. Firstly, although GBL did not undergo cationic homopolymerization [168, 170], it copolymerized itself with epoxy and was reacted into the cross-linked network of SU-8 and GBL. The disappearance of peak at 1770 cm^{-1} (due to carbonyl C=O stretching in GBL) indicated that the original GBL was also consumed during the curing. Secondly, the GBL, which is a small molecule, acted as a fugitive molecule during crosslinking. GBL solvent in the SU-8 resist decreased the viscosity and made the SU-8 molecule more mobile, leading to decreased diffusion resistance of SU-8 molecule during crosslinking. The mobility and decreased diffusion resistance increased both the GBL-epoxy copolymerization and epoxy-epoxy homopolymerization.

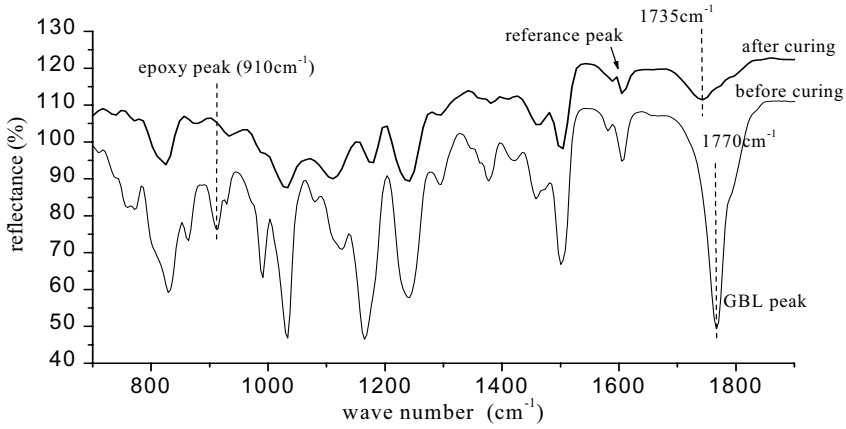

Figure 5.3 FTIR spectra of Sample A2 before and after curing (70s UV exposure @ 10 mW/cm^2 followed by PEB 10 min @ 95°C)

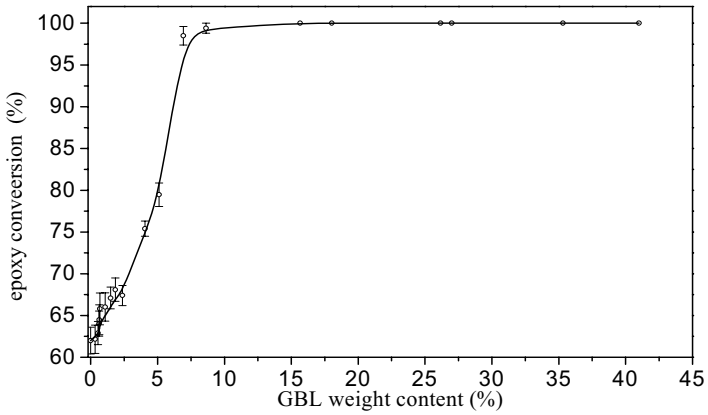

Figure 5.4 Effect of GBL content on epoxy conversion of the SU-8-GBL system (Sample Group C)

GBL, a five-membered ring monomer, is known to be unreactive with photoinitiators, because of a small ring strain[160]. However, it has to be stressed that the inability to easily form a high molecular weight homopolymer does not imply that the GBL ring can not be opened at all[159]. In fact, ring opening reaction occurs in GBL in the presence of Lewis acid at elevated temperature [257]. Mars et al [165] reported the copolymerization of Diglycidyl Ether of Bisphenol A (DGEBA) with GBL. It was also reported that spiroorthoesters (SOE) was formed during the cross-linking of epoxy with lactone[161] (Reaction I, Figure 2.6). SOE is presented as an intermediate product [165]. Further reactions of SOE itself (Reaction II, Figure 2.6) and SOE to epoxy group

(Reaction III, Figure 2.6) resulting in carbonyl C=O group in polyester (Figure 2.6). GBL can act as a bridge for the cross-linking of epoxy groups (Reaction III, Figure 2.6). The appearance of peak at 1735 cm^{-1}, attributable to stretching of carbonyl C=O in linear ester[161], confirms the cross-linking reaction of GBL and epoxy by copolymerization[162]. Reacted GBL acts as a bridge between two epoxy groups in the network of cured SU-8 (Figure 2.6), leading to longer aliphatic chain in the network as well as higher epoxy conversion.

Figure 5.5 compares the solid state ^{13}C NMR spectra of cured samples A1 and A2. The NMR results clearly show the difference between cured A1 and A2. The peak assignment of the spectra was done by reference searching[160, 186, 187, 258-262]. The peaks at 155.1 ppm, 143.3 ppm, 127.7 ppm and 110.7 ppm (peaks ***a, b, c, d***) can be assigned to the carbon in benzene ring. The peak at 69.7 ppm (peak ***e***) is ascribed to the carbon in ether groups. In the spectrum of Sample A1 (i.e. GBL content is 0%), the peaks at 50.1 ppm (peak ***f***) and 44.2 ppm (peak ***g***) are attributed to the carbon on an un-reacted epoxy ring[187, 258]. The obvious peaks ***f*** and ***g*** confirm the residual epoxy groups due to the low epoxy conversion in cured Sample A1. In the spectrum of Sample A2 (i.e. GBL content is 27%), no peaks are present at 50.1 ppm and 44.2 ppm (i.e. no peaks ***f*** and ***g***), indicating that there is no residual unreacted epoxy group detected in the cured sample. Four additional peaks appeared at 179.1 ppm (peak ***L***), 63.5 ppm (peak ***M***), 27.7 ppm (peak ***N***) and 21.8 ppm (peak ***P***) in the spectrum of Sample A2. The peak at 179.1 ppm (peak *L*) was attributed to carbon in carbonyl (C=O) group[258, 261-264], peak *M* at 63.5 ppm was assigned to carbon atom in ether bond[258, 263]. The ^{13}C NMR results confirm the reaction of GBL with SU-8 molecule. The peaks at 27.7 ppm and 21.8 ppm (peaks ***N*** and ***P***) were assigned to carbons in $–CH_2$ bonds respectively[258, 263].

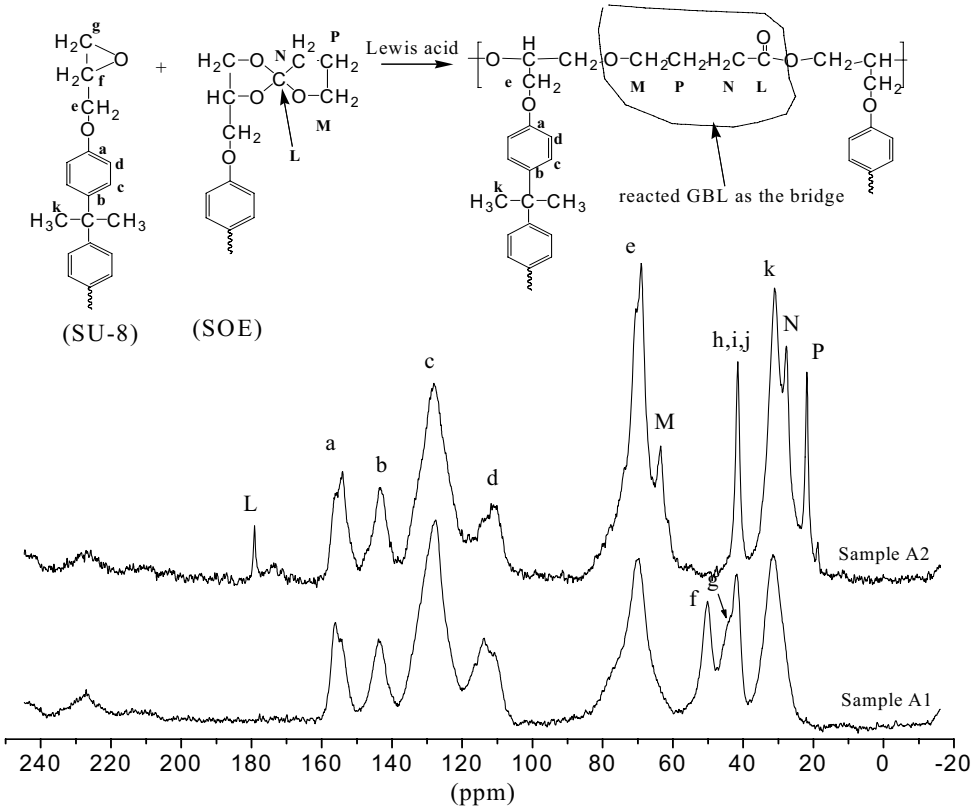

Figure 5.5 13C NMR spectra of non-softbaked and long-softbaked SU-8

GBL reacts randomly with SU-8 and it is proposed that GBL distributes evenly in cured SU-8. Figure 5.6 shows our hypothesis of one possible network structure of SU-8 cured with GBL. The suggested network structure is based on SU-8 structure (Figure 2.3), the reported chemical reactions (Figure 2.6), above NMR spectra and the peak assignment. The SU-8 network shown in Figure 5.6 is formed from reactions of epoxy groups in one SU-8 molecule. GBL reacted randomly with SU-8 molecule. It should be noted that reactions also take place between different SU-8 octa-functional molecules, and there may be functional groups (i.e. epoxy and SOE) randomly remaining in the network.

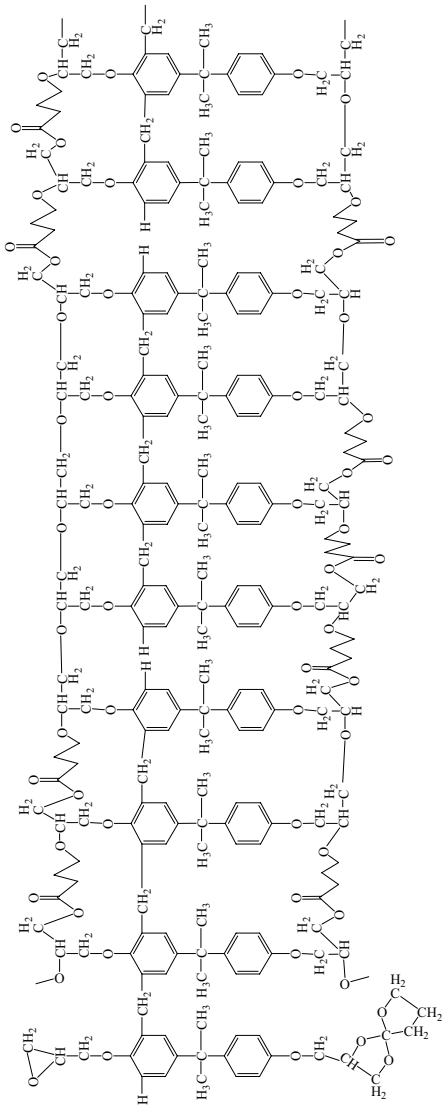

Figure 5.6 Possible network structure of SU-8 cured with GBL(mole ratio for GBL/epoxy is 1:2)

During the cross-linking reaction, some GBL reacts with SU-8. Excess GBL remaining in the cured system can be removed by long-time vacuum baking process. The amount (by weight) of GBL incorporated into the network can be calculated by measuring the weight difference between original SU-8-GBL mixture and the cured system after vacuum extraction. Figure 5.7 shows the weight fraction of GBL in SU-8 samples after UV exposure, PEB and vacuum extraction. It can be seen that samples with original GBL weight fraction less than 0.32 do not change their weight during the

exposure/PEB/extraction cycle. On the other hand, the GBL weight fraction of those samples with original GBL content of 0.4 or higher decreass rapidly during the PEB process (at 95°C).

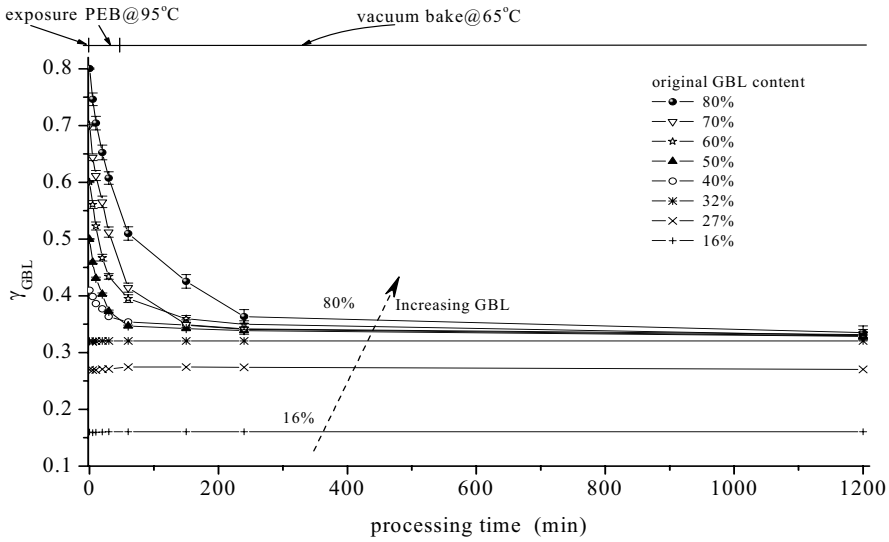

Figure 5.7 SU-8-GBL weight change during processing

The weight loss is due to the evaporation of unreacted GBL. The GBL weight fraction kept decreasing in the vacuum extraction process. The boiling point of GBL can be predicted using the Clausius-Clapeyron equation[265, 266]

$$\ln(\frac{P_1}{P_2}) = \frac{\Delta H_{vap}}{R}(\frac{1}{T_2} - \frac{1}{T_1}) \tag{5-3}$$

where $T_1$and T_2 are boiling points at pressure of P_1 and P_2 respectively, ΔH_{vap} is the enthalpy of vaporization. The boiling point T_1 at P_1=1 atm is 204°C [122] and ΔH_{vap} = 45.2 KJ/mol [267], then the boiling point T_2 is 66°C at P_2=0.01 atm. Thus, our vacuum extraction (<0.01atm) process at 65°C was efficient for removal of unreacted GBL.

γ_{GBL} tended to be stable at about 0.33-0.35 when the vacuum baking time was longer than 10 hours and did not further decrease after γ_{GBL} reached this stable value. Figure 5.7 shows that no more GBL can be physically removed from the cured SU-8 after 10

hours (600 min) of vacuum baking. Figure 5.8 plots the equilibrium γ_{GBL} (after 48 hours of vacuum baking) of SU-8-GBL system with different original GBL content. The equilibrium γ_{GBL} is the same as the original GBL weight fraction if the original GBL weight fraction is less than 0.32. This means there is no weight difference between the original mixture and the cured system when the GBL weight percentage in the mixture is less than 32%, indicating that there is no unreacted GBL in the cured system. The equilibrium γ_{GBL} is about 0.33 when the original GBL is higher than 33%. Even when the original GBL content is as high as 80% of the mixture, the equilibrium γ_{GBL} is stable at 0.33~0.34 after the cured system is vacuum baked at 65°C for 48 hours. The results show that the maximum GBL incorporation is about 33% (w/w) of the original SU-8-GBL mixture.

Assuming GBL does not homopolymerize[159, 268, 269], since there are 8 epoxy groups per SU-8 molecule (Figure 2.3), 1 mole SU-8 at most can react with 8 moles of GBL. The mole ratio 1:8 is equivalent to the weight ratio of 2:1 for SU-8 and GBL considering the molecular weight of SU-8 and GBL are 1396 and 86 respectively. GBL can totally react with SU-8 when the SU-8/GBL weight ratio is higher than 2:1 (equivalent to GBL weight percentage less than 33%). Higher proportion of GBL does not react and remains in the material acting as a plasticizer. The unreacted GBL evaporated during the vacuum baking process, leading to the weight change of the resist. This explains why the equilibrium γ_{GBL} was about 0.33, whatever the original GBL weight percentage was. The SU-8 which has GBL weight content of 0.33 has a mole ratio for GBL: epoxy of 1:1. The result verifies that GBL does not homopolymerize but copolymerized with epoxy.

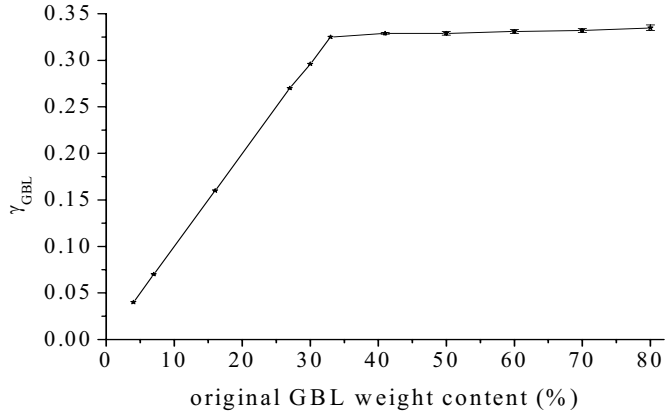

Figure 5.8 The equilibrium γ_{GBL} of SU-8-GBL system

5.3.2 Network properties of cured SU-8

The network properties of cured SU-8 are affected by the epoxy conversion and GBL content in the resist. We investigated the effect of epoxy conversion (Group B, section 5.2.1.2) and GBL content (Group C, section 5.2.1.3) on these network properties of cured SU-8: molecular weight between cross-links (M_c) and glass transition temperature (T_g). Figure 5.9 shows the effect of epoxy conversion on M_c. Very high *Mc* value was obtained at low epoxy conversion. The M_c value is 2869 g/mol for SU-8 with epoxy conversion of 27.2%. M_c value decreases rapidly from 2433 g/mol, 882 g/mol, 634 g/mol to 294 g/mol when the epoxy conversion increases from 34.5% to 49%, 52% and 62% respectively. When more epoxy end groups react and high epoxy conversion is achieved, the SU-8 resist is highly cross-linked, which gives very low M_c value shown in Figure 5.9. The M_c value is 178 g/mol and 136 g/mol when the epoxy conversion increases to 78.9% and 90%. The calculated theoretical value of SU-8 fully cured without GBL is 116.3 g/mol. Our experimental results agree with the theoretical calculation. Matějka and coworkers [164] studied the cationic polymerization of DGEBA in the presence of GBL and found that the cross-link density remains at a low level until a fairly high conversion (about 75%) whereafter the rise is rapid. In our results, the inflexion point for the M_c versus epoxy conversion curve is at conversion of 55% under the processing conditions (Section 5.2).

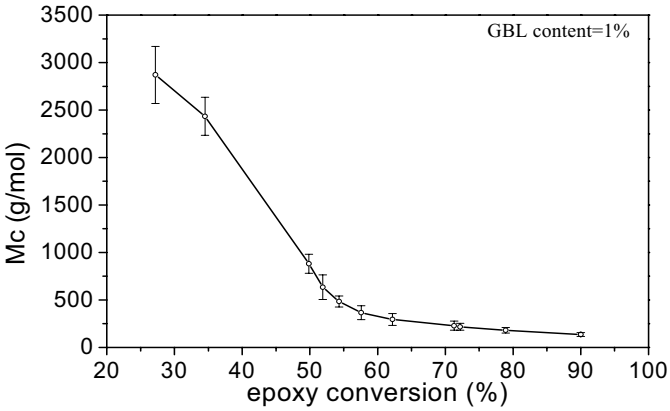

Figure 5.9 Effect of epoxy conversion on M_c

In low epoxy conversion range (<50%), although the resist has gelled, there remains large portion of unreacted SU-8 molecules as well as unreacted epoxy groups in partially reacted SU-8 molecules. Chain extension rather than crosslinking can predominate. Long chains and loosely cross-linked domains largely accounts for the low modulus[243], which results in high M_c value. Figure 5.10 shows the storage modulus of SU-8 resist with varied epoxy conversions. High epoxy conversion led to high storage modulus.

The inflexion point for the curve in Figures 5.9 can be explained by vitrification during SU-8 curing. Vitrification is the transformation from liquid or rubbery material to glassy material[270] . At vitrification, the material solidifies and the chemical reactions can be stopped (the curing reaction kinetics goes from chemistry driven to diffusion controlled [271]), T_g can, therefore, equal or exceed the curing temperature[272]. Under the processing conditions stated in Section 5.2, SU-8 vitrifies when the epoxy conversion reaches 55% (Figure 5.11). T_g of SU-8 resist was measured by DMA. Figure 5.11 shows the T_g *versus* conversion curve. T_g of uncured SU-8 is 50°C[137, 138]. It increases monotonously with the increase of conversion and remains at low value in low conversion range until the conversion reaches 55%, where T_g is 95°C which is

equal to the curing temperature (PEB temperature). The experimentally measured T_g does not change significantly when conversion is higher than 55%.

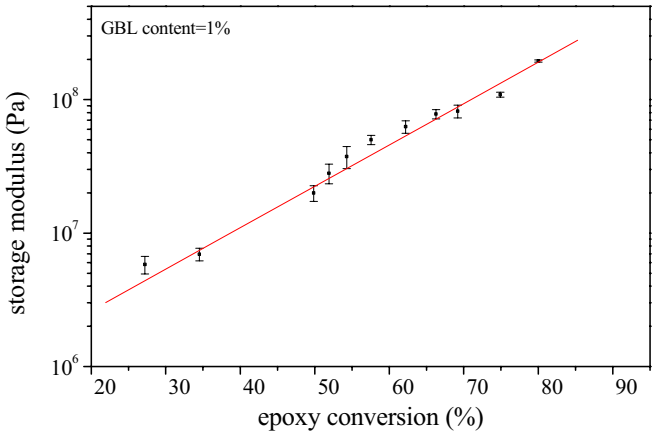

Figure 5.10 Effect of epoxy conversion on the storage modulus of cured SU-8 resist

The relationship between T_g and conversion for thermosetting materials has been theoretically[273-275] and experimentally[137, 271, 276-278] studied. The most used relationship between T_g and conversion is the DiBenedetto equation[274] expressed as

$$\frac{T_g - T_{go}}{T_{g\infty} - T_{go}} = \frac{\lambda x}{1-(1-\lambda)x} \tag{5-4}$$

where λ is an adjustable parameter included between 0 and 1, x is the conversion, T_{go} is the glass transition temperature of uncured material and $T_{g\infty}$ is the glass transition temperature of fully cured material.

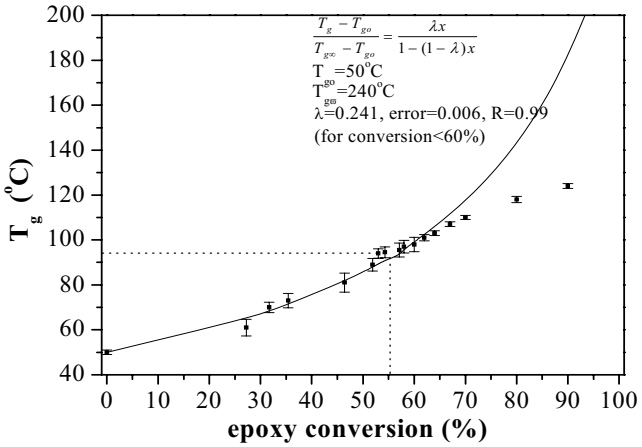

Figure 5.11 Relationship between measured T_g and epoxy conversion of SU-8

The measured T_g of uncured SU-8 is 50°C, which is close to reported values [110, 137]. T_g of fully cured SU-8 used for the theoretical prediction is 240°C, which has been selected from the literature [110, 137]. The measured T_g (Figure 5.11) did not fully follow the prediction using equation (5-4). The measured data fits the theoretical curve well only in the low conversion range (x<60%) (Figure 5.11). In the high conversion range, the measured T_g is lower than the predicted value. Other researchers have also found that the relation between T_g and the conversion of a cationically cured epoxy resin exhibited the typical behavior of thermosets described in Equation 5-4 only for conversion up to 80% and highly converted samples had lower T_g than the predicted value[277]. This may be explained by two factors. One is that the processing temperature used to cure the SU-8 was 95°C (the PEB temperature). The processing temperature significantly affects the T_g. At vitrification, the T_g value is almost equal to the processing temperature. After vitrification, T_g value becomes slightly higher than the processing temperature. Indeed, Feng[137] found that T_g of SU-8 was coincident with the baking temperature over the temperature range of 25°C–220°C.

Secondly, relaxation of the interactions through ion pairs of highly converted thermosets may also result in low T_g [277]. In our study, the data reported in Figures 5.9, 5.10 and 5.11 were obtained by varying UV exposure and PEB at 95°C. Although SU-8 crosslinking reactions mainly took place during the PEB process, epoxy groups partially reacted before PEB. Sensu [279] found that 9% epoxy of SU-8 reacted before PEB even at low UV exposure dose (125mJ/cm^2). In our study, high epoxy conversion was obtained by the high UV exposure dose used. We measured the conversion of SU-8 exposed to UV light for 500 sec before PEB and found the conversion to be higher than 60%. For the highly-UV-exposed SU-8, the PEB acted as an annealing process and the crosslinked SU-8 was relaxed in the PEB. The progress of the cationic polymerization

in the vitrifying network is believed to be affected by the difficult segmental diffusion of the bulk counter-anion in the early stages. Clusters of weak ion pairs formed in the glassy materials during high UV exposure relaxed to tight but independent ion pairs when some mobility is permitted by PEB [277]. Thus, highly converted samples have lower T_g than the theoretical prediction.

The presence of GBL in SU-8 during the curing helped to achieve high epoxy conversion up to 100%, depending on the amount of GBL (Samples group C, section 5.2.1.3). But increased GBL also led to low cross-link density and decreased T_g (Figure 5.12 and 5.13). The GBL content in the SU-8-GBL mixture strongly affected the cross-link density. In the long-softbaked SU-8 (Samples group A1, section 5.2), the GBL content was zero and the crosslinking reaction occured between epoxy groups leading to tight network structures[123] and low M_c indicating very high cross-link density. In SU-8-GBL system, GBL acted as a bridge between epoxy groups which gave high *Mc* value. On the other hand, SOE may not fully polymerize [280, 281] and a proportion of SOE may remain unreacted at the chain end [281]. The unreacted SOE remains incorporated as end groups and leads to long chains between cross-links and this reduces the final crosslinking density. This explains the rapid increase in the M_c versus GBL content curve (Figure 5.12). The M_c value increases rapidly until the curve stabilizes at 33%, thereafter the M_c value does not change significantly. Previous experimental results suggested that the maximum amount of GBL which can react with SU-8 was 33%. Beyond this critical value, excess GBL remained unreacted in the resist. Excess GBL was removed by vacuum baking. So M_c value reached a stable value when the original GBL content was higher than 33%. The effect of GBL content on T_g agreed with the above results (Figure 5.13). T_g decreased from 90°C to 72°C when GBL content increased from 0 to 33% and remained stable beyond the critical point.

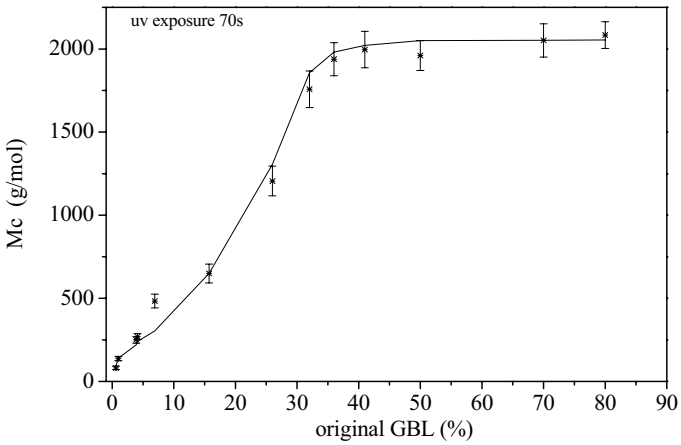

Figure 5.12 Molecular weight between crosslinks of the cured SU-8-GBL system

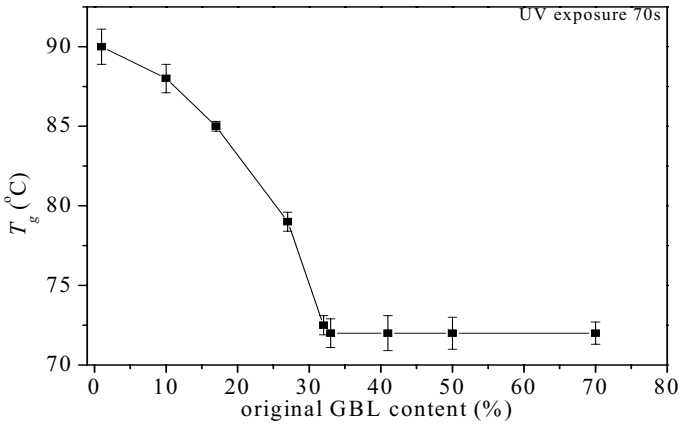

Figure 5.13 Effect of original GBL content on *Tg*

5.3.3 Kinetics of thermal degradation of cured SU-8

We will first discuss the thermal degradation of crosslinked SU-8 with low GBL content (i.e. 1%). Kinetics of thermal degradation of SU-8 was studied using thermal gravimetric analysis. Figure 5.14 shows TGA and DTG curves of low-GBL-content SU-8 with varied epoxy conversion (Samples groups B, section 5.2.1.2). Even unexposed SU-8 resist was thermally stable. Thermal decomposition did not take place until the temperature was over 300°C. Thermal degradation behavior of low-GBL-content SU-8 followed a one-stage reaction, which was similar to reported results of epoxy resin[177, 255, 282]. 2% weight loss occured at progressively higher temperature with increasing conversion at 326°C, 337°C, 346°C and 372°C with

conversions of 0%, 50%, 72% and 95% respectively. Residual weights at 700°C were also progressively higher with higher conversions: 33.2%, 33.5%, 37.5% and 38.1% for conversion of 0%, 50%, 72% and 95% respectively. The results suggested that cured SU-8 networks with higher epoxy conversion are more stable and harder to decompose than that with lower epoxy conversion.

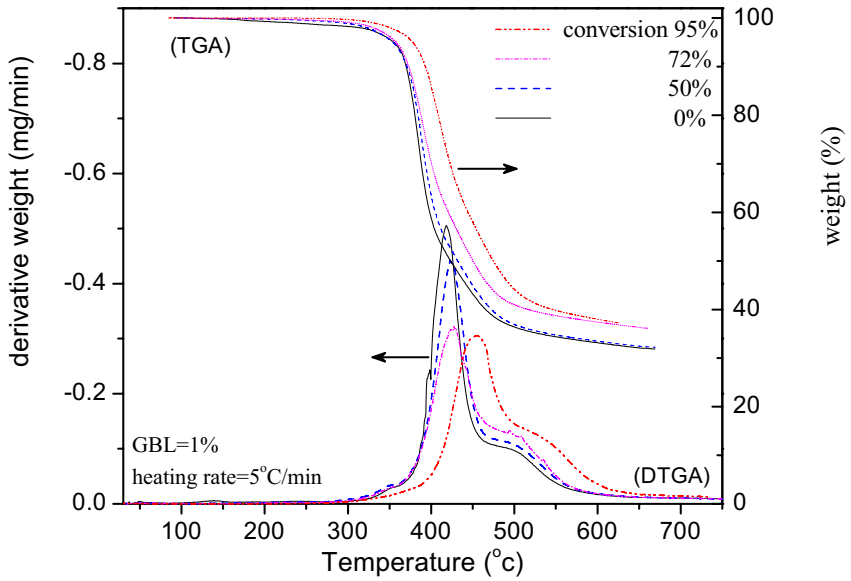

Figure 5.14 TGA and DTGA curves of cured SU-8 with varied epoxy conversion

Thermal degradation reactions can be described by the equation [283]

$$\Re = A(1-\alpha)^n e^{-\frac{E_a}{RT}} \tag{5-5}$$

where $\Re$ is the degradation rate and other parameters (α, n, A and Ea) are as described for Equation (5-1). If the temperature T rises during the degradation reaction, the degradation rate $\Re$ will rise to a maximum value, then return to zero as the reactant is exhausted [283]. If the temperature rises at a constant rate β, then by differentiation of equation (5-5):

$$\frac{d\Re}{dt} = \Re\left(\frac{E_a \beta}{RT^2} - An(1-\alpha)^{n-1} e^{-\frac{E_a}{RT}}\right) \tag{5-6}$$

where t is time.

The maximum degradation rate occurs at the temperature (T_m) when equation (5-6) equals to zero, then we can obtain the relationship between heating rate β and temperature T_m by the previously described equation (5-1). Kissinger plot is relatively simple and the activation energy can be obtained easily from the relationship between β and temperature T_m at the peak value of the DTGA curve. Figure 5.15 plots typical Kissinger plot of low-GBL-content SU-8 with varied epoxy conversion. The thermal degradation activation energy can be obtained fron the slope of the line in Figure 5.15.

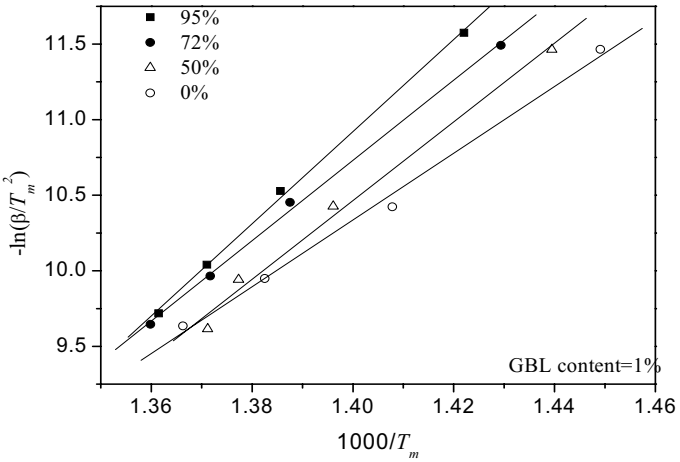

Figure 5.15 Kissinger plot of low-GBL-content SU-8 with varied epoxy conversions

Figure 5.16 plots the effect of epoxy conversion on thermal degradation activation energy of SU-8. Generally, high epoxy conversion led to higher activation energy. There is an inflexion point at 55% for the E_a *versus* conversion curve. In the low conversion range (<55%), the E_a increased slightly with increase of epoxy conversion. E_a increased from 183.6 KJ/mole to 187.4 KJ/mole, 187.5 KJ/mole and 190.5KJ/mol when the conversion increased from 0% to 22%, 28% and 50% respectively. Beyond the inflexion point, E_a increased rapidly with the increase of epoxy conversion. The inflexion point at 55% for the E_a versus conversion curve is attributed to the vitrification of the cured SU-8 network as shown in Figure 5.11 when the T_g (95°C) of cured network equals to PEB temperature (95°C).

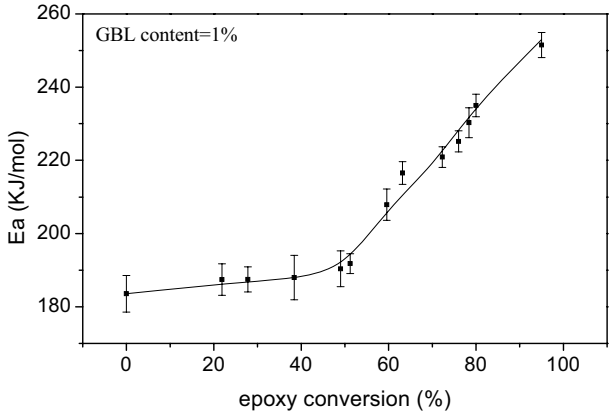

Figure 5.16 Effect of epoxy conversion on thermal degradation activation energy of SU-8

The density of crosslinks affects the E_a. Network with a low cross-link density requires less thermal or chemical energy to degrade a given mole into its volatile products[284, 285]. Figure 5.17 shows that E_a decreases exponentially with the increase of M_c. In low M_c range (M_c<310), E_a decreases dramatically from 251.5 KJ/mole to 191.8 KJ/mol when M_c increases from 125 g/mol to 310 g/mol. E_a does not change significantly in the high M_c range: E_a slightly decreases from 191.8 KJ/mol to187.4 KJ/mol when M_c increases from 310 g/mol to 2900 g/mol.

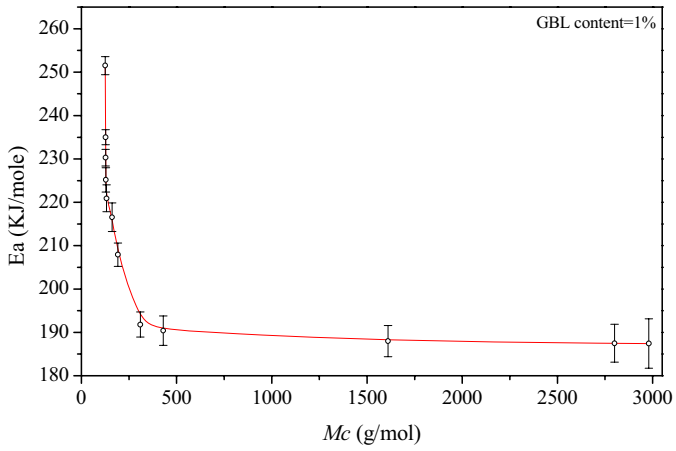

Figure 5.17 Effect of M_c on thermal degradation activation energy of SU-8

In Figure 5.14, the thermal stability difference between TGA curves of uncured (unexposed, 0% conversion) and 50% cured SU-8 networks was very small. This can be explained by the artifact caused by the further thermal curing of SU-8 during the

heating up process in TGA measurement. Figure 5.18 shows the first and second DSC scans of the unexposed SU-8. The DSC scan of the unexposed SU-8 shows exothermic peaks at the temperature range of 180°C~350°C. The peaks disappear in the second re-scan curve. The exothermic peaks are due to the crosslinking reaction of SU-8 initiated by high temperature. Triarylsulfonium hexafluoroantimonate salt is the photoinitiator in SU-8. Triarylsulfonium hexafluoroantimonate salt is well known to have a high degree of photosensitivity with excellent thermal stability and is reported to be stable till 150°C [139]. When SU-8 was heated up to 180°C, triarylsulfonium hexafluoroantimonate salt was thermally initiated, leading to crosslinking reactions. The thermal curing of SU-8 during the TGA and DCS scans was confirmed by the non-dissolution of thermally scanned SU-8 in SU-8 developer. The originally uncured but thermally scanned (from room temperature to 360°C) SU-8 was not dissolved by the SU-8 developer, even with prolonged development time of 24 hours.

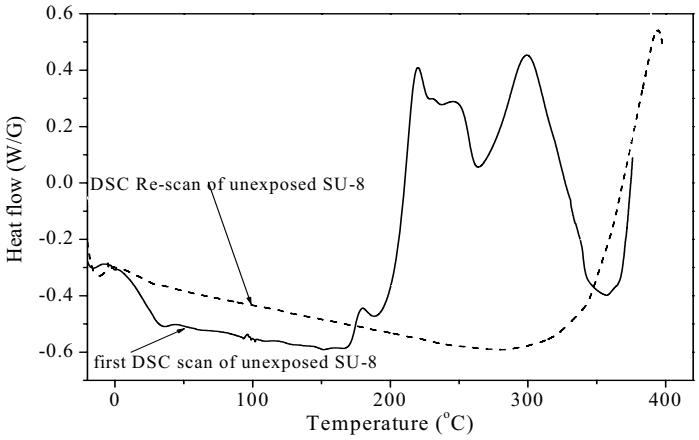

Figure 5.18 DSC curves of uncured and cured SU-8 (heating rate=5°C/min)

We will next discuss the effect of varying GBL on thermal stability. The GBL content in the resist also significantly affected the degradability of cured SU-8. Figure 5.19 shows the TGA and DTG curves of SU-8 cured with varied GBL content. Thermal degradation of SU-8 cured without GBL was typically a one-stage reaction. The resist was stable till the temperature was higher than 300°C; 2% weight loss occurred at

319°C and the main weight change occurred at 450°C. At 5% GBL content, 2% weight loss occurred at 259°C and the main weight loss (indicated by the main DTGA peak) appeared at 421°C. The TGA curve of 5% GBL curve was similar to the 0% curve, but there was an additional peak at 320°C on the DTGA curve. This can be assumed to be the transition from a one-stage reaction to a two-stage reaction as GBL is added. Increasing GBL in the resist changed the decomposition from a one-stage reaction to a two-stage reaction. As GBL content increased, the first-stage weight loss began at around 150°C instead. There were additional peaks at the 150°C-350°C region on the DTGA curves of high-GBL-content (≥17%) SU-8. The 2% weight loss of high-GBL-content SU-8 occurred before 150°C. The two-stage decomposition was distinct for GBL content of 17% and higher. TGA and DTGA curves were quite similar for the resist cured in the presence of 41%, 50% and 70% GBL. This can also be explained by the maximum reactable GBL with SU-8 of 33%. Any GBL proportion higher than 33% remained unreacted and was extracted during the long time vacuum baking process. Thus both the degradation behavior and kinetics had little change when the original GBL content was higher than 33%.

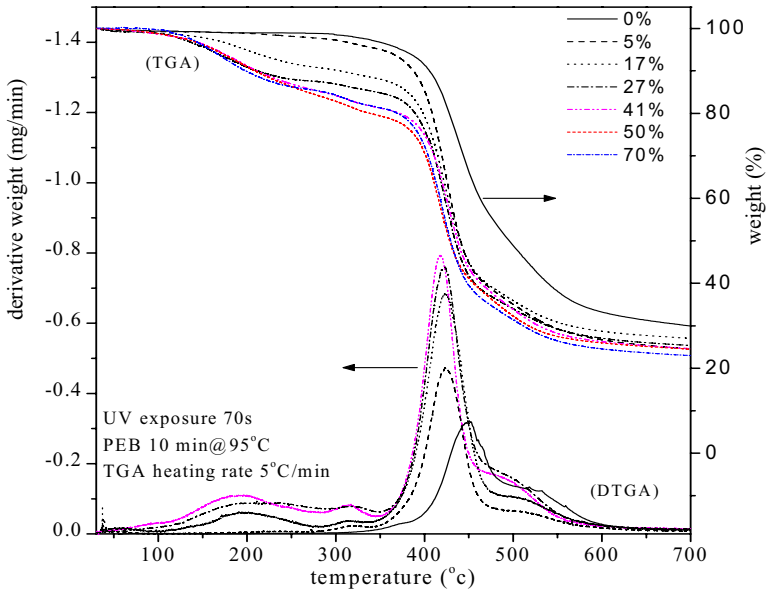

Figure 5.19 TGA and DTGA curves of CU-8 cured with varied GBL content

The effect of original GBL content in SU-8 on thermal degradation activation energy is shown in Figure 5.20. SU-8 resist cured without GBL had degradation activation energy of 230KJ/mol. Even very small amount (1%) of GBL dramatically reduced the degradation activation energy to 213.5KJ/mole. E_a value monotonously decreased with the increase of GBL content until the GBL content reached 33%, where E_a was 171KJ/mole. E_a remained unchanged at this value even when the original GBL content was as high as 70%. This was because the maximum amount of GBL reacted into SU-8 network was 33%. Further increase of the GBL content beyond 33% had no effect on the chemical curing of SU-8 and excess GBL was extracted from the resist. A dramatic effect of the presence of GBL on the degradability of an aliphatic polycarbonate was reported by other researchers[286].

GBL gives easier degradability in three aspects. First, GBL resulted in long chains between aliphatic crosslinks which are relatively unstable. Secondly, GBL offered additional ester structural units with ether linkage which was more decomposable than C-C bond[177, 286, 287]. Thirdly, GBL in the resist decreased T_g of the resist resulting in lower thermal stability.

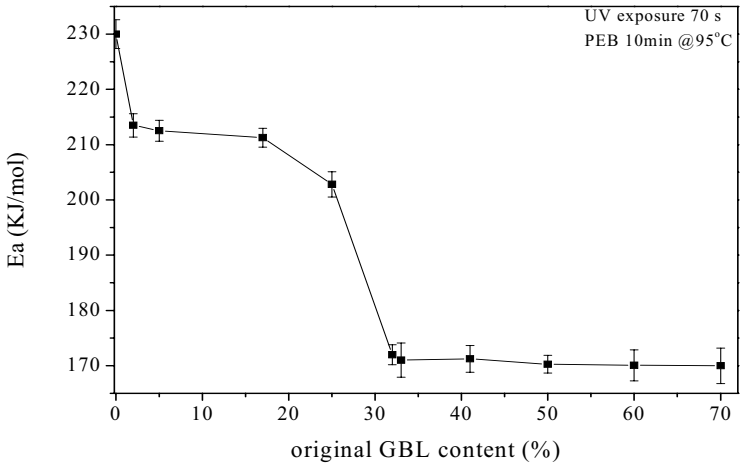

Figure 5.20 Effect of GBL content on thermal degradation activation energy of SU-8

5.3.4 Chemical degradation of cured SU-8 in concentrated H_2SO_4

Figure 5.21 shows the typical mass loss rate of cured SU-8 in concentrated sulfuric acid. The mass loss of SU-8 in the acid followed a linear trend ($R^2 > 0.99$) with respect to the dissolution time. The sample was 2cm long by 2cm wide by 100um thick and the dissolution occurred from the top surface (Section 5.2.8), A linear relationship between the change in thickness and dissolution time can be deduced from the linear relationship between the mass loss and dissolution time. This suggested that the SU-8 dissolution in the acid was controlled by surface erosion mechanism[288-291].

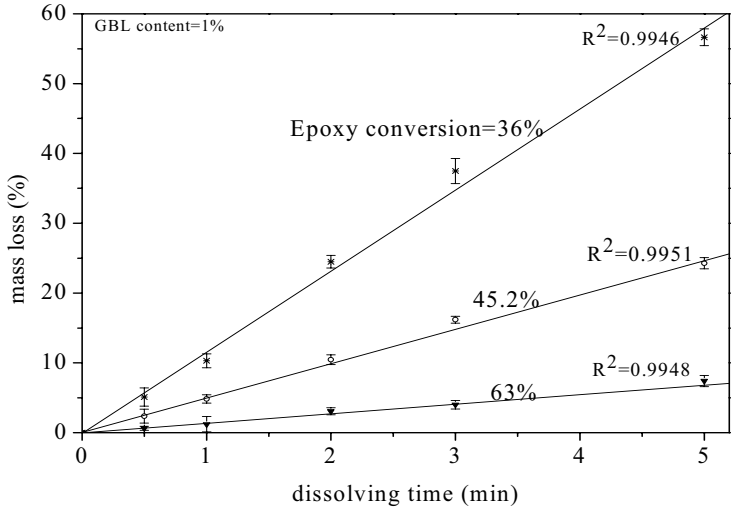

Figure 5.21 Mass loss of SU-8 resist in concentrated sulfuric acid

The dissolution rate was significantly affected by epoxy conversion (Figure 5.22). For the sample group B, high conversion led to low dissolution rate. This is because high conversion means low M_c value and dense network structure. Different M_c values were obtained by different epoxy conversion (sample group B, section 5.2.1.2). Figure 5.23 shows the effect of M_c on dissolution rate. The presence of GBL (samples group C, section 5.2.1.3) also greatly affected the dissolution rate (Figure 5.24). The presence of GBL led to increased dissolution rate. The dissolution rate of SU-8 cured with very little GBL was very low. The dissolution rate of sample A1 (where 0% GBL content was assumed) was 0.8 um/min. The dissolution rate increased to 2.2±0.6 um/min,

5.0±1.4 um/min, 6.0±1.2 um/min, 7.6±1.5 um/min and 9.7±1.5 um/min when the GBL content increased to 0.6%, 1.7%, 4.1%, 15.6% and 26.2%. Further, GBL resulted in a loose network structure (high M_c value) and additional ester bonds, leading to higher dissolution rate.

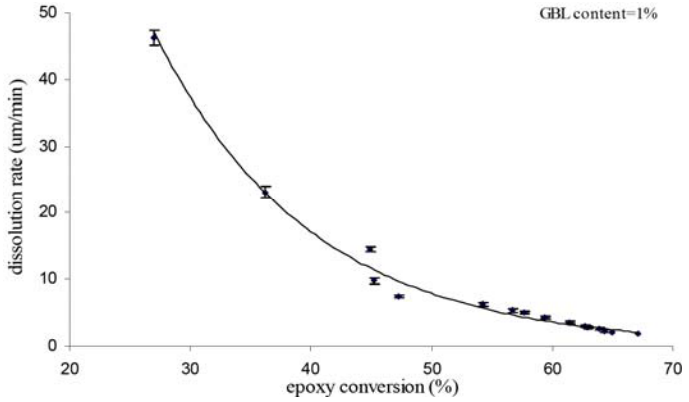

Figure 5.22 Effect of epoxy conversion on the dissolution rate

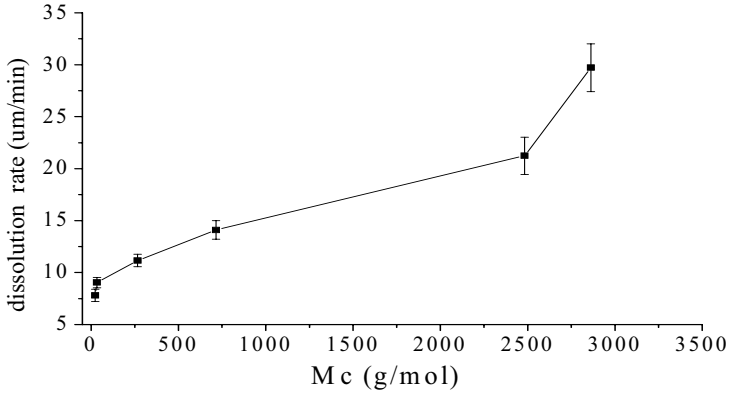

Figure 5.23 Effect of M_c on dissolution rate

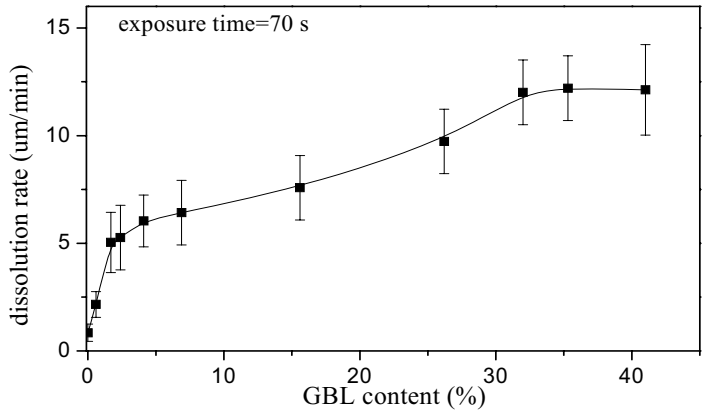

Figure 5.24 Effect of original GBL content on dissolution rate

5.3.5 Degradation products

Dissolution products of SU-8 cured with/without GBL were investaged using ^{13}C NMR and GC/MS examination. The network difference between cured zero-GBL SU-8 (long-softbaked SU-8 100) and 27%-GBL SU-8 (non-softbaked SU-8 100) is that there are linear lactones in cured 27%-GBL SU-8. Figures 5.25 shows the NMR spectra of zero-GBL and 27%-GBL SU-8 SU-8 100 dissolved in H_2SO_4. There is clear difference between the two NMR spectra.

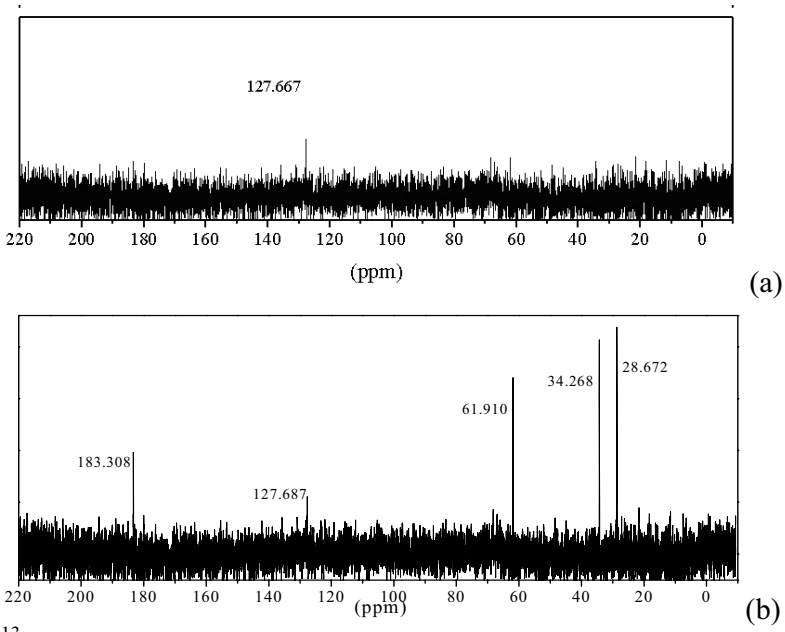

Figure 5.25 ^{13}C NMR spectrum of (a) cured zero-GBL SU-8 sample and (b) cured 27%-GBL SU-8 sample dissolved in concentrated H_2SO_4

For zero-GBL SU-8 sample, the NMR spectrum gave little information of the degradation fragment. Previous studies in this chapter showed that SU-8 cured without GBL has very low M_c value, very high degradation activation energy and high stability because of the dense network. Lightly cured zero-GBL SU-8 sample can be dissolved by concentrated H_2SO_4, leading to very low concentration of degradation products in the neutralized solution. NMR has relatively low sensitivity[189, 190], and the minimum detectable concentration is in the order of mMol/l [191]. The degradation products of zero-GBL SU-8 sample were not detectable using NMR spectroscopy.

For 27%-GBL SU-8 sample, several peaks were detected. The peak at 183.31 ppm was assigned to carbonyl (C=O) group. The peak at 127.69 ppm was attributed to aromatic carbons. The peak at 61.91 ppm was assigned to carbon in C-O group and the peaks at 34.27 ppm and 28.67 ppm were due to carbons in alkyl chains. Since the examined sample was clear solution neutralized using sodium hydroxide, it can be said that the examined samples contained only water soluble fragments. The NMR spectrum of cured A2 suggests that the network of this resist was broken into water soluble fragments by sulfuric acid dissolution and the fragments contained carbonyl, aromatic, alkyl and other groups.

GC/MS has been widely used in studies of thermal degradation of polymers[177, 192] and polymer structural identification[193]. It offers very high sensitivity with detection limits of 0.01-0.1 *u*g/L[194]. Although the concentration of degradation products in the examined solution was very low, GC/MS successfully separated the fragments. Figure 5.26 compares the chromatographic separation of degradation products from zero-GBL SU-8 (long-softbaked SU-8 100) and 27%-GBL SU-8 (non-softbaked SU-8 100). The very strong peaks at retention time of 1.52 min (m/z=74) were due to diethyl ether, which was the solvent used in the GC/MS examination.

In order to zoom in the peaks of dissolution products, the spectra at high retention time range (>4.15 min) was also enlarged in Figure 5.26. For both samples, there were five peaks (peaks ***II***, ***III***, ***IV***, ***V*** and ***VI***) at retention times of 6.54 min, 10.65 min, 15.30 min, 19.58 min and 20.54 min respectively. The corresponding mass (m/z) values were 292, 358, 431, 508 and 559 respectively. These peaks can be assigned to fragments from bis-phenol-A-related structures. There was an extra peak (peak ***I***) at retention time of 5.07 min on the curve of 27%-GBL SU-8 sample. The corresponding mass (m/z) value was 273. Since the difference between the two samples is the presence of GBL in 27%-GBL

SU-8 sample. It is safe to say that the network of cured 27%-GBL SU-8 sample should also have GBL-related structure while the cured zero-GBL SU-8 sample should not have GBL-related structures. Since the peak ***I*** at retention time of 5.07 did not appear in the chromatographic separation of long-softbaked SU-8, this peak was most possibly to be assigned to the GBL-related fragment.

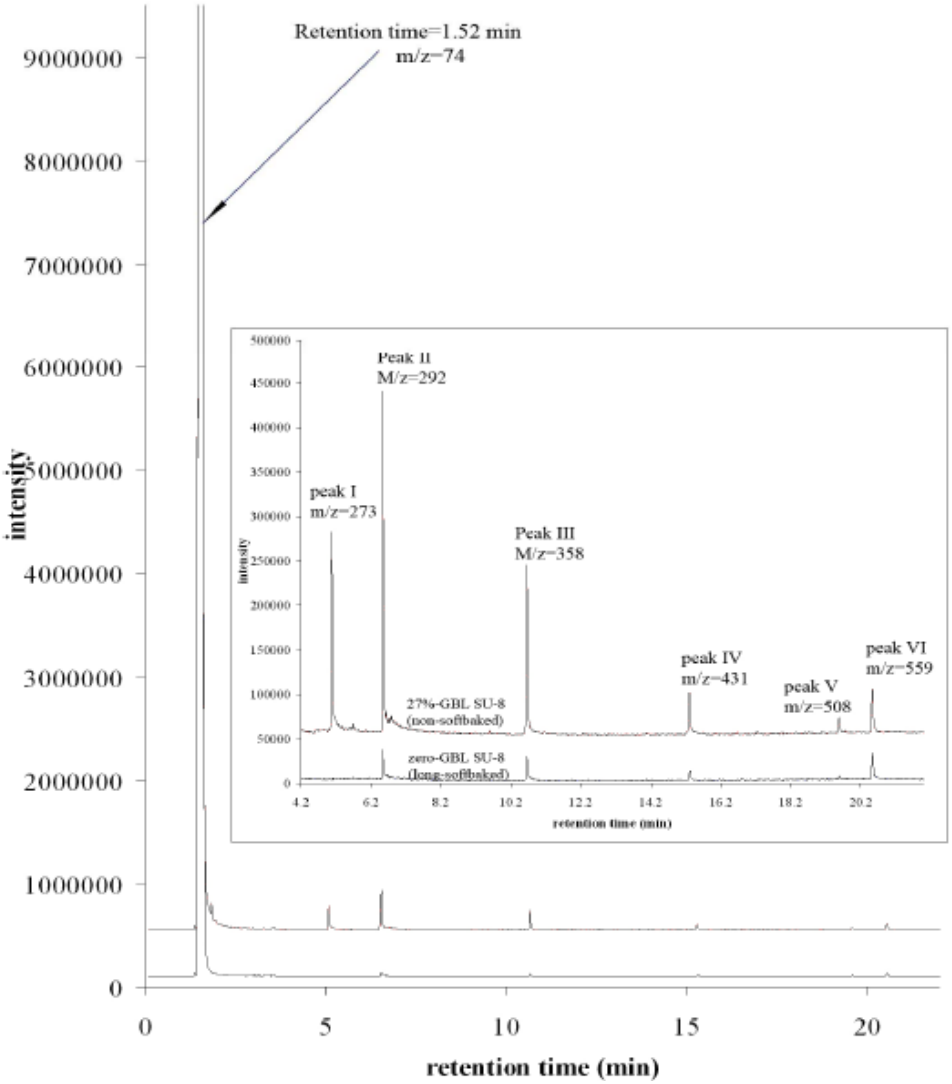

Figure 5.26 Chromatographic separation of SU-8 degradation products

The heights of all peaks for 27%-GBL SU-8 sample were much higher than those for zero-GBL SU-8 sample. This is because 27%-GBL SU-8 sample dissolved much faster in the acid than zero-GBL SU-8 sample. Since the solution preparations for both samples were the same, the degradation products concentration was much higher for the

27%-GBL sample than that for the zero-GBL sample. Thes results further confirm that SU-8 cured with GBL has better degradability than SU-8 cured without GBL.

The chemical structures of degradation products were suggested based on SU-8 molecular, chemical reactions described in section 5.3.1 and mass spectra from the GC/MS examination. Suggested structures are summarized in table 5.2. Detailed mass spectra for peaks in Figure 5.26 are shown in Figure 5.27.

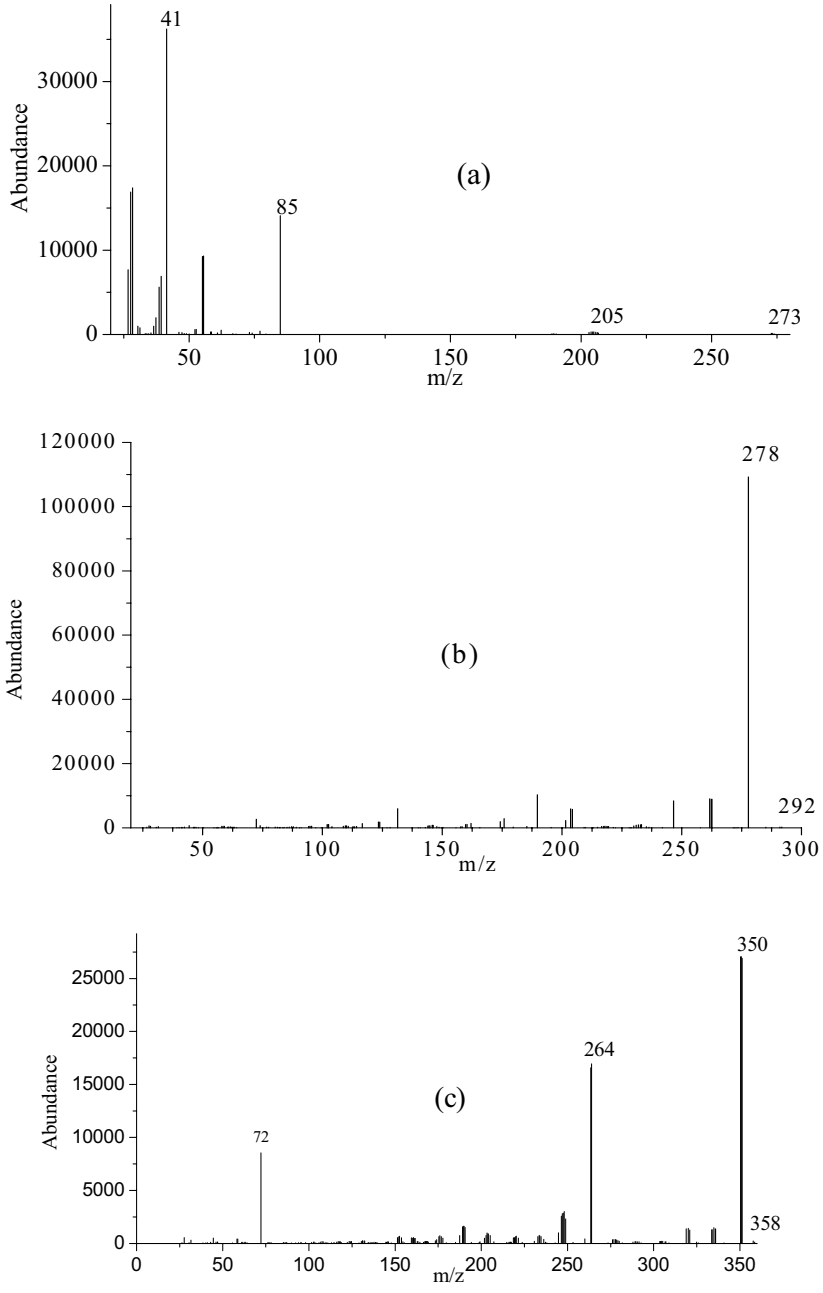

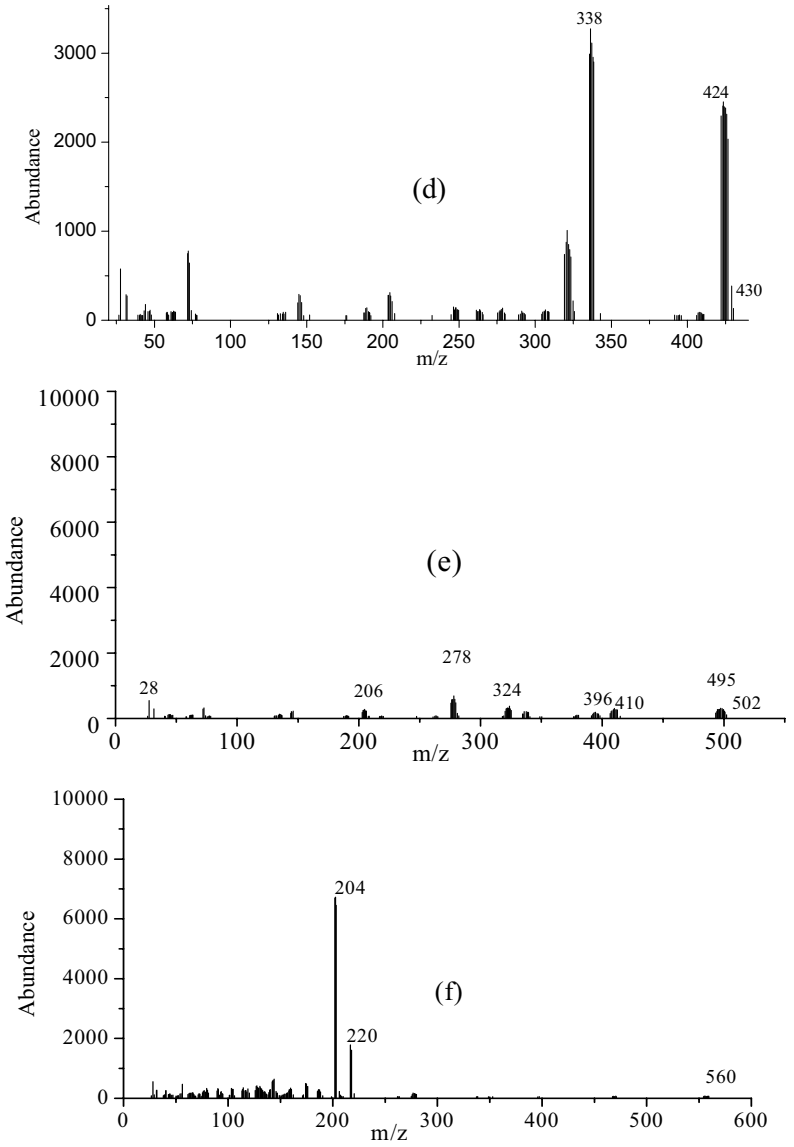

Figure 5.27 Mass spectrum of degradation (a) fragment ***I***, (b) fragment ***II***, (c) fragment ***III***, (d) fragment ***IV***, (e) fragment ***V*** and (f) fragment ***VI***

The chemical fragments in Table 5.2 tally with our proposed structure in Figure 5.6. Fragments ***II*** to ***VI*** are due to epoxy-epoxy polymerization and fragment ***I*** is due to GBL-epoxy polymerization. Figure 5.28 shows the fragments in the cured SU-8 network.

It should be noted that the examined liquid samples were extracted from aqueous solutions since degradation products with very small molecular weight might not be

extracted and there was no very small molecule detected. The nondetectability of very small molecular weight fragments may be also because the separation peaks overlap with the very strong peak of diethyl ether at retention time of 1.52 min.

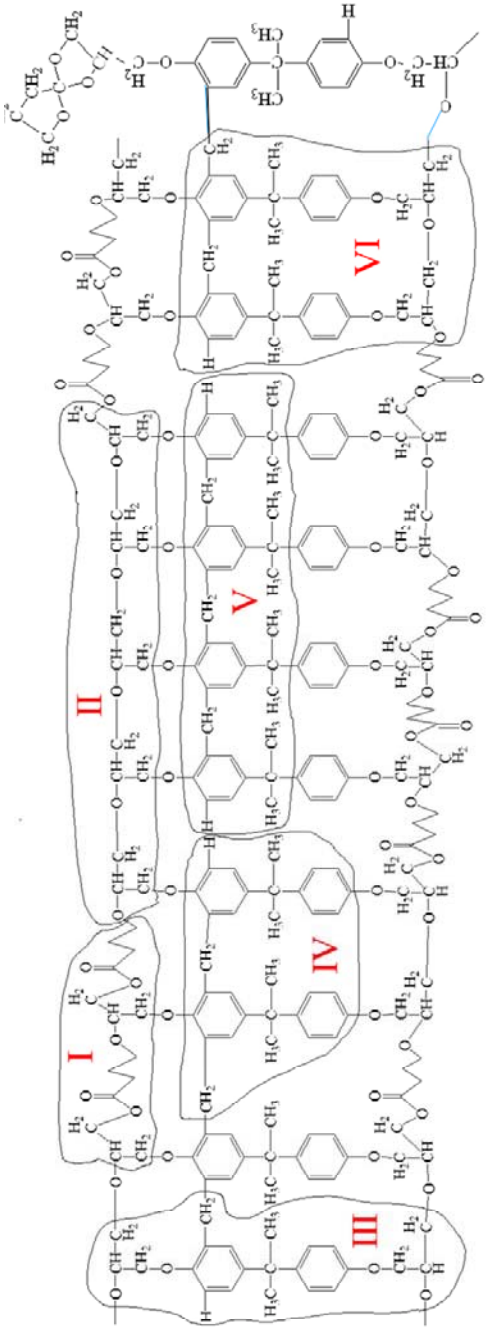

Figure 5.28 Suggested degradation fragments in the cured SU-8 network

Table 5.2 Suggested chemical structure of the degradation fragments of SU-8

Peak No.	m/z	Suggested structure
I	273	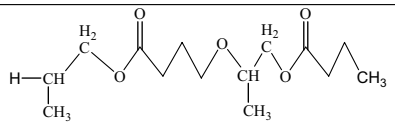
II	292	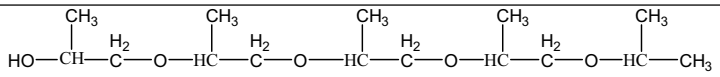
III	358	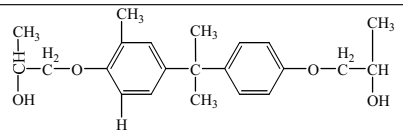
IV	431	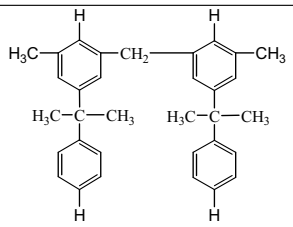
V	508	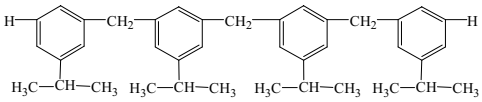
VI	559	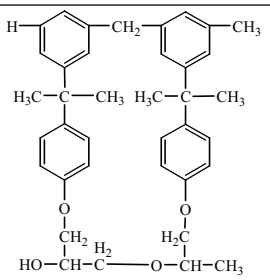

5.4 Summary

Chemical reaction during the curing of SU-8 resist in the presence of GBL was investigated. FTIR and ^{13}C NMR spectra indicated that GBL in SU-8 resist acted as a reactant during the curing of this resist. Up to 33 weight% of GBL can react with SU-8 during the curing. The network properties of cured SU-8 were affected by curing conditions. High epoxy conversion led to low M_c value indicating dense cross-link density. High conversion also led to high T_g. Vitrification of SU-8 occurred at the conversion of 55%. Beyond vitrification, both M_c and T_g did not change significantly. The presence of GBL during curing of SU-8 led to long chains between cross-links and

low cross-link density. T_g also decreased with the increase of GBL content. Thermal degradation of cured SU-8 was also investigated. Kinetic studies showed that the network properties of cured SU-8 strongly affected the degradability. The thermal degradation activation energy of SU-8 decreased exponentially with the increase of M_c. E_a decreased dramatically with the increase of M_c in the low M_c range and did not change significantly in the high M_c range. The presence of GBL resulted in faster degradability of cured SU-8 because GBL resulted in long chains between crosslinks and low cross-link density as well as GBL offered additional ester structural units with C-O bond. GC/MS studies of the degradation products confirmed our postulated reaction of GBL with epoxy at a maximum molar ratio (GBL: epoxy) of 1:1.

Chapter 6 Electroformed metallic mold and UV embossing using the mold

6.1 Introduction

SU-8, an epoxy-based resist, strongly adheres to most materials and, without further treatment, is not a suitable mold material for further polymer molding. An approach which exploits the advantages of SU-8 but avoids its drawbacks is to use electroforming to replicate in metal a pattern formed in SU-8; the metallic mold is liberated from the SU-8 master by dissolution of the master. Such a metallic mold would be mechanically strong and impermeable to molding resin. It could also be surface treated to have low adhesion to most materials. Such micro-molds would have good durability for many kinds of micro-molding, including UV embossing, thermal embossing, micro-injection molding and soft lithography[33].

In this chapter, Argon (Ar) plasma treatment will be used to increase the hydrophilicity of SU-8. SU-8 gratings with very high aspect ratio and dense microchannels over the entire surface of a 100mm silicon wafer will be fabricated and modified by Ar-plasma treatment. With very high aspect ratio microchannels, long plasma time is needed to get surface activation at the bottom of the deep microchannels. Since the seed layer for electroforming is very thin (sub-micron), excessively long plasma time may etch away the seed layer. Detailed studies to monitor changes in SU-8 roughness, surface energy and chemical composition will be conducted to determine the optimum process window. Very high aspect ratio and dense copper gratings over large area will be fabricated by electroforming from plasma treated SU-8 masters. The copper gratings will then be surface treated and used as a mold for UV embossing.

6.2 Experimental details

All sample preparation and characterization stated in this chapter were carried out at the Micromachine Centre, School of MAE, NTU unless otherwise specially described in the text. All chemicals used were from Sigma-Aldrich (St. Louis, MO, USA) unless otherwise stated.

6.2.1 Fabrication of high aspect ratio SU-8 mold

The substrates used are Piranha solution cleaned and dehydrated 4-inch silicon wafers (see section 3.2). Bare Si wafers were used as substrates for SU-8 patterning to study the SU-8 surface modification. 100 um thick SU-8 100 was spin coated on to Si wafers and soft baked at 95C for 30 min, using a hotplate. Then the samples were exposed to UV light using a J500-IR/VIS Mask Aligner from Optical Associates Inc. Flat SU-8 surface was obtained by exposing without any mask, patterned SU-8 surface was obtained by exposing through Mask D (Figure 4.3). Mask D has 1000um long, 10um wide dark field lines separated by 10um wide light field lines. The exposure time was 50 s for flat SU-8 and 40 s for patterned SU-8. Soft cushion technology (detailed procedures are described in section 4.3) was employed during the exposure. The UV exposed samples were then baked at 65°C and 95°C for 3min and 10 min respectively. After the samples were slowly cooled down to room temperature, they were developed for 10 min, using SU-8 developer (propylene glycol methyl ether acetate (PGMEA)). Then the patterned SU-8 samples were baked at 120°C for 20 min and slowly cooled down. The processing parameters are summarized in table 6.1.

For the samples used for electroforming, metal layers were deposited onto the pre-cleaned substrates to act as the seed or sacrificial layer. The metal deposition was done using a direct currenct/radio frequency (DC/RF) powered multi-target magnetron sputtering system from Coaxial power system Ltd. (Spectrum House, Finmere Road,

Eastbourne, E. Sussex BN22 8QL UK). A first layer of 500nm thick Titanium was sputtered to improve the adhesion between the seed layer (Cu) and the silicon. A second layer, of 300nm thick Copper, was used as the seed layer. The substrates were further treated using γ-glycidoxypropyltrimethoxysilane (γ-GPS) to promote the adhesion between SU-8 and the substrates. The 1% silane solution was prepared by adding appropriate amount of γ-GPS in deionized water. Acetate acid was used to adjust pH value to 5.0. The solution was constantly stirred for 60 min for hydrolysis. The solution was then applied onto Si wafer by immersing into the γ-GPS solution for 10 min. After the wafer was taken out from the solution, a gentle flow of compressed N_2 gas was used blow off the excessive solution. Then the wafer was baked at 93°C for 60 min using a hot plate.

SU-8 100 was spin coated onto the substrates and soft baked using a hotplate. Masks B (Figure 4.3(a)) and D (Figure 4.3(c)) were used to fabricate the SU-8 master for electroforming. Exposure time was 70 s for Mask B and 40 s for Mask D. The processing parameters are also summarized in table 6.1.

Table 6.1 SU-8 processing parameters for large area patterns

<table>
<tr><th>Sample</th><th>Mask</th><th>Substrate</th><th>rpm</th><th>Soft bake</th><th>Exposure</th><th>PEB</th><th>Develop</th><th>Hardbake</th></tr>
<tr><td>1</td><td>Nil</td><td rowspan="2">Bare wafers</td><td rowspan="4">3000</td><td rowspan="4">10 min at 65°C; 30 min at 95°C; ramp cooling</td><td>50s</td><td rowspan="4">3 min at 65°C; 10 min at 95°C; ramp cooling</td><td rowspan="4">10 min</td><td rowspan="3">20 min at 120°C; ramp cooling</td></tr>
<tr><td>2</td><td>D</td><td rowspan="2">40s</td></tr>
<tr><td>3</td><td>D</td><td rowspan="2">With seed layers</td></tr>
<tr><td>4</td><td>B</td><td>70 s</td><td>Nil</td></tr>
</table>

6.2.2 SU-8 surface modification for high wettability

Silicon wafers with both patterned and flat SU-8 were cut into 2 cm by 2 cm for plasma treatment. Ar-plasma treatment was carried out in a March PX-500^{TM} Cleaning System operated at a radio frequency (RF) of 13.56 MHz. The glow discharge was produced

using a power of either 200 W or 100 W. The argon flow rate was 350 sccm (standard cubic centimeters per minute). Before introducing argon into the plasma chamber, the base pressure in the chamber was reduced to 50 mTorr. Varied Ar-plasma treatment time was employed to study the effect of plasma time on the SU-8 surface energy.

The surface energy was calculated from the contact angle of three liquids using the Lifshitz Van der Waals Acid Base (LWAB) approach. Distilled water and glycerol were chosen to be the polar pair and diiodomethane was chosen as the apolar liquid. The contact angle measurements were carried out using the sessile drop method by a FTA 200 system from First Ten Ångstroms (Portsmouth, VA, USA) at the Materials Laboratory, School of MAE, NTU. Test liquid drops, each of 25 μl, were dispensed through a gauge 22 sized dispensing needle by a stepper motor-driven syringe at the rate of 5 μl/sec. The surface roughness was measured using a WYKO optical profilometer (OP) (Veeco Instruments Inc., New York, USA) in Vertical Scan Imaging (VSI) mode at the Precision Engineering and Nanotechnolgy Centre, School of MAE, NTU. Since the surface roughness is increased by plasma treatment, the true contact angle was calculated according to Wenzel's equation [292]:

$$\cos\theta_m = r\cos\theta \tag{7-1}$$

where θ_m is the measured contact angle or Wenzel's angle, θ is the true contact angle on a flat surface (hereafter referred to as the contact angle), and r is a roughness factor which is defined as the ratio of actual area to the projected area of the solid. In this study, the detailed topography of the SU-8 surfaces was measured by OP analysis, and r was computed using the actual surface area and projected area from OP measurement. The true surface energy was calculated using the true contact angle.

Chemical compositions of SU-8 surfaces with varying plasma treatment times were

characterized by X-ray Photoelectron Spectroscopy (XPS) at the Materials Labortary, School of MAE, NTU. The measurements were made on an AXIS Ultra spectrometer (Kratos Analytical Ltd., Manchester, England) with a non-monochromatized Kα X-ray source (1486.6 eV). SU-8 samples were mounted on standard sample studs using double-sided adhesive tape. The X-ray source was operated at a reduced power of 150 W (15 kV and 10mA). The operating pressure in the analysis chamber was maintained at $3.0x10^{-9}$ Torr or lower during the measurements. The core-level spectra were obtained at a photoelectron take-off angle (α, measured with respect to the sample surface) of 90°. All binding energies (BEs) were referenced to the C1s neutral carbon-to-carbon peak at 285.0 eV, so as to compensate for the effects of charging.

6.2.3 Electroforming of high aspect ratio copper mold

The electroforming was carried out using a homemade acidic bath. The Silicon wafers which had previously been patterned over their entire surface with SU-8 grating were used for electroforming. The electrolyte was composed of $CuSO_4 \cdot 5H_2O$ (30g/l), H_2SO_4 (275g/l) and chloride ions (50ppm). The concentration of H_2SO_4 was obtained by adding 155 ml 96% H_2SO_4, and 0.11 ml 35% HCl solution was added into each liter of the electrolyte to achieve the concentration of chloride ions. The PH value of the electrolyte was 1 (measured with PH test paper). Pure copper plate (99.9%) was used as the anode. The copper plate was 150 mm long, 100 mm wide and 25 mm thick. The distance between the anode and cathode (the wafer) was 150 mm. A square-wave pulse current with 0.1-sec-off and 0.9-sec-on was employed in the plating and the temperature was 28°C. The current density used was 4-20mA/cm^2. The metal deposition process began at the bottom of the deep channels. After the channels were completely filled, the electroforming process was further continued and eventually produced a continuous surface more or less parallel to the seed layer. The electroforming took approximately

72 hours. Since the sample was overplated, SU-8 was enveloped by the electroformed copper and copper seed layer (Figure 6.1).

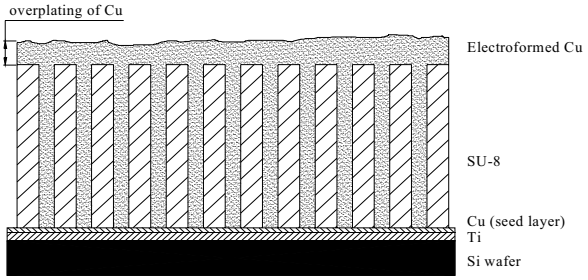

Figure 6.1 Schematic drawing of the electroforming

It was necessary to remove the Silicon wafer, Titanium layer and Copper seed layer in order to expose the SU-8 resist for removal. The Si substrates were dissolved using KOH solution (29% by weight). The etching bath was heated to 80°C using a hotplate and continuously stirred using a magnetic stirrer. Since KOH does not etch Cu[293], no special protecting was employed during the KOH etching. The resulting electroform with titanium layer and copper seed layer was then thoroughly rinsed using DI water and dried with compressed air. The thin titanium layer was etched away using a Ti etchant (H_2O:HF (49%):H_2O_2(30%) ratio of 20:1:1) solution at room temperature. Then the copper electroform was immersed into a copper etchant (30% ferric chloride in DI water) for 20 sec to remove the copper seed layer.

SU-8 was removed using concentrated sulfuric acid. The copper electroforms were immerged into excessive concentrated sulfuric acid (96%~98%) with pattern side facing upwards and ultrasonic agitation was applied. The ultrasonic agitation source was 1210E-MT Bransonic® ultrasonic cleaner with a frequency of 47 kHz and power of 80 W. The removal process took 25-30 min. The temperature of ultrasonic water bath was controlled to be lower than 30°C during the whole process. The copper will be corroded

by the strong acid if the temperature is higher than 45°C. The copper molds then were thoroughly rinsed using DI water and dried.

6.2.4 Polymer replication from the copper mold by UV embossing

The copper mold defined using Mask D was used to demonstrate the suitability of electroformed micro mold for UV embossing. The mold was surface treated by Ar/H_2 plasma treatment and coating with a siloxane release agent. The plasma treatment was carried out in a March PX-500^{TM} Cleaning System with glow discharge power of 200 W and Ar and Hydrogen gas flow rates of 120 sccm and 80 sccm respectively (3:2 Ar/H_2 mixture) for 10 minutes. The gas flow rate and ratio were selected based on previous study on nickel surface, which was done by other researchers in this group. The copper mold was then immersed in a 1% solution of N-(beta-aminoethyl)-gamma-aminopropyltrimethoxy-silane coupling agent in ethanol/distilled water (95/5) with ultrasonic agitation for 2 minutes. Then, it was thoroughly rinsed with a large amount of distilled water to remove the excess coupling agent and baked at 130°C for 1 hour. It was then immersed in the release solution comprising 4% of GP-657 / GP-32 / ANCAMINE^{TM} K54 (0.0968/1/ 0.011 (w/w)) in heptane[294] with ultrasonic agitation for 5 minutes. GP-657 and GP-32 are oligomeric silicones functionalized with amine/alkoxy and epoxy respectively from Genesee Polymers Corporation (Burton, MI, USA). ANCAMINE^{TM} K54 is a tertiary amine catalyst from Air Products Corporation (Crewe, England). The surface treated mold was then baked in an oven at 100°C for 48 hours and then at 130°C for 6 hours. After surface treatment, the mold was ready for use in UV embossing.

Since reactive epoxy, amine and alkoxyl groups are present in the release agents and hydroxyl groups exist on the plasma-treated metal surface[295], after the heat treatment,

a crosslinked silicone network formed through the epoxy/amine condensation polymerization is chemisorbed onto the metallic stamp through the well-known silane chemistry, as illustrated in Figure 6.3.

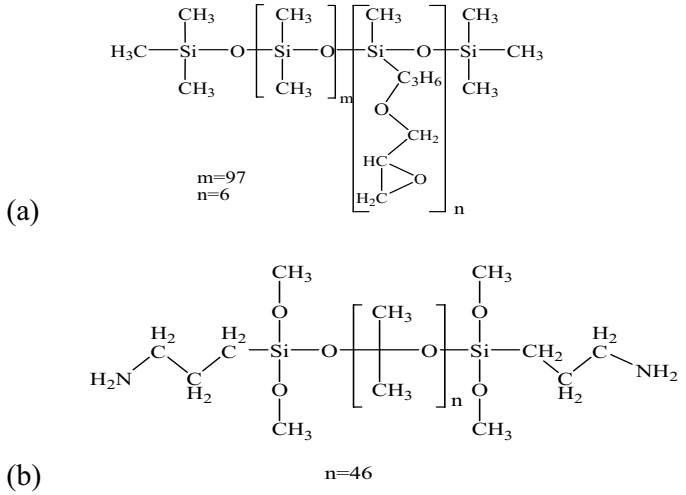

Figure 6.2 Chemical structures of (a) GP-32 and (b) GP-657

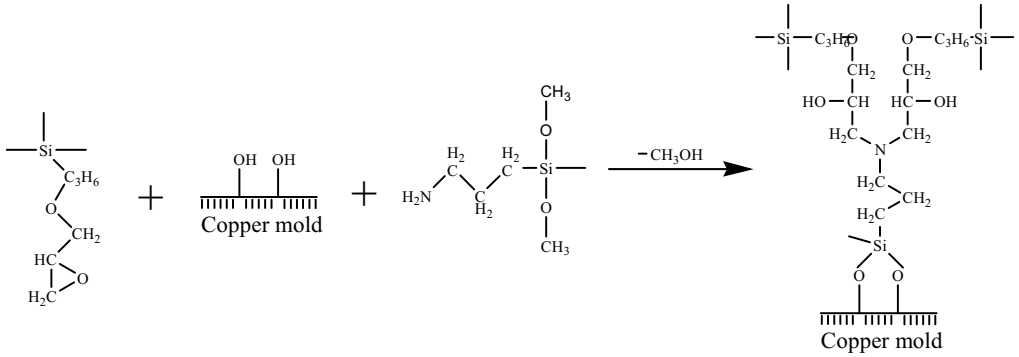

Figure 6.3 Reaction mechanism of the release agent on the copper mold

The resin used for UV embossing was a mixture of monomers SR349, SR508, SR351 (Sartomer Company Exton, PA, USA) and siliconised acrylate EB350 (from UCB SA Company, Brussels, Belgium) with weight percentages of 68%, 20%, 10% and 2% respectively. Irgacure 651 (CIBA Speciality Chemicals, Basel, Switzerland) was used as the UV photoinitiator in a 0.3% proportion by weight. The resin was poured onto the copper mold and degassed at 65°C for 15 min using a vacuum oven. Then the resin was laminated over with a 75 um thick Melinex® 454 polyester film (DuPont Company),

and the polyester/resin/mold sandwich was exposed to UV light at room temperature in atmosphere environment, using a SUSS MA6 mask aligner for 45 sec. The MA6 uses a mercury arc lamp with a 365nm-UV intensity of 8.1 mW/cm^2. The embossing was then peeled slowly from the copper master and examined with SEM.

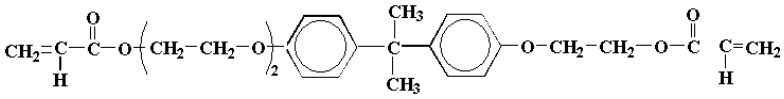

SR349 Ethoxylated (3) Bisphenol A Diacrylate

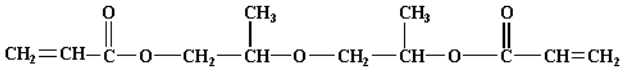

SR508 Dipropylene Glycol Diacrylate

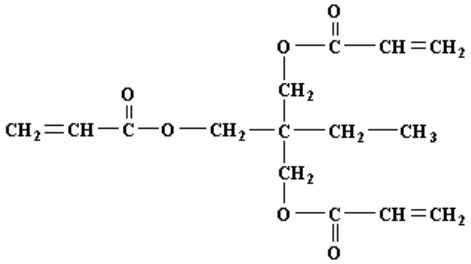

SR351 Trimenthylolpropane Triacrylate

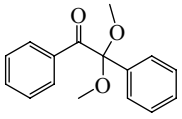

Irgacure 651

Figure 6.4 Structures of monomers SR349, SR508, SR351 and photoinitiator Irgacure 651

6.3 Results and discussion

6.3.1 Surface energy and roughness

In general, polymer surfaces are usually non-polar. Most synthetic polymers have surface energies in the low forties mJ/m^2[228] and have very low wettability[296-298]. Figure 6.5 shows the effect of Ar-plasma treatment time and power on the water contact angle on flat SU-8 surface. For untreated SU-8, the water contact angle and surface energy were 73.1±2.8° and 45.5 mJ/m^2 respectively indicating that untreated SU-8 is hydrophobic. The water contact angle monotonically decreased with increase of plasma

treatment time. With RF power of 200 W, the angle decreased rapidly from 73.1±0.28° to 47.9±0.9°, 41.0.±0.7° and 34.8±0.8° when the Ar-plasma treatment time increased from 0 sec to 10, 20 and 30 sec respectively; the contact angle did not change significantly for plasma treatment times of 60 sec or longer.

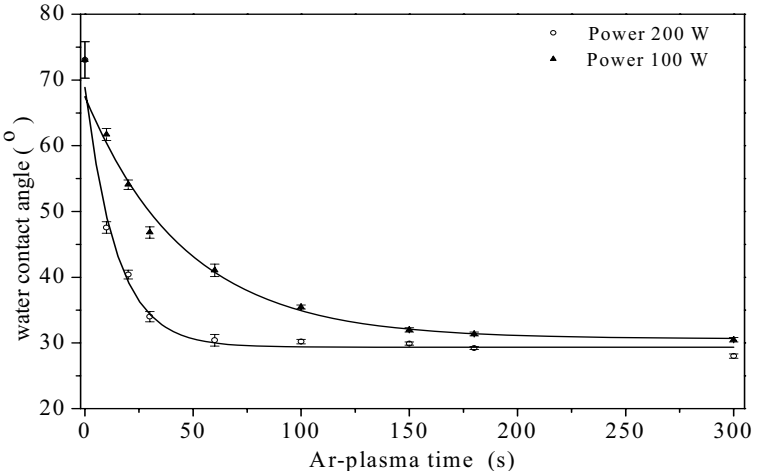

Figure 6.5 Effect of (a) Ar-plasma time on water contact angle

Figure 6.5 also shows that the decrease of water contact angle of SU-8 surface with 200 W RF power was much more rapid than with 100 W RF power at the beginning of the plasma treatment. For the long-time plasma treatment (≥ 150 sec), the effect of RF power on the water contact angle of SU-8 surface was not significant. The water contact angle decreased from 73.1±2.8° to 32.9±0.3° and 30.8±0.3° with plasma treatment at 100 W and 200W respectively using relatively long (150 sec) treatment time.

Figure 6.6 plots water contact angle versus total applied plasma energy. It shows that different power ratings in the plasma treatment lead to approximately the same water contact angle when plasma energy is the same; total energy applied to the plasma system determines the degree of surface modification. Our results agree with a previous study using Ar/H_2 on copper leadframes[299]. 200W RF plasma was used for subsequent experiments.

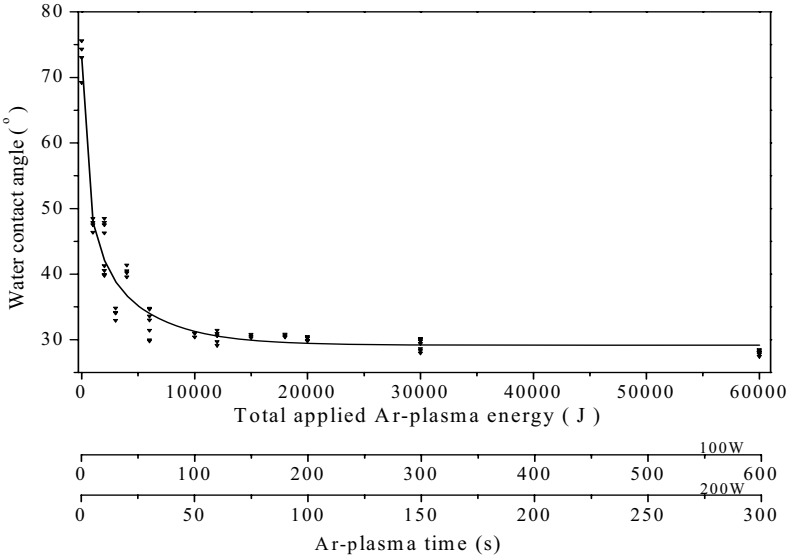

Figure 6.6 Effect of total applied plasma energy on water contact angle

The effect of plasma treatment time on actual and true surface energies is shown in Figure 6.7. Actual surface energy includes effects of surface roughness and chemical structure whilst true value includes only chemical effects. For plasma times of 30s or less, true and actual surface energies are about the same because the surface roughness is small (Figure 7.7). For plasma treatment times of 60s or more, actual surface energy is slightly higher than true surface energy since surface roughness has increased, though the absolute value of roughness is still small. Ar plasma treatment significantly increases SU-8 surface energy. True surface energy of untreated SU-8 is 45.5±0.3mJ/m^2 and increases to 51.4±0.9mJ/m^2 when the SU-8 is subjected to 10 sec Ar plasma treatment. The surface energy curves plateau at 20 to 30 sec Ar plasma times and then gradually increase monotonically with further increase of plasma treatment. At the plasma time of 300 sec, the surface energy is 56.4±0.1 mJ/m^2. The initial rapid increase of surface energy is due to the rapid increase in the surface roughness (Figure.6.8) as well as in the oxygen content (discussed below).

Plasma treatment of polymer surfaces increases their roughness by ablation of atoms and molecular fragments. The roughness (Ra) of untreated SU-8 surface was 12.5±1.4

nm. Ra increased rapidly to 24.8±2.0 nm at 10 sec treatment time and reached a more or less constant value of 28.5 nm for plasma treatment times of 60 sec or longer. Longer plasma times (up to 300 sec investigated) did not result in any further roughening; this is fortunate because a lengthy treatment is desirable to make the SU-8 wettable for electroforming and smoothness in the SU-8 mold and electroformed replica are needed for the sake of the demolding of UV embossings from the replica.

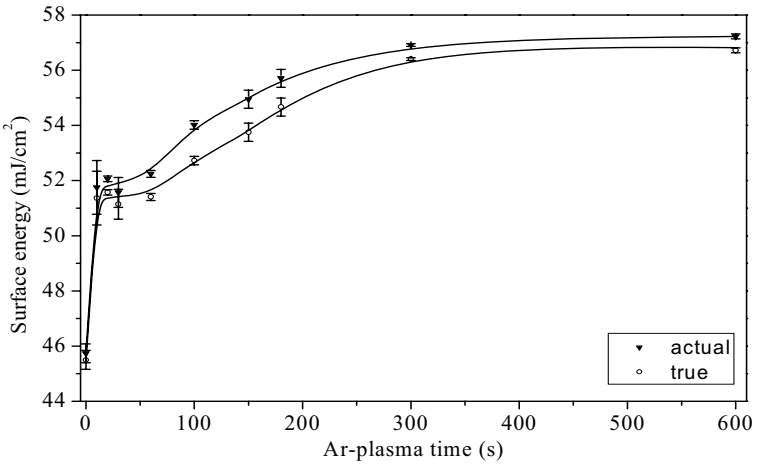

Figure 6.7 Effect of Ar-plasma on surface energy of SU-8 (RF power 200 W)

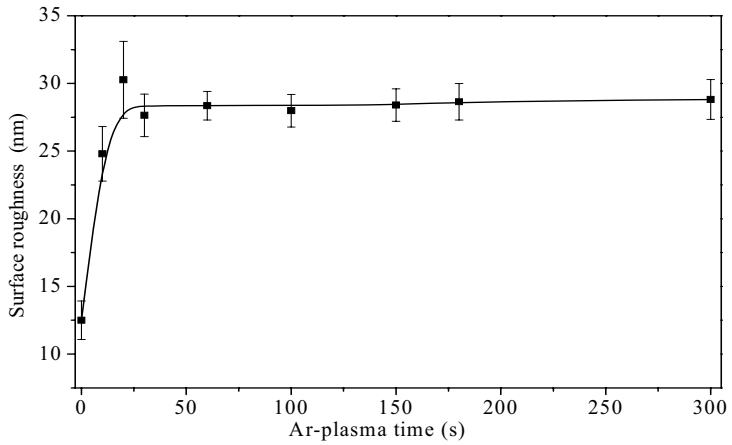

Figure 6.8 Effect of Ar-plasma on SU-8 surface roughness (RF power 200 W)

For the sidewalls of deep channels in SU-8 resist, the Ra was more than 0.2μm (Figure C.1 and C.2, Appendix C). No distinguishable roughness change on the side wall was detected after the plasma treatment because the original surface roughness of the side wall was much higher than the roughness change introduced by the plasma treatment.

6.3.2 Chemical composition of plasma treated surface

Figure 6.9 shows deconvolved XPS C 1s core-level spectra of SU-8 surface subjected to different plasma times with 200W RF power. The C1s spectra show a high-intensity peak at 285.0 eV which represents carbon atoms bonded to carbon or hydrogen (C–C/C–H). The shoulder occurring at a higher binding energy of 286.6 eV is attributed to C in ether bond (C–O–C). With argon plasma treatment, a new, low amplitude, peak at 289.3 eV was detected and this was attributed to C in peroxide (C–O–O–). Argon plasma treatment results in surface radicals which convert to peroxides when exposed to air. The ratio of deconvolved peak areas at 286.6 eV and 289.3 eV to the total C 1s peak area is a measure of the percentage surface content of C-O and C-O-O- respectively.

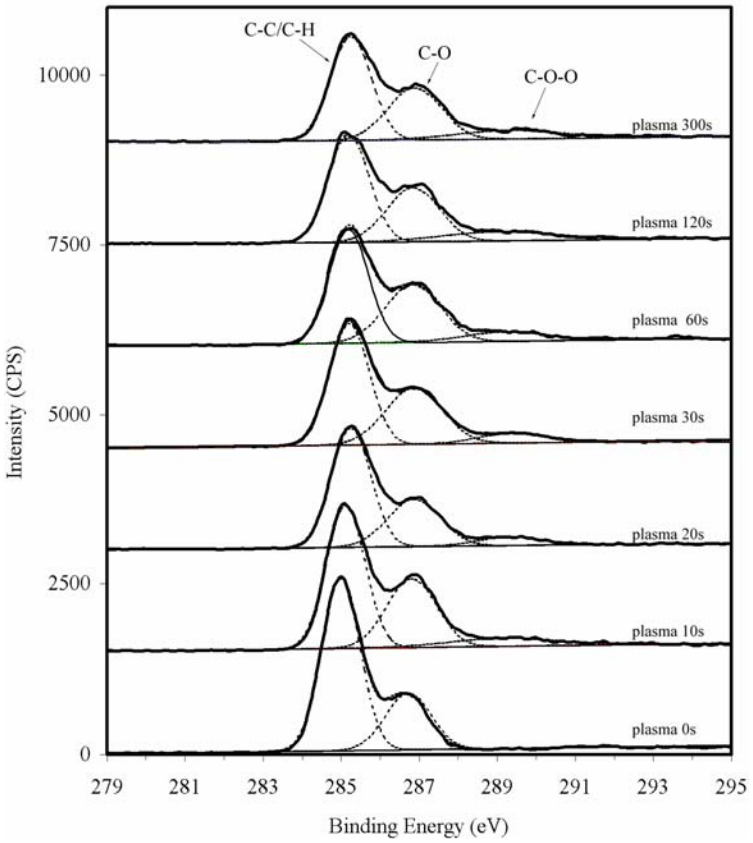

Figure 6.9 XPS C 1s core-level spectra of Ar-plasma treated SU-8 (RF power 200 W)

Figure 6.10 shows that the C-O-O- percentage increases from 0 with no argon plasma treatment to 5.7±0.2% with a short argon plasma treatment time of 10 s (power =

200W); the C-O-O- percentage saturates at a level of about 7.4±0.2% with 30s and longer plasma. Figure 6.10 shows that the C-O content on the surface also increases when the sample is subjected to plasma treatment. The C-O content is 32.2±0.2% on untreated SU-8 surface (much larger than the corresponding C-O-O content) but increases to 35.7±0.2% with 30s plasma time. Beyond that, the C-O content does not plateau but increases slowly; the C-O content is 37.0±0.2%, 39.2±0.1%, 41.8±0.1% and 42.7±0.1% at plasma times of 60s, 120s, 300 s and 600s respectively. Figure 6.10 also shows that the total C-O and C-O-O- content increases rapidly for plasma time of 30s or shorter and then more slowly at longer treatment times.

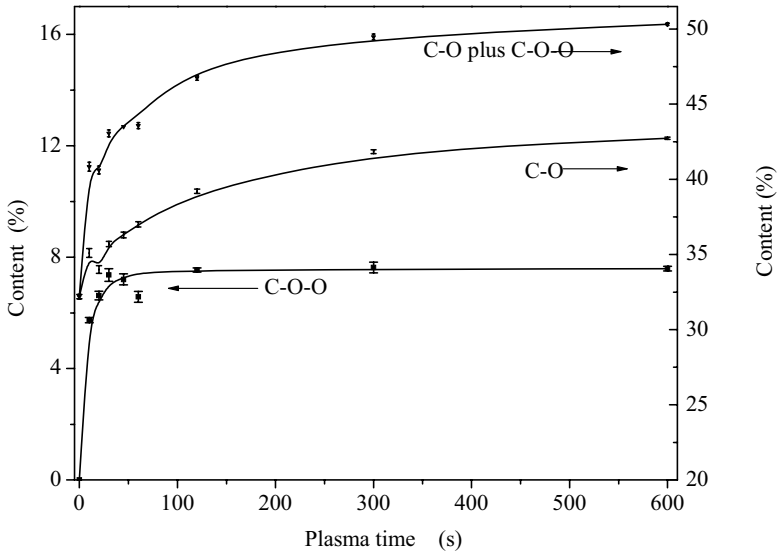

Figure 6.10 Percentage content of C-O-O- group, C-O group on the SU-8 surface and total content of C-O-O- plus C-O groups on the SU-8 surface (RF power 200 W)

Figure 6.11 shows the deconvolved XPS O 1s core-level spectra of SU-8 surface subjected to different plasma times. It should be noted that the O 1s peak is very close to one of the Sb 3d peaks and the peaks are partially overlapped. The spectra were deconvolved to determine the O 1s peak area. In the deconvolution, the O 1s peak was fixed at about 529.9 eV and the Sb 3d peaks at 528.4 and 537.8 eV respectively. Figure 6.11 also shows that the Sb concentration increases when the plasma time increases. We

attribute this to selective polymer surface etching by Argon plasma. Since Sb atoms are much heavier than C and O atoms, the etching rate of Sb is lower than that of C and O. The O 1s and C 1s raw peak areas were normalized using the machine sensitivity factors of 0.78 and 0.278 respectively. The O/C ratio was calculated by dividing the normalized O 1s peak area by the normalized C 1s peak area. Figure 6.12 shows that the O/C ratio is 0.25±0.01 without Argon plasma treatment and increases rapidly to 0.46±0.02 at 30s treatment time (at 200 W). Beyond 30s plasma time, the O/C ratio increases slowly.

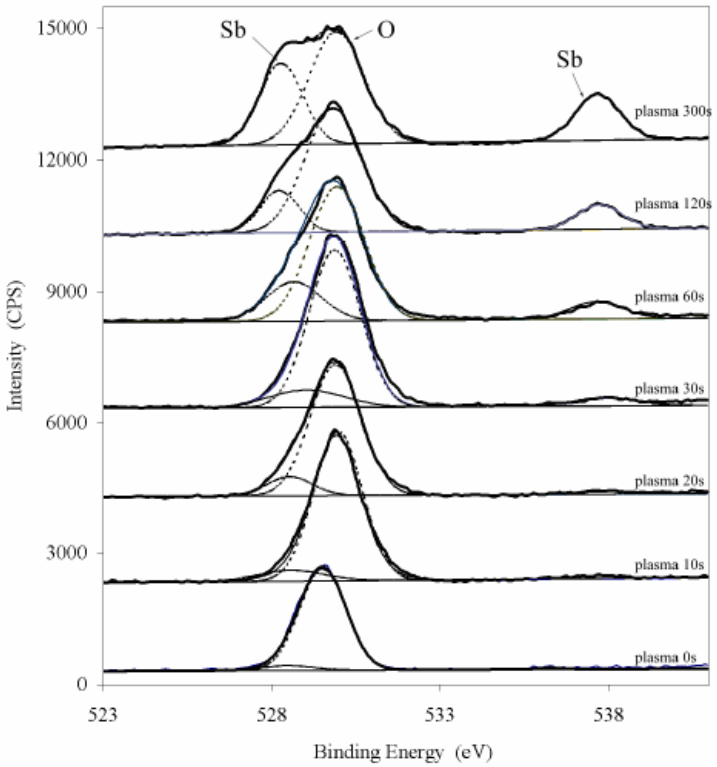

Figure 6.11 XPS O 1s core-level spectra of Ar-plasma treated SU-8(RF power 200 W)

In the first 30 sec of plasma treatment, both the surface roughness and chemical changes contribute towards the rapid surface energy increase. At longer Ar-plasma treatment times (≥60s), the roughness on the surface reaches a stable state but the O/C ratio still increases, albeit slowly, leading to a gradual increase of the surface energy. The argon plasma increases the oxygen content on the SU-8 surface. The concentration of C-C/C-

H groups decreases whilst the C-O and C-O-O groups increase. The C-C/C-H groups are nonpolar whilst C-O and C-O-O- groups are relatively polar and hydrophilic. The increase of C-O and C-O-O- groups on the SU-8 surface significantly increases the surface wettability. Others have also observed enhanced surface wettability of plasma-treated polymers and this has been associated with a wide range of structural changes on the surfaces including creation of free radicals, generation of polar groups, degradation of molecular chains, formation of chain crosslinking and increase of surface roughness[228, 231, 300-303].

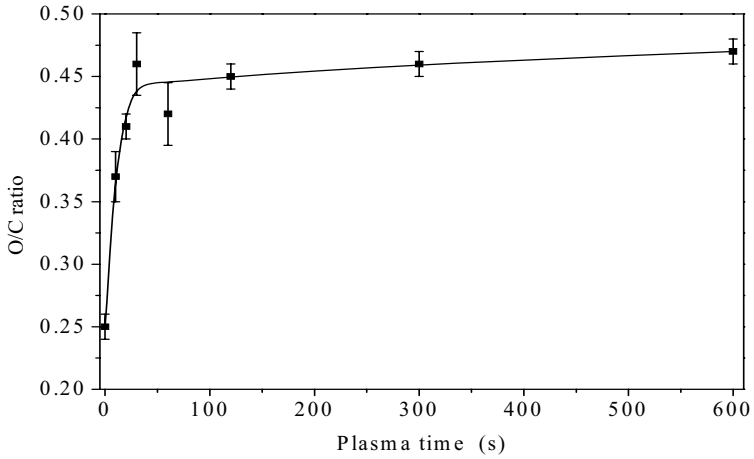

Figure 6.12 Effect of Plasma time on O/C ratio in the SU-8 surface (RF power 200 W)

6.3.3 Electroformed copper mold from patterned SU-8

Between 60 to 600s (RF power = 200W), the surface energy increases without significant increase in the surface roughness. High surface energy and low surface roughness are both desirable for electroforming since they lead to improved wettability without excess roughening. For subsequent experiments, the plasma time was chosen to be 180s (chosen arbitrarily to be more than the inflexion time at 60s). The water contact angle of the untreated and Ar-plasma treated SU-8 gratings was measured to be 124.3±4.6º and 7.9±1.4º respectively (Figures 6.13 (a) and (b)). The wettability of untreated and Ar-plasma treated SU-8 gratings was confirmed visually using the electrolyte. An electrolyte drop was applied onto the top of untreated and plasma treated

SU-8 gratings. The electrolyte did not spread and remained an approximately spherical bead on the untreated SU-8 surface (Figure 6.13(c)). The electrolyte drop flowed away when the sample was tilted and there was no residual electrolyte left on the SU-8 grating. An electrolyte drop on the surface of a 180s (200W) Ar-plasma treated grating spread along the direction of the channels (Figure 6.13(d)). After the bulk surface electrolyte was blown from the grating surface using a gentle airflow, electrolyte was observed in the narrow channels. Figure 6.14 shows the electrolyte in the narrow channels. The results indicate that the electrolyte was able to fill the deep and narrow microchannels and contact the metallic seed layer at the bottom of the channels. This contact made ion diffusion and metal deposition possible during the electroforming process. With the untreated SU-8 microstructure, the electroforming circuit remained open and there was no current and no electro-deposition. 180 sec of treatment with Ar-plasma at 200 W provided sufficient wetting of the grating surface for satisfactory electroforming.

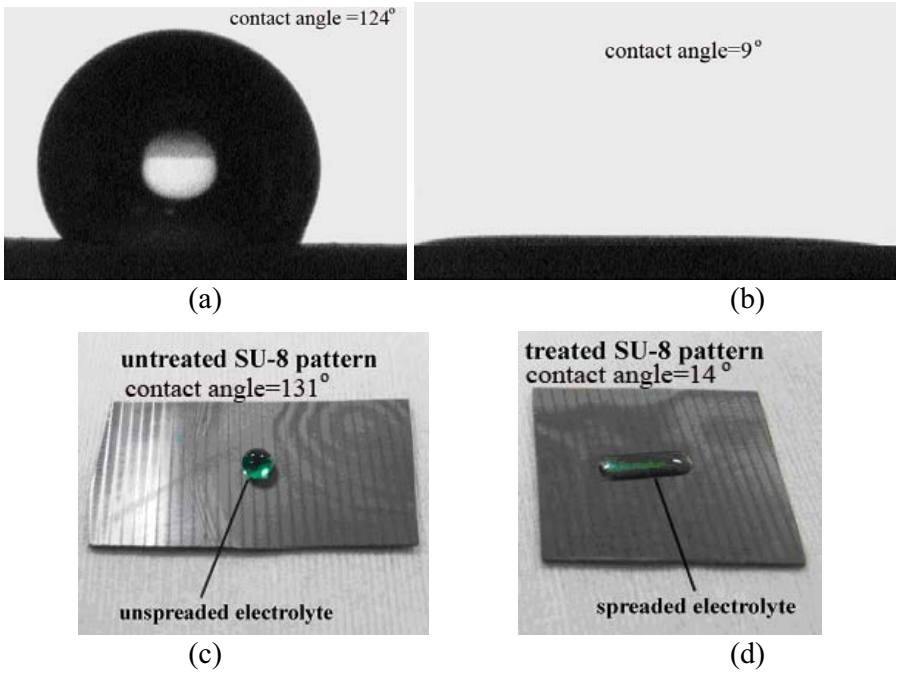

Figure 6.13 Water on (a) untreated and (b) Ar-plasma treated SU-8 pattern. Electrolyte on (c) untreated and (d) Ar-plasma treated SU-8 pattern. (Plasma time=180s, power=200 W)

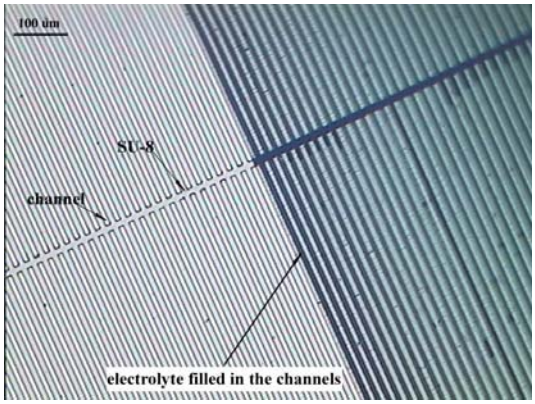

Figure 6.14 Electrolyte spread along the direction of channel and remained in the channels (The SU-8 grating was Ar-plasma treated for 180 sec at 200W)

Figures 6.15(a) and 6.15(b) show the SU-8 grating before and after electroforming respectively. The pre-electroforming cross-section was obtained by breaking the wafer and the electroformed SU-8 cross-section was obtained by manually cutting with a knife. Figures 6.16(a) and 6.16(b) show respectively the cross sectional and top views of the copper mold after SU-8 removal. The deformation of the Cu microwalls was produced by the cutting. The SU-8 was completely removed from the deep channels. The measured width and height of these copper bars were 7.6±0.3μm and 116.0±0.7 μm respectively, giving an aspect ratio of 15.3, which matches the aspect ratio of the SU-8 mold microchannels; as expected, the electroforming faithfully replicated the wettable SU-8 mold. The width of the channels separating the copper bars was 12.7±0.5 μm and the aspect ratio of these channels was 9.2.

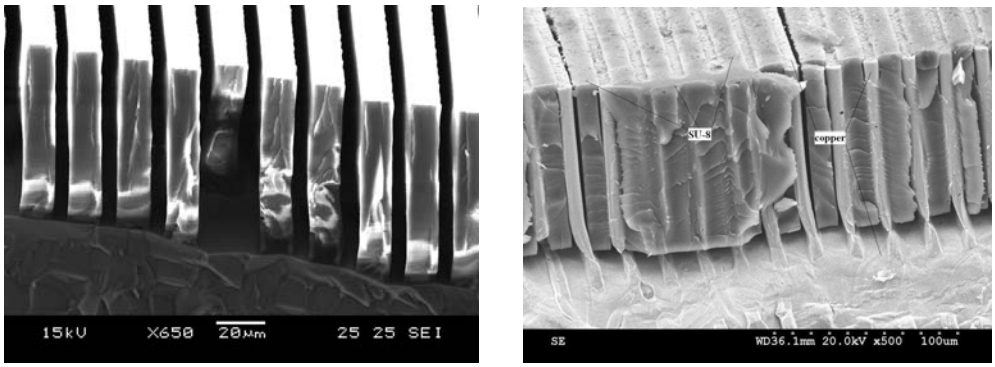

(a) (b)

Figure 6.15 (a) High aspect ratio SU-8 grating and (b) Electroformed metallic structure with SU-8 grating defined using Mask D (exposed for 40 s, Sample 3 in Table 6.1)

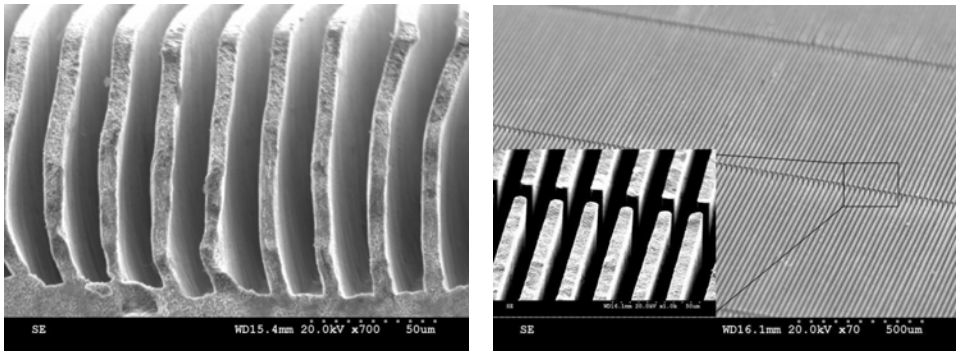

(a) (b)

Figure 6.16 (a) Cross section and (b) Top view of copper mold after SU-8 removal (defined using Mask D)

The SU-8 grating fabricated using Mask B was previously shown in Figure 4.6, Figure 6.17 shows the grating after copper electroforming. In Figure 6.17, SU-8 is not removed. The dimensions were measured using SEM after removing the SU-8 grating. The measured height of copper bars is 118.1±0.9 μm, the averaged width of copper bars is 78.6±1.1 μm, the averaged width of channels separating the copper walls is 12.3±0.7 μm. The copper mold defined using Mask B is shown in Figure 6.18.

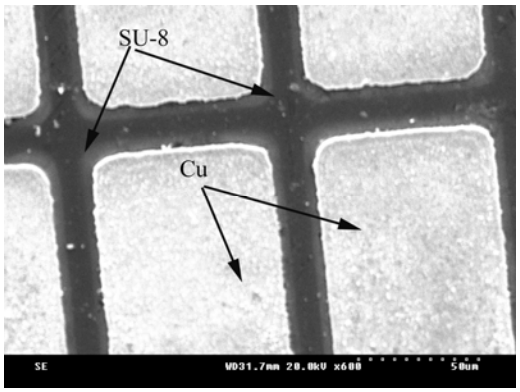

Figure 6.17 SU-8 grating defined using Mask B and the electroformed Cu

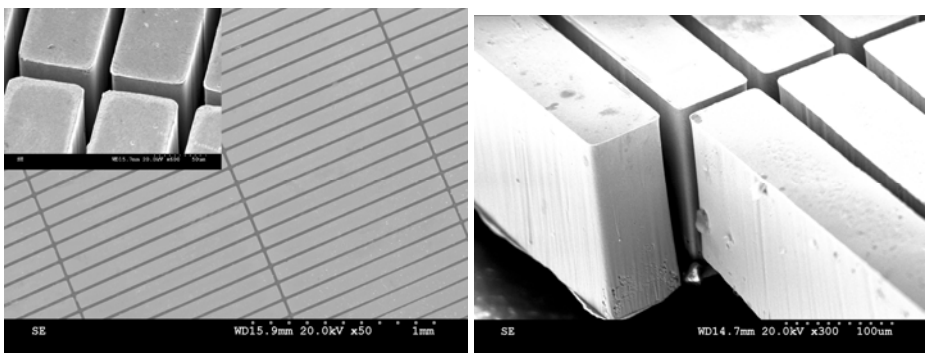

Figure 6.18 (a) Top view and (b) Cross section of copper mold after SU-8 removal (defined using Mask D)

6.3.4 UV embossed polymer grating with very high aspect ratio

The high aspect ratio polymer grating UV embossed from the siliconized copper mold defined using Mask D is shown in Figure 6.19. The measured height and width of the polymer microwalls were 114.9±1.1 μm and 12.5±0.4 μm respectively, giving an aspect ratio of 9.2. The width of channels separating the polymer bars was 7.8±0.3 μm and the aspect ratio of these channels was 14.7.

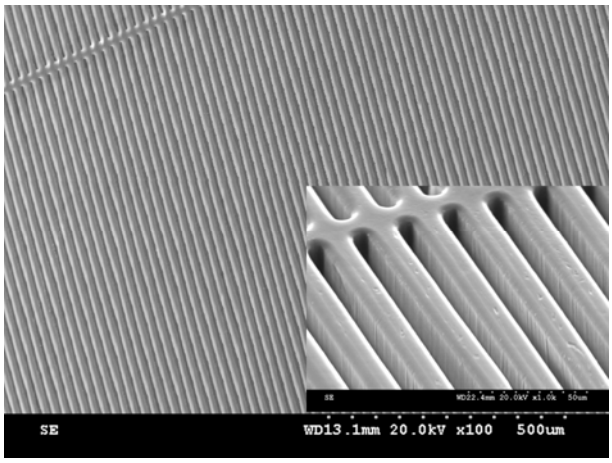

Figure 6.19 Polymer grating replicated from Cu mold by UV embossing (embossed at room temperature)

6.4 Summary

The hydrophobic nature of untreated SU-8 (surface energy of 45.5 ± 0.3 mJ/m^2) prevents electroforming electrolytes from contacting the seed layer at the bottom of VHAR and dense microchannels in SU-8. This problem is likely to affect more complex microstructure architectures of similar aspect ratio and density needed for diverse applications. Under Ar plasma, the surface energy increases rapidly initially and then begins to saturate before the electroforming seed layer at the base of the microstructure is eroded. The surface roughness plateaus whilst the oxidation continues to rise, albeit slowly, on the same timescale (around 30s under the process conditions we employed). An argon plasma time of 180s, resulting in an actual surface energy of 55.7 ± 0.3 mJ/m^2,

enabled the electrolyte to fill the narrow and very high aspect ratio (15.3) microchannels in SU-8, contacting the seed layer and completing the electroforming circuit. A copper grating with alternating microchannels and microwalls of aspect ratios of 15.3 and 9.2 respectively was successfully electroformed over the entire 100 mm diameter wafer using a 180 sec-Ar-plasma treated SU-8 master. The copper mold was demonstrated to be useful for UV embossing. This technique permits the low-cost fabrication of durable high aspect ratio metallic molds for high volume fabrication of microstructures using UV embossing.

Chapter 7 Conclusions and recommendations

A new theoretical model has been developed to predict the profiles of micro channels in thick SU-8. The predicted frofiles compare well with experimental values. The process combining soft cushion technology and dose reduction was developed to fabricate whole-wafer-covered dense SU-8 gratings with both VHAR microchannels and VHAR SU-8 walls. After the argon plasma treatment, the SU-8 gratings were successfully used as the mold for electroforming. In order to effectively remove the cured SU-8, kinetics during curing of SU-8 resist in the presence of GBL, network properties, thermal and chemical degradation of cured SU-8 were investigated. The electroformed metallic mold was used for UV embossing after successful removal of the SU-8.

7.1 Diffraction, refraction and reflection model for thick resist UV lithography

Diffraction, refraction and reflection have significant effects on mask replication, profile characteristics and processability of VHAR channels in SU-8 photolithography. Reflection and diffraction lead to UV exposure of the photoresist underneath the dark field areas of the mask causing gelation and crosslinking, which then increases the width and slopes of SU8 microwalls. The “stray” UV light was enough to cause substantial dimensional difference between the mask and the microstructures, even unresolved microchannels. The previously reported classical model accounting for diffraction only is inadequate to accurately predict the profile characteristics of VHAR microchannels in thick SU-8. A new model incorporating the effects of diffraction at the edge of the dark field mask lines, refraction at the air/resist interface and reflection from the silicon wafer surface on the profile characteristics of VHAR microchannels in thick SU-8 has been developed. The effects of light reflection at the wafer surface, varying UV exposure time and air gap

(resulting from edge bead) between the resist and mask on pattern size and microchannel profiles were theoretically modeled and experimentally verified. Longer exposure time was experimentally observed to result in smaller (i.e. less steep) side wall angle and narrower microchannels. The calculated mask replication fidelity and taper angle using the new diffraction-refraction-reflection (DRR) model was compared with experimental results. The new DRR model produced much superior predictions of the observed trends and actual microchannel width and sidewall angle as a function of exposure dose compared with the classical diffraction-only model. However, the calculated microchannel width and sidewall angle at high exposure dose agreed better with the experimentally observed values indicating that reflection at the silicon substrate and refraction at air/SU-8 interface were significant. In the lower exposure range, the predicted channel widths were less than the experimentally observed data. The larger than calculated actual microchannel width for the low exposure dose was due to the leaching of unreacted resist in the developer from DMA studies.

7.2 Soft cushion technology and dose reduction

The process combining soft cushion technology and dose reduction was developed to fabricate whole-wafer-covered dense SU-8 gratings with both VHAR microchannels (AR=18) and VHAR SU-8 walls (AR=10). The soft cushion bends the wafer during UV exposure, thereby mechanically flattening the resist surface and reducing the air gap between the resist and mask during exposure of the resist. This procedure improves the pattern replication and uniformity resolution over virtually the entire surface of the 100mm-diameter wafer. Dose reduction technology reduces the energy deposited at all points in the resist, and in particular the “stray” energy deposited under the dark field by diffraction, refraction and reflection so as to decrease the negative effect of stray UV light on the fabrication of VHAR microchannels.

7.3 Curing and degradation of SU-8 resist in the presence of GBL

Chemical reaction during the curing of SU-8 resist in the presence of GBL was investigated. GBL is a reactive solvent during the SU-8 processing and so we used FTIR and ^{13}C NMR spectra to show that GBL reacts during the curing of SU-8. It reacts with epoxy and is crosslinked into the network. The presence of GBL helps to achieve epoxy conversion as high as 100%, depending on the amount of GBL in the resist. Up to 33 weight% of GBL can react with SU-8 during the curing and excess GBL beyond that remains unreacted in the cured SU-8-GBL system which can be removed by vacuum baking.

The network properties of cured SU-8 are affected by curing conditions. At constant GBL content, high epoxy conversion leads to high T_g and low M_c value indicating dense cross-link density. Vitrification of SU-8 occurs at 55% epoxy conversion. Beyond vitrification, both M_c and T_g do not change significantly. The presence of GBL during the curing of SU-8 leads to long chains between cross-links, low cross-link density and T_g lowering.

Thermal degradation of cured SU-8 was also investigated. Kinetic studies show that the network properties of cured SU-8 strongly affect the degradability. The thermal degradation activation energy of SU-8 (E_a)decreases exponentially with increase of M_c in the low M_c range (high cross-link density, after vitrification) but does not change significantly in the high M_c range (low cross-link density, before vitrification). The presence of GBL gives easier degradability of cured SU-8 because GBL results in long chains between crosslinks, low cross-link density and ester structural units with easily degradable C-O bond. ^{13}C NMR spectrum and GC/MS results showed that the network of cured SU-8 was broken into water soluble fragments by sulfuric acid dissolution and the fragments contained carbonyl, aromatic, alkyl and other groups

7.4 SU-8 mold for copper electroforming and UV embossing using the copper mold

SU-8 is intrinsically hydrophobic. Unpatterned SU-8 has a water contact angle of 73.1±2.8° and surface energy of 45.5±0.3 mJ/m^2. Dense micropatterns further make the surface super-hydrophobic. When electroforming from SU-8 surfaces patterned with VHAR and dense microchannels, the electrolyte cannot contact the seed layer at the bottom and the electroforming circuit is mostly open even with agitation - the process cannot proceed. In order to overcome the hydrophobicity and consequent low wettability of polymeric surfaces, surface treatment is essential. We developed a simple but effective method of increasing the wettability of hydrophobic SU-8 grating. Argon plasma treatment oxidizes and roughens the surface leading to increased surface energy. An argon plasma time of 180s at RF power of 200W, resulting in an actual surface energy of 55.7 ± 0.3 mJ/m^2, enabled the electrolyte to fill the narrow and VHAR (15.3) microchannels in SU-8, contacting the seed layer and completing the electroforming circuit. A large area VHAR and dense copper grating with alternate microwalls and microchannels of aspect ratios of 15.3 and 9.2 respectively over the entire 100mm-diameter area was fabricated by copper electroforming from a plasma treated SU-8 master. This copper mold was used as a mold for UV embossing, demonstrating the feasibility of this technique for the creation of durable molds for mass replication.

7.5 Recommendations for future works

Although there have been many achievements in this research, there is much potential work that could be done to enhance this research. Four key areas of research are suggested.

The first concerns plasma treatment and electroforming. Dense copper gratings with very high aspect ratio were successfully fabricated via photolithography and

electroforming. Nickel provides much better properties (such as higher hardness, better anti-corrosion property) for using as mold in replication than copper does. It is worth further extending the plasma treatment and electroforming to the fabrication of nickel molds.

The second concers methods for large-scale polymeric replication and patterning with sub-micro and nano level dimension are suggested. Since the resolution of SU-8 resist is micro scale, it is not suitable to fabricate the master with nano scale structure. E-beam lithography or focus ion beam (FIB) writing, which are able to fabricate nano-scale structures, can be employed to fabricate the master.

The third area of further research relates to embossing. UV embossing is an attractive patterning technique for many diverse biomedical applications. UV embossing resins have a wide range of properties so that micro-patterned properties can be easily tailored. Versatile micropatterns including both high and low aspect ratio microstructures can be readily fabricated [43]. The embossed film is foldable and can be used for foldable devices like e-paper. Micro devices with high aspect ratio structures on foldable substrates can be UV embossed.

The final area of further research concerns biological applications of the VHAR channel. Biological applications of microstructures are rapidly increasing. Further research on the high aspect ratio pattern in bio- and chemical application, such as biosensor, is worthy doing.

References

1. R. Turner, Y. Desta, K. Kelly, J. Zhang, E. Geiger, S. Cortez and D.C. Mancini, Tapered LIGA HARMs. Journal of Micromechanics and Microengineering, 2003. **13**: p. 367-372.
2. Y. Chen and A. Pepin, Nanofabrication: Conventional and Nonconventional methods. Electrophoresis, 2001. **22**: p. 187-207.
3. B.W.S. J.R. Sheats, Microlithography Science and Technology. Marcel Dekker, New York, 1998.
4. R.L. Brainard, G.G. Barclay, E.H. Anderson and L.E. Ocola, Resists for next generation lithography. Microelectronic Engineering, 2002. **61-62**: p. 707-715.
5. L.R. Harriott, Overview:Next generation lithography. Materials Science in Semiconductor Processing, 1998. **1**: p. 93-97.
6. C.A. Mills, E. Martinez, F. Bessueille, G. Villanueva, J. Bausells, J. Samitier and A. Errachid, Production of structures for microfluidics using polymer imprint techniques. Microelectronic Engineering, 2005. **78-79**: p. 695-700.
7. O. Rotting, W. Ropke, H. Becker and C. Gartner, Polymer microfabrication technologies. Microsystem Technologies, 2002. **8**: p. 32-36.
8. H. Becker and C. Gartner, Polymer microfabrication methods for microfluidic analytical applications. Electrophoresis, 2000. **21**: p. 12-26.
9. M. Halik, H. Klauk, U. Zschieschang, T. Kriem, G. Schmid, W. Radlik and K. Wussow, Fully patterned all-organic thin film transistors. Applied Physics Letters, 2002. **81**(2): p. 289-291.
10. Z.N. Bao, J.A. Rogers and H.E. Katz, Printable organic and polymeric semiconducting materials and devices. Journal of Materials of Chemistry, 1999. **9**(9): p. 1895-1904.
11. A. Goessl, M.D. Garrison, J.B. Lhoest and A.S. Hoffman, Plasma lithography - thin-film patterning of polymeric biomaterials by RF plasma polymerization I: Surface preparation and analysis. Journal of Biomaterials Science-Polymer Edition, 2001. **12**(7): p. 721-738.
12. E. Ostuni, R. Kane, C.S. Chen, D.E. Ingber and G.M. Whitesides, Patterning mammalian cells using elastomeric membranes. Langmuir, 2000. **16**(20): p. 7811-7819.
13. J.H. Ward, R. Bashir and N.A. Peppas, Micropatterning of biomedical polymer surfaces by novel UV polymerization techniques. Journal of Biomedical Materials Research, 2001. **56**(3): p. 351-360.
14. C. Miller, H. Shanks, A. Witt, G. Rutkowski and S. Mallapragada, Oriented Schwann cell growth on micropatterned biodegradable polymer substrates. Biomaterials, 2001. **22**: p. 1263-1269.
15. S. Gaspar, M. Mosbach, L. Wallman, T. Laurell, E. Csoregi and W. Schuhmann, A method for the design and study of enzyme microstructures formed by means of a flow-through microdispenser. Analytical Chemistry, 2001. **73**(17): p. 4254-4261.
16. F. Zee and J.W. Judy, Micromachined polymer-based chemical gas sensor array. Sensors and Actuators B-Chemical, 2001. **72**(2): p. 120-128.
17. D.L. Pugmire, E.A. Waddell, R. Haasch, M.J. Tarlov and E. Locascio, Surface characterization of laser-ablated polymers used for microfluidics. Analytical Chemistry, 2002. **74**(4): p. 871-878.
18. T. Rohr, C. Yu, M.H. Davey, F. Svec and J.M.J. Frechet, Porous polymer monoliths: Simple and efficient mixers prepared by direct polymerization in the channels of microfluidic chips. Electrophoresis, 2001. **22**(18): p. 3959-3967.
19. R.P. Lanza, R. Langer and J. Vacanti, Principles of Tissue Engineering. 2000. **2nd Edition**.
20. S.Y. Chou, P.R. Krauss and P.J. Renstrom, Imprint of sub-25 nm vias and trenches in polymers. Applied Physics Letters, 1995. **67**(21): p. 3114-3116.
21. M.T. Gale, C. Gimkiewicz, S. Obi, M. Schnieper, J. Sochtig, H. Thiele and S. Westenhofer, Replication technology for optical microsystems. OPTICS AND LASERS IN ENGINEERING, 2005. **43**(3-5): p. 373-386.

22. Y. Lu and S.C. Chen, Micro and nano-fabrication of biodegradable polymers for drug delivery. Advanced Drug Delivery Reviews, 2004. **56**(11): p. 1621-1633.
23. Y. Xia, J.J. McClelland, R. Gupta, D. Qin, X.-M. Zhao, L.L. Sohn, R.J. Celotta and G.M. Whitesides, Replica molding using polymeric materials: A practical step toward nanomanufacturing. Advanced Materials, 2004. **9**(2): p. 147-149.
24. N. Bogdanski, H. Schulz, M. Wissen, H.-C. Scheer, J. Zajadacz and K. Zimmer, 3D-Hot embossing of undercut structures ?an approach to micro-zippers. Microelectronic Engineering, 2004. 7**3-74:** p. 190-195.
25. V. Grigaliunas, V. Kopustinskas, S. Meskinis, M. Margelevicius, I. Mikulskas and R. Tomasiunas, Replication technology for photonic band gap applications. Optical Materials, 2001. 1**7(**1-2): p. 15-18.
26. S. Rudschuck, D. Hirsch, K. Zimmer, K. Otte, A. Braun, R. Mehnert and F. Bigl, Replication of 3D-micro- and nanostructures using different UV-curable polymers. Microelectronic Engineering, 2000. 5**3(**1-4): p. 557-560.
27. M. Heckele and W.K. Schomburg, Review on micro molding of thermoplastic polymers. Journal of Micromechanics and Microengineering, 2004. 1**4:** p. R1-R4.
28. N. Gadegaard, S. Mosler and N.B. Larsen, Biomimetic Polymer Nanostructures by Injection Molding. Macromolecular Materials and Engineering, 2003. 2**88:** p. 76-83.
29. Y. Takagaki, E. Wiebicke, H. Kostial and K.H. Ploog, Fabrication of GHz-range surface-acoustic-wave transducers on LiNbO3 using imprint lithography. Nanotechnology, 2002. 1**3:** p. 15-17.
30. J. Melin, K. Hedsten, A. Magnusson, D. Karlen, H. Rodjeg 鋉 d, K. Persson, J. Bengtsson, P. Enoksson and F. Nikolajeff1, Microreplication in a silicon processing compatible polymer material. *J*ournal of Micromechanics and Microengineering, 2005. 15**:** p. s116-s121.
31. Y. Lu and S.C. Chen, Micro and nano-fabrication of biodegradable polymers for drug delivery. *A*dvanced Drug Delivery Reviews, 2004. 56**:** p. 1621?1633.
32. M.A. Unger, H.P. Chou, T. Thorsen, A. Scherer and S.R. Quake, Monolithic microfabricated valves and pumps by
multilayer soft lithography. S*c*ience, 2000. 288**:** **p**. 113-116.
33. Y. Xia and G.M. Whitesides, Soft Lithography. A*n*nu. Rev. Mater. Sci., 1998. 28: **p**. 153-184.
34. D. Pisignano, L. Persano, G. Gigli, P. Visconti, T. Stomeo, M.D. Vittorio, G. Barbarella, L. Favaretto and R. Cingolani, Planar organic photonic crystals fabricated by soft lithography. N*a*notechnology, 2004. 15(**7)**: p. 766-770.
35. M. Madou, Fundamentals of microfabrication. 1997: CRC Press.
36. D. Suh, J. Rhee and H.H. Lee, Bilayer reversal imprint lithography: direct metal-polymer transfer. N*a*notechnology, 2004. 15: **p**. 1103-1107.
37. J.H. Ng and L.L. Ilag, Biochips beyond DNA: technologies and applications. B*i*otechnology Annual Review, 2003. 9: **p**. 1-149.
38. R.M. McCormick, R.J. Nelson, M.G. Alonso-Amigo, D.J. Benvegnu and H.H. Hooper, Microchannel electrophoretic separations of DNA in injection-molded plastic substrates. A*n*alytical Chemistry, 1997. 69: **p**. 2626-2630.
39. C.G. Choi, Fabrication of optical waveguides in thermosetting polymers using hot embossing. J*o*urnal of Micromechanics and Microengineering, 2004. 14(**7)**: p. 945-949.
40. T. Rohr, C. Yu, M.H. Davey, F. Svec and J.M.J. Frechet, Imprinting by hot embossing in polymer substrates using a template of silica glass surface-structured by the ablation of LIBWE method. A*p*plied Physics A: Materials Science & Processing, 2004. 79(**4-**6): p. 827-828.
41. L.J. Heyderman, H. Schift, C. David, J. Gobrecht and T. Schweizer, Flow behaviour of thin polymer films used for hot embossing lithography. M*i*croelectronic Engineering, 2000. 54: **p**. 229-245.
42. W.S. Kim, J.H. Lee, S.Y. Shin, B.S. Bae and Y.C. Kim, Fabrication of ridge waveguides by UV embossing and stamping of sol-gel hybrid materials. I*E*EE Photonics Technology Letters, 2004. 16(**8)**: p. 888-1890.
43. M.B. Chan-Park, Y. Yan, W.K. Neo, W. Zhou, J. Zhang and C.Y. Yu, Fabrication of high aspect ratio poly(ethylene glycol)-containing microstructures by UV embossing. L*a*ngmuir,

2003. 19(**10**): p. 4371-4380.
44. S. Obi, M.T. Gale, A. Kuoni and N.D. Rooij, Replication of optical MEMS structures in sol-gel materials. M*i*croelectronic Engineering, 2004. 73-**74: p**. 157-160.
45. C. Malins, T.G. Harvey, P. Summersgill, P.R. Fielden and N.J. Goddard, Embossed polymer leaky waveguide devices for spectroscopic analysis. A*n*alyst, 2001. 126**(8)**: p. 1293-1297.
46. P.R. Krauss and S.Y. Chou, Nano-compact disks with 400 Gbit/in(2) storage density fabricated using nanoimprint lithography and read with proximal probe. A*p*plied Physics Letters, 1997. 71(**21**): p. 3174-3176.
47. S.Y. Chou, P.R. Krauss, W. Zhang, L.J. Guo and L. Zhuang, Sub-10 nm imprint lithography and applications. J*o*urnal of Vacuum Bcience & Technology B, 1997. 15(**6**): p. 2897-2904.
48. M.B. Esch, S. Kapur, G. Irizarry and V. Genova, Influence of master fabrication techniques on the characteristics of embossed microfluidic channels. L*a*b On A Chip, 2003. 3: **p**. 121-127.
49. W.W. Flack, S. Kulas and D.W. Minsek, Process Characterization of an Ultra-thick Strippable Photoresist Using a Broadband stepper. S*P*IE 2000, 2000: p. #3999-47.
50. T.L. Edwards, S.K. Mohanty, R.K. Edwards and A. Frazier, Rapid tooling using SU-8 for injection molding microfluidic components. S*P*IE 4177 (2000): p. 82-89.
51. A.P. Gadre, M.J. Kastantin, S. Li and R. Ghodssi, An integrated BioMEMS fabrication technology,. I*n*ternational Semiconductor Device Research Symposium (ISDRS) December 5-7, 2001, Washington D.C.: p. 186-189.
52. M. Kubenz, U. Ostrzinski, F. Reuther and G. Gruetzner, Effective baking of thick and ultra-thick photoresist layers by infrared radiation. M*i*croelectronic Engineering, 2003. 67-**68: p**. 495-501.
53. B. Loechel, Thick-layer resists for surface micromachining. J*o*urnal of Micromechanics and Microengineering, 2000. 10: **p**. 108-115.
54. F.-G. Tseng and C.-S. Yu, High aspect ratio ultrathick micro-stencil by JSR THB-430N negative UV photoresist. S*e*nsors and Actuators A: Physical, 2002. 97-**98: p**. 764-770.
55. B. Loechel, R. Demmeler, M. Rothe, W. Bruenger, S. Fehlberg and G. Gruetzner, Application of optical lithography for high aspect ratio microstructures. J*o*urnal of Vacuum Bcience & Technology B, 1996. 14: **p**. 4179-4183.
56. C.K. Malek and S. Das, Swelling behaviour of poly(methylmethacrylate) thick resist layers in deep X-ray lithography. J*o*urnal of Synchrotron Radiation, 2003. 10: **p**. 272-279.
57. N. Dumbravescu, Experiments for 3-D structuring of thick resists by gray tone lithography. M*a*terials Science in Semiconductor Processing, 2000. 3: **p**. 569-573.
58. H. Lorenz, M. Despont, P. Vettiger and P. Renaud, Fabrication of photoplastic high-aspect ratio microparts and micromolds using SU-8 UV resist,. M*i*crosystem Technologies, 1998. 4(3**)**: p. 143-146.
59. W.W. Flack, S. White and B. Todd, Process Characterization of One Hundred Micron Thick Photoresist Films. S*P*IE Microlithography: p. 1999 #3678-49.
60. V. Conedera, B.L. Goff and N. Fabre, Potentialities of a new positive photoresist for the realization of thick moulds. J*o*urnal of Micromechanics and Microengineering, 1999. 9: **p**. 173-175.
61. S. Roth, L. Dellmann, G.-A. Racine and N.F.d. Rooij, High aspect ratio UV photolithography for electroplated structures. J*o*urnal of Micromechanics and Microengineering, 1999. 9: **p**. 105-108.
62. H. Miyajima and M. Mehregany, High-Aspect-Ratio Photolithography for MEMS Applications. I*E*EE Journal of Microelectromechanical Systems, 1995. 4(4**)**: p. 220-229.
63. C.-H. Lin, G.-B. Lee, B.-W. Chang and G.-L. Chang, A new fabrication process for ultra-thick microfluidic microstructures utilizing SU-8 photoresist. J*o*urnal of Micromechanics and Microengineering, 2002. 12: **p**. 590-597.
64. W.W. Flack, H.-A. Nguyen and E. Capsuto, Characterization of an Ultra-Thick Positive Photoresist for Electroplating Applications. F*u*ture Fab Intl., 2004. 17.
65. G. Bleidiessel, G. Gruetzner, F. Reuther, S. Fehlberg, B. Loechel and A. Maciossek,

Dependence of the quality of thick resist structures on resist baking. M*i*croelectronic Engineering, 1998. 41/**42: p**. 433-436.
66. G.E. Flores, W.W. Flack and E. Tai, An Investigation of the Properties of Thick Photoresist Films. S*P*IE, 1994. 219**5-64: p**. 734-751.
67. B. Lochel, A. Maciossek, H.J. Quenzer and B. Wagner, Ultraviolet Depth Lithography and Galvanoforming for Micromachining. J*o*urnal of The Electrochemical Society, 1996. 143**(1)**: p. 237-244.
68. P.W. Leech and H. Zeidler, M icrorelief structures for anti-counterfeiting applications. M*i*croelectronic Engineering, 2003. 65: **p**. 439-446.
69. T. Kohlmeier, V. Seidemann, S. Buttgenbach and H.H. Gatzen, An investigation on technologies to fabricate microcoils for miniaturized actuator systems. M*i*crosystem Technologies, 2004. 10(**3**): p. 175-181.
70. B. Lochel, A. Maciossek, M. Konig, H.J. Quenzer and H.-L. Huber, Galvanoplated 3D structures for micro systems. M*i*croelectronic Engineering, 1994. 23(**1-**4): p. 455-459.
71. J.D. Williams and W. Wang, Study on the postbaking process and the effects on UV lithography of high aspect ratio SU-8 microstructures. J*o*urnal of Microlithography, Microfabrication, and Microsystems, 2004. 3(4**)**: p. 563-568.
72. H. Lorenz, M. Despont, N. Fahrni, N. LaBianca, P. Renaud and P. Vettiger, SU-8: a low-cost negative resist for MEMS. J*o*urnal of Micromechanics and Microengineering, 1997. 7: **p**. 121-124.
73. C.-R. Yang, G.-W. Hsieh, Y.-S. Hsieh and Y.-D. Lee, Microstructuring characteristics of a chemically amplified photoresist synthesized for ultra-thick UV-LIGA applications. J*o*urnal of Micromechanics and Microengineering, 2004. 14: **p**. 1126-1134.
74. Y. Cheng, C.-Y. Lin, D.-H. Wei, B. Loechel and G. Gruetzner, Wall profile of thick photoresist generated via contact printing. I*E*EE Journal of Microelectromechanical Systems, 1999. 8(1**)**: p. 18-25.
75. F.-G. Tseng and C.-S. Yu, Angle effect of ultrasonic agitation on the development of thick JSR THB-430N negative UV photoresist. M*i*crosystem Technologies, 2002. 8: **p**. 363-367.
76. C.K. Chung, C.J. Lin, L.H. Wu, Y.J. Fang and Y.Z. Hong, Selection of mold materials for electroforming of monolithic two-layer microstructure. M*i*crosystem Technologies, 2004. 10: **p**. 467-471.
77. C.K. Chung, C.J. Lin, C.C. Chen, Y.J. Fang and M.Q. Tsai, Combination of thick resist and electroforming technologies for monolithic inkjet application. M*i*crosystem Technologies, 2004. 10: **p**. 462-466.
78. M.K. Ghantasala, J.P. Hayes, E.C. Harvey and D.K. Sood, Patterning, electroplating and removal of SU-8 moulds by excimer laser micromachining. J*o*urnal of Micromechanics and Microengineering, 2001. 11: **p**. 133-139.
79. R.A. Lawes, Manufacturing tolerances for UV LIGA using SU-8 resist. J*o*ural of Micromechanics and Microengineering, 2005. 15: **p**. 2198-2203.
80. A. Bertsch, H. Lorenz and P. Renaud, 3D microfabrication by combining microstereolithography and thick resist UV lithography. S*e*nsors and Actuators A: Physical, 1999. 73(**1-**2): p. 14-23.
81. S.K. Sampath, L.S. Clair, X. Wu, D.V. Ivanov, Q. Wang, C. Ghosh and K.R. Farmer, Rapid MEMS prototyping using SU-8, wafer bonding and deep reactive ion etching. U*n*iversity/Government/Industry Microelectronics Symposium, 2001. Proceedings of the Fourteenth Biennial, 2001: p. 158-161.
82. C. Harris, Y. Desta, K.W. Kelly and G. Calderon, Inexpensive, quickly producable X-ray mask for LIGA. M*i*crosystem Technologies. 5(4**)**: p. 189-193.
83. Y.-J. Chuang, F.-G. Tseng and W.-K. Lin, Reduction of diffraction effect of UV exposure on SU-8 negative thick photoresist by air gap elimination. M*i*crosystem Technologies, 2002. 8(4**-**5): p. 308-313.
84. E. L'Hostis, P.E. Michel, G.C. Fiaccabrino, D.J. Strike, N.F.d. Rooij and M. Koudelka-Hep, Microreactor and electrochemical detectors fabricated using Si and EPON SU-8. S*e*nsors and Actuators B: Chemical, 2000. 64(**1-**3): p. 156-162.
85. P.E. Michel, G.C. Fiaccabrino, N.F.d. Rooij and M. Koudelka-Hep, Integrated sensor

for continuous flow electrochemiluminescent measurements of codeine with different ruthenium complexes. A*n*alytica Chimica Acta, 1999. 392**(2-**3): p. 95-103.
86. T. Akiyama, U. Staufer, N.F.d. Rooij, L. Howald and L. Scandella, Lithographically defined polymer tips for quartz tuning fork based scanning force microscopes. M*i*croelectronic Engineering, 2001. 57-**58: p**. 769-773.
87. R.K. Vestergaard and S. Bouwstra, Electroplated compliant metal microactuators with small feature sizes using a removable SU-8 mould. M*i*crosystem Technologies, 2000. 6: **p**. 214-217.
88. J.A.v. Kan, I. Rajta, K. Ansar, A.A. Bettiol and F. Watt, Nickel and copper electroplating of proton beam micromachined SU-8 resist. M*i*crosystem Technologies, 2002. 8(6): p. 383-386.
89. J. Voldman, M. Toner, M.L. Gray and M.A. Schmidt, Design and analysis of extruded quadrupolar dielectrophoretic traps. J*o*urnal of Electrostatics, 2003. 57(**1**): p. 69-90.
90. T. Mappes, S. Achenbach, A. Last, J. Mohr and R. Truckenmuller, Evaluation of optical qualities of a LIGA-spectrometer in SU-8. M*i*crosystem Technologies, 2004. 10: **p**. 560-563.
91. J. Liu, B. Cai, J. Zhu, D. Chen, Y. Li, J. Zhang, G. Ding, X. Zhao and C. Yang, A novel device of passive and fixed alignment of optical fiber. M*i*crosystem Technologies, 2004. 10: **p**. 269-271.
92. N.-T. Nguyen and T.-Q. Truong, A fully polymeric micropump with piezoelectric actuator. S*e*nsors and Actuators B: Chemical, 2004. 97(**1**): p. 137-143.
93. C. Luo, A. Govindaraju, J. Garra, T. Schneider, R. White, J. Currie and M. Paranjape, Releasing SU-8 structures using polystyrene as a sacrificial material. S*e*nsors and Actuators A: Physical, 2004. 114**(1)**: p. 123-128.
94. M. Agarwal, R.A. Gunasekaran, P. Coane and K. Varahramyan, Scum-free patterning of SU-8 resist for electroforming applications. J*o*urnal of Micromechanics and Microengineering, 2005. 15(**1**): p. 130-135.
95. P. Jin and K. Jiang, Ultrathick SU-8 fabrication for microreciprocating engines. J*o*urnal of Microlithography, Microfabrication, and Microsystems, 2004. 3(4**)**: p. 569-573.
96. C.-C. Yang, T.-C. Peng, Y.-H. Huang, M.-C. Wu, C.-L. Ho and W.-J. Ho, A Simple and Low-Cost Fabrication of Polymeric Vertical Microlens Using Dip Method. I*E*EE Photonics Technology Letters, 2005. 17(**3**): p. 603-605.
97. D.S. Kim, K.-C. Lee, T.H. Kwon and S.S. Lee, Micro-channel filling flow considering surface tension effect. J*o*urnal of Micromechanics and Microengineering, 2002. 12(**3**): p. 236-246.
98. G.M. Kim, B. Kim, M. Liebau, J. Huskens, D.N. Reinhoudt and J. Brugger, Surface modification with self-assembled monolayers for nanoscale replication of photoplastic MEMS. J*o*urnal of Microelectromechanical Systems, 2002. 11(**3**): p. 175-181.
99. J.A.v. Kan, J.L. Sanchez, B. Xu, T. Osipowicz and F. Watt, Micromachining using focused high energy ion beams: Deep Ion Beam Lithography. N*u*clear Instruments and Methods in Physics Research Section B: Beam Interactions with Materials and Atoms, 1999. 148**: p**. 1085-1089.
100. R. Yang, D.L. Feeback and W. Wang, Microfabrication and test of a three-dimensional polymer hydro-focusing unit for flow cytometry applications. S*e*nsors and Actuators A: Physical, 2005. 118**(2)**: p. 259-267.
101. M. Han, W. Lee, S.-K. Lee and S.S. Lee, 3D microfabrication with inclined/rotated UV lithography. S*e*nsors and Actuators A, 2004. 111**: p**. 14-20.
102. O.V. Makarova, D.C. Mancini, N. Moldovan, R. Divan, C.-M. Tang, D.G. Ryding and R.H. Lee, Microfabrication of freestanding metal structures using graphite substrate. S*e*nsors and Actuators A: Physical, 2003. 103**(1-**2): p. 182-186.
103. S. Lee, D. Kim, M.D. Bryant and F.F. Ling, A micro corona motor. S*e*nsors and Actuators A: Physical, 2005. 118**(2)**: p. 226-232.
104. V. Kudryashov, X.-C. Yuan, W.-C. Cheong and K. Radhakrishnan, Grey scale structures formation in SU-8 with e-beam and UV. M*i*croelectronic Engineering, 2003. 67-**68: p**. 306-311.
105. J.C. Galas, B. Belier, A. Aassime, J. Palomo, D. Bouville and J. Aubert, Fabrication of

three-dimensional microstructures using standard ultraviolet and electron-beam lithography. Journal of Vacuum Bcience & Technology B, 2004. 22(**3**): p. 1160-1162.
106. B. Lochel, A. Maciossek, H.-J. Quenzeer and B. Wagner, UV depth lithography and galvanoforming for micromachining. i*n* proc. 2nd Int. Symo. Electrochem. Microfabrication, 186th Meet. Electrochem. Soc., Miami Beach, FL. Oct. 1994: p. 100-111.
107. J. Hormes, J. Gottert, K. Lian, Y. Desta and L. Jian, Materials for LiGA and LiGA-based microsystems. N*u*clear Instruments and Methods in Physics Research Section B: Beam Interactions with Materials and Atoms, 2003. 199**: p**. 332-341.
108. C.G.K. Malek, SU8 resist for low-cost X-ray patterning of high-resolution, high-aspect-ratio MEMS. M*i*croelectronics Journal, 2002. 33(**1-**2): p. 101-105.
109. J.D. Williams and W. Wang, Using megasonic development of SU-8 to yield ultra-high aspect ratio microstructures with UV lithography. M*i*crosystem Technologies, 2004. 10: **p**. 694-698.
110. N. LaBianca and J.D. Gelorme, High aspect ratio resist for thick film applications. P*r*oc SPIE, 1995. 243**8: p**. 846-849.
111. N. LaBianca, J. Gelorme, K. Lee, E. Sullivan and J. Shaw, high aspect ratio optical resist chemistry for MEMS applications. 4*t*h Int. Symp. on Magnetic Materials, Processes, and Devices, The Electrochem. Soc., 1995: p. 386-396.
112. K.Y. Lee, N. LaBianca, S.A. Rishton, S. Zolgharnain, J.D. Gelorme, J. Shaw and T.H.-P. Chang, Micromachining applications of a high resolution ultrathick photoresist. J.Vac. Sci. Technol. B, 1995. 13(**6**): p. 3012-3016.
113. A.G. Peele, B.Y. Shew, K.D. Vora and H.C. Li, Overcoming SU-8 stiction in high aspect ratio structures. M*i*crosystem Technologies, 2005. 11: **p**. 221-224.
114. H. Lorenz, L. M and R. P, Mechanical characterization of a new high-aspect-ratio near UV-photoresist. M*i*croelectron. Eng., 1998. 41/**42: p**. 371-374.
115. F.E.H. Tay, J.A. vanKan, F. Watt and W.O. Choong, A novel micro-machining method for the fabrication of thick-film SU-8 embedded micro-channels. J*o*urnal of Micromechanics and Microengineering, 2001. 11: **p**. 27-32.
116. L. Dellmann, S. Roth, C. Beuret, G. Racine, H. Lorenz, M. Despont, P. Renaud, P. Vettiger and N.d. Rooij, Fabrication process of high aspect ratio elastic structures for piezoelectric motor applications. T*r*ansducers 1997, Chicago: p. 641-644.
117. E.H. Conradie and D.F. Moore, SU-8 thick photoresist processing as a functional material for MEMS applications. J*o*urnal of Micromechanics and Microengineering, 2002. 12: **p**. 368-374.
118. R. Feng and R.J. Farris, The characterization of thermal and elastic constant for an epoxy photoresist SU8 coating. J*O*URNAL OF MATERIALS SCIENCE, 2002. 37: **p**. 4793-4799.
119. S.H. Cho, S.H. Kim, N.-E. Lee, H.M. Kim and Y.W. Nam, Micro-scale metallization on flexible polyimide substrate by Cu electroplating using SU-8 photoresist mask. T*h*in Solid Films, 2005. 475**(1-**2): p. 68-71.
120. web site: http://mems.mirc.gatech.edu/SU8/Data%20Sheet%202-25.pdf.
121. web site: http://mems.mirc.gatech.edu/SU8/Data%20Sheet%2050-100.pdf.
122. Material safety data sheet for SU-8, MicroChem Corp.
123. J.M. Shaw, J.D. Gelorme, N.C. LaBianca, W.E. Conley and S.J. Holmes, Negative photoresists for optical lithography. I*B*M Journal of Research and Development, 1997. 41: **p**. 81-94.
124. L. Dellmann, S. Roth, C. Beuret, L. Paratte, G.-A. Racine, H. Lorenz, M. Despont, P. Renaud, P. Vettiger and N.F. deRooij, Two steps micromoulding and photopolymer high-aspect ratio structuring for applications in piezoelectric motor components. M*i*crosystem Technologies. 4(3**)**: p. 147-150.
125. M. Despont, H. Lorenz, N. Fahrni, J. Brugger, P. Renaud and P. Vettiger, High-aspect-ratio, ultrathick, negative-tone near-UV photoresist for MEMS applications. M*i*cro Electro Mechanical Systems, 1997. MEMS '97, Proceedings, IEEE., Tenth Annual International Workshop on, 1997: p. 518 -522.
126. T. Ouchi, A. Imada, T. Sato and H. Sakata, Direct coupling of VCSELs to plastic

optical fibers using guide holes patterned in a thick photoresist. I*E*EE Photonics Technology Letters, 2002. 14(**3**): p. 263-265.
127. A.L. Bogdanov and S.S. Peredkov, Use of SU8 photoresist for very high aspect ratio x-ray lithography. M*i*croelectronic Engineering, 2000. 53: **p**. 493-496.
128. C. Cremers, F. Bouamrane, L. Singleton and R. Schenk, SU-8 as resist material for deep x-ray lithography. M*i*crosystem Technologies, 2001. 7: **p**. 11-16.
129. A.A. Bettiol, I. Rajta, E.J. Teo and J.A.v. Kan, Proton beam micromachining: electron emission from SU-8 resist during ion beam irradiation. N*u*clear Instruments and Methods in Physics Research Section B: Beam Interactions with Materials and Atoms, 2002. 190**: p**. 154-159.
130. J.A.v. Kan, A.A. Bettiol, B.S. Wee, T.C. Sum, S.M. Tang and F. Watt, Proton beam micromachining : a new tool for precision three-dimensional microstructures. S*e*nsors and Actuators A: Physical, 2001. 92(**1-**3): p. 370-374.
131. Z.-G. Ling, K. Lian and J. Zhang, Characterization and application of pag diluted SU-8. I*n*ternational Journal of Computational Engineering Science, 2003. 4(3**)**: p. 529-532.
132. Y. Yagci and W. Schnabel, On the mechanism of photoinitiated cationic polymerization in the presence of polyols. D*i*e Angewandte Makromolekulare Chemie, 1999. 270**: p**. 38-41.
133. C. Decker, T.N.T. Viet and H.P. Thi, Photoinitiated cationic polymerization of epoxides. P*o*lymer International, 2001. 50: **p**. 986-997.
134. J.V. Crivello and R. Naraya, Novel Epoxynorbornane Monomers. 1. Synthesis and Characterization. M*A*CROMOLECULES, 1996. 29: **p**. 433-438.
135. V.K. Varadan, K.J. Vinoy and K.A. Jose, RF MEMS and Their Applications: Chapter 2 MEMS materials and fabrication
techniques. 2003: John Wiley & Sons.
136. D.J. Russell, Controlling photoimaging of epoxies by blending to a specific molecular weight. J*o*urnal of Applied Polymer Science, 1990. 41(**7-**8): p. 1753-1764.
137. R. Feng and R.J. Farris, Influence of processing conditions on the thermal and mechanical properties of SU8 negative photoresist coatings. J*o*urnal of Micromechanics and Microengineering, 2003. 13: **p**. 80-88.
138. C.-H. Lin, G.-B. Lee, S.-H. Chen and G.-L. Chang, Micro capillary electrophoresis chips integrated with buried SU-8/SOG optical waveguides for bio-analytical applications. S*e*nsors and Actuators A: Physical, 2003. 107**(2)**: p. 125-131.
139. J.V. Crivello, Photoinitiated Cationic Polymerization. A*n*nual Review of Materials Science, 1983. 13: **p**. 173-190.
140. web site http://www.somisys.ch/processing.htm.
1*4*1. J. Zhang, K.L. Tan, G.D. Hong, L.J. Yang and H.Q. Gong, Polymerization optimiation of SU-8 photoresist and its applications in microfluidic systems and MEMS. J*o*urnal of Micromechanics and Microengineering, 2001. 11: **p**. 20-26.
142. Z.-g. Ling, K. Lian and L. Jian, Improved patterning quality of SU-8 microstructures by optimizing the exposure parameters",. i*n* Proc. SPIE vol. 3999, SPIE, 2000: p. 1019-1027.
143. B. Eyre, J. Blosiu and D. Wiberg. Taguchi optimization for the processing of EPON SU-8 resist. in IEE*E MEMS'98. 1*998.
144. M. Brunet, T. O'Donnell, J. O'Brien, P. McCloskey and S.C.o. Mathuna, Thick photoresist development for the fabrication of high aspect ratio magnetic coils. J*o*urnal of Micromechanics and Microengineering, 2002. 12: **p**. 444-449.
145. C.-H. Ho and W. Hsu, Experimental investigation of an embedded root method for stripping SU-8 photoresist in the UV-LIGA process. J*o*urnal of Micromechanics and Microengineering, 2004. 14: **p**. 356-364.
146. P.I. Hagouel, I. Karafyllidis and A.R. Neureuther, Dependence of developed negative resist profiles on exposure energy dose: experiment, modeling, and simulation. M*i*croelectronic Engineering, 1998. 413**42: p**. 351-354.
147. R.K. Kupka, F. Bouamrane, C. Cremers and S. Megtert, Microfabrication: LIGA-X and applications. A*p*plied Surface Science, 2000. 164**: p**. 97-110.
148. F.G. Tseng, Y.J. Chuang and W.K. Lin, Reduction of diffraction effect of UV exposure on Su-8 negative thick PR by air gap elimination. P*r*oc. HARMST 4th Workshop on High

Aspect Ratio Micro-structure Technology (Baden-Baden, Germany) 2001: p. 73-74.
149. H. Lorenz, M. Despont, N. Fahrni, J. Brugger, P. Vettiger and P. Renaud, High-aspect-ratio, ultrathick, negative-tone near-UV photoresist and its applications for MEMS. S*e*nsors and Actuators A: Physical, 1998. 64(**1**): p. 33-39.
150. J. O'Brien, P.J. Hughes, M. Brunet, B. O'Neill, J. Alderman, B. Lane, A. O'Riodan and C. O'Driscoll, Advanced photoresist technologies for microsystems. J*o*urnal of Micromechanics and Microengineering, 2001. 11(**4**): p. 353-358.
151. P.M. Dentinger, K.L. Krafcik, K.L. Simison, R.P. Janek and J. Hachman, High aspect ratio patterning with a proximity ultraviolet source. M*i*croelectronic Engineering, 2002. 61-**62: p**. 1001-1007.
152. H.-K. Chang and Y.-K. Kim, UV-LIGA process for high aspect ratio structure using stress barrier and C-shaped etch hole. S*e*nsors and Actuators A: Physical, 2000. 84(**3**): p. 342-350.
153. C.G.K. Malek and S.S. Das, Adhesion promotion between poly(methylmethacrylate) and metallic surfaces for LiGA evaluated by shear stress measurements. J*o*urnal of Vacuum Science & Technology B, 1998. 16(**6**): p. 3543-3546.
154. C.H. Lin, H.L. Chen and L.A. Wang, A study on adhesion and footing issues of HMDSO films as bottom antireflective coating for deep UV lithographies. M*i*croelectronic Engineering, 2001. 57-**58: p**. 555-561.
155. L. Guerin, M. Bossel, M. Demierre, S. Calmes and P. Renaud, Simple and low cost fabrication of embedded microchannels by using a new thick-film photoplastic. i*n* Proc. Transducers 1997, Chicago, (1997): p. 1419-1422.
156. B.-Y. Shew, H.-C. Li, C.-L. Pan and C.-H. Ko, X-ray micromachining SU-8 resist for a terahertz photonic filter. J*o*urnal of Physics D: applied physics, 2005. 38: **p**. 1097-1103.
157. T. Moore, R. Adhikari and P. Gunatillake, Chemosynthesis of bioresorbable poly(g-butyrolactone) by ring-opening polymerisation: a review. B*i*omaterials, 2005. 26: **p**. 3771-3792.
158. L. Ubaghs, M. Waringo, H. Keul and H. Hocker, Copolymers and Terpolymers of Tetramethylene Urea, gamma-Butyrolactone, and Ethylene Carbonate or 1,2-Propylene Carbonate. M*A*CROMOLECULES, 2004. 37: **p**. 6755-6762.
159. A. Duda, S. Penczek, P. Dubois, D. Mecerreyes and R. Jerome, Oligomerization and copolymerization of y-butyrolactone - a monomer known as unable to homopolymerize, 1 Copolymerization with E-caprolactone. M*a*cromolecular Chemistry and Physics, 1996. 197**(4)**: p. 1273 -1283.
160. H. Fukuzaki and Y. Aiba, Direct copolymerization of L-lactic acid with y-butyrolactone in the absence of catalysts. M*a*kromol. Chem., 1989. 190**: p**. 1553-1559.
161. X. Ramis, J.M. Salla, C. Mas, A. Mantecon and A. Serra, Kinetic study by FTIR, TMA, and DSC of the curing of a mixture of DGEBA resin and gamma-butyrolactone catalyzed by ytterbium triflate. J*o*urnal of Applied Polymer Science, 2004. 92(**1**): p. 381 - 393.
162. M. Fedtke, J. Haufe, E. Kahlert and G. Muller, Cationic copolymerization of phenyl glycidyl ether with lactones. Characterization of the reaction mixture with chromatographic methods. D*i*e Angewandte Makromolekulare Chemie, 1998. 255**: p**. 53-59.
163. P. Chabanne, L. Tighzert and J.-P. Pascault, Monoepoxy Polymerization Initiated by BF3-Amine Complexes in Bulk. III. Influence of y-Gutyrolactone on Polymer Formation. J*o*urnal of Applied Polymer Science, 1994. 53(**6**): p. 787-806.
164. L. Matejka, K. Dusek, P. Chabanne and J.P. Pascault, Cationic polymerization of diglycidyl ether of bisphenol A. III. Comparison of the theory with experiment. J*o*urnal of Polymer Science Part A: Polymer Chemistry, 1997. 35: **p**. 665-672.
165. C. Mas, X. Ramis, J.M. Salla, A. Mantecon and A. Serra, Copolymerization of Diglycidyl Ether of Bisphenol A with g-Bυtyrolactone Catalyzed by Ytterbium Triflate: Shrinkage during Curing. J*o*urnal of Polymer Science: Part A: Polymer Chemistry, 2003. 41: **p**. 2794-2808.
166. C. Mas, A. Mantecon, A. Serra, X. Ramis and J.M. Salla, Influence of Lanthanide Triflate Compounds on Formation of Networks from DGEBA and g-Bυtyrolactone. J*o*urnal of Polymer Science: Part A: Polymer Chemistry, 2004. 42: **p**. 3782?791.
167. T. Takata, A. Tadokoro and T. Endo, Anionic ring-opening alternating

copolymerization of a bicyclobis(-butyrolactone) with epoxide. MACROMOLECULES, 1992. 25(10): p. 2782-2783.
168. Matejka, P. Chabanne, L. Tighzert and J.P. Pascault, Cationic Polymerization of Diglycidyl Ether of Bisphenol A. Journal of Polymer Science Part A: Polymer Chemistry, 1994. 32(8): p. 1447-1458.
169. P. Chabanne, L. Tighzert, J.-P. Pascault and B. Bonnetot, Epoxy polymerization initiated by BF3-amine complexes. I. Synthesis and characterization of BF3-amine complexes and BF3-amine complexes dissolved in -butyrolactone. Journal of Applied Polymer Science, 1993. 49(4): p. 685-699.
170. A. Hofman, R. Szymaski, S. Somkowski and S. Penczek, Structure of active species in the cationic polymerization of -propiolactone and -caprolactone. Die Makromolekulare Chemie, 1984. 185(4): p. 655-667.
171. L. Matejka, K. Dusek, P. Chabanne and J.P. Pascault, Cationic polymerization of diglycidyl ether of Bisphenol A. II. theory. Journal of Polymer Science Part A: Polymer Chemistry, 1997. 35(4): p. 651 - 663.
172. F. Fraga, S. Burgo and E.R. Nunez, Curing Kinetic of the Epoxy System BADGE n=0,1,2 DCH by Fourier Transform Infrared Spectroscopy (FTIR). Journal of Applied Polymer Science, 2001. 82(13): p. 3366-3372.
173. N. Eidelman, D. Raghavan, A.M. Forster, E.J. Amis and A. Karim, Combinatorial Approach to Characterizing Epoxy Curing. Macromolecular Rapid Communications, 2004. 25(1): p. 259-263.
174. M.-L. Lin, K.-H. Chang, F.-C. Chang, M.-S. Li and C.-C. Ma, The Epoxy-Polycarbonate Blends Cured with Aliphatic Amine--I. Mechanism and Kinetics. Journal of Polymer Science: Part B: Polymer Physics, 1997. 35: **p.** 2169?181.
175. Y.-S. Li, M.-S. Li and F.-C. Chang, Kinetics and Curing Mechanism of Epoxy and Boron Trifluoride Monoethyl Amine Complex System. Journal of Polymer Science: Part A: Polymer Chemistry, 1999. 37: p**.** 3614-3624.
176. A. Gupta, R. Singhal and A.K. Nagpal, Reactive Blends of Epoxy Resin (DGEBA) Crosslinked by Anionically Polymerized Polycaprolactam: Process of Epoxy Cure and Kinetics of Decomposition. Journal of Applied Polymer Science, 2004. 92: p**.** 687-697.
177. B.-L. Denq, W.-Y. Chiu, K.-F. Lin and M.-R.S. Fuh, Thermal Degradation Behavior of Epoxy Resin Blended with Propyl Ester Phosphazene. Journal of Applied Polymer Science, 2001. 81: p**.** 1161-1174.
178. K.-D. Ahn, D.K. Han, S.-H. Lee and C.-W. Lee, New Aromatic tert-Amines for Application as Photoinitiator Components in Photocurable Dental Materials. Macromolecular Chemistry and Physics, 2003. 204: **p.** 1628-1635.
179. J. Choi, J. Harcup, A.F. Yee, Q. Zhu and R.M. Laine, Organic/Inorganic Hybrid Composites from Cubic Silsesquioxanes. Journal of American Chemical Society, 2001. 123: **p.** 11420-11430.
180. G. Rajagopalan, K.M. Immordino, J.W.G. Jr. and S.H. McKnight, Diffusion and reaction of epoxy and amine in polysulfone studied using Fourier transform infrared spectroscopy: xperimental results. Polymer, 2000. 41: p**.** 2591-2602.
181. M.-S. Lin and C.-C. Chiu, Protection of epoxy resin against thermo-oxidation via co-curing epoxy/resole (I). Polymer Degradation and Stability, 2000. 69: p**.** 251-253.
182. R.J. Varley, J.H. Hodgkin and G.P. Simon, Toughening of Trifunctional Epoxy System. V. Structure 朕 roperty Relationships of Neat Resin. Journal of Applied Polymer Science, 2000. 77: p. **2**37-248.
183. A.M. Zaper and J.L. Koenig, Solid State Carbon-13 NMR Studies of Vulcanized Elastomers. II Sulfur Vulcanization of Natural Rubber. Rubber Chemistry and Technology, 1987. 60: p. **2**52.
184. C.-C. Wang and C.-Y. Chen, Detection of Lead Ion Binding on Bifunctional Chelating/Ion-Exchange Resins by Cross-Polarization/Magic-Angle Spinning Solid-State Nuclear Magnetic Resonance. Journal of Applied Polymer Science, 2002. 85: p. **9**19-928.
185. D.D. Granger, Solid State NMR of Polymers, ed. L. Mathias. 1991, New York: Plenum Press. 179-200.

186. E.M. Woo, Y.-P. Huang, L.L. Chang, H.-M. Kao, R.-R. Wu and C.-C. Su, Model Compound Study on Network-Forming Reactions Between Poly(4-Vinyl Phenol) and an Epoxy. Jour*n*al of Macromolecular Science Part B-Physics, 2004. B43(2)**: p**. 365-383.
187. M.I.B. Tavares, J.R.M. D'Almeida and S.N. Monteiro, 13C Solid-State NMR Analysis of the DGEBA/TETA Epoxy System. Jour*n*al of Applied Polymer Science, 2000. 78: p. **2**358-2362.
188. N. Egger, K. Schmidtrohr, B. Blumich, W.D. Domke and B. Stapp, Solid-state NMR investigation of Cationic Polymerized Epoxy-resins. Jour*n*al of Applied Polymer Science, 1995. 44(2): **p**. 289-295.
189. S. Casares, M. Sadqi, O. Lo′ pez-Mayorga, F. Conejero-Lara and N.A.J.v. Nulandy, Detection and Characterization of Partially Unfolded Oligomers of the SH3 Domain of a-Spectrin. Biophy*s*ical Journal, 2004. 86: p. **24**03-2413.
190. M.M. Spence, S.M. Rubin, I.E. Dimitrov, E.J. Ruiz, D.E. Wemmer, A. Pines, S.Q. Yaoi, F. Tiani and P.G. Schultzi, Functionalized xenon as a biosensor. Proce*e*dings of the National Academy of Sciences of the United States of America, 2001. 98(19): **p**. 10654-10657.
191. N.P. Cheremisinoff, Polymer characterization: Laboratory Techniques and Analysis. 1996, Westwood, New Jersey: Noyes Publications.
192. S. Sundarrajan, M. Surianarayanan, K.S.V. Srinivasan and K. Kishore, Thermal Degradation Processes in Polysulfide Copolymers Investigated by Direct Pyrolysis Mass Spectrometry and Flash Pyrolysis-Gas Chromatography/Mass Spectrometry. MACRO*M*OLECULES, 2002. 35: p. **33**31-3337.
193. M. Jun, Y. Shao, C.-T. Ho, U. Koetter and S. Lech, Structural Identification of Nonvolatile Dimerization Products of Glucosamine by Gas Chromatography-Mass Spectrometry, Liquid Chromatography-Mass Spectrometry, and Nuclear Magnetic Resonance Analysis. Journ*a*l of Agricultural and Food Chemistry, 2003. 51: p. **63**40-6346.
194. Z. Kuklenyik, J. Ekong, C.D. Cutchins, L.L. Needham and A.M. Calafa, Simultaneous Measurement of Urinary Bisphenol A and Alkylphenols by Automated Solid-Phase Extractive Derivatization Gas Chromatography/Mass Spectrometryt. Analy*t*ical Chemistry, 2003. 75(24): **p**. 6820-6825.
195. C.-H. Ho, K.-P. Chin, C.-R. Yang, H.-M. Wu and S.-L. Chen, Ultrathick SU-8 mold formation and removal, and its application to the fabrication of LIGA-like micromotors with embedded roots. Senso*r*s and Actuators A, 2002. 102: p. **13**0-138.
196. P.M. Dentinger, W.M. Clift and S.H. Goods, Removal of SU-8 photoresist for thick film applications. Micro*e*lectronic Engineering, 2002. 61-62: **p. 99**3-1000.
197. M. Chatzichristidi, I. Raptis, C.D. Diakoumakos, N. Glezos, P. Argitis and M. Sanopoulou, Strippable aqueous base developable negative photoresist for high aspect ratio micromachining. Micro*e*lectronic Engineering, 2002. 61-62: **p. 72**9-735.
198. T.W. Greene and P.G.M. Wuts, Protective Groups in Organic Synthesis. 3rd Edition ed. 1999: Wiley, London.
199. W.M. Moreau, Semiconductor Lithography. 1988, New York: lenum Press.
200. G. McGall, Light-directed synthesis of high-density oligonucleotide arrays using semiconductor photoresists. Proc. Natl. Acad. Sci. USA, 1996. 93: p. **13**555-13560.
201. J.F. Cooper, G.B. Balazs and P.H.e. al, US patent 6096283. 2000.
202. G. Hong, A.S. Holmes and M.E. Heaton, SU8 resist plasma etching and its optimisation. Micro*s*ystem Technologies, 2004. 10: p. **35**7-359.
203. J.A. McGeough, M.C. Leu, K.P. Rajurkar, A.K.M.D. Silva and Q. Liu., Electroforming Process and Application to Micro/Macro Manufacturing. Annal*s* of the CIRP, 2001. 50(2): **p.** 499-514.
204. N.S. Qu, K.C. Chan and D. Zhu, Surface roughening in pulse current and pulse reverse current electroforming of nickel. Surfa*c*e and Coatings Technology, 1997. 91(3): **p.** 220-224.
205. Z.-J. Wei, Y.-Y. Wang, C.-C. Wan and C.-H. Huang, Study of wetters in nickel electroforming of 3D microstructures. Mater*i*als Chemistry and Physics, 2000. 63: p. **23**5-239.
206. S.-Y. Chiu, J.-M. Shieh, S.-C. Chang, K.-C. Lin, B.-T. Dai, C.-F. Chen and M.-S. Feng, Characterization of additive systems for damascene Cu electroplating by the superfilling profile monitor. Journ*a*l of Vacuum Bcience & Technology B, 2000. 18(6): **p.** 2835-2841.

207. J.C. Hu, T.C. Chang, C.W. Wu and C.J. Chen, Effects of a new combination of additives in electroplating solution on the properties of Cu films in ULSI applications. Jour*a*l of Vacuum Science and Technology A, 2000. 18(4): **p.** 1207-1210.
208. J.M. Shieh, S.C. Chang, B.T. Dai and M.S. Feng, Investigation of superfilling and electrical characteristics in low-impurity-incorporated Cu metallization. Japan*e*se Journal of Applied physics Part 1, 2002. 41(8): **p.** 5104-5107.
209. F. Hu and K.C. Chan, Electrocodeposition behavior of Ni-SiC composite under different shaped wave. Appli*e*d Surface Science, 2004. 233(1-4**):** p. 163-171.
210. K.P. Wong, K.C. Chan and T.M. Yue, Modeling of electrocrystallization for pulse current electroforming of nickel. Appli*e*d Surface Science, 2001. 178(1-4**):** p. 178-189.
211. K.P. Wong, K.C. Chan and T.M. Yue, Influence of spike current in different shaped waveforms on the hardness and grain size of nickel electroforms. Journ*a*l of Materials Processing Technology, 2001. 117(1-2**):** p. 97-104.
212. K.P. Wong, K.C. Chan and T.M. Yue, A study of surface finishing in pulse current electroforming of nickel by utilizing different shaped waveforms. Surfa*c*e and Coatings Technology, 1999. 115(2-3**):** p. 132-139.
213. H. Yang and S.-W. Kang, Improvement of Thickness Uniformity in Nickel Electroforming for the LIGA Process. Inter*n*ational Journal of Machine Tools and Manufacture, 2000. 40: p. **10**65-1072.
214. S.H. Oh, K.-C. Lee, J. Chun, M. Kim and S.S. Lee, Micro heat flux sensor using copper electroplating in SU-8 microstructures. Journ*a*l of Micromechanics and Microengineering, 2001. 11: p. **22**1-225.
215. C. Massin, G. Boero, F. Vincent, J. Abenhaim, P.-A. Besse and R.S. Popovic, High-Q factor RF planar microcoils for micro-scale NMR spectroscopy. Sensor*s* and Actuators A: Physical, 2002. 97-98: **p. 28**0-288.
216. T. Kohlmeier and H.H. Gatzen, Challenges in using photosensitive embedding material to planarize multi-layer coils for actuator systems. Journ*a*l of Magnetism and Magnetic Materials, 2002. 242?45: **p. 114**9?152.
217. O.V. Makarova, C.-M. Tang, D.C. Mancini, N. Moldovan, R. Divan, D.G. Ryding and R.H. Lee, Development of a freestanding copper antiscatter grid using deep X-ray lithography. Microsy*s*tem Technologies, 2003. 9(6-7): p**.** 395-398.
218. I.-h. Song and P.K. Ajmera, Use of a photoresist sacrificial layer with SU-8 electroplating mould in MEMS fabrication. Journal of Micromechanics and Microengineering, 2003. 13: p. 81**6-**821.
219. N.J. Shirtcliffe, S. Aqil, C. Evans, G. McHale, M.I. Newton, C.C. Perry and P. Roach, The use of high aspect ratio photoresist (SU-8) for super-hydrophobic pattern prototyping. Journal of Micromechanics and Microengineering, 2004. 14: p. 13**84**-1389.
220. B. He, N.A. Patankar and J. Lee, Multiple Equilibrium Droplet Shapes and Design Criterion for Rough Hydrophobic Surfaces. Langmui*r*, 2003. 19(12): p**.** 4999-5003.
221. A. Kawai and H. Nagata, Wetting Behavior of Liquid on Geometrical Rough Surface Formed by Photolithography. 1994. 3*3*(Japan**se** Journal of Applied Physics): p. L1283-L1285.
222. Z. Yoshimitsu, A. Nakajima, T. Watanabe and K. Hashimoto, Effects of Surface Structure on the Hydrophobicity and Sliding Behavior of Water Droplets. Langmui*r*, 2002. 18: p. 58**18**-5822.
223. D. Oner and T.J. McCarthy, Ultrahydrophobic Surfaces. Effects of Topography Length Scales on Wettability. Langmui*r*, 2000. 16: p. 77**77**-7782.
224. M. Nordstrom, R. Marie, M. Calleja and A. Boisen, Rendering SU-8 hydrophilic to facilitate use in micro channel fabrication. Journal of Micromechanics and Microengineering, 2004. 14: p. 16**14**-1617.
225. M. Noeske, J. Degenhardt, S. Strudthoff and U. Lommatzsch, Plasma jet treatment of five polymers at atmospheric pressure: surface modifications and the relevance for adhesion. Interna*t*ional Journal of Adhesion & Adhesives, 2004. 124: p. 1**71-**177.
226. K.S. Kim, K.H. Lee, K. Cho and C.E. Park, Surface modification of polysulfone ultrafiltration membrane by oxygen plasma treatment. Journal of Membrane Science, 2002. 199: p. 1**35-**145.

227. L. Tuek, M. Nitschke, C. Werner, K. Stana-Kleinschek and V. Ribitsch, Surface characterisation of NH3 plasma treated polyamide 6 foils. Colloid*s* and Surfaces A: Physicochemical and Engineering Aspects, 2001. 195: p. 8**1 -** 95.
228. W. Lin and Y.-L. Hsieh, Argon Glow Discharge and Vapor-Phase Grafting of Vinyl Monomers on Wettability of Polyethylene. Journal of Polymer Science Part B: Polymer Physics, 1997. 35(7): p. **1**145-1159.
229. F.-G. Tseng, K.-H. Lin, H.-T. Hsu and C.-C. Chieng, A surface-tension-driven fluidic network for precise enzyme batch-dispensing and glucose detection. Sensors and Actuators A, 2004. 111(1): p**. 1**07-117.
230. Y.W. Chen-Yang, C.W. Chen, S.C. Tseng, J. Huang and Y.Z. Wu, Surface modification of bi-axially expanded poly(tetrafluoroethylene) by plasma polymerization of ethylene. Surface and Coatings Technology, 2004. 176: p. 1**48-**156.
231. S. Bhowmik, T.K. Chaki, S. Ray, F. Hoffman and L. Dorn, Effect of Surface Modification of High-Density Polyethylene by Direct Current and Radio Frequency Glow Discharge on Wetting and Adhesion Characteristics. Metallu*r*gical and Materials Transactions A, 2004. 35A: p. 8**65-**877.
232. J. Zhang, K.L. Tan and H.Q. Gong, Characterization of the polymerization of SU-8 photoresist and its applications in micro-electro-mechanical systems (MEMS). Polymer Testing, 2001. 20: p. 69**3-**701.
233. J. Liu, B. Cai, J. Zhu, G. Ding, X. Zhao, C. Yang and D. Chen, Process research of high aspect ratio microstructure using SU-8 resist. Microsy*s*tem Technologies, 2004. 10(4): p. **2**65-268.
234. A. Kaye, R.F.T. Stepto, W.J. Work, J.V. Aleman and A.Y. Malkin, Definition of the terms relating to the non-ultimate mechanical properties of polymers. Pure an*d* Applied Chemistry, 1998. 70(3): p**. 7**01-754.
235. R.D. Guenther, Modern optics. 1990, U.S.A.: John Wiley & Sons.
236. M.V. Klein, Optics. 1970: John Wiley & Sons.
237. E.D. Palik, Handbook of optical constants of solids. 1985, Orlando: Academic Press.
238. web site: http://www-ccd.lbl.gov/ccd_data.html.
239. K.*H*. Gil, S.S. Lee and Y. Youm, Equations of exposure time and X-ray mask absorber thickness in the LIGA process. Microsy*s*tem Technologies, 2001. 7: p. 1-5**.**
240. Handbook of microlithography, micromachining, and microfabrication, Volume 1: Microlithography: SPIE Optical Engineering Press.
241. G. Feiertag, W. Ehrfeld, H. Lehr, A. Schmidt and M. Schmidt, Accuracy of structure transfer in deep X-ray lithography. Microel*e*ctronic Engineering, 1997. 35: p. 55**7-**560.
242. W. Schlesing, M. Buhk and M. Osterhold, Dynamic mechanical analysis in coatings industry. Progres*s* in Organic Coatings, 2004. 49: p. 19**7-**208.
243. V.M. Litvinov and A.A. Dias, Analysis of network structures of UV-cured acrylates by 1H NMR relaxation, 13C NMR spectroscopy, and dynamic mechanical experiments. MACROMO*L*ECULES, 2001. 34: p. 40**51**-4060.
244. MicroChem data sheet, website: http://www.cise.columbia.edu/clean/process/SU8_2035-2100.pdf.
245. J. Hossenlopp, L. Jiang, R. Cernosek and F. Josse, Characterization of epoxy resin (SU-8) film using thickness-shear mode (TSM) resonator under various conditions. Journal of Polymer Science Part B: Polymer Physics, 2004. 42(12): p**.** 2373-2384.
246. S.K. Rath, F.Y.C. Boey and M.J.M. Abadie, Cationic electron-beam curing of a high-functionality epoxy: effect of post-curing on glass transition and conversion. Polymer International, 2004. 53(7): p. **8**57-862.
247. J. Zhang, M.B. Chan-Park and S.R. Conner, Effect of exposure dose on the replication fidelity and profile of very high aspect ratio microchannels in SU-8. Lab On *A* Chip, 2004. 4(6): p. **6**46-653.
248. C. Liu, J. Yu, X. Sun, J. Zhang and J. He, Thermal degradation studies of cyclic olefin copolymers. Polymer Degradation and Stability, 2003. 81: p. 19**7-**205.
249. F. Yakuphanoglu and M. Sekerci, The crystallization kinetics and thermal conductivity of alumina/fluorescein sodium salt (Al2O3/FSS) composites. Journal of Physics D: applied

physics, 2005. 38: p. 74-77.
250. Y.W. Song, H.S. An, M.J. Shim and S.W. Kim, Thermal decomposition characteristics of DGEBA/MDA/GN System for insulating materials. Proceedings of 1998 International Symposium on Electrical Insulating Materials, in conjunction with 1998 Asian International Conference on Dielectrics and Electrical Insulation and the 30th Symposium on Electrical Insulating Materials, Toyohashi, Japan, Sept. 27-30, 1998.
251. M. Day, J.D. Cooney and D.M. Wiles, The thermal stability of poly(aryl-ether-ether-ketone) as assessed by thermogravimetry. Journal of Applied Polymer Science, 1989. 38(2): p. 323-337.
252. Y.-K. Lee, D.-J. Kim, H.-J. Kim, T.-S. Hwang, M. Rafailovich and J. Sokolov, Activation Energy and Curing Behavior of Resol- and Novolac-Type Phenolic Resins by Differential Scanning
Calorimetry and Thermogravimetric Analysis. Journal of Applied Polymer Science, 2003. 89: p. 2589-2596.
253. A. Babanalbandi, D.J.T. Hill, D.S. Hunter and L. Kettle, Thermal stability of poly(lactic acid) before and after g-radiolysis. Polymer International, 1999. 48: p. 980-984.
254. W. Tang, X.-G. Li and D. Yan, Thermal decomposition kinetics of thermotropic copolyesters made from trans-p-hydroxycinnamic acid and p-hydroxybenzoic acid. Journal of Applied Polymer Science, 2004. 91(1): p. 445-454.
255. J.-Y. Lee, M.-J. Shim and S.-W. Kim, Thermal degradation of epoxy/natural zeolite composites. JOURNAL OF MATERIALS SCIENCE, 2001. 36: p. 4405-4409.
256. F. Reuther, K. Pfeiffer, M. Fink, G. Gruetzner, H. Schulz, H.-C. Scheer, F. Gaboriau and C. Cardinaud, Mix and match of nanoimprint and UV lithography. Proceedings of SPIE Vol. 4343-85, 2001.
257. K.K. Dietliker, Chemistry and technology of UV and EB formulation for coatings, inks and paints, Volume 3, photoinitiators for free radical and cationic polymerization. 1997: John Wiley and Sons Ltd.
258. J.A. Dean, Lange's handbook of chemistry. 15 ed. 1999: McGraw-Hill INC.
259. S.L. Chew and J.A. Meyers, Identification and quantitation of gamma-hydroxybutyrate (NaGHB) by nuclear magnetic resonance spectroscopy. Journal of forensic sciences, 20003. 48(2): p. 292-298.
260. H. Kurosu and Q. Chen, Structural studies of Polymer Blends by Solid-sate NMR. Annual Reports on NMR spectroscopy, 2004. 52: p. 167-199.
261. E.P.d. Silva, M.I.B. Tavares, L.A. Fraga and M.A.C. Kaplan, Evaluation of the diethylene glycol bis(allyl carbonate)/acrylic acid copolymer behavior by solid-state 13C-NMR. Journal of Applied Polymer Science, 2004. 96(3): p. 740-745.
262. D.M. Mowery, R.A. Assink, D.K. Derzon, S.B. Klamo, R.L. Clough and R. Bernstein, Solid-State 13C NMR Investigation of the Oxidative Degradation of Selectively Labeled Polypropylene by Thermal Aging and g-Irradiation. MACROMOLECULES, 2005. 38: p. 5035-5046.
263. S.L. Chew and J.A. Meyers, Identification and quantitation of gamma-hydroxybutyrate (NaGHB) by nuclear magnetic resonance spectroscopy. Journal of forensic sciences, 2003. 48(2): p. 292-298.
264. X. Zhang and D.H. Solomon, Phase Structures of Hexamine Cross-lonked Novolac Blends. 1. Blends with Polt(methyl methacrylate). MACROMOLECULES, 1994. 27: p. 4919-4926.
265. K. Chatterjee, A. Hazra, D. Dollimore and K.S. Alexander, Estimating vapor pressure curves by thermogravimetry: a rapid and convenient method for characterization of pharmaceuticals. European Journal of Pharmaceutics and Biopharmaceutics, 2002. 54: p. 171-180.
266. T.V. Sorokina, D. Dollimore and K.S. Alexander, Evaporation of the fragrance component, cinnamyl alcohol, using simultaneous TG 肪 TA. Thermochimica Acta, 2002. 392-393: p. 315-321.
267. A.A. Yevstropov, B.V. Lebedev, Y.G. Kiparisova, V.A. Alekseyev and G.A. Stashina, Thermodynamic parameters of transformation of ?butyrolactone into poly-?butyrolactone at

normal pressure in the range of 0?00K. Polymer Sci*e*nce U.S.S.R., 1980. 22(11): p. 26**85**-2692.
268. H. Sawada, Thermodynamics of Polymerization. Marcel Dekk*e*r, Inc., New York and Base,1976.
269. G. Odian, Principles of Polymerization, 3rd Ed. Wiley-Interscience, New York 1991.
270. J. Lopez, C. Ramirez, A. Torres, M.J. Abad, L. Barral, J. Cano and F.J. Diez, Isothermal Curing by Dynamic Mechanical Analysis of Three Epoxy Resin Systems: Gelation and Vitrification. Journal of *A*pplied Polymer Science, 2002. 83: p. 78?5.
271. H. Teil, S.A. Page, V. Michaud and J.-A.E. M 銖 son, TTT-Cure Diagram of an Anhydride-Cured Epoxy System Including Gelation, Vitrification, Curing Kinetics Model, and Monitoring of the Glass Transition Temperature. Journal of A*p*plied Polymer Science, 2004. 93: p. 1774-178**7.**
272. M.T. Aronhime and J.K. Gillham, In Advances in Polymer Science, Vol.78, K.Dusek, Ed. Springer-Verlag: New York, 1986.
273. R.A. Venditti and J.K. Gillham, A relationship between the glass transition temperature (Tg) and fractional conversion for thermosetting systems. Journal of Ap*p*lied Polymer Science, 1996. 64(1): p. 3-14**.**
274. J.P. Pascault and R.J.J. Williams, Glass Transition Temperature Versus Conversion Relationships For Thermosetting Polymers. Journal of Po*l*ymer Science: Part B: Polymer Physics, 1990. 28: p. 85-95.
2**75**. A.T. DiBenedetto, Prediction of the Glass Transition Temperature of Polymers: A Model Based on the Principle of Corresponding States. Journal of Po*l*ymer Science: Part B: Polymer Physics, 1987. 26: p. 1949-196**9.**
276. L. Nunez, F. Fraga, A. Castro, M.R. Nuunez and M. Villanueva, TTT cure diagram for an epoxy system diglycidyl ether of bisphenol A/1,2 diamine cyclohexane/calcium carbonate filler. Polymer, 2001. 42: p. 3581-358**7.**
277. H. Degrand, F. Cazaux, X. Coqueret, B. Defoort, F. Boursereau and G. Larnac, Thermal effects on the networkstructure of diglycidylether of bisphenol-A polymerized by electron-beam in the presence of an iodonium salt. Radiation Phy*s*ics and Chemistry, 2003. 68: p. 885-891.
278. F.Y.C. Boey and W. Qiang, Glass-transition temperature-conversion relationship for an epoxy-hexahydro-4-methylphthalic anhydride system. Journal of Ap*p*lied Polymer Science, 2000. 78(3): p. 511 - **5**16.
279. Y. Sensu, A. Sekiguchi, S. Mori and N. Honda, Profile simulation of SU-8 thick film resist. Proceedings o*f* SPIE Vol. 5753, 2005: p. 1170-1185.
280. E. Klemm, L. Haase, D. Gorski and H.-H. Horhold, Untersuchungen zur Substanzpolymerisation spirocyclischer Orthoester mit Et3O+SbCl6-. Acta Polymeri*c*a, 1982. 33(7): p. 429-4**32**.
281. C. Mas, A. Mantecon, A. Serra, X. Ramis and J.M. Salla, Improved Thermosets Obtained from Cycloaliphatic Epoxy Resins and g-Butyrolactone with Lanthanide Triflates as Initiators. I. Study of Curing by Differential Scanning Calorimetry and Fourier Transform Infrared. Journal of Po*l*ymer Science: Part A: Polymer Chemistry, Vol. ,, 2005. 43: p. 2337-234**7.**
282. A. Singh, J. Jayaram, M. Madou and S. Akbar, Pyrolysis of Negative Photoresists to Fabricate Carbon Structures for Microelectromechanical Systems and Electrochemical Applications. Journal of Th*e* Electrochemical Society, 2002. 149(3): p. E78-**E83**.
283. H.E. Kissinger, Reaction kinetics in differential thermal analysis. Analytical Ch*e*mistry, 1957. 29: p. 1072-107**6.**
284. M.A. Uddin, H.P. Chan and C.K. Chow, Thermal and Chemical Stability of a Spin-Coated Epoxy Adhesive for the Fabrication of a Polymer Optical Waveguide. Chemistry of *M*aterials, 2004. 16(23): p. 4806-**4**811.
285. H. Lee and K. Neville, Handbook of epoxy resins ; McGraw-Hill:New York, 1967.
286. L. Lu and K. Huang, Synthesis and characteristics of a novel aliphatic polycarbonate, poly[(propylene oxide)-co-(carbon dioxide)-co-(-butyrolactone)]. Polymer Inter*n*ational, 2005. 54(6): p. 870 - **8**74.
287. M. Shirai, A. Kawaue, H. Okamura and M. Tsunooka, Photo-cross-linkable Polymers Having Degradable Properties on Heating. Chemistry of *M*aterials, 2003. 15(21): p. 4075-**4**081.

288. D.S. Muggli, A.K. Burkoth and K.S. Anseth, Crosslinked polyanhydrides for use in orthopedic applications: Degradation behavior and mechanics. Journal of Bi*o*medical Materials Research, 1999. 46(2): p. 271-2**78**.
289. W.H. Lo and J. Yu, Effects of the energy dissipation rate and surface erosion on the biodegradation of poly(hydroxybutyrate-co-ydroxyvalerate) and its blends with synthetic polymers in an aquatic medium. Journal of Ap*p*lied Polymer Science, 2001. 83(5): p. 1036-**1**045.
290. J. Yu, Biodegradation-based Polymer Surface Erosion and Surface Renewal for Foul-release at Low Ship Speeds. Biofouling, 2*0*03. 19: p. 83-90.
2**91**. A.R. Mollo and O.I. Corrigan, An Investigation of the Mechanism of Release of the Amphoteric Drug Amoxycillin from Poly(d,l-Lactide-co-glycolide) Matrices. Pharmaceutica*l* Development and Technology, 2002. 7(3): p. 333-34**3**.
292. R.N. Wenzel, Resistance of Solid Surfaces to Wetting by Water. Journal of In*d*ustrial and Engineering Chemistry, 1936. 28: p. 988-994.
293. K.R. Williams and R.S. Muller, Etch Rates for Micromachining Processing. Journal of Mi*c*roelectromechanical Systems, 1996. 5: p. 256-269.
294. Y.H. Yan, M.B. Chan-Park, W.C. Ching and C.Y. Yue, Interaction of anti-adhesive silicone films with UV embossing resin. Applied Surfa*c*e Science, 2005. 249(1-4): p. 33**2-3**39.
295. M.B. Chan-Park, J. Gao and A.H.L. Koo, Surface characterization of nickel alloy plasma-treated by O-2/CF4 mixture. Journal of Ad*h*ension Science and Technology, 2003. 17(15): p. 1979-**2**004.
296. K.L. Mittal and J.R. Susko, Metallized Plastics. 1. Fundamental and Applied Aspects. 1989, New York: Plenum.
297. J.S. Kong, D.J. Lee and H.D. Kim, Surface modification of low-density polyethylene (LDPE) film and improvement of adhesion between evaporated copper metal film and LDPE. Journal of A*p*plied Polymer Science, 2001. 82(7): p. 1677-**16**90.
298. W.T. Li, R.B. Charters, B. Luther-Davies and L. Mar, Significant improvement of adhesion between gold thin films and a polymer. Applied Surfa*c*e Science, 2004, in press.
299. S. Yi, C.Y. Yue, J.-H. Hsieh, L. Fong and S.K. Lahiri, Effects of oxidation and plasma cleaning on the adhesion strength of molding compounds to copper leadframes. JOURNAL OF AD*H*ESION SCIENCE AND TECHNOLOGY, 1999. 13(7): p. 753--**85**6.
300. M.B. Chan-Park, J. Zhang, J. Gao and E. Liu, Photografting of argon plasma-treated graphite/PEEK laminate to enhance its adhesion. JOURNAL OF AD*H*ESION SCIENCE AND TECHNOLOGY, 2002. 16(14): p. 1883-**1**900.
301. M. Hudis, in Techniques and *Applications of Plasma Chemistry, J.R. Hollahan* and A.T. Bell, Editors. 1974, John Wiley & Sons: New York. p. 113.
302. M. Kuzuya, J. Niwa and H. Ito, Nature of Plasma-Induced Surface Radicals of Powdered Polyethylene Studied by Electron Spin Resonance. MACROMOLECULE*S*, 1993. 26: p. 1990-199**5.**
303. M. Kuzuya, S.-i. Kondo and Y. Sasai, Plasma Techniques for Preparation of Controlled Drug Release System. Plasmas and P*o*lymers, 2001. 6(6): p. 145-16**2**.

Appendix A

Related Publications

[1] Jun Zhang, W. X. Zhou, Mary B. Chan-Park and Samuel R. Conner, Argon plasma modification of SU-8 for very high aspect ratio and dense copper electroforming, Journal of Electrochemical Society, 152(10), C716-C721, 2005.

[2] Jun Zhang, Mary B. Chan-Park, Jianmin Miao and Tie T Sun, Reduction of diffraction effect for fabrication of very high aspect ratio microchannels in SU-8 over large area by soft cushion technology, Microsystems Technologies, 11(7), 519-525, 2005

[3] Jun Zhang, Mary B. Chan-Park and Samuel R. Conner, Effect of exposure dose on the replication fidelity and profile of very high aspect ratio microchannels in SU-8, Lab On A Chip, 4 (6): 646-653 2004

[4] Mary B Chan-Park, Jun Zhang, Yehai Yan and C. Y. Yue, Fabrication of Large SU-8 Mold with High Aspect Ratio Microchannels by UV Exposure Dose Reduction, Sensors and Actuators B: Chemical, 101 (1-2): 175-182 2004

[5] Mary B. Chan-Park, Yehai Yan, Wee Koon Neo, Wenxiu Zhou, Jun Zhang and Chee Yoon Yue, Fabrication of high aspect ratio poly(ethylene glycol) microstructures by UV embossing, Langmuir, 19, 4371-4380 (2003)

Appendix B

Surface morphology of SU-8 subjected to Ar plasma treatment

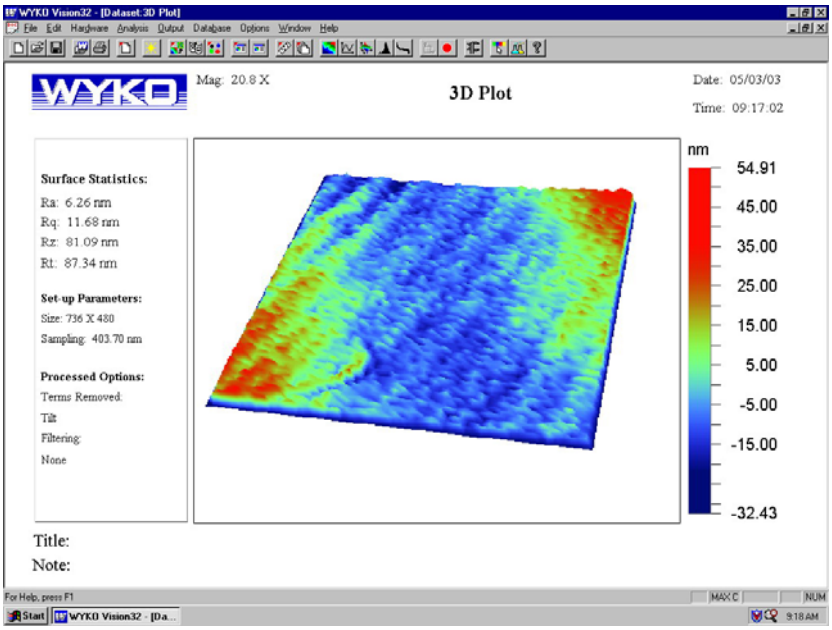

Figure B.1 plasma time= 0 sec

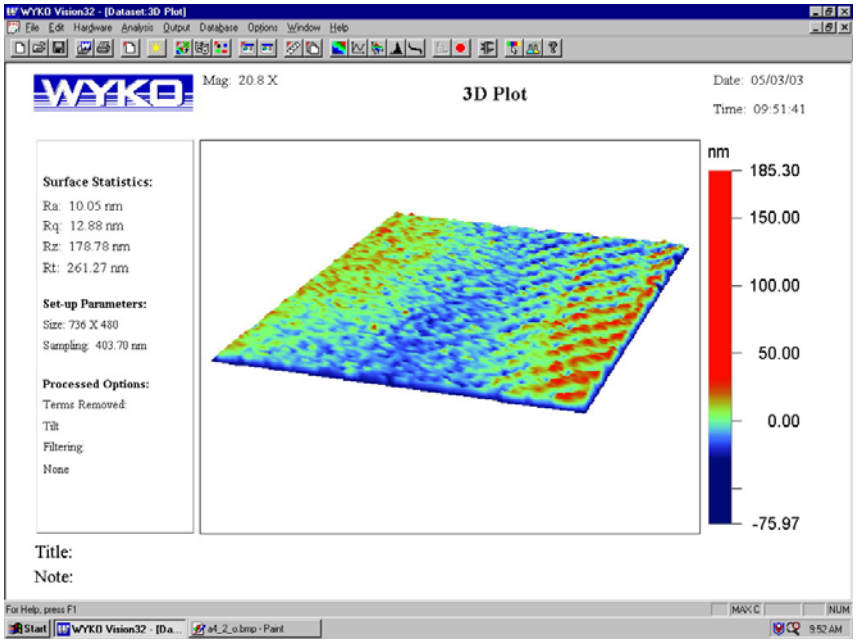

Figure B.2 Plasma time=30 sec

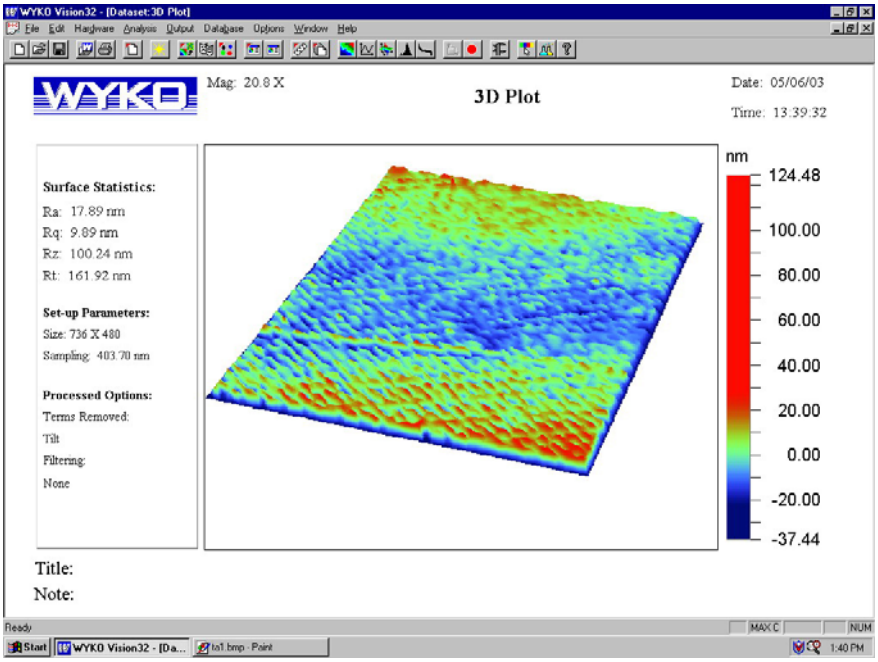

Figure B.3 plasma time=5 min

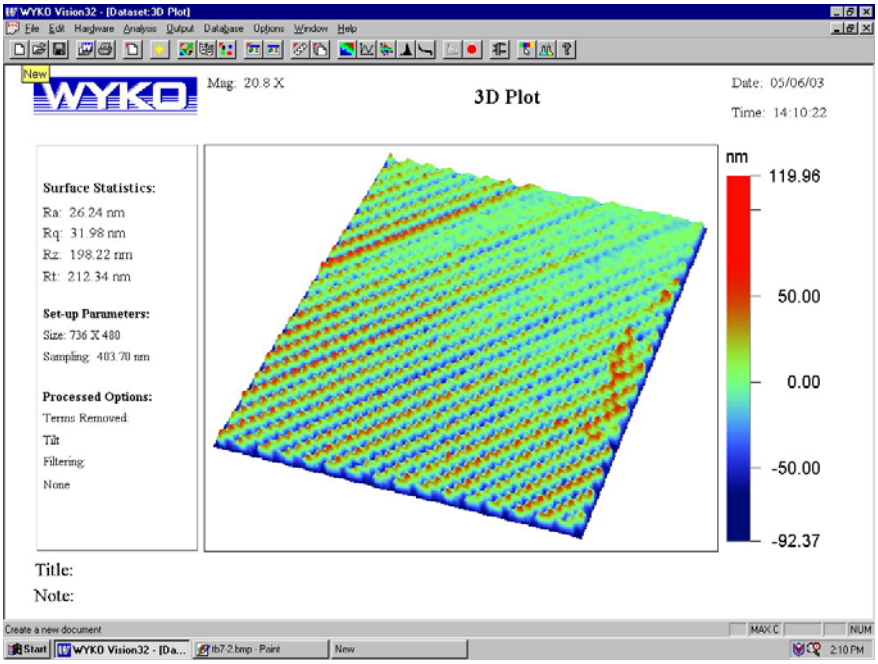

Figure B.4 plasma time=10 min

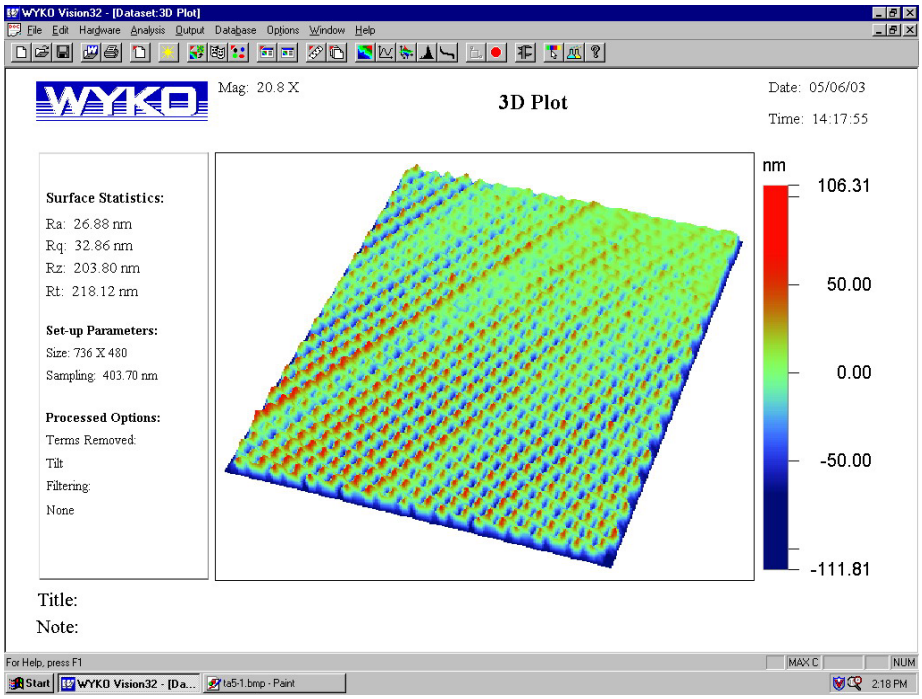

Figure B. 5 plasma time=30 min

Appendix C

Surface morphology of side wall of deep channels in SU-8 resist

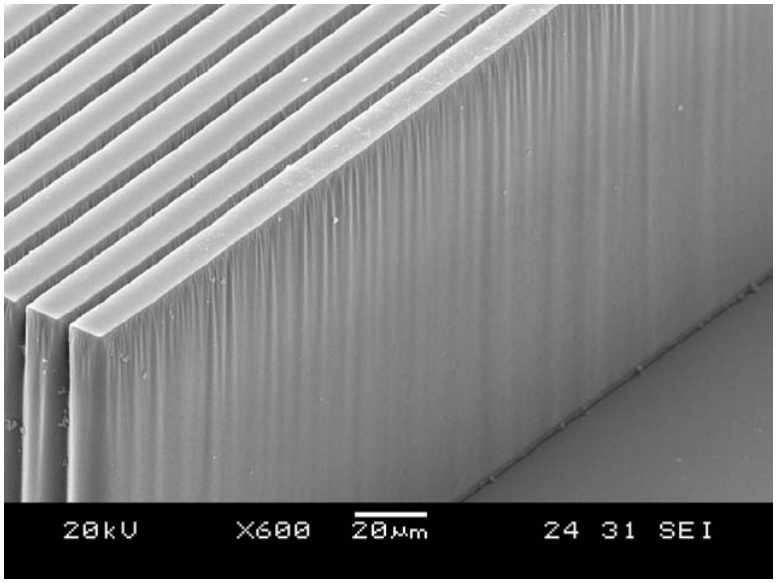

Figure C.1 SEM photograph of SU-8side wall (100 µm SU-8, exposed for 60 sec)

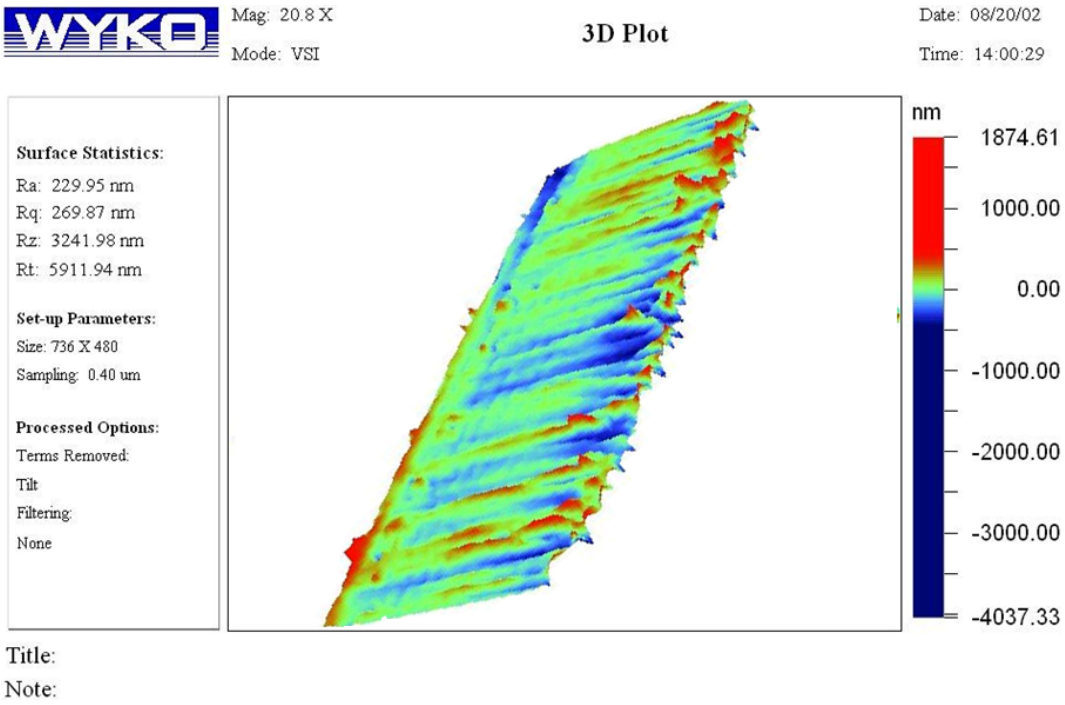

Figure C.2 OP result of the side wall roughness (100 µm SU-8, exposed for 60 sec)

Appendix D

FTIR spectra of SU-8 with different processing parameters

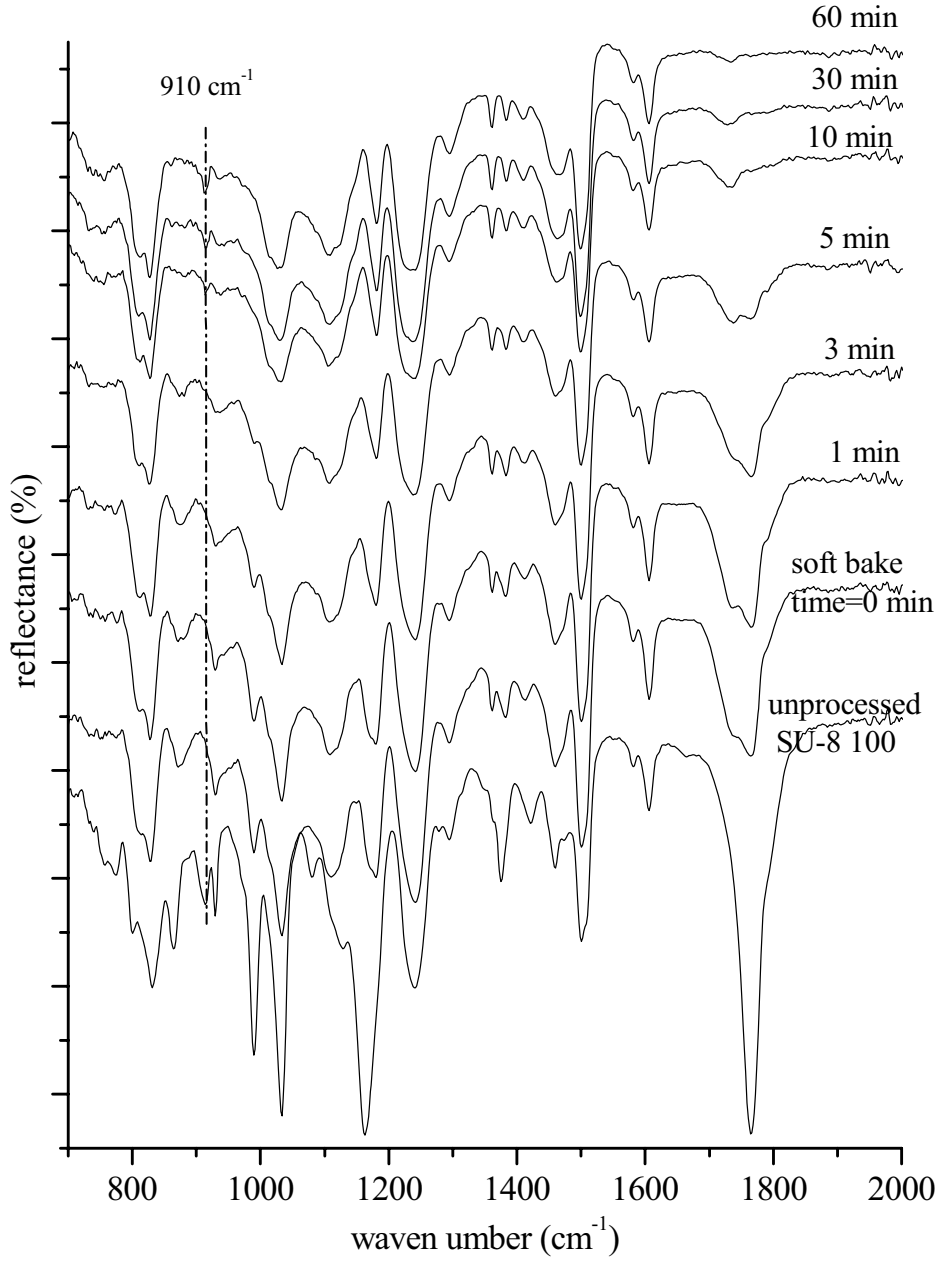

Figure D.1 FTIR spectra of SU-8 subjected to different softbake time at 95°C (100 μm thick SU-8 100, exposed for 70s, PEB 10 min at 95°C, no hard bake)

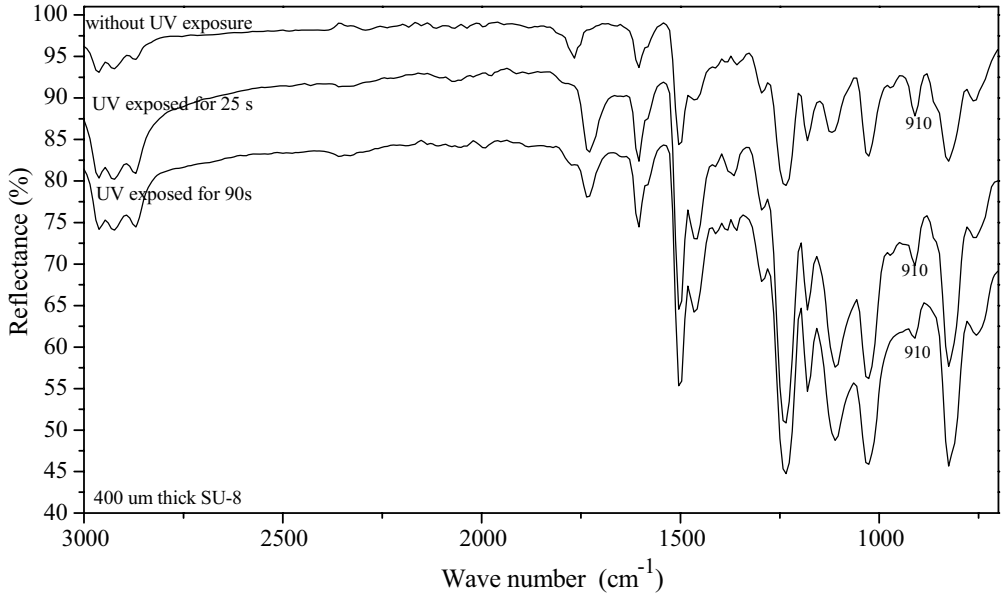

Figure DC.2 FTIR spectra of SU-8 subjected to different exposure time
(100μm thick SU-8 100, softbake 30 min at 95°C, PEB 10 min at 95°C, no hardbake)

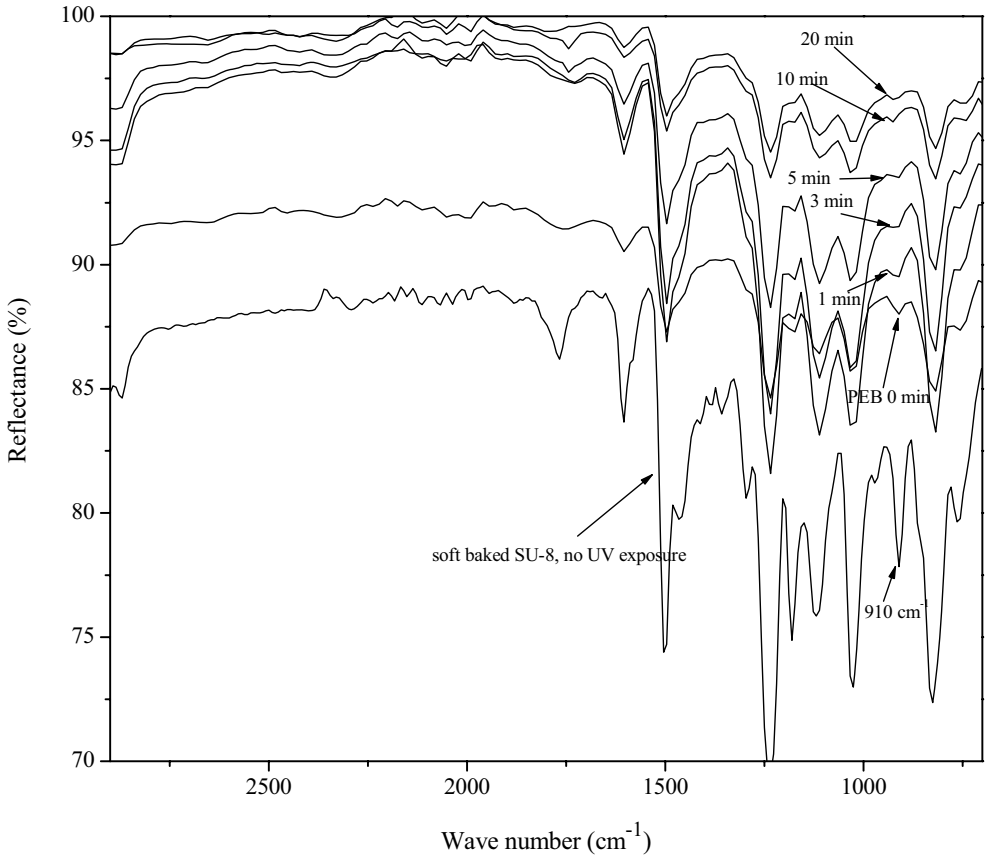

Figure D.3 FTIR spectra of SU-8 subjected to different PEB time at 95°C
(100μm thick SU-8 100, softbake 30 min at 95°C, exposed for 70 sec, no hardbake)

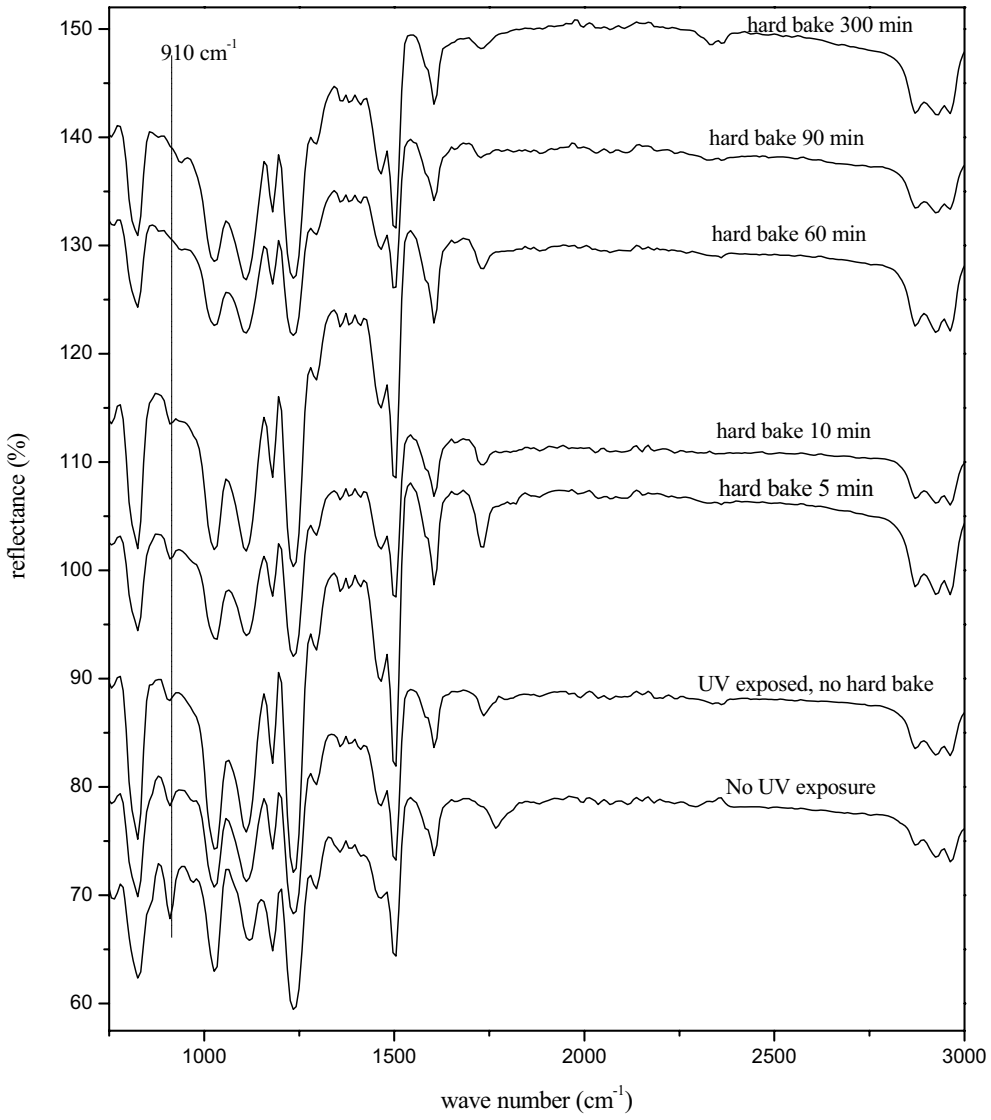

Figure D.4 FTIR spectrum of SU-8 films subject to different hard bake time at 150°C (100 μm thick SU-8 100, softbake 30 min at 95°C, exposed for 70 sec, PEB 10 min at 95°C)

Appendix E

Program code for diffraction refraction and reflection model calculation

```
  DIMENSION X(1000),XMU(1000),CU(1000),SU(1000),z(10000)
  character*12  xml
  character*6 sl
  REAL N1,N2,R,lanbda
  DOUBLE PRECISION sinst,cst,timagr,imagr,trealr,realr

     write(*,*) 'please input the thickness'
     read(*,*) s

dz=0.02
 nz=int((s)/dz)

 write(*,*) 'please input the width of opening'
 read(*,*) width
 dy=0.2
 ND=int(width/dy)

write(*,*)' input the gap'
read(*,*) gap

   write(*,*)' please in put the file name to save the results:'
  read(*,*) xml

 write(*,*) ' '
 write(*,*) '       I am doing calculation, it will take a while.'
 write(*,*) '       I am doing calculation, it will take a while.'

write(*,*) ' '
  write(*,*) ' '
  write(*,*) '       Please don"t close this window. Thank you'
    write(*,*) ' '
   write(*,*) ' '

  alfa=-52.0/10000.0
  N1=1.67
  N2=6.55
  sn=n2/n1
  PI=3.1415926535
  pii=2*pi
  xlbd=0.365
   xlbdl=xlbd
   lanbda=xlbd

     open(6,file=xml,status='new')

 do1818  kk=1,nz
   z(kk)=dz*kk
   if(z(kk).gt.gap) then
```

```
          lanbda=0.365/1.67
           endif

        write(*,*)'z=',z(kk)
           DO 100 I=1,600

                X(I)=-7.5+0.025*i
                     IF(X(I).EQ.0.0) then
                      X(I)=0.00001
                     endif

c       calculate the dirrfraction part using Fresnel approximation
                     wx=x(i)*((2/(xlbdl*z(kk))))**0.5
                        CALL CUU(CU(I),su(i),wx,I,z(kk))
         if(wx.le.0.0) then
         cu(i)=-cu(i)
         su(i)=-su(i)
         endif


611       rd=1.0

           if(z(kk).le.gap) then
           go to 2121
           endif

c       rr=sqrt(z(kk)**2+(y-x(i))**2)*(z(kk)-gap)/z(kk)
c       rd=exp(0.5*alfa*rr)

c2121      XMU(I)=((0.5-CU(I))**2+(0.5-SU(I))**2)*rd*0.5
2121      alr=cu(i)*rd
          ali=su(i)*rd

          trealr=0.0
           timagr=0.0
        tr=0.0
        ti=0.0
        timagd=0.0
        treald=0.0

               if(z(kk).le.gap) then
               goto 1121
               endif

                 if(iw.eq.0.) then
                 GOTO 1121
                 endif

           ww1=(2*s-z(kk))**2
```

```
        DO 666 IS=1,ND
             Y=IS*DY
            a=WW1+(x(i)-y)**2
             ror=sqrt(a)

c ***************************************
        call rii(gap,s,x(i),y,z(kk),ri1,ri2t,yi)
        call rdd(gap,x(i),y,z(kk),rd1,rd2,yd)
        ax=(s-gap)/(2*s-Z(kk)-gap)
        ri2=ri2t*ax
        rr=ri2t-ri2
        cstaii=sqrt(1-((yi-x(i))/ri2)**2)
        cstii=0.5*(1.0+cstaii)
c****************************************
             ror1=ror
                c=S+z(KK)
                d=abs(x(I)-y)
                sinst=d/sqrt(c**2+d**2)
                cst=sqrt(1.0-sinst**2)
                    xx1=sqrt(n2*n2-(n1*sinst)**2)
                    b=xx1*(n1/n2)**2/(n1*cst)
                    r=(1.-b)/(1.+b)
        rd=rd1+rd2
        ri=ri1+ri2
        rrt=ri1+ri2t
                   absri=exp(0.5*alfa*rir2t)
        sitaref=(pii*rrt)/lanbda

        realr=cstii*r*absri*cos(sitaref)*dy/rrt/lanbda
         trealr=trealr+realr
                imagr=cstii*r*absri*sin(sitaref)*dy/rrt/lanbda
                timagr=timagr+imagr

        tr=trealr
        ti=timagr

666       CONTINUE

1121             al1=alr+TR
                al2=ali+TI
1122     final=((0.5-al1)**2+(0.5-al2)**2)*0.5
         write(6,*) final
100     CONTINUE
1818    continue
121         format(f7.5)
c188         WRITE(*,*) ' ALL IS DONE'

         END
```

```
                SUBROUTINE CUU(CWU, swu, U, IJ, z)
                xx=0.0
                dx=0.005
                x=0.0
                CUX=0.0
                swu=0.0
                UX=ABS(U)
10          sita=x**2*3.1415926/2
                rol=(x**2+z**2)**0.5
                xx=cos(sita)*dx
                yy=sin(sita)*dx
                cuX=cuX+xx
                swu=swu+yy
                x=x+dx
                if(x.le.uX) goto 10
             CWU=CUX
                RETURN
                END


          SUBROUTINE rdd(ga, xa, ya, za, rda1, rda2, yda)
          n0=1.0
          n1=1.67
          yda=ya
          if(ya.ge.xa) then
          dyd=-0.0001
          goto 100
          endif

          if(ya.lt.xa) then
          dyd=0.0001
          goto 100
          endif

100       yda=yda+dyd

          rda1=sqrt(ga**2+(ya-yda)**2)
          rda2=sqrt((za-ga)**2+(yda-xa)**2)

          xx1=n0*((ya-yda)/rda1)
          xx2=n1*((yda-xa)/rda2)

          dxx=abs(xx1-xx2)
          if (dxx.lt.0.0001) then
           goto 200
          endif
          goto 100
200       return
          end
```

```
      SUBROUTINE rii(ga,ta,xa,ya,za,ria1,ria2,yia)
      n0=1.0
      n1=1.67

      yia=ya
      if(ya.ge.xa) then
      dyi=-0.0001
      goto 100
      endif

      if(ya.lt.xa) then
      dyi=0.0001
      goto 100
      endif

100   yia=yia+dyi

      ria1=sqrt(ga**2+(ya-yia)**2)
      ria2=sqrt((2*t-za-ga)**2+(yia-xa)**2)

      xx1=n0*((ya-yia)/ria1)
      xx2=n1*((yia-xa)/ria2)

      dxx=abs(xx1-xx2)
      if (dxx.lt.0.0001) then
       goto 200
      endif

      goto 100

200   return

      end
```

Appendix F

Basic introduction to NMR and CPMAS ^{13}C NMR

Nuclear Magnetic Resonance[1, 2, 3, 4, 5, 6, 7,8]

NMR spectroscopy is frequently used to investigate the structure of molecules and materials. The power of NMR lies in its ability to probe physical properties of materials in a nondestructive manner and over a wide variety of conditions (primarily temperature and state). Particularly important to this experiment is NMR's utility in determining the structure and dynamics in solid-state crystalline and amorphous materials.

F.1.1 Nuclear spin and magnets

Electrons, neutrons and protons, the three particles which constitute an atom, have an intrinsic property called spin. This spin is defined by the fourth quantum number for any given wave function obtained by solving relativistic form of the Schrödinger equation (SE). It represents a general property of particles which we can describe using the properties of electrons. Electrons flowing around a coil generate a magnetic field in a given direction; this property is what makes electric motors work. In much the same way electrons in atoms circulate around the nucleus, generating a magnetic field. This generated field has an angular momentum associated with it. It so turns out that there is also an angular momentum with the electron particle itself, denoted the spin, and this gives rise to the spin quantum number, m_s.

Spin angular momentum is quantized and can take different integer or half-integer values depending on what system is under study. Like the electron, protons and neutrons also have a spin angular momentum which can take values of + ½ and –½. In

[1] J.W. Akitt, NMR and Chemistry, An introduction to modern NMR spectroscopy, Chapman & Hall, London, 1992
[2] R.J. Abraham, J. Fisher, and P. Loftus, Introduction to NMR Spectroscopy, John Wily and Sons, Chichester, 1988
[3] C. Dybowski, R. L. Lichter, NMR Spectroscopy Techniques Vol 5, Marcel Dekker, Inc, New York, 1987
[4] E. Fukushima, S. B. W. Roeder, Experimental Pulse NMR: A Nuts and Bolts Approach, Addison-Wesley Pub. Co., Reading, MA, 1981
[5] R.K. Harris, Nuclear Magnetic Resonance Spectroscopy,Pitman, London,1983
[6] A. Carrington, A.D. McLachlan, Introduction To Magnetic Resonance, Chapman and Hall, London 1967
[7] J.R. Dyer, Applications of Absorption Spectroscopy by Organic Compounds, Prentice-Hall, Englewood Cliffs, NJ 1965.
[8] Jack L. Koenig, Spectroscopy of Polymers, 2nd edition, Elsevier, 1999.

the atomic nucleus, protons can pair with other antiparallel protons, much in the same way electrons pair in a chemical bond. Neutrons do the same. Paired particles, with one positive and one negative spin, thus have a net spin of zero "0". We can see that a nucleus with unpaired protons and neutrons will have an overall spin, with the number unpaired contributing 1/2 to the overall nuclear spin quantum number, I. When this is larger than zero, a nucleus will have a spin angular momentum and an associated magnetic moment, μ, dependent on the direction of the spin. It is this magnetic moment that we manipulate in modern NMR experiments.

It is worth noting here that nuclei can have more than one unpaired proton and one unpaired neutron, much in the same way electronic structure in transition metals can have many unpaired spins. For example ^{27}Al has an overall spin I=5/2.

F.1.2 Values of spin angular momentum

The spin angular momentum of a nucleus can take ranges from +I to –I in integral steps. This value is known as the magnetic quantum number, *m*. For any given nucleus, there is a total (2I+1) angular momentum states. Spin angular momentum is a vector quantity. The z component of which, denoted I_z, is quantised:

$$I_z = mh/2\pi \qquad \text{(F.1)}$$

where *h* is Planck's constant.

The resultant magnetic moment of this nucleus is intrinsically connected with its spin angular momentum. In the absence of any external effects the magnetic moment of a spin ½ nuclei lies approximately 52.3° from the angular momentum axis or 127.7° for the opposing spin. This magnetic moment is intrinsically related to *I* with a proportionality constant γ, called the gyromagnetic ratio

$$\mu=\gamma I \qquad \text{(F.2)}$$

F.1.3 Spin behavior in a magnetic field

If we take the case of nuclei which have a spin of a half like ^{1}H, ^{13}C or ^{19}F. The nucleus thus has two possible magnetic moments it could take, often referred to as up or down, +0.5 -0.5, or to be more in tune with physicists... α and β. The energies of each state are degenerate - that is to say that they are the same. The effect is that the number of atoms (*population*) in the up or α state is the same as the number of atoms in the β state. If we place a nucleus in a magnetic field the angular momentum axis coincides with the field direction. The resultant magnetic momenta, space quantised from the

angular momentum axis, no longer have the same energy since one states has a z-component aligned with an external field and are lower in energy (positive I values) and the other opposes the external field and is higher in energy. This causes a population bias toward the lower energy states.

The energy of a magnetic moment μ when in a magnetic field B_0 (the zero subscript is used to distinguish this magnetic field from any other applied field) is the negative scalar product of the vectors:

$$E = -\mu_z B_0 \qquad (F.3)$$

We've already defined $\mu_z=\gamma I_z$. So placing this in the above equation we get:

$$E = -mh\gamma B_0 / 2\pi \qquad (F.4)$$

F.1.4 Resonance

The energy gap between α and β states is $(h\gamma B_0)/2\pi$. We get resonance between the states, there for equalising populations, if we apply a radiofrequency with the same energy as the energy difference ΔE between the spin states. The energy of a photon is $E=h\nu$, where ν is its frequency.

$$\Delta E = h\gamma B_0 / 2\pi \qquad (F.5)$$

i.e. the frequency of electromagnetic radiation required to produce resonance of an specific nucleus in a field B is:

$$\nu = \gamma B_0 / 2\pi \qquad (F.6)$$

It is this frequency that we are concerned with, and detect in NMR. And it is this frequency which describes the sample we are observing. But importantly: it is this resonance that gives rise to the NMR spectrum

F.1.5 Nuclear shielding

It would appear from the above equation that all nuclei of the same isotope, which take the same the gyromagnetic ratio, resonate at the same frequency. This of course is not the case. Since the gyromagnetic ratio of a given isotope does not change we can only rationalise this by stating that the effect of the external magnetic field is different for different nuclei. Local effects of other nuclei, especially spin-active nuclei, and local electron effects shield each nucleus differently from the main external field.

It was stated that the energy of a spin state is defined by $E= -\mu_z B_0$. We can see that by shielding the strength of the magnetic field, the experienced effect, or *effective*

magnetic field at the nucleus is lower: $B_{effective} < B_0$. Thus the energy gap is different, and hence the frequency required to achieve resonance deviates from the expected value. These differences due to nuclear shielding give rise to many peaks (frequencies) in an NMR spectrum.

F.1.6 Relaxation

The nuclear relaxation back to the thermal equilibrium distribution is a product of several distinct relaxation mechanisms. The simplest of these is spin-lattice relaxation; the energized nuclei lose their energy to the surrounding crystal lattice by stimulated emission. This exponential relaxation is quantifiable and labeled T1, the longitudinal relaxation time.

T1 relaxation manifests itself in the NMR signal as a dampening parameter, resulting in a gradual decrease in amplitude of the signal. The exponential decay of the demodulated NMR signal is referred to as the Free Induction Decay (FID). The spin-spin relaxation (T2) is a catchall for the several causes of the broadening of a line-shape as well as increasing the dampening of the Free Induction Decay. In practice, usually T2 dominates T1 in determining the FID decay time. One phenomenon that affects T2 is the presence of slight inhomogeneities in the static magnetic field. These inhomogeneities shift the Larmor frequency slightly for different nuclei, depending on the exact local value of B0. Immediately after the initial RF pulse, all the nuclei are precessing precisely in phase with one another. Due to slightly varied precession rates, they gradually begin to dephase, resulting in destructive interference of the magnetization vectors. This manifests itself in two different ways. First, the destructive interference increases the dampening of the observed FID. Second, due to the varying Larmor frequencies, there is a broadening effect on the theoretical delta function line-shape. Another factor contributing to the spin-spin relaxation time is the dipole-dipole coupling between nuclei. In a solid crystalline structure or a molecule (i.e. not just an isolated proton), the magnetic dipole of a nucleus causes significant changes to the magnetic moment of a neighboring nucleus. This variation is random with respect to the orientation of B0, so it produces a random distribution of magnetic fields at the nucleus, and dephasing can occur between nuclei experiencing different local magnetic fields. In this manner, the dipole-dipole interactions also significantly broaden a line-shape, contributing to the observed spin-spin relaxation time. T_1 is always larger (slower) than T_2.

F.1.7 Chemical Shift

When an atom is placed in a magnetic field, its electrons circulate about the direction of the applied magnetic field. This circulation causes a small magnetic field at the nucleus which opposes the externally applied field. The magnetic field at the nucleus (the effective field) is therefore generally less than the applied field by a fraction σ.

$$B = B_o (1-\sigma) \qquad (F.7)$$

The electron density around each nucleus in a molecule varies according to the types of nuclei and bonds in the molecule. The opposing field and therefore the effective field at each nucleus will vary. This is called the chemical shift phenomenon. The chemical shift of a nucleus is the difference between the resonance frequency of the nucleus and a standard, relative to the standard. This quantity is reported in ppm and given the symbol delta, δ.

$$\delta = (\nu - \nu_{ref}) \times 10^6 / \nu_{ref} \qquad (F.8)$$

In NMR spectroscopy, this standard is often tetramethylsilane, $Si(CH_3)_4$, abbreviated TMS. The chemical shift is a very precise metric of the chemical environment around a nucleus. For example, the hydrogen chemical shift of a CH_2 hydrogen next to a Cl will be different than that of a CH_3 next to the same Cl. It is therefore difficult to give a detailed list of chemical shifts in a limited space. The animation window displays a chart of selected hydrogen chemical shifts of pure liquids and some gasses.

NMR spectrometer

In its most basic form NMR spectroscopy takes advantage of the magnetic properties of nuclei with non-zero angular momentum. By placing nuclei in a static magnetic field and irradiating them with a radio-frequency (RF) pulse it is possible to change their spin orientation. After the perturbation, the nuclei gradually return to their equilibrium state; during this “relaxation time”, the nuclear spin vectors precess around the direction of the static magnetic field with certain discrete energies, depending on the spin orientation. This precession can be detected as an induced voltage in a RF coil placed perpendicular to the static field. By carefully selecting the energy (which is determined by the frequency) of the incident RF radiation, recording the RF subsequently radiated by the nuclei, and analyzing the signals in both time and

frequency space, it is possible to determine the characteristic spectrum of energy levels of the nuclei.

The basic arrangement of an NMR spectrometer is shown in Figure G.1. The sample is positioned in the magnetic field and excited via pulsations in the radio frequency input circuit. The realigned magnetic fields induce a radio signal in the output circuit which is used to generate the output signal. Fourier analysis of the complex output produces the actual spectrum. The pulse is repeated as many times as necessary to allow the signals to be identified from the background noise. The NMR experimental is carried out by placing the sample in solution in a glass tube between the poles of the magnet. The tube is spun rapidly to minimize any magnetic anisotropy.[9]

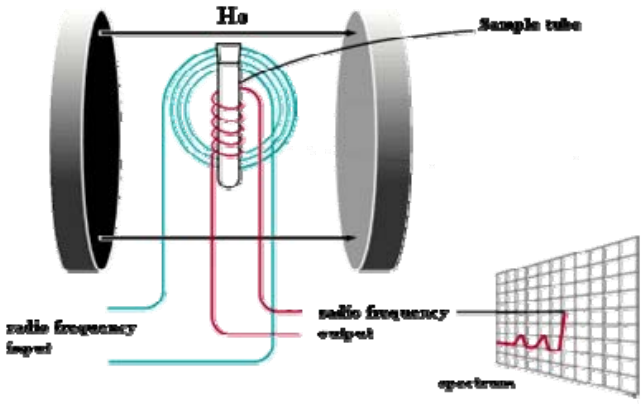

Figure F.1 schematic drawing of NMR spectrometer

Solid state NMR and CPMAS ^{13}C NMR [10-13]

Despite the success of solution NMR, there remain fundamental limits on the size and physical state of molecules amenable to study with solution-state NMR. In any condensed phase a nuclear spin experiences a great number of interactions. This should in general lead to a very broad and featureless signal. However, in liquids, e.g. a solution of an organic compound, most of these interactions will average out because the molecule occurs in a great many different orientations and can rotate around freely. Orientational averaging causes the signal to become much narrower, so that it is able to

[9] Brian S. Furniss, Antony J. Hannaford, Peter W. G. Smith and Austin R. Tatchell, Vogel's Textbook of Practical Organic Chemistry, 5th edition, Prentice Hall, 1996

[10] D. Campbell, R. A. Pethrick, and J. R. White, Polymer Characterization: Physical techniques, 2nd edition, Stanley Thornes (Publishers), UK, 2000.

reveal information in great detail. In solids, however, this narrowing does not happen. For a long time NMR on solids was considered a rather impossible task. High-resolution solid-state NMR methods have no inherent molecular weight limit, and have for many years been used to determine details of molecular structure for high molecular weight systems[11].

Technically, the differences between liquid- and solid-state NMR are predominantly due to the strong anisotropic interactions present in solid materials[12] [13]. In solution NMR, spectra consist of a series of very sharp transitions, due to averaging of anisotropic NMR interactions by rapid random tumbling. By contrast, solid-state NMR spectra are very broad, as the full effects of anisotropic or orientation-dependent interactions are observed in the spectrum. Original NMR experiments focused on 1H and 19F NMR, for reasons of sensitivity. However, anisotropies in the local fields of the protons broadened the 1H NMR spectra such that no spectral lines could be resolved. The only cases where useful spectra could be obtained was for isolated homonuclear spin pairs (e.g., in H2O), or for fast moving methyl groups. Much of the original solid state NMR in the literature focuses only upon the measurement of 1H spin-lattice relaxation times as a function of temperature in order to investigate methyl group rotations or motion in solid polymer chains. The situation changed when it was shown by E.R. Andrew[14] and I.J. Lowe[15] that anisotropic dipolar interactions could be suppressed by introducing artificial motions on the solid - this technique involved rotating the sample about an axis oriented at 54.74º with respect to the external magnetic field. This became known as magic-angle spinning (MAS). With a number of special techniques/equipment, including magic-angle spinning, cross polarization, special 2D experiments, enhanced probe electronics, etc. solid state NMR spectra can provide the same type of information that is available from corresponding solution

[11] C. M. Rienstra, L. Tucker-Kellogg, C. P. Jaroniec, M. Hohwy, B. Reif, M. T. McMahon, B. Tidor, T. Lozano-Perez, and R. G. Griffin, De novo determination of peptide structure with solid-state magic-angle spinning NMR spectroscopy. *Proccedings of the national Academy of Sciences of the United States of America*, 2002. 99: p. 10260-10265.
[12] M. Mehring, Principles of High Resolution NMR in Solids, Springer, Berlin. 1983.
[13] K. Schmidt-Rohr and H.W. Spiess, Multidimensional Solid State NMR and Polymers, Academic Press, New York. 1994.
[14] E. R. Andrew, A. Bradbury, and R. G. Eades, Nuclear magnetic resonance spectra from a crystal rotated at high speed. *Nature Materials*, 1958. 182: p. 1659.
[15] I. J. Lowe, Free induction decays of rotating solids. *Physical Review Letters*, 1959. 2: p. 285.

NMR spectra. Solid-state CPMAS NMR (Cross Polarization Magic-Angle Spinning NMR) is widely used to study polymorphism either qualitatively or quantitatively[16] [17].

F.1.8 Magic Angle Spinning (MAS)

Magic angle spinning (MAS) is commonly employed in solid-state NMR spectroscopy. This is a trick that is used to narrow the otherwise broad line-shapes of solid samples. Several factors contribute to line-shape broadening in solids, including dipole-dipole interactions and chemical shift anisotropies.

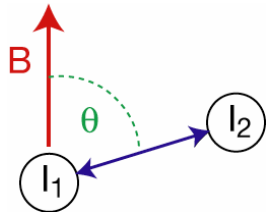

Figure F.2 dipolar coupling

Nuclear spins exhibit a dipole moment, which interacts with the dipole moment of other nuclei (dipolar coupling). The magnitude of the interaction is dependent on the spin species, the internuclear distance, and the orientation of the vector connecting the two nuclear spins with respect to the external magnetic field B (see figure). The maximum dipolar coupling is given by the dipolar coupling constant *d*,

$$d = \frac{\hbar \mu_0}{4\pi} \frac{\gamma_1 \gamma_2}{r^3} \qquad \text{(F.9)}$$

where r is the distance between the nuclei,

γ_1 and γ_2 are the gyromagnetic ratios of the nuclei.

In a strong magnetic field, the dipolar coupling depends on the orientation of the internuclear vector with the external magnetic field by [14,15]

$$D \propto 3\cos^2\theta - 1 \qquad \text{(F.10)}$$

where θ is the angle between the nuclear magnetization vector and the static magnetic field (B0).

[16] S. R. Byrn, R. R. Pfeiffer, and J. G. Stowell, Solid state chemistry of drugs. West Lafayette: SSCI. 1999.
[17] T. L. Threlfall, Analysis of organic polymorphs, a review. *Analyst*, 1995. 120: p. 2435-2460.

This factor goes to zero as approaches 54.74° (the so-called “magic angle”). Rotating the sample rapidly around some axis z’ effectively averages components of the nuclear magnetization vectors such that the net magnetization vector points only in the z’ direction. So the sample is rotated about an axis, which is aligned at the magic angle with respect to the B0 field. This causes all forms of the internuclear vector containing the factor $(3\cos^2\theta - 1)$ to vanish, greatly reducing the line-width of solid-state spectra.

F.1.9 Cross Polarization

Cross polarization is a double-resonance experiment in which the energy levels of 1 H and 13C spins are matched to Hartman-Hahn condition. The low abundance of ^{13}C leads to poor absorption of the RF pulse in a NMR experiment. This limitation can be over come by exciting the protons in a sample followed by a sequence of two series of long-time pulses which make the ^{13}C and ^{1}H nuclei resonate at the same frequency. The latter is called the "Hartman-Hahn" condition and the process is called "cross-polarization" and the time of cross polarization is called the "contact time" or "spin-lock time". This cross polarization acts as a strong pulse for the carbon 13 nuclei. Under this condition, energy may be exchanged between the two coupled spin systems. The result is growth of the 13 C magnetization at the expense of the 1H magnetization. Cross polarization requires that nuclei are dipolar coupled to one another, and surprisingly, it even works while samples are being spun rapidly at the magic angle (though not if the spinning rate is greater than the anisotropic interaction). Hence the acronym CPMAS NMR (Cross Polarization Magic-Angle Spinning NMR). When combined with MAS, polarization from abundant nuclei like 1H, 19F and 31P can be transferred to dilute or rare nuclei like 13C, 15N, 29Si in order to enhance signal to noise and reduce waiting time between successive experiments.

Solid state ^{13}C-NMR with CP and MAS is particularly useful for the investigation of polymer systems.

Appendix G Basic introduction to Gas Chromatography/Mass Spectrometry (GC/MS) [8,18, 19]

The combination of gas chromatography and mass spectrometry (GC-MS) is a very powerful technique for analyzing organic materials which can be vaporized at or below 250° C and is particularly suitable for the analysis of mixtures of volatile and low relative molecular mass compounds (< 800). In the simplest terms the GC/MS instrument represents a device that separates chemical mixtures (the GC component) and a very sensitive detector (the MS component) with a data collector (the computer component). GC is used to separate the mixture of compounds into its individual component. The mass spectrum of each individual component can be obtained using MS and is searched against the library mass spectra. A mixture of compounds to be analysed is initially injected into the GC where the mixture is vaporized in a heated chamber. The gas mixture travels through a GC column, where the compounds become separated as they interact with the column. Those separated compounds then immediately enter the mass spectrometer. The combination of GC-MS can provide complete chemical information about the unknown mixture, such as molecular weight, chemical formula and molecular structure.

This section provides some basic principles of GC/MS.

G.1 Gas chromatography (GC)

In gas chromatography a mixture of gaseous or semi-volatile compounds (analytes) are passed through a column in a carrier gas stream (helium is frequently used, the carrier gas itself should be inert). The inner walls of the column are coated with a solid substrate. The time required for a given compound to elute from the column depends on

[18] Daniel C. Harris, Quantitative Chemical analysis, 6th edition, W. H. Freeman and Company, New York, 2003

[19] Marvin C. McMaster, Christopher McMaster, GC/MS: A Practical User's Guide, Wiley, 1998.

the level of interaction that occurs between the compound and the solid substrate (the stationary phase). Compounds that interact little with the stationary phase will exist mostly in the carrier gas stream (the mobile phase) and will pass through the column quickly. The level of interaction of the compound with the stationary phase depends on several properties of the compound itself, but as a general rule heavier molecules require more time to elute.

G1.1 The separation process in gas chromatography

The analytes after sampling are placed in the inlet/injector port of the GC where they are vaporized and injected onto the head of the chromatographic column. The injector port is a self sealing, heated body that allows vaporization of the sample and then transfer to the capillary column. A glass liner is used in the port to allow for cleaning and to give a surface suitable for the vaporization of the analyte of interest. A system in the injection port for allowing all or some of the analytes through to the column is called the split/splitless injector. The split injector mode allows for the expansion of the volatilized sample in the case of liquid injections and prevents overloading of the column. The splitless mode is used for trace analysis and SPME fibres where the analytes are pre-concentrated onto a fibre and overloading of the column is unusual.

The sample is transported through the column by the flow of an inert, gaseous mobile phase, the carrier gas. The carrier gas used must be chemically inert to prevent interaction with the analytes; commonly used gases include nitrogen, helium. The column itself contains a liquid stationary phase which is adsorbed onto the surface of a thin fused-silica (purified silicate glass) capillary tube.

G.1.2 GC oven and GC column

The GC oven is a programmable oven designed to run a GC column. The oven temperatures can be programmed to provide a linear ramp which will allow the analytes to achieve separation at different rates thus providing the mass spectrometer with the pure sample for analysis.GC ovens usually require an operating range from about 5˚C to about 400˚C although the majority of GC analyses are carried out between temperatures of 75˚C and 200˚C. Temperature programming is an essential feature of all GC column ovens and is necessary to handle a sufficiently wide molecular and polarity range of samples. Linear programming is the most common although other functions of time are often available. The temperature program can be controlled by a microprocessor

incorporated in the programmer or can be controlled from a central computer that governs the operation of the whole instrument.

The column is used to contain the stationary phase. Columns may be made of glass, stainless steel, plastic and many other materials. Packed GC columns are usually made of stainless steel or glass and open tubular column almost exclusively fused quartz. The GC column can be a packed or open tubular. It is a very long thin tube. Typical lengths for a GC column are 10-100 meters, while the inside diameter of the columns are on the order of 200-530 micrometers. The column itself resides inside of the GC oven. In a typical run the oven will begin at a temperature close to ambient for several minutes. The oven temperature is then slowly increased to a final temperature of 200-250 C for several minutes, for a total run time of 20-40 minutes. These numbers are all general, with actual values depending on many factors.

G.2 Mass Spectrometer (MS)

Mass spectrometry is a technique for separating ions by their mass-to-charge (m/z) ratios. It allows the detection of compounds by separating ions by their unique mass. A mass spectrometer is a device used for mass spectrometry, and produces a mass spectrum of a sample to find its composition. This is normally achieved by ionizing the sample and separating ions of differing masses and recording their relative abundance by measuring intensities of ion flux. All mass spectrometers consist of three distinct regions: 1) Ionizer 2) Ion Analyzer 3) Detector

G.2.1 Ionizer

Ionizer is used to product ions. Two potential methods exist for ion production. The most frequently used method is electron ionisation (EI) and the occasionally used alternative is chemical ionisation (CI).

EI is the classic method for MS ionization and was the dominant technique for many years. In EI the molecules are volatilized with heat. A electron beam (typically 70eV) ionize the sample molecules by electron ejection or electron attachment, resulting in the loss of one electron. A molecule with one electron missing is called the molecular ion and is represented by $M^{+\cdot}$ (a radical cation). When the resulting peak from this ion is seen in a mass spectrum, it gives the molecular weight of the compound. Due to the large amount of energy imparted to the molecular ion it usually fragments producing further smaller ions with characteristic relative abundances that provide a 'fingerprint'

for that molecular structure. This information may be then used to identify compounds of interest and help elucidate the structure of unknown components of mixtures.

EI has high sensitivity and yields a long-lasting stable ion current. Because of the extensive use of EI, standard spectral catalogues are available for comparison and identification purposes. The limitations of EI are primarily the requirement that the sample be vaporized by heating, thus higher mass and thermally labile compoundas may not be amenable to analysis.

CI is based on the use of reagent gas at "high" pressure which softly ionizes a gaseous sample by proton transfer or charge transfer. In CI, the reagent gas at a pressure (about 1 Torr) is subjected to a closed EI source which is of high electron energy (250-500eV rather than 70 eV in EI). If methane is the reagent gas, $CH_4^{+\bullet}$ then encounters a neutral gas molecule. Since the methane is at 1 Torr and the sample gas pressure is at about 10^{-5}-10^{-6} Torr, the most likely encounter is another methane molecule. This encounter produces a reaction that creates CH_5^+ ions and $CH_3^\bullet$ radicals. The primary reactant is usually CH_5^+, which protonates any gas phase sample molecule more basic than methane, thus ionize the sample molecule to produce molecular ions. CI is a less energetic way of ionizing a molecule hence less fragmentation occurs with CI than with EI, hence CI yields less information about the detailed structure of the molecule, but does yield the molecular ion; sometimes the molecular ion cannot be detected using EI, hence the two methods complement one another. Once ionised a small positive is used to repel the ions out of the ionisation chamber.

G.2.2 Ion Analyzer

Molecular ions and fragment ions are accelerated by manipulation of the charged particles through the mass spectrometer. Uncharged molecules and fragments are pumped away. The ion analyzer separates ions according to the mass/charge (m/z) ratio. the type of ion analyzer used determines the mass resolution and the dependence of the resolution on mass. Several types of ion analyzers are used in MS including, such as magnetic sector, quadrupole analyzer, tim-of-flight (TOF), and ion trap

The magnetic sector instrument was the basis of MS spectrometry for many years, it is based on the principle that ionize substances moving through a magnetic field do so in curved paths. Due to momentum characteristics, heavier substances will curve less than lighter ones. Cycling the strength of the magnetic field causes the ions of different masses to strike a detector at different times in the cycle.

A quadrupole analyzer is a mass filter that creates a quadrupole electric or negative field with a direct current component and a radio-frequency (RF) component in such a manner to allow transmission only of ions having a selected mass-to-charge ratio. The system consists of four rods which form the parallel sides of a rectangular tube. Th erods have charges of the same type opposing each other. A DC voltage superimposed on a RF field connected to the quadrupole creates an electric field between the poles. Ions of a known mass will pass through this field and are detected. Variation of the field allows different ions to be detected.

G.2.3 Detector

There are many types of detectors, but most work by producing an electronic signal when struck by an ion. Timing mechanisms which integrate those signals with the scanning voltages allow the instrument to report which m/z strikes the detector. The mass analyzer sorts the ions according to m/z and the detector records the abundance of each m/z. Regular calibration of the m/z scale is necessary to maintain accuracy in the instrument. Calibration is performed by introducing a well known compound into the instrument and "tweaking" the circuits so that the compound's molecular ion and fragment ions are reported accurately.

F.3 GC/MS

Gas chromatography-mass spectrometry (GC/MS) combines the fine separating power of GC with the uniquely powerful detection capabilities of MS. Figure H.1 shows the sketch drawing of GC/MS. It is able to separate a mixture of compounds and identify them accurately leading to an extremely powerful tool particularly when dealing with unknown compounds.

Once the sample solution is introduced into the GC inlet through the sample injector it is vaporized immediately because of the high temperature (250 degrees C) and swept onto the column by the carrier gas. The sample flows through the column experiencing the normal separation processes. As the various sample components emerge from the column opening, they flow into the capillary column interface. This device is the connection between the GC column and the MS. Some interfaces are separators and concentrate the sample via removal of the helium carrier. The sample then enters the ionization chamber. Some of the molecular ions fragment into smaller daughter ions and neutral fragments in the ionization chamber. Both positive and negative ions are formed but only positively charged species will be detected. The next

component is a mass analyzer (filter), which separates the positively charged particles according to their mass. After the ions are separated according to their masses, they enter a detector and then on to an amplifier to boost the signal.

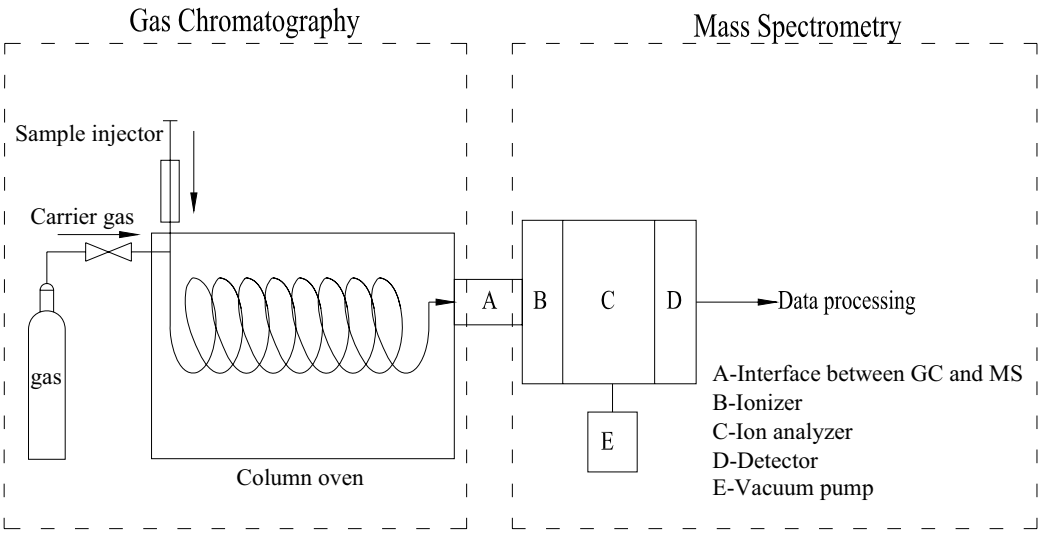

Figure G.1 Schematic of GC/MS